The University of Nottingham

UNITED KINGDOM · CHINA · MALAYSIA

Experimental and numerical investigations of diamond and related materials controlled-depth machining using pulsed laser ablation

Guillaume Bastien Jérémy Cadot

MEng, MSc, BEng

Thesis submitted to the University of Nottingham for the degree of Doctor of Philosophy

Department of Mechanical, Materials and Manufacturing Engineering, Faculty of Engineering.

October 9, 2017

Abstract

Pulsed laser ablation is a non-conventional machining technique that is used to machine complex parts in ultra-hard materials and for minute part geometry, which are otherwise not readily accessible with conventional tooling. The constant development of new materials with enhanced properties, as well as the demand for products with improved functionality have led to a renewed interest for alternative machining. Pulsed laser ablation is regarded as a promising technology with potential to machine a wide range of materials and shapes. The use of non-mechanical methods is advantageous due to the reduced tool-wear for ultra-hard materials and minute geometry. However, these advantages pose significant challenges since the removal rate of the material in term of shape and amount is controlled through a set of operating parameters. It is therefore necessary to have a comprehensive understanding of the process and the relation between such parameters and the effect of the laser on the surface. Furthermore, the process itself is hard to monitor online due to the short temporal and small spatial space it occurs within, and this makes it more complex to establish a detailed understanding of the process, and the optimum parameters to control the machining.

The main objective of this thesis is to develop mathematical frameworks that have the capability to predict the removal rate of pulsed laser ablation for the main operating parameters (feed speed, power, position, etc.) and the physical processes occurring during pulsed laser ablation of diamond and related materials for nanosecond laser pulses at 1064 nm and 248 nm. This is addressed using two modelling approaches: a physical model that simulates the mass and heat conservation in the system coupled with a collisional radiative model for the plasma, and a simplified approach based on geometrical aspect built on the idea that trenches represent the simplest element of the machining method enabling quantification of the relation between the control parameters and the removal rate.

In the physical approach, the system is modelled using the conservation of mass and energy with the capability to accurately predict the position of the interfaces (graphitisation front and surface), and the amount of material removed. The model is validated against boron doped diamond and is used to estimate the activation energy and rate of graphitisation for tetrahedral amorphous carbon. The framework developed provides accurate results for

two different carbon allotropes with a high content of sp^3 bounds for a range of fluence.

A geometrical approach for the prediction of the material removal during large pulsed laser ablation machining task has been developed. Since, the objective of this model is for it to be integrated into Computer-Aided Design/Computer-Aided Manufacturing (CAD/CAM) packages, the model needs to be computationally efficient and should require as little empirical data as possible to be accurately calibrated. This framework has been validated against three materials, graphite POCO AF-5, a mechanical poly-crystalline diamond CVD Mechanical, and a metal-matrix poly-crystalline diamond CMX850. The model enables the prediction of material removal for large machining tasks and is being used with an optimisation procedure for the machining parameters (power, feed speed, etc.) for CAD/CAM packages.

Finally, the physical model is coupled with a collisional radiative model for the plasma, and it enables the prediction of the pressure over the crater. Experimental investigations have confirmed that melting of the graphite only occurs for a fluence over 30 $J.cm^{-2}$. TEM analysis and Raman spectroscopy also show an increase in the disorder of the graphite lattice with an increase of fluence which is coherent with thermal damage and constraint growth of the graphite crystal at the graphitisation front. The fluence threshold for the melting of the graphite lattice is in agreement with the prediction of the model.

The work developed in this thesis contributes to the understanding of the ablation process and graphitisation process during pulsed laser ablation of diamond and related material, and demonstrates how a simplified modelling approach can be used to improve current capabilities of this technology for large micro-machining tasks.

Acknowledgements

To Sophie for helping me making the best possible research and supporting me during the whole time as a PhD. The PhD research and thesis would dramatically worse without her help along the way.

This thesis is the result of the work of many people. I have been constantly supported by my supervisors, Prof. Dragos Axinte and Prof. John Billingham, who were always available for discussions, interested in my work, and encouraging.

I would also like to particularly thank Professor Michael Schimdt and Dr. Tanvir Hussain for their helpful comments about the thesis and the interesting discussion during my Ph.D. viva that greatly improved the quality of this thesis.

I would also like to thank Pablo Lozano Torrubia for always being there to talk with me and listening to my ranting and that, in the end, a discussion cannot end.

This work could have not been possible without my friends and colleagues in the office, who have shared with me the hard work of doing and finishing a PhD. I would also like to thank all the people participating in the STEEP project. They have made it a great experience sharing and working within international group getting the best of the research done within the project. I would like also to thank Amir Rabani for making the STEEP project working smoothly. I would also particularly thank Florence Drouvin without whom the daily life as a PhD student and the administration would have been much more painful.

Finally, I would like to thank all of those who have supported me during this time, since all the experiences and opportunities that I have had during these three years would have not been possible without you.

Publications arising from the thesis

G. B. J. Cadot, D. A. Axinte, and J. Billingham. "Continuous trench; pulsed laser ablation for micro-machining applications". In: *International Journal of Machine Tools and Manufacture* 107 (2016), pp. 8–20. ISSN: 08906955. DOI: 10.1016/j.ijmachtools.2016.04.011. URL: (Link) .

G. B. J. Cadot, J. Billingham, and D. A. Axinte. "A study of surface swelling caused by graphitisation during pulsed laser ablation of carbon allotrope with high content of sp^3 bounds". In: *Journal of Physics D: Applied Physics* 50 (2017), p. 245301. DOI: 10.1088/1361-6463/aa70fe. URL: (Link) .

G. B. J. Cadot, K. Thomas, J. Best, A. Taylor, D. A. Axinte, J. Michler, and J Billingham. "Investigation of the fluence on the micro-structure due to phase transition in nanosecond pulsed laser processing of diamond." In: *Carbon – Under Review –* (2017), pp. 1–36. ISSN: 08906955.

Related publications arising from the thesis

A. Bilbao-Guillerna, D. A. Axinte, J Billingham, and G. B. J. Cadot. "Waterjet and laser etching : the nonlinear inverse problem Subject Category : Subject Areas :" in: *Royal Society Open Science* 4 (2017), p. 161031. DOI: 10.1098/rsos.161031. URL: (Link) .

A. Bilbao-Guillerna, R. Thiruvallur-Eachambadib, G. B. J. Cadot, D. A. Axinte, J. Billingham, and M. Rommel. "Novel approach based on continuous trench modelling to predict focused ion beam prepared freeform surfaces". In: *Applied Surface Science – Under Review* (2017).

Conference arising from the thesis

G. B. J. Cadot, A. Bilbao-Guillerna, D. A. Axinte, and J. Billingham. "Modelling pulsed laser ablation using continuous trench for micro-machining applications". In: *AILU Micro-Nano Workshop*. AILU. 14th September 2016, Southampton, 2016.

Magazine article arising from the thesis

G. B. J. Cadot, J. Mei, A. Bilbao-Guillerna, D. A. Axinte, and J. Billingham. "Dedicated software platform simulates laser machining". In: *The Laser User* 83 (2017), pp. 34–35.

Contents

List of Figures

List of Tables

List of Listings

Glossary

DLC Diamond Like Carbon, a family of carbon material exhibiting a non-negligible proportion of sp3 liaison between the carbon atoms. These materials display diamond like properties for hardness and strength[8]. 1

PE Primary Electrons, the electron beam accelerated in the column of a scanning electronic microscope,[9]. 92

Acronyms

AFM Atomic Force Microscope. 111

AWJ Abrasive Water Jet. 1, 3, 70, 71

BSE Back-Scattered Electrons. xiv, xxi, 92, 93, 106, 255–258, 260, 261

BWF Breit-Wigner-Fano. 98, 99

CAD/CAM Computer-Aided Design/Computer-Aided Manufacturing. iii, 2, 5, 6, 73, 75, 76, 149, 150, 246, 250

CCD Charge-coupled device. 95, 96

CR Collisional-Radiative. 44, 55, 248

DLC Diamond Like Carbon. 1, 6, *Glossary:* DLC

EDM Electrical Discharge Machining. 1, 3

EM Electro-Magnetic. 11, 12

EOS Equation Of State. 6, 28–31, 35–37, 55–57, 249

FIB Focused Ion Beam. 1, 3, 102, 104–106, 108

IR Infra-Red. 20, 42–44, 95, 242

KL Knudsen Layer. 26, 27

LIP Laser Induced Plasma. 248, 249

LTE Local Thermal Equilibrium. 22, 44

PE Primary Electrons. 92, 93, 255–258, 260, *Glossary:* PE

PLA Pulsed Laser Ablation. viii, xi, xxi, 1–8, 14, 32, 56, 71, 72, 74–76, 91, 149, 150, 240, 241, 243–247, 249, 250, 257

PLM Pulsed Laser Machining. 2

R&D Research and Development. 3

SE Secondary Electron. xxi, 92, 93, 106, 256–260

SEM Scanning Electron Microscope. xiv, 7, 91–93, 105, 106, 111, 260, 261

ta-C Tetrahedral amorphous carbon. 113, 247

TEM Transmission Electron Microscope. 7, 102, 103, 106

UV Ultra-Violet. xiii, 41–44, 95, 100

VIS Visible light. xiii, 41–44, 95, 242

WLI White-Light Interferometer. xvi, 109–111

Nomenclature

Physical and mathematical constants

a_0	Bohr Raduis, [m]
k_B	Boltzmann Constant, $\left[\mathrm{m}^2 \cdot \mathrm{kg} \cdot \mathrm{s}^{-2} \cdot \mathrm{K}^{-1}\right]$
m_C	Mass of the carbon atom, [kg]
$\mathtt{e}$	Charge of the electron, $[\mathrm{A} \cdot \mathrm{s}]$
$m_{\mathtt{e}^-}$	Mass of the electron, [kg]
$\mathfrak{R}$	Ideal gas constant, $\left[\mathrm{kg} \cdot \mathrm{m}^2 \cdot \mathrm{K}^{-1} \cdot \mathrm{s}^{-2} \cdot \mathrm{mol}^{-1}\right]$
$\mathfrak{E}_{ion}^{\mathrm{H}}$	Ionisation energy of an hydrogen atom, $[\mathrm{kg} \cdot \mathrm{m}^2 \cdot \mathrm{s}^{-2}]$
π	Mathematical constant Pi
$\mathtt{h}$	Planck constant, $[\mathrm{m}^2 \cdot \mathrm{kg} \cdot \mathrm{s}^{-1}]$
Ry	Ryberg energy, $[\mathrm{kg} \cdot \mathrm{m}^2 \cdot \mathrm{s}^{-2}]$
$\mathtt{c}$	Speed of light in the vacuum, $[\mathrm{m} \cdot \mathrm{s}^{-1}]$
ε_0	Vacuum permittivity, $\left[\mathrm{A}^2 \cdot \mathrm{s}^4 \cdot \mathrm{kg}^{-1} \cdot \mathrm{m}^{-3}\right]$

Symbols

$\mathrm{C}_\mathrm{j}^\mathrm{k}$	Symbol for the carbon heavy species belonging to the j-th level and the k-th charge state
$\partial_x \{y(x)\}$	Symbol for the partial derivative for the function y(x) with respect to the variable x
$\mathtt{e}^-$	Symbol for the electron
$\mathtt{d}_x \{y(x)\}$	Symbol for the total derivative for the function y(x) with respect to the variable x

Variables

$\mathcal{A}$	Ablation rate used for the model described in Chapter 5, $[\mathrm{m} \cdot \mathrm{s}^{-1}]$
α	Absorption coefficient of the material, $[\mathrm{m}^{-1}]$

$\mathtt{E}_a$ Activation energy for the graphitisation, $[\mathrm{kg} \cdot \mathrm{m}^2 \cdot \mathrm{s}^{-2}]$

$\mathbf{Z}^{k+}$ Charge of the heavy species with an ionisation degree k, dimensionless

ς Effective Cross section for the atomic process such as Inverse Bremstrahlung for neutral electron ($\varsigma_{IB}^{n,e}$), single photoionisation (ς_{PI}), etc., $[\mathrm{m}^2]$

$[\mathtt{e}^-]$ Density of the electrons, $[\mathrm{m}^{-3}]$

$\Xi\left(\right)$ Effective energy transfer for an atomic process such as Inverse Bremstrahlung for neutral electron ($\Xi_{n,e}\left(IB\right)$), single photoionisation ($\Xi\left(PI\right)$), etc., $[\mathrm{s}^{-1}]$

$\left[\mathrm{C}_{\mathrm{j}}^{\mathrm{k}}\right]$ Density of the carbon heavy species belonging to the j-th level and the k-th charge state, $[\mathrm{m}^{-3}]$

ρ Density of the material, $[\mathrm{kg} \cdot \mathrm{m}^{-3}]$

D Thermal Diffusivity of the material, $\mathrm{D} = \frac{\kappa}{\rho c_p}$, $[\mathrm{m}^2 \cdot \mathrm{s}^{-1}]$

d Spatial length, $[m]$

$A^*_{\mathrm{C}_{\mathrm{i}}^{\mathrm{k}} \rightarrow \mathrm{C}_{\mathrm{j}}^{\mathrm{l}}}$ The Einstein coefficient for the spontaneous emission between the fictitious electronic levels $\mathrm{C}_{\mathrm{i}}^{\mathrm{k}}$ and $\mathrm{C}_{\mathrm{j}}^{\mathrm{l}}$, $[\mathrm{s}^{-1}]$

$A_{\mathrm{C}_{\mathrm{i}}^{\mathrm{k}} \rightarrow \mathrm{C}_{\mathrm{j}}^{\mathrm{l}}}$ The Einstein coefficient for the spontaneous emission between the electronic levels $\mathrm{C}_{\mathrm{i}}^{\mathrm{k}}$ and $\mathrm{C}_{\mathrm{j}}^{\mathrm{l}}$, $[\mathrm{s}^{-1}]$

ϵ Kinetic energy for an atomic processes such as Inverse Bremstrahlung, photoionisation, etc., $\left[\mathrm{kg}^2 \cdot \mathrm{m}^2 \cdot \mathrm{s}^{-2}\right]$

$F_{\rho e,}$ Energy flux, $[\mathrm{kg} \cdot \mathrm{s}^{-3}]$

E_p Energy per pulse of the laser, $[\mathrm{kg} \cdot \mathrm{m}^2 \cdot \mathrm{s}^{-2}]$

E Total energy, $[\mathrm{kg} \cdot \mathrm{m}^2 \cdot \mathrm{s}^{-2}]$

$\Delta\mathfrak{E}_{i,j}^{k,n}$ Energy difference between the electronic level belonging to the the i-th level and the k-th charge state and the j-th level and the n-th, $\Delta\mathfrak{E}_{i,j}^{k,n} = \mathfrak{E}_j^n - \mathfrak{E}_i^k$, $[\mathrm{kg} \cdot \mathrm{m}^2 \cdot \mathrm{s}^{-2}]$

$\mathfrak{E}_j^k$ Energy of the electronic level belonging to the the j-th level and the k-th charge state, $[\mathrm{kg} \cdot \mathrm{m}^2 \cdot \mathrm{s}^{-2}]$

$\Theta\left(\right)$ Effective energy transfer for an atomic process such as Inverse Bremstrahlung for neutral electron ($\Theta_{n,e}\left(IB\right)$), single photoionisation ($\Theta\left(PI\right)$), etc., $\left[\mathrm{kg}^2 \cdot \mathrm{m}^2 \cdot \mathrm{s}^{-3}\right]$

H Enthalpy of the system, $[\mathrm{kg} \cdot \mathrm{m}^2 \cdot \mathrm{s}^{-2}]$

G Gaunt factor for the species considered, dimensionless

κ Heat conductivity of the material, $\left[\mathrm{kg} \cdot \mathrm{m} \cdot \mathrm{s}^{-3} \cdot \mathrm{K}^{-1}\right]$

S Heat source for the heat equation, $[\mathrm{kg} \cdot \mathrm{m}^2 \cdot \mathrm{s}^{-3}]$

$\mathfrak{i}(t)$ Instantaneous intensity of laser pulse, $[\mathrm{kg} \cdot \mathrm{s}^{-2}]$

ΔH Enthalpy of transition between phases such as liquid $\rightarrow$ gas, solid $\rightarrow$ liquid, etc., $[\mathrm{kg} \cdot \mathrm{m}^2 \cdot \mathrm{s}^{-2}]$

κ Imaginary part of the complex refractive index for a medium, dimensionless

$\bar{\epsilon}$ Normalised electron kinetic energy to the specific energy between the two levels, $\Delta\mathfrak{E}_{i,j}^{k,l}$, for the transition considered, dimensionless

ν_{laser} Frequency of the laser wavelength such as $\mathsf{c} = \lambda\nu_{\mathrm{laser}}$, $[\mathrm{s}^{-1}]$

ω_0 Radius of a $\mathrm{TEM}_{(00)}$ laser pulse after the focusing element at the focal plan, [m]

f_l Pulse repetition frequency of the laser, $[\mathrm{s}^{-1}]$

λ Wavelength of the laser wave such as $\mathsf{c} = \lambda\nu_{\mathrm{laser}}$, [m]

M Mach Number, dimensionless

$F_{\rho,}$ Mass flux, $[\mathrm{kg} \cdot \mathrm{m}^{-2} \cdot \mathrm{s}^{-1}]$

m Mass of the system or particle, [kg]

Υ, χ and r^* Parameters of the simplified ablation rate, $\mathcal{A}$, model presented in Chapter 5, $[\mathrm{m}^2 \cdot \mathrm{s}^{-1}]$, [m] and [m] respectively.

M Molar mass of the system, $\left[\mathrm{kg} \cdot \mathrm{mol}^{-1}\right]$

$\mathcal{Z}^k$ Partition function of the k-th charge state, dimensionless

s Arc length of a curve, [m]

z Position of the first axis in the system of reference and the position of specific area of interest such as interfaces, depth of material ablated, [m]

r Radial distance such that the radial distance between the centre of the beam and the position of the point on the surface, [m]

y Position of the third axis in the system of reference and the position of specific area of interest such as interfaces, depth of material ablated, [m]

x Position of the second axis in the system of reference and the position of specific area of interest such as interfaces, depth of material ablated, [m]

$\underline{x}$ Vector position on a planar surface such as $\underline{x} = (x, y)$, ([m],[m])

$\mathcal{P}_{\mathrm{p}}$ Peak power of the laser pulses, $[\mathrm{kg} \cdot \mathrm{m}^2 \cdot \mathrm{s}^{-3}]$

$\mathcal{P}$ Average power of the laser, $[\mathrm{kg} \cdot \mathrm{m}^2 \cdot \mathrm{s}^{-3}]$

P Pressure, $[\mathrm{kg} \cdot \mathrm{m}^{-1} \cdot \mathrm{s}^{-2}]$

p Profile of a trench, [m]

C_r Rate of graphitisation for the Arrhenuis law of the graphitisation rate, $[\mathrm{m} \cdot \mathrm{s}^{-1}]$

γ Ratio of the isochoric specific heat and the isobaric specific heat, dimensionless

m Reduced Mach Number, dimensionless

R Reflectivity of the electro-magnetic wave at the interface between two materials with different complexe refractive index

e Specific energy density of the system, $[\mathrm{m}^2 \cdot \mathrm{s}^{-2}]$

Δh Specific enthalpy of transition between phases such as liquid $\rightarrow$ gas, solid $\rightarrow$ liquid, etc., $[\mathrm{m}^2 \cdot \mathrm{s}^{-2}]$

h Specific enthalpy of the system, $[\mathrm{m}^2 \cdot \mathrm{s}^{-2}]$

c_p Specific heat of the material, $\left[\mathrm{m}^2 \cdot \mathrm{s}^{-3} \cdot \mathrm{K}^{-1}\right]$

g_j^k Statistic weight for the j-th electronic level of the k-th charge state, dimensionless

Z_s Position of the surface using a planar reference system such as Z_s is only dependent on x, y and the time t, [m]

T_{c_i} The critical temperature as defined in a phase diagram for the material i, [K]

T Temperature of the system (solid target, species, plasma, etc.), [K]

τ Temporal length, $[s^{-1}]$

t Time of the system, [s]

$\underline{B}$ Magnetic field vector, $\left[\mathrm{kg} \cdot \mathrm{s}^{-2} \cdot \mathrm{A}^{-1}\right]$

$\underline{E}$ Electric field vector, $\left[\mathrm{kg} \cdot \mathrm{m} \cdot \mathrm{s}^{-3} \cdot \mathrm{A}^{-1}\right]$

$\underline{n}$ Complex refractive index for a medium, dimensionless

v Speed of the interfaces, fluids, solids , etc., $[\mathrm{m} \cdot \mathrm{s}^{-1}]$

D Diameter of a $\mathrm{TEM}_{(00)}$ laser pulse before the focusing element, [m]

E_p Energy per pulse of the laser, $[\mathrm{kg} \cdot \mathrm{m}^2 \cdot \mathrm{s}^{-2}]$

n Real part of the complex refractive index for a medium, dimensionless

W_c Work needed to reach the critical size for a thermodynamic stable spherical phase from a metastable phase, $[\mathrm{kg} \cdot \mathrm{m}^2 \cdot \mathrm{s}^{-2}]$

z_R Rayleigh length of the focused beam along the propagation axis, [m]

Chapter 1

Introduction

1.1 Motivation

High demand for materials with superior wear resistance, high hardness, low thermal conductivity, high thermal resistance and chemical stability dictates research in material science. However, their properties make them difficult to machine. Development of new materials requires the use of new machining techniques such as Abrasive Water Jet (AWJ), Electrical Discharge Machining (EDM) and Pulsed Laser Ablation (PLA). They enable efficient machining of materials such as diamond, Diamond Like Carbon (DLC) and super-alloys of Titanium, Aluminium and Nickel. Conventional techniques such as milling, drilling and turning are not effective for machining of complex geometry components in ultra-hard material such as diamond composites. These processes usually lead to extensive tool wear [10] (limited cost effectiveness) or damage to the surface of the material during the manufacturing process [11–13] (quality of the resulting workpiece).

The research contained in this thesis has been carried out within the context of the STEEP ITN [14] project, a Marie Curie Initial Training Network focused on the machining by energy beams (AWJ, PLA and Focused Ion Beam (FIB)) modelling, control and characterization of the surface and subsurface after material processing. The main objective of the STEEP project is to develop a model-based path optimization capability to detach the machining from the "soft" tool issues for PLA, AWJ and FIB. For conventional

machining, a hard tool is pushed against the processed materials. This strains the material and leads to elastic deformation, plastic deformation and fracture. The strain created by the tool is the direct cause of the material removal. The strain does not extend far away from the contact area therefore the removal of the material is precisely located around the shape of the tool. For "soft" tools, the removal rate does not have a finite shape hence the rate of removal have not an intrinsic shape. Within the STEEP modelling framework, the removal rate can be estimated using a empirically calibrated model. The development of a numerically efficient model in a CAD/CAM is the first step towards a wider use for these technologies as advanced machining processes.

Pulsed Laser Machining (PLM) is one of the most investigated non-conventional machining techniques. Laser machining is an eco-friendly and contact-free manufacturing technique. Industrial lasers have a very long life-time compared to conventional tools and the development of laser technology during the last three decades has resulted in lasers with shorter pulses and higher power. It is now affordable for most companies to have high power pulsed lasers for manufacturing processes. With pulsed laser ablation, it is now possible to concentrate a large amount of energy on a very small volume. This enables the development of a collection of new technologies [15]. Pulsed laser machining is also the focus of a lot of attention from the public body for advanced research in laser processing technologies. Several projects focused on laser machining have been founded during the FP7 framework. Some of these projects reinforce the laser capability in terms of new wavelength, increased power or in-line beam shaping capability for industrial uses [16–18]. Some of the projects focus on improving the machining process for free-form shaping [14, 19, 20]. There are also projects supporting the development of new machining technologies and improving PLA applicability [21]. For the last 20 years, there has been a colossal effort in the development of

beam delivery systems and in-line beam shaping capabilities. All of these innovations have generated an extensive industrial sector relying on laser technologies [22]. The growing laser market represents $9.33B globally, 25% of which is for material processing. Research and Development (R&D) and military represent 7% of this market.

Thus, PLA is one of the most promising techniques for the processing of high hardness and superior wear resistance as the material removal mechanisms are not based on the generation of stress in the material. The deposition of a large amount of energy in a localised space generates a huge increase of temperature (for high energy pulses the temperature can reach the critical temperature T_c [23, 24]), which vaporises the material. PLA is also an interesting tool for micro-nano manufacturing [25–28]. The size of the tool is only limited by the diffraction limit. In practice the beam spot, defined at $1/e^2$ of the diameter, can be as small as 15μm. This gives great accuracy for the removal of material in a specific area and the production of microns size features and nano-scale texturing. The processing rate of PLA is also very high compared to FIB for the same tasks. PLA also offers new possibilities of machining that are not possible with traditional techniques. PLA enables the manufacturing of innovative 3D shapes which it is not possible to manufacture using traditional machining such as EDM, AWJ, etc. due to the small scale and mechanical properties of the final workpiece. It is now possible to pattern the surface of ultra-hard materials with a specific density and shape of abrasive element to produce the desired removal rate [29]. The advanced manufacturing technology research group at University of Nottingham has a strong experience processing diamond and related materials for industrial applications and is member of DIPLAT [20], a European project consortium demonstrating the capabilities of the laser for advanced functionalities on ultra-hard materials.

Nevertheless, there are still significant challenges to address in order to deliver the full potential of PLA, and its promising capabilities are still under investigation for research and industrial purposes. These challenges are presented in the following sections.

1.2 Research problem

Pulsed laser ablation is already used to produce free-forms based an extensive empirical analysis of a number of iterations for the beam path strategy (in term of the beam path, feed speed, power, etc.). The machining process relies on a large amount of experimental trials so it is an expensive and unreliable process for industries. Mathematical modelling is key for the development of pulsed laser ablation machines for free-form milling. It enables the generation of micro-features in a predictable and repeatable manner. This is challenging because the removal process is highly non-linear, highly dependent on the material's optical and thermal properties and on the properties of the laser. The amount of material removal depends on many parameters and interdependency of these parameters is not yet fully understood. The phenomena during PLA are still a research subject; the relation between the power of the laser, the feed speed, the polarization of the laser and the material have not been entirely explored. PLA is a particularly difficult phenomenon to model because it involves several physical domains such as atomic physics, plasma physics, thermodynamics, fluid mechanics and electromagnetisms. A full description of the physics during laser ablation is a complicated matter that has never been fully attempted. Additionally, PLA causes the material to reach a temperature close to critical temperature and a pressure of up to 2 GPa [30]. In this domain, the properties of the materials have been poorly studied and a major

lack of thermodynamics and optical data hamper the attempts to produce an accurate model for high energy ablation [30]. Physical studies have shown a far-reaching association of different physical domains (thermodynamics, plasma physics, fluid mechanics, etc.) [30–35]. Diamond and related material have been relatively well experimentally studied [28, 29, 36–38]. However, the physics behind the ablation rates of diamond and related material might not well understood, mainly due to the lack of models for the ablation of diamond considering the dynamics position of the interfaces (graphite to diamond and the surface) and the change of density during the transition between diamond to graphite. Compared to most materials, diamond and related materials transform into graphite during laser ablation therefore particular questions need to be addressed in the modelling that have not yet been fully addressed in the literature. An improved understanding of diamond ablation will enable the determination of an appropriate machining parameters reducing thermal damages and optimising machining time to generate free-forms.

In order to improve the applicability of PLA, a numerical model for CAD/CAM must be developed. Significant work has already been published to address this issue [39–43]. The model is currently able to predict the footprint as a function of the power and the surface texture. Particular attention has been given to overlapping of pulses and provides relatively accurate results for low overlapping pulses [40]. The future model must fully address the question of the overlapping for a range of materials. The development of new mathematical models for PLA is challenging due to the following reasons:

1. PLA is a soft tool because is does not have mechanical contact with the workpiece. The amount of material removed is dependent on the machining energy-dependent parameters (power, beam shape), the surface texture of the processed materials of the workpiece and the

kinematic parameters of the beam such as feed speed and angle of interaction. It is difficult to separate the influence of each parameter. The determination of the influence of each parameter is key to the development of a CAD/CAM model.

2. The influence of the material is important. The ablation rate is highly dependent on the material characteristics. Different workpiece materials are ablated very differently, for example graphite does not exhibit any redeposition and melting whereas materials such as Aluminium and Silicon present large melted areas and redeposition. The study needs to be done on several materials to verify the universality of the modelling proposed approach.

3. PLA is by definition multi-physical. The interaction between the physics is complicated and deeply rooted. The physical modelling of PLA is complex and requires experience in multiple physical domains. The physical simulation of diamond and related material requires the development of a new modelling framework for the density jump at the transition between the graphite and the diamond.

4. The physical description of PLA requires large quantities of experimental data up to extremely high temperatures. The thermal and optical data available are scarce, especially for DLC [8], due to experimental limitation for the measurement of properties of thin film materials. The complete simulation of carbon material requires the availability of Equation Of State (EOS) [23] for all the allotropes of carbon over the range of temperature and pressure [32, 44] occurring during the ablation which are currently unavailable to the public. Furthermore, the graphitisation process is a metastable process thus it cannot be predicted using only the EOS of carbon. Therefore, it is necessary to

investigate the material properties for the allotropes of carbon used in the literature.

5. Another significant challenge is that online control systems for PLA are still in a developmental stage due to the difficulty in observing the process during machining. This makes it difficult to monitor the instantaneous relation between the process parameters (feed speed, power, etc.) and process footprint on the target surface. It is therefore necessary to relate the parameters of the system to measurements (surface measurements, SEM, Transmission Electron Microscope (TEM), Raman spectroscopy, etc.).

1.3 Objectives of the study

The main goal of the study is to improve the understanding of diamond and related materials PLA and to provide a reliable geometrical model for large machining tasks. This goal is divided into several objectives in an attempt to establish a detailed knowledge of the ablation processes and determine the relevant parameters for the machining of diamond and related materials. The specific objectives of the study are:

1. The construction of a model for the understanding of the phenomena occurring during pulsed laser ablation of carbon allotropes with high content of sp^3 bounds. The model should be based on a new framework including the jump of density at the diamond-graphite interface. Appropriate research of experimental data should be completed to ensure good results for high fluence tests. This study with a physical model gives an insight to the process on a fundamental level.

2. Investigation of the physical processes leading to swelling of the surface

and the ablation of the surface for the interaction between the diamond and nanosecond laser pulse which allows high removal rates. Since the model will predict graphitisation for any carbon allotropes with high content of sp^3 bounds, it should be validated for at least two different types of carbon allotrope to provide evidence of versatility. A particular focus will be given to the position of the interfaces.

3. The development of a new continuous modelling framework for PLA. It will specifically take into account the overlapping of pulses and enable the accurate prediction of large machining tasks. Similarly, a calibration procedure for the continuous model will be developed such that an operator is able to calibrate in a reasonable amount of time. Since the new framework is embedded as part of a CAD/CAM package, it should be simple enough to be calibrated using a minimal amount of empirical data and the computational cost of the model should be as small as possible to enable the simulation of topography changes for several tens of thousand of pulses.

4. In addition to the development of the new methodology for the modelling framework and associated calibration procedure, the model will be validated for several materials to provide evidence of the versatility of the model. The model will be validated for three carbon allotropes such as graphite, a pure mechanical diamond grade and a metal-matrix polycrystalline diamond such as CMX850.

5. In addition to the new mathematical framework for PLA, a detailed study of the thermal load effect on the target micro-structure for diamond is required to enhance the current understanding of the phenomena. The study of a single pulse laser ablation will provide a fundamental understanding of the ablation mechanisms. This will

be carried through the investigation of the crater using Raman spectroscopy or TEM analysis to investigate the micro-nano crystalline structure of the graphitic material after the ablation.

Chapter 2

Literature review

Given the growing demand and use of pulsed laser systems in research and industry, there has been extensive research into the improvement of pulsed laser system capabilities, understanding, and range of applications. In this chapter, a comprehensive review of the available literature is presented for the physical phenomena occurring during pulsed laser ablation and the mathematical tools used to support the development and understanding of the technology. First, a comprehensive description of the removal mechanisms during nanosecond pulse laser ablation is presented including the material ejection, evaporation, and volumetric removal with the modelling strategy employed. Then, a detailed review of the different modelling approaches for the nanosecond ablation of high sp^3 bonds carbon allotrope is given, including models using the conservation of momentum, mass and energy to calculate the evolution of the physical system. Simplified approaches focussing on the geometrical description of the material removal are also presented for pulsed laser ablation. Finally, a summary is given of the current gaps in knowledge that have motivated the development of this work.

2.1 Ablation mechanisms during pulsed laser ablation

As explained previously, laser radiation is focused on the target, causing a temperature increase in the material. In this section, the mechanisms leading

to the removal/ablation of the target are explained.

2.1.1 Reflection mechanisms

Laser radiation is essentially an Electro-Magnetic (EM) wave, which is associated by an electric ($\underline{E}$) and a magnetic ($\underline{B}$) field vector. During contact with the interface, the change of refractive index induces a reflection of a part of the incident energy. Using Snell's law,

$$\sin \underline{\theta}_t = \frac{\underline{n}_1}{\underline{n}_2} \sin \underline{\theta}_i, \tag{2.1}$$

with $\underline{\theta}_t$, $\underline{n}_1$, $\underline{n}_2$ and $\underline{\theta}_i$ respectively the complex angle of transmittance, the complex refractive index of the incident material, the complex refractive index of the transmitted material, and the complex angle of incidence, and using the Fresnel formulae,

$$r_{\parallel} = \frac{\underline{n}_2 \cos \underline{\theta}_i - \underline{n}_1 \cos \underline{\theta}_t}{\underline{n}_2 \cos \underline{\theta}_i + \underline{n}_1 \cos \underline{\theta}_t} a_{\parallel} \tag{2.2}$$

$$r_{\perp} = \frac{\underline{n}_1 \cos \underline{\theta}_i - \underline{n}_2 \cos \underline{\theta}_t}{\underline{n}_1 \cos \underline{\theta}_i + \underline{n}_2 \cos \underline{\theta}_t} a_{\perp} \tag{2.3}$$

$$t_{\parallel} = \frac{2\underline{n}_1 \cos \underline{\theta}_i}{\underline{n}_2 \cos \underline{\theta}_i + \underline{n}_1 \cos \underline{\theta}_t} a_{\parallel} \tag{2.4}$$

$$t_{\perp} = \frac{2\underline{n}_1 \cos \underline{\theta}_i}{\underline{n}_1 \cos \underline{\theta}_i + \underline{n}_2 \cos \underline{\theta}_t} a_{\perp} \tag{2.5}$$

the amount of light that is reflected and transmitted can be computed [45]. The equations show that the proportion of light reflected/transmitted also depends on the direction of the field oscillation in the plane formed by the propagation vector of the light and the normal to the plane of the reflecting surface. The part of the field that oscillates in the plane, called p-polarised ($r_{\parallel}$ and $t_{\parallel}$), is less reflected than the part that oscillates perpendicularly to the plane, called s-polarised ($r_{\perp}$ and $t_{\perp}$). For a low incidence angle, $\underline{\theta}_i$, the

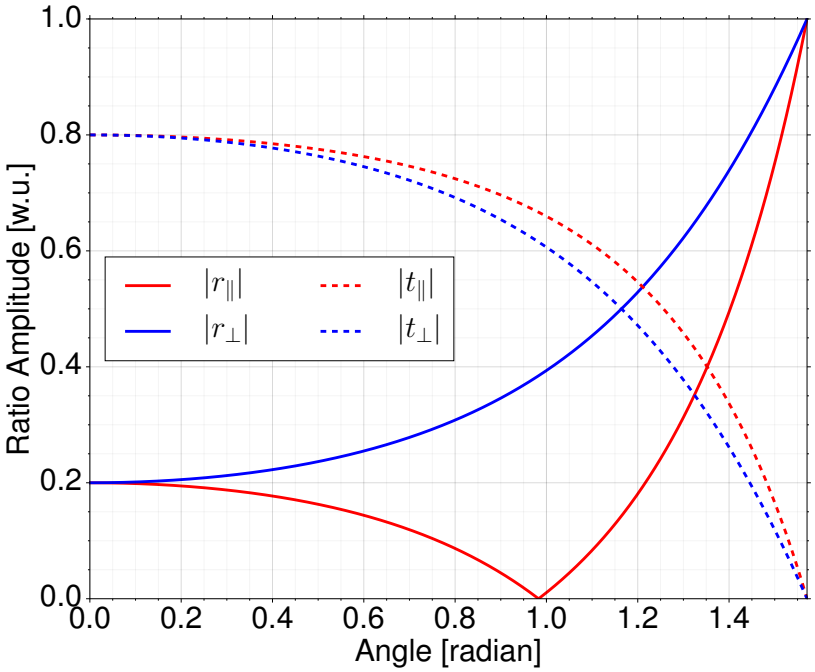

Figure 2.1 : The absolute ratio of the amplitude of the reflected and transmitted wave compared to the incident wave in the case of a reflection between air ($n_1 = 1$) and glass ($n_2 = 1.5$) as a function of the incident angle and for the two polarisations.

reflection coefficient, R, weakly depends on the polarisation, see Figure 2.1. Moreover, the reflection coefficient is almost constant for a low incidence angle. For modelling of the interaction between a single pulse of laser with the target, the ablation depth is rarely greater than 6 µm and the maximum incidence angle between the normal of the surface and the propagation vector of the EM fields is less than 20°. Therefore, the reflection coefficient can usually be considered as a constant [46, 47].

For the case of the interaction between a transparent medium (such as air or vacuum) and an opaque medium (metal) at perpendicular incidences, it is found that the reflectivity is equal to:

$$R = \frac{(n_2 - n_1)^2 + \kappa_2^2}{(n_2 + n_1)^2 + \kappa_2^2}. \tag{2.6}$$

Interestingly, the reflectivity depends on the imaginary part of the complex

refractive index which is related to the absorption coefficient,

$$\delta_p = \frac{1}{\alpha} = \frac{\lambda}{4\pi\kappa}, \tag{2.7}$$

The reflection is therefore important for materials with high absorption, such as metals. Usually, Equation 2.6 is used to calculate the amount of reflected energy during pulsed laser ablation [48]. All the theoretical calculations done in previous studies have assumed that the transition between the two media is along a straight line.

However it must be noted that this assumption is, for certain cases, inappropriate to correctly model the absorption of laser by the target. The fundamental work done by Bergström [49] during his doctoral thesis is particularly interesting with regards to the understanding of the scattering and total absorption of the light by rough metal surfaces. The study of light scattering as a function of the surface roughness using Fresnel-equations and 3D ray-tracing shows that the total absorption is highly dependent on the surface roughness and can increase by up to five times the value of the smooth surface [49, p.181–209]. It must be noted that the increase in the total absorption is due to the increase in the average number of scattering events. With ϵ_l a finite amount of energy transported by a beam of light, the energy remaining after n interactions is equal to

$$\epsilon_l(n) = \epsilon_l \prod_{k=1}^{n} R(\theta_i(k)), \tag{2.8}$$

with $R(\theta_i(k))$ the value of the reflectivity coefficient during the k^{th} scattering event. This equation shows that if the reflectivity coefficient is low (e.g. semi-conductor/insulator), the increased number of scattering events does not significantly enhance the amount of energy absorbed by the target, since the first scattering event transfers most of the beam energy to the target, see

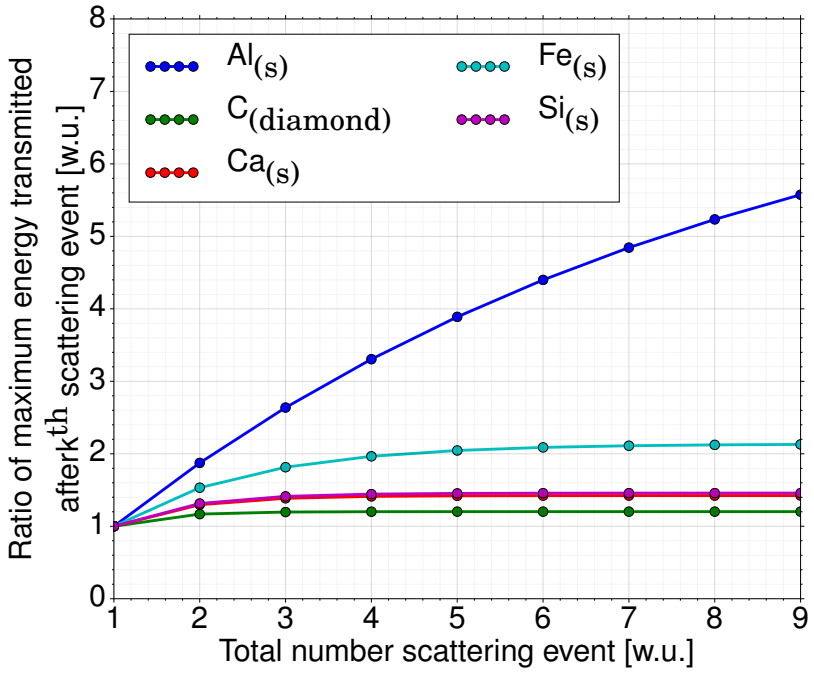

Figure 2.2 : Ratio of the maximum absorbed energy for a beam over the energy absorbed after the first scattering event as a function of the number of scattering events for a non polarised beam.

Figure 2.2. In contrast, multiple scattering is efficient for materials with a high reflectivity coefficient such as Aluminium, see Figure 2.2. Although the maximum energy deposited increases with the number of scattering events, the spatial distribution of the energy transmitted cannot easily be retrieved. A full 2D/3D ray-tracing method must therefore be applied to extract the real distribution. There are a few examples in the literature that have considered the variation of the distribution with the surface topography for PLA [35, 50]. These studies found that the spatial distribution is affected by the aspect ratio of the crater. For a low aspect ratio (when the crater depth divided by the crater width is inferior to 0.5) the spatial distribution is homogeneous over the whole crater, whereas for high aspect ratios (> 2) the energy deposited is concentrated in the centre of the crater due to multiple scattering. The ray-tracing method is efficient to compute the refracted ray but requires a lot of precomputing [51] or simplification of the surface profile [35], which can be

complicated or computationally expensive to execute for a changing surface.

Another method for determining the spatial distribution of the beam into the target is to solve the full Maxwell systems [52, 53]. The main advantage of this method compared to a ray-tracing model is that the profile of the surface is implicitly taken into account and does not require special treatment of the interface between materials. However, the system needs to be solved for the whole set of elements in the simulation and can require a large amount of computational time especially for small wavelengths. In effect, the minimum size of the element needs to be at least 5 elements per wave length to correctly resolve the electric field [52].

The optical properties of the material only change during phase transition [31] ($Al_{(s)} \rightarrow Al_{l}$) and are usually considered as independent of temperature. This approach is limited and more recent studies offer a more comprehensive approach for the variation of the optical properties with temperature. For metal, it is possible to obtain the optical properties from the electrical resistivity using an adapted Drude model for the particular material [54, 55]. The variation of the optical properties over the material is commonly applied only at the surface. This is usually a good approximation for the evaluation of the absorption and reflection of the energy in the material since the variation of optical properties with temperature is often lower than 1 order of magnitude. However the approximation is not valid if the variation is large on a small length scale, as presented by Lutey [54]. Using the conservation of electrical and magnetic fields at the interface between the elements, it is possible to calculate the transmission and reflection of the electro-magnetic flux in the backward and forward direction for a 1D model. The precise evaluation of the difference between the approach used by Lutey [54] and variation of the properties only with the surface temperature is not presented. Therefore, quantitative evaluation of the new methods is not possible. It

must be noted that determination of the electromagnetic field in the material might only be achieved using the Maxwell equations due to the characteristic size of the temperature variation. In effect, the geometrical optics cannot be applied if the variation of refractive index occurs in a distance smaller than the wavelength.

Once the material passes the interface between the vacuum/air and the material, the photon will directly interact with the bulk of the material. The interaction between the light and bulk occurs mainly through the response of the electron to the oscillating electro-magnetic field. In the next section, this complex interaction between the photon and the lattice through the electron will be described in detail. The well known categorisation of material between metal, semiconductor and insulator is primordial in the description of the interaction between the photon and the lattice.

2.1.2 Laser absorption mechanisms

The initial mechanisms that convert the light from the laser beam into heat involve excitation of the electrons to states of higher energy. The discontinuous electronic energy levels of a single atom interacting with the rest of the atoms in the lattice generate an energy band for which the fine energy structure is not distinguishable. The electrons in the crystal fill the lowest energy band available until no electrons are left. The energy state of the highest energy electron at absolute zero is called the Fermi level, and is the level for which no electron will have enough energy to rise above. Using the band structure diagram and the Fermi level it is possible to gain information about the optical properties of the solid. The absorption of the light by the electron in the lattice requires the existence of an attainable energy state.

In the case of metal, as it is for gold in Figure 2.3, the electrons can move

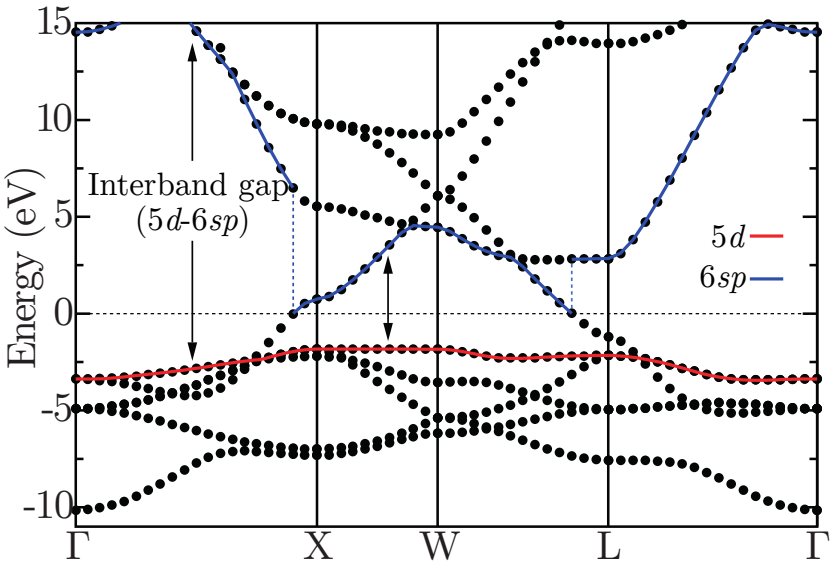

Figure 2.3 : The energy band structure of gold from Rangel et al. [56]. The red line shows the topmost occupied band for the 5d level while the blue line indicates the 6sp-like bottommost empty band. The energy level is referenced to the Fermi level.

freely within energy bands, therefore electrons absorb low energy photons. For gold, the Fermi level crosses the 6sp band allowing the electrons to continuously move to a higher energy state in the fine structure of the band. This generates a high absorption of photons for low energy since the transition is allowed and only requires the interaction between one photon and one electron. This response is characteristic from metals for which the free electrons mainly interact with the photons via mechanisms such as inverse Bremsstrahlung [57]. For high energy photons the interband transitions can also participate in the optical response of the material, however they have a high energy threshold corresponding to the energy separation between the conduction and the valence band. The interaction between the oscillating electrical field and an electron can be understood using a semi-classical approach with Newton's second law. It is found that the dielectric function

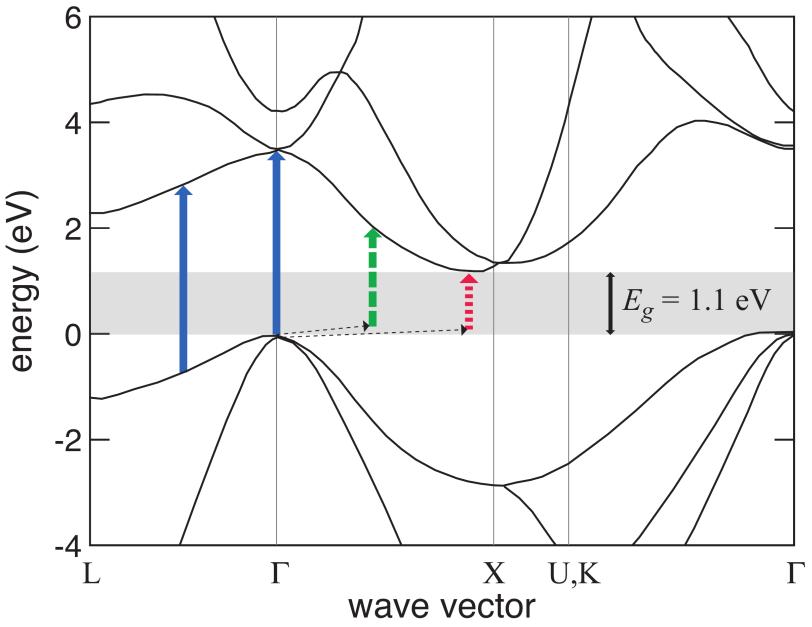

Figure 2.4 : The energy band structure of silicon from Chelikowsky and Cohen [58] and Tull [59]. Direct and indirect electron transition across the band represented by arrows.

for the free electron for a wavelength ω is

$$\epsilon_r = 1 + \frac{\omega_p^2}{\omega_0^2 - \omega^2 - \imath\gamma\omega} \text{ with } \omega_p = \sqrt{\frac{ne^2}{m_e\epsilon_0}} \tag{2.9}$$

with γ, ω_p, n, e, m_e, ϵ_0 and ω_0 respectively the dumping factor, the plasma frequency, the density of free-carriers, the electron charge, the electron mass and the vacuum dielectric permittivity and the natural frequency of the oscillator [60]. For low frequency of the laser pulse, the free electron contribution dominates the optical response. However, for high frequency the free electron does not have the time to respond to the oscillating field and the material behaves like an insulator or semiconductor.

For a semiconductor and insulator, the Fermi level is between two energy bands. Therefore, electrons cannot freely flow in the valence band and the promotion of electrons from the valence to the conduction bands due to interaction with the light requires a specific amount of energy. Figure

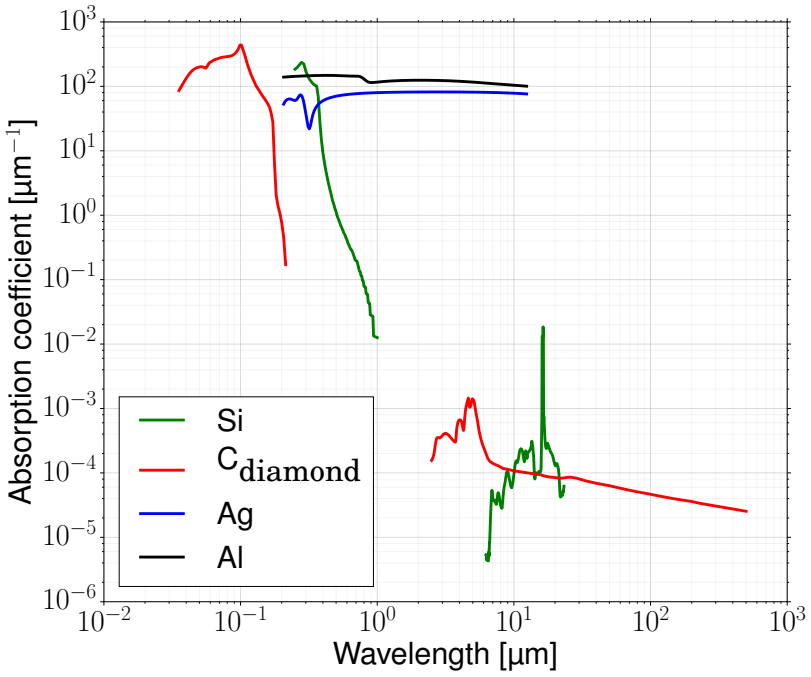

Figure 2.5 : Absorption coefficient for Aluminium[61], silver[61], diamond (Phillip and Taft [62] for short wavelength and Dore et al. [63] for long wavelength) and Silicon (Green and Keevers [64] for short wavelength and Chandler-Horowitz and Amirtharaj [65] for long wavelength) at 300 K.

2.4 shows the energy band structure for silicon, giving an example of the phenomena occuring between the laser and a semiconductor/insulator. At absolute zero only direct transitions are allowed, therefore the minimum band gap is around 3.43 eV and requires photons with a wavelength inferior to 362 nm. The threshold of absorption only occurs at low temperature. At a non-zero temperature, additional mechanisms allow the laser absorption of one photon by the solid. The rise in temperature induces a rise in the energy in the lattice of the material. Energy is partially stocked through the generation of vibration in the lattice, the phonons. The photons travelling through the lattice can interact with the phonons and this leads to an indirect transition between the valence and the conduction band. In effect, the three-body interaction allows the exchange of energy and momentum that is required for a transition at another wave vector. However, the probability of the

three-body interaction is much lower than the two-body interaction, resulting in a lower absorption coefficient. The minimum band gap is around 1.1 eV which corresponds to 1100 nm and a sharp rise of the absorption coefficient. For lower wavelengths, the probability of interaction increases due to higher availability of phonons with the appropriate momentum.

The absorption coefficient presented in Figure 2.5 shows the optical response for four different materials, of which two are metal (Silver and Aluminium), one is a semiconductor (Silicon) and one is an insulator ($C_{diamond}$). The absorption coefficients of the metals are similar and weakly depend on wavelength, whereas for insulators and semiconductors the absorption coefficient exhibits a dramatic increase from the indirect band gap (1.1 µm for Silicon [58] and 0.229 µm for diamond [66]) and a stabilisation after the direct band gap (0.362 µm for Silicon [58] and 0.169 µm for diamond [66]). Interestingly, diamond also exhibits a higher order of interactions between several phonons and a photon between 2 µm and 8 µm, see Figure 2.5 [67]. This is another mode for the absorption of photons during the interaction and is mainly present in the Infra-Red (IR) absorption spectrum of the solid. The absorption mechanisms described above correctly explain the optical response of the solid for low intensity of the laser pulse (the linear part of the interaction), however additional mechanisms occur for high intensity laser pulse, and these are presented below.

The multiphoton band-to-band transition also participates in the absorption however due to the multi-body interaction (several photons and an electron) its yield is extremely low. In effect, for semiconductors and insulators the direct band gap energy may be overcome by the interaction of multiple photons with one electron, leading to promotion to the conduction band. This phenomenon occurs mainly during the interaction with ultrashort pulses and is commonly used for two-photon polymerisation [25]. Due to

the low yield, it only occurs for ultrashort pulses such as the two-photon absorption for 100 fs pulses at 620 nm on a Silicon target [68]. It must be noted that the change of absorption mechanisms is highly dependent on the wavelength. For a Silicon target and an 80 fs pulse at 800 nm, theoretical and experimental investigations have shown that the direct interaction with the electron in the conduction band and the laser light can be the dominant absorption mechanisms [69]. In effect, for a temperature above absolute zero the amount of electrons in the conduction band due to fluctuation of the energy state can be sufficiently great for absorption of the laser light for ultra-short pulses. Energetic electrons in the conduction band interact with the valence electrons and promote them to the bottom of the conduction band via collisions. The yield is highly dependent on the amount of electrons in the conduction band and the process leads to an "avalanche" of electrons promoted to the conduction band. This process is called avalanche ionisation. It must be noted that multi-photon absorption can be highly enhanced by defects in the target surface. This has been widely studied for materials used in optics such as BaF_2. Experimental studies have shown that defects on the surface (which perturb the electronic states) can initiate the ablation process by promoting surface damage that later enhances absorption [70]. The promotion of electrons from the valence to the conduction band drives the creation of electron-hole plasmas that can form early in the absorption of the pulse [71]. The high density of free electrons in the target causes the material to behave like a metal and dramatically increases the reflection and the absorption coefficient [72].

2.1.3 Laser heating mechanisms

Complex mechanisms for the absorption of the laser light have been presented and it is clear that the absorption mechanisms can greatly vary depending

on the electronic states, the wavelength of the photon, the instantaneous intensity and defects on the surface. However, for all the processes presented above, the photons interact only with electrons thus leading to a temperature increase in the electron population. The target has an electron population with high energy and a cold lattice [73]. In the solid, the population of electrons is in Local Thermal Equilibrium (LTE) and can be described by one temperature (experimental investigation for Aluminium estimated the thermalisation time at around 100 fs [74]) and the population of heavy particles in the lattice is also in LTE after 39 fs [75, p.103]. However, the electrons and the lattice between each other are not in LTE [24]. In effect, the electron-phonon interaction time for the energy is in the order of 5–10 ps [75, p.105-109]. For ultra-short pulses, the lattice heating is delayed compared to the electronic heating. Due to the low heat capacity of the electron cloud, the temperature of the electrons increases to well above critical temperature [76] and generates a large amount of electron emission at the surface. After several hundred picoseconds, the electron and lattice temperatures converge to the same value. For short pulses ($>$ 1 ns), the coupling between the electron temperature and the lattice temperature is strong due to the long interaction time between the two populations. Therefore, the temperatures of the electrons and the lattice are the same during the heating process by the laser pulses. At this point, the following mechanisms are highly dependant on the intensity of the pulse. For ultrashort pulses, if the lattice does not have time to heat sufficiently, the ablation mechanisms are called “non-thermal”. Whereas, for short pulses, the lattice has enough time to heat sufficiently and the removal mechanisms are called “thermal”. In the following subsection, the phenomena leading to material removal will be described in detail.

2.1.4 Laser removal/ablation mechanisms

In this subsection, the thermal mechanisms will be presented. It must be noted that the removal mechanisms for thermal ablation are functions of local heating and can be determined from the solution of the heat equation,

$$\partial_t H_g = \partial_x \left[\mathrm{D} \partial_x H \right] + S, \tag{2.10}$$

with H, D and S respectively being enthalpy of the material, thermal diffusivity and the heat source induced by the laser. The enthalpy is generically calculated as

$$H(T) = \int_{T_0}^{T} \rho(T) c_p(T)\, dT, \tag{2.11}$$

with c_p and T being the specific heat and temperature, respectively. The heating rate can be as high as 10^9 K.s^{-1} [77, p. 98] and the temperature gradient can be as high as 10^4 K.µm^{-1}, leading to melting, evaporation, volumetric ablation, plasma breakdown and material ejection.

2.1.4.1 Surface melting

The temperature increase in the material can lead to the formation of a transient pool of molten material [78, 79]. This transient pool has different material properties but, more importantly, the material can move depending on the force governing its motions. For a large melting pool and large gradient, a large convection area can be created in the crater [52]. This increase in fluid motion increases the heat flow to the colder area surrounding the crater. Moreover, due to the size of the crater, the heat flow to the cold area is strong and can freeze the deformation that occurs during the laser-target interaction [80, 81]. In most cases, due to the size of the melting pool, gravity is not a driving force for fluid motion. The driving forces for surface deformation for thin melting pools are the pressure above the crater and the surface tension,

which both depend on temperature [82]. The deformation of borosilicate glass by a CO_2 laser creates protrusion and depression in the melted area, see Figure 2.6. The formation of specific structures is observed for a wide variety of materials and is due to gradient variation in the surface tension, leading to the creation of protrusion when the gradient is positive and depression when it is negative [83]. The variation in the surface tension can be used to create a variety of shapes such as sombrero shaped crater [84] or the formation of nanotips [80].

Surface melting is the first to step towards ablation of the material. Surface melting alone cannot explain the removal of material from the target, however it is possible to explain the surface deformation just above the threshold of melting. It is also an important phenomenon to consider if one is interested in the final shape of the crater and in the creation of rims around craters which are observable from short pulses for a wide range of materials (ceramics [47], metal [85]). It has also been found that the creation of a strong temperature gradient in the crater causes high speed of material flow (≈ 10 m.s^{-1}) due to the Marangoni effect [86]. This flow can lead to Rayleigh-Taylor instability development and creates a wavy pattern on the surface of the molten pool [86]. If the flow is strong enough, inertia forces at the edge of the crater are stronger than the surface tension and droplet ejection occurs [86]. In the next sections, the surface melting will play a direct role in the material removal with the increase of the laser power.

2.1.4.2 Thermal Evaporation

One of the effects of material melting is to delay further increase of temperature, since the enthalpy of melting is consumed during temperature elevation [87]. However, for high power pulses, the elevation of temperature is not stopped by the melting and the temperature increases to even higher values.

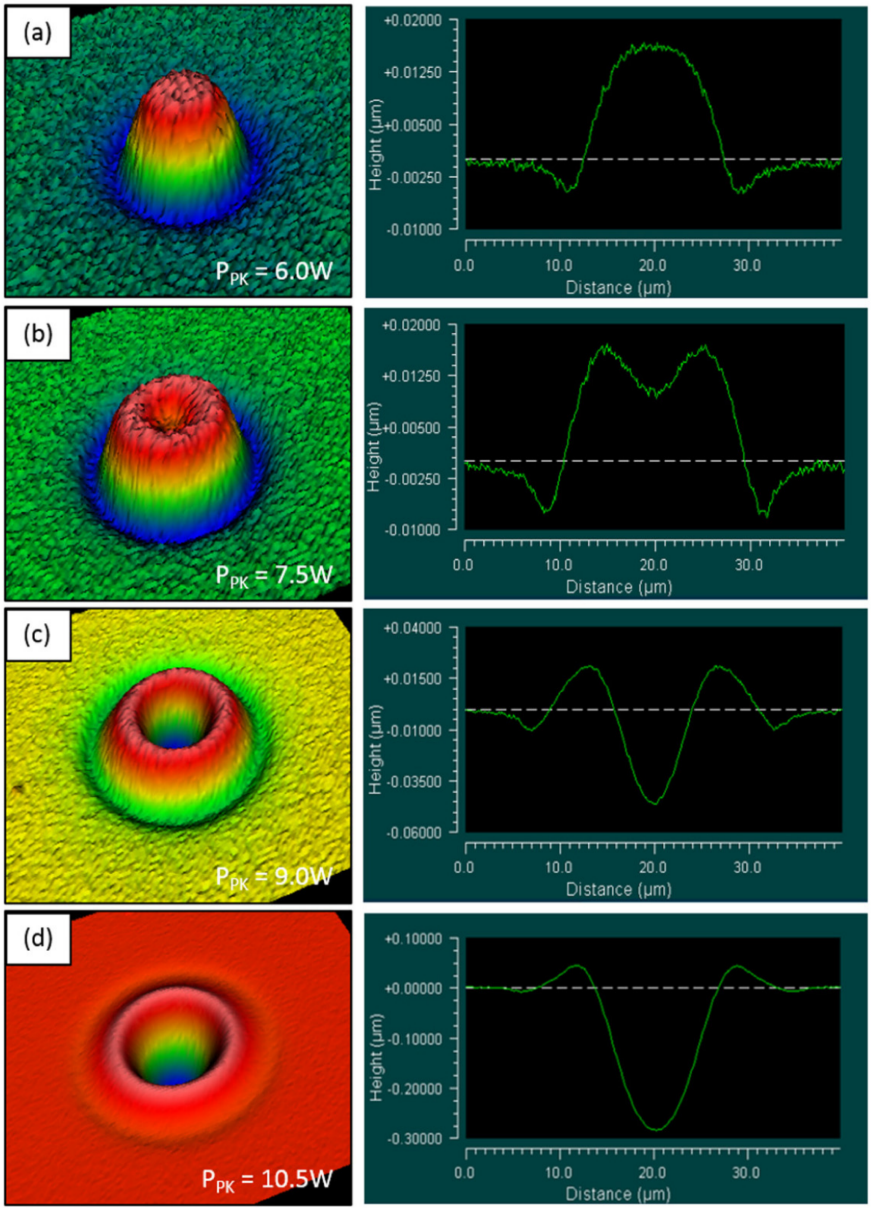

Figure 2.6 : Deformation for a borosilicate glass target induced by microseconds pulsed CO_2 laser after 1 hour annealing from Wlodarczyk et al. [81].

Unlike the melting process, this can be considered as an instantaneous transition from the solid-phase to the melted-phase using a temperature threshold. Vaporisation is not an instantaneous process [88] and its rate for a material is related to the temperature at the surface and the pressure vapour such that

$$\dot{m} = \sqrt{\frac{M}{2\pi R T_s}} P_v \tag{2.12}$$

with $\dot{m}$, M, R, T_s and P_v respectively the rate of evaporation, the molar mass, the gas constant, the surface temperature and the pressure vapour. Miotello and Kelly [34] investigated the material removal due to the thermal process and it has been shown that the amount of materials removed by direct vaporisation during nanosecond ablation can be low (less than 100 atomic layers for the materials presented) for a temperature just above boiling point. Equilibrium evaporation of material during pulsed laser ablation reaches temperatures well above boiling point due to low efficiency of direct evaporation for a short time [89]. It must be noted that the enthalpy of vaporisation is usually higher than the total amount of energy necessary to increase the temperature to the critical point. Therefore, vaporisation is a highly penalised process as it requires a large amount of energy. One way to increase the amount of material ablated would be to increase the contact surface between the gas and liquid. This occurs during boiling with heterogeneous nucleation of vapour in the bulk of the liquid. However, it has been found that this process is also not effective during nanosecond pulsed laser ablation since the time necessary to grow and diffuse the bubble to the surface is too long [34]. Furthermore, experimental results support the idea that the temporal length of the pulses has a strong influence on the amount of material ablated by vaporisation [78]. In effect, it has been found that for graphite, longer pulses lead to a higher yield [78] for the same amount of energy deposited.

During fast evaporation and condensation a thin layer (a few mean free paths) known as the Knudsen Layer (KL) is used to describe the transition from a thermal and kinetic non-equilibrium to a Maxwell-Boltzmann equilibrium distribution for the vapour particles. Thus, the connection between the target and the plume is consistently modelled under high thermal load of the target. A variety of models are used to describe the KL for different

conditions (atmospheric ablation, vacuum ablation, etc.) [90–93]. In the case of ablation in an ambient environment, the approach developed by Knight et al. [90] is well adapted [23, 30]. The KL is treated as a gas dynamic discontinuity [90] for which analytical expressions are derived that link temperature, pressure, density and velocity along both sides of the KL.

Thermal vaporisation is often the main ablation process for short pulses at low energy [89] or long pulses (> 1 µs) [47]. In effect, for low energy and temporally long pulses the temperature in the material does not exceed the critical temperature and does not progress to the development of metastable phases [30, 34]. The target is in equilibrium with the vapour phase and follows the binodal in the thermodynamics coordinates, as shown in Figure 2.7. Thermal evaporation has been successfully applied to predict numerous experimental results (Nb [94], YBCO [94], graphite [95], TiC [46], Alumina [47], etc.). However, it has been found that vaporisation alone cannot explain the high amount of ablated material observed for high energy short pulses for graphite [32], Silicon [96, 97] and Aluminium [98, 99]. In effect, the evaporation process is not an efficient mechanism to relax material that is heated at a high rate ($> 10^9$ K.s^{-1}) [100, p.90] and the increase in energy density is inexorable for high power laser pulses. In the next section, the relaxation mechanism for superheated material will be presented in detail.

2.1.4.3 Explosive boiling or homogeneous nucleation

Only thermodynamics quasi-equilibrium states have been discussed so far. In effect, the transition from solid into liquid into vapour by vaporisation can be described using a continuum model assuming quasi-equilibrium processes for the transition between phases. The early work of van der Waals [101] on the continuity of gaseous and liquid states has provided useful insight into the transition of the liquid to the vapour states. Phenomenologically, the van

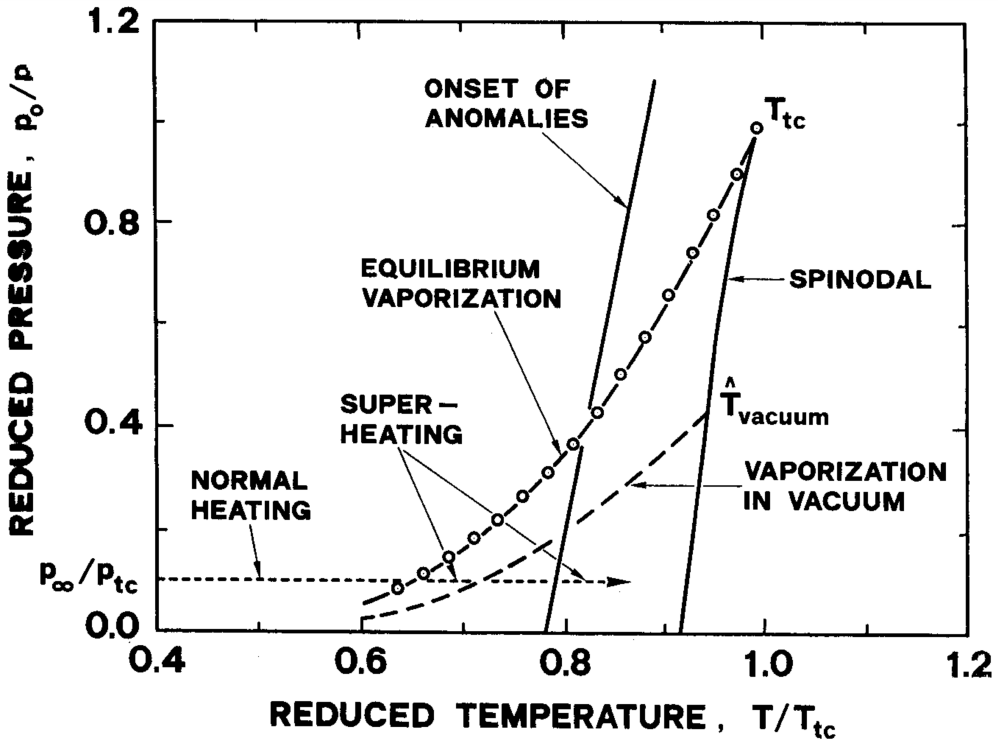

Figure 2.7 : Typical p–T diagram of a metal close to the critical point from Miotello and Kelly [34].

der Waals gas laws are derived from the ideal gas law and assume that the total volume available is reduced by the space taken by the particle (atom or molecule) and the real pressure is reduced due to the internal cohesive force. The correction of the ideal gas law gives the following gas law of van der Waals,

$$\left(P + \frac{a}{V_m^2}\right)(V_m - b) = RT, \tag{2.13}$$

with P, V_m, R, T, a and b respectively pressure, molar volume, gas constant, temperature, the coefficient for average attraction between particles, and the coefficient for the volume excluded by the particles. The van der Waals gas laws are a relatively simple EOS that describe the thermodynamic state of a gas and liquid using the same law. This is the first law that could be used to predict the transition between liquid and gas as a continuous state. The formulation has issues with the representation of the compressibility

of a real fluid and has since been replaced by other formulations [102–106]. However, the law presents a simple way to discuss qualitatively the different states of matter and the transition from one to another. In effect, the law presents several characteristics that are close to reality for the transition of states where a critical point (T_c, P_c and ρ_c) exists and where several phases (different densities) are present for the same pressure and temperature. The thermodynamic diagrams (P–ρ and T–ρ) presented in Figure 2.8 are qualitatively similar (for the position of the different phases) to the "real" (state-of-art) EOS as can be seen for Silicon [23], Copper [30] and silica [107]. It must be noted that the van der Waals equation cannot be applied to the transition from solid to liquid and solid to gas, therefore no discussion will be given regarding melting or sublimation.

The main applicability of the van der Waals EOS is the description of the gas. However, the EOS presents several areas for which it provides additional information about the phase state for the liquid and gas phase. The isotherms present an anomaly for which the derivative of pressure with respect to density at constant temperature is negative,

$$\left(\frac{\partial P}{\partial \rho}\right)_{T,n} < 0. \tag{2.14}$$

The state described by the van der Waals equation for which a decreasing pressure induces an increasing density is not mechanically stable [108] and should not be observable. This region in the thermodynamic diagram is the Spinodal region. In Figure 2.8, it is the dark red region. Experimentally, a state of the fluids for which the density reduces for an increase of pressure has never been observed and one of the van der Waals EOS predictions is that certain regions in the thermodynamics diagram are not attainable under quasi-equilibrium conditions.

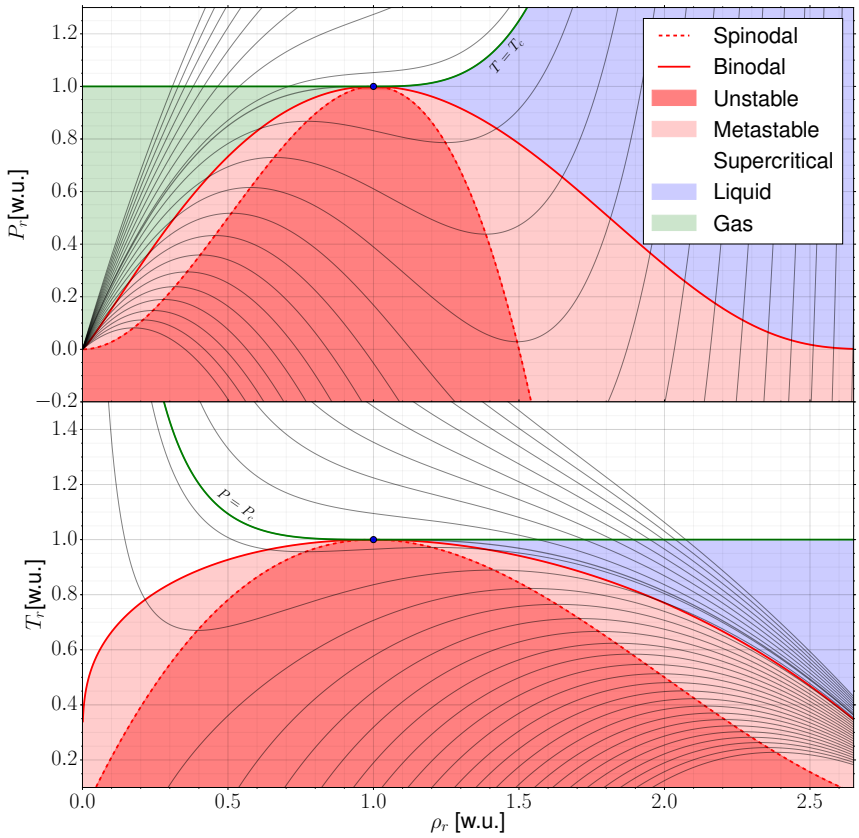

Figure 2.8 : P–ρ and T–ρ diagrams for a van der Waals gas with the pressure, temperature and density normalised to the critical values. The blue dot is the critical point. The lines in the two diagrams are isothermal for the P–ρ diagram and isobar for the T–ρ diagram.

Furthermore, the van der Waals EOS predicts that the transition from liquid to gas occurs within a range of pressure on an isotherm, whereas experiments have found that the transition occurs at constant pressure, the pressure vapour, for a specific temperature. The constant pressure for the phase transition is not present in the original work of van der Waals [101]. However, the pressure vapour can be indirectly calculated with the van der Waals EOS using the Maxwell construction. It has been found experimentally that the pressure vapour is equal to the pressure for which three solutions of density can be found and that the area between the isotherm and the constant pressure is equidistant from the two loops connecting the three

intersections. This is expressed by,

$$\int_{V_g}^{V_l} p_{\mathrm{vdW}}(V)|_{T=\mathrm{cst}} dV - P_{sat}(V_g - V_l) = 0, \tag{2.15}$$

with $p_{\mathrm{vdW}}(V,T)$ V_g, V_l, and P_{sat} respectively the pressure using the van der Waals EOS, the molar volume of the gas, the molar volume of the liquid and the pressure vapour. Using Equation 2.15, the position of two stable densities for a constant pressure and temperature are found. The binodal (coexistence of the two phases) curve is presented in Figure 2.8. The experimental correction found by Maxwell can be understood theoretically using the free energy of Gibbs definition,

$$dG = -SdT + VdP. \tag{2.16}$$

Calculating the difference of Gibbs energy in the fictitious cycle from the gas to the liquid shows that its Gibbs energy is null, supporting the experimental correction done by Maxwell and the coexistence of the two phases [109]. The binodal is not confounded with the spinodal therefore a region exists for a stable phase that is not thermodynamically favoured. These regions, shown in light red in Figure 2.8, are called metastable [110] since any perturbation could induce a dramatic and homogeneous phase transition.

In effect, the creation of an interface between the two phases has an energy cost due to the surface tension and results in metastability of the phase over the thermodynamic criteria. Any defects, impurities, walls or radiation could reduce the potential for the creation of the interface and allow nucleation of the thermodynamically favoured phase. The absence of defects allows persistence of the current phase to much higher temperatures until the phase reaches conditions close to the spinodal [111, 112]. It should however be noted that the presence of defects might not be enough to generate phase

transition before superheating occurs if the heat rate is sufficiently high [100, p. 90]. Early work on the stability of metastable liquid and nucleation kinetics presented in the book written by Skripov [100] is particularly interesting for the comprehension of phenomena occurring during transition inside the metastable phase. This work is still relevant to current research of explosive boiling/volumetric ablation for PLA [23, 30, 107].

Homogeneous bubble nucleation in superheated liquid has been widely studied, leading to several formulations for the frequency of spontaneous nucleation rate [107]. However, the formulations only offer slight corrections to one another for the different phenomena considered and offer similar predictions [107]. The theory is based on the spontaneous creation of vapour bubbles of different radii in the superheated liquid. The critical radius (r_c) of the bubbles is defined such that mechanical and chemical equilibrium is achieved,

$$p_{\text{bubble}} = p_{\text{liquid}} + \frac{2\sigma}{r_c}, \text{ and} \tag{2.17}$$

$$\mu_{\text{bubble}}(p_{\text{bubble}}, T) = \mu_{\text{liquid}}(p_{\text{liquid}}, T), \tag{2.18}$$

with σ, and μ respectively the surface tension of the liquid and the chemical potential. For a given pressure and temperature of the liquid, the intersection of these two conditions provides the critical pressure and radius of the bubble [100, p. 24]. Bubbles with a radius larger than the critical value participate to the phase transition, whereas bubbles with a radius smaller than the critical value collapse due to surface tension and do not participate to the phase transition. Thus, the dynamics of phase transition are governed by the frequency of spontaneous nucleation of the bubbles with critical radius r_c. Bubbles below the critical radius do not participate to the global phase transition however due to the random vaporisation/condensation processes some of them can grow up to the critical radius. The solution of Dömer and

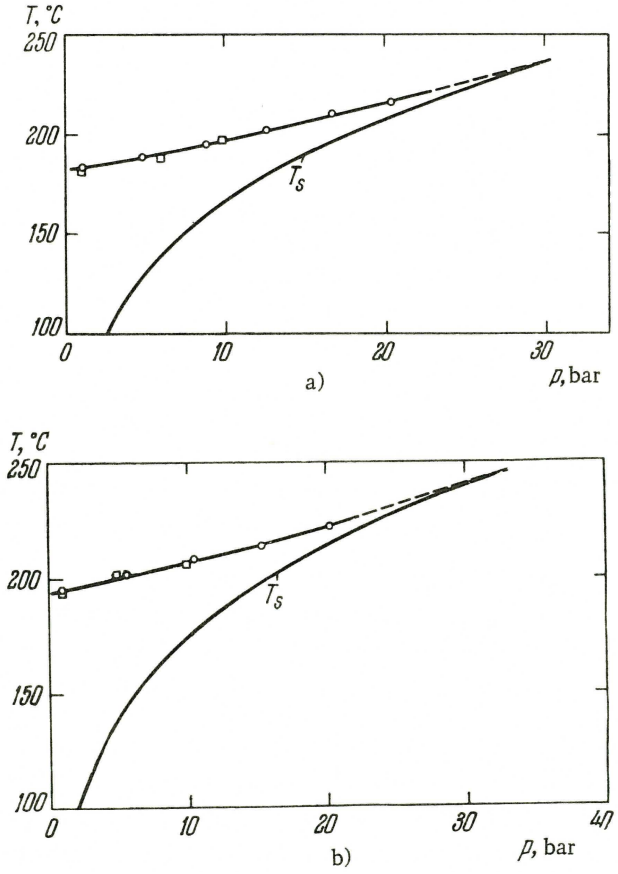

Figure 2.9 : Temperature of maximum superheating of n-hexane (a) and hexafluorobenzene (b) at different pressures [100, p. 76]

Volmer is obtained by considering the bubbles as spherical, behaving like a perfect gas, and in mechanical equilibrium with the liquid without being in chemical equilibrium. It is found that the spontaneous nucleation rate for bubbles at the critical radius is,

$$J_1 = N_1 \sqrt{\frac{6\sigma}{(3-b)\pi m}} \exp\left[-\frac{\Delta H_{\text{liq}\to\text{gas}}}{kT}\right] \exp\left[-\frac{W_c}{kT}\right] \quad \text{with } b = 1 - \frac{p_{\text{liquid}}}{p_{\text{bubble}}}, \tag{2.19}$$

with N_1, m, $\Delta H_{\text{liq}\to\text{gas}}$, k and W_c respectively the number of molecules per unit volume of the metastable phase, the mass of the molecule, the heat of vaporisation per molecule, the Boltzmann constant and the work done by bubbles reaching the critical size. Equation 2.19 can be used to calculate the maximum temperature of the liquid for a specific nucleation

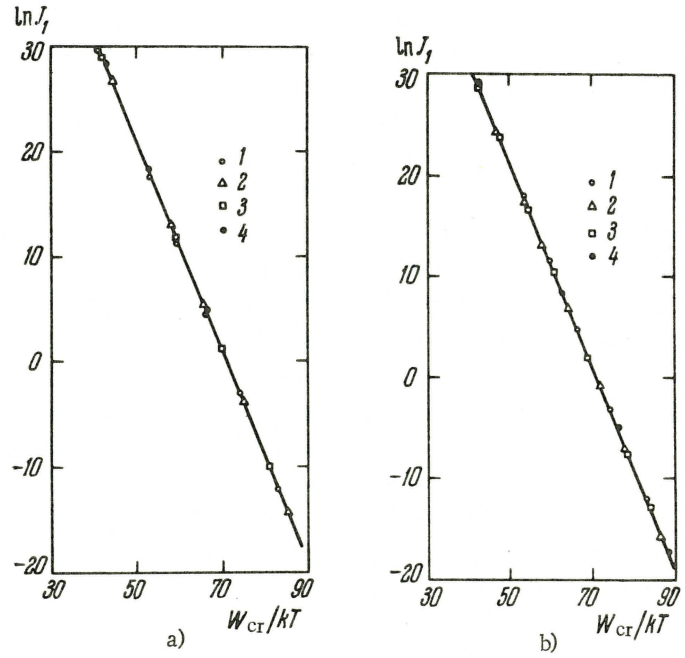

Figure 2.10 : Theoritical dependence of the frequency of spontaneous nucleation on the Gibbs number; a) diethyl ether$_p$ at 1 (1), 5 (2), 10 (3) and 15 (4) bar; b) results for atmospheric pressure for diethyl ether (1), n-hexane (2), n-pentane (3) and benzene (4) [100, p. 123]

frequency ($J_1 = cst$). Experimental measurements of the maximum liquid superheat (T_{su}) in bubble chambers or with droplets have shown that the model provides good agreement with reality, see Figure 2.9. The discrepancy between predicted and experimental values is usually less than 1-2 K.

The theory has been derived approximately using several significant assumptions but it nonetheless provides accurate results for a wide range of conditions and liquids. Figure 2.10 shows the theoretical dependence of the frequency of spontaneous nucleation on the Gibbs number ($G = W_c/kT$). It is clear that for practical applications the nucleation frequency can be correctly estimated using a much simpler formulation,

$$\ln J_1 \simeq 71 - G, \tag{2.20}$$

for a wide range of pressures and liquids. The inverse of the frequency

of spontaneous nucleation is equivalent to the mean time for an expected embryo to form in the liquid. Applying the approximations above for a droplet of 1 cm^3, it is possible to obtain the typical order for the stability of the superheated liquid in the metastable state. For example when $G = 100$, the typical time is around 10^{13} seconds. However, for $G = 40$, the typical time is around 10^{-13} seconds. This is shorter than the time of formation of the embryo using molecular dynamics [100, p. 124], therefore the typical time cannot be less than 10^{-11} seconds. This example seems to provide extreme values for the stability of the superheated liquid, however using ether at atmospheric pressure, for which $T(G \to \infty) = T_s = 34.5$ °C, $T(G = 100) = 140$ °C and $T(G = 40) = 148$ °C, the extreme values of stability correspond to similar thermodynamic states [100]. Therefore, the transition between stable and extremely unstable superheated liquid can be seen as a threshold process as described for PLA [34, 113]. The theory proposed for homogeneous bubble nucleation has been mainly derived from non-local experiments for which the global state of a small droplet ($\sim$ 10-50 mm^3) is studied [114]. Furthermore experimental results are the average of numerous experiments due to the stochastic nature of the process, therefore the local process (in time and space) of homogeneous nucleation has not been studied in detail.

The work presented in the manuscript of Faik et al. [107] is particularly interesting for the development of a local criterion for homogeneous boiling during a transition in the metastable zone. In effect, it has been found that the transition of a single phase liquid crossing the binodal is not accompanied by any peculiarity. The liquid follows the EOS without "noticing" the thermodynamically predicted equilibrium with the other phase (at least as long as this phase is absent) [114]. Therefore, for a liquid element following a thermodynamic path across the binodal, the Maxwell construction does not represent the thermodynamic states and the phase transition occurs due to

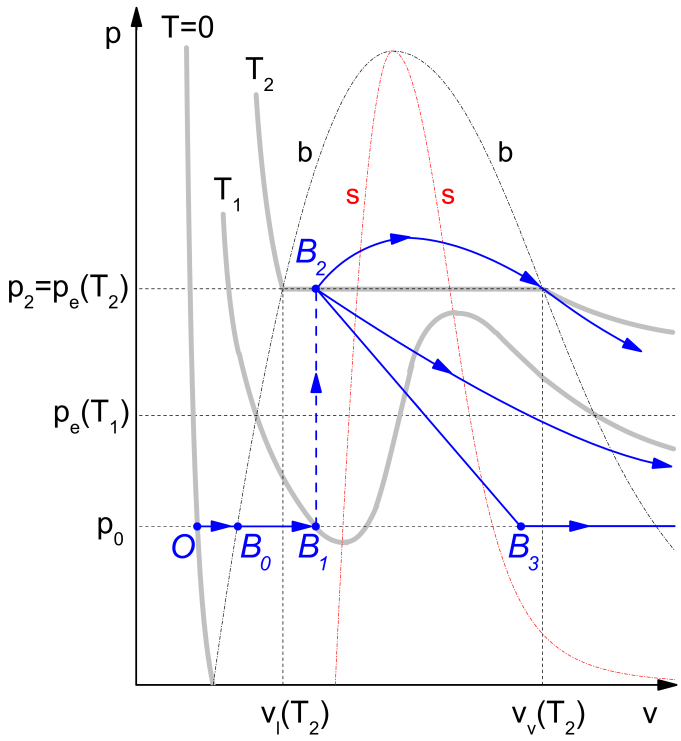

Figure 2.11 : Schematic representation of the evolution of the thermodynamic state of heated matter on the (v,p) phase plane. O(origin)→ (fast heating in the stable zone) B_0 → (fast heating in the metastable zone) B_1 → (transition from the metastable state to the stable state on the Maxwell construction) B_2 → (hydrodynamic motion) B_3.

homogeneous nucleation of critical bubbles. It is argued that during ultrafast heating (q $\simeq 10^{11}$ J.g^{-1}.s^{-1}), the target will enter the metastable zone without notable increase of pressure. As the element penetrates deeper into the metastable phase, the thermodynamic barrier between the metastable EOS and the equilibrium EOS is reduced. Once the element reaches a certain thermodynamic point B_1, it transits to the equilibrium EOS on the point B_2, see Figure 2.11. As the thermodynamic barrier decreases, the time scale for the transition also decreases by several orders (as for the frequency of homogeneous nucleation). For example, the transition time between the metastable EOS and the equilibrium EOS near the spinodal is approximately equal to 10^{-12} seconds, which is practically instantaneous for the time scale

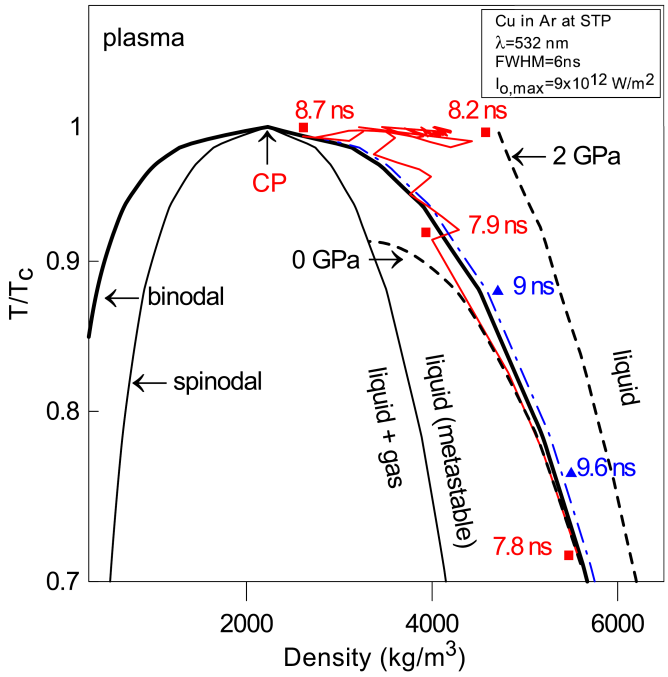

Figure 2.12 : Path of the surface cell during the nanosecond ablation of Cu projected on the phase diagram [30].

of the ablation process [107]. Thus, due to the time scale of the phase transformation, the internal energy and the density of the liquid element in the metastable EOS must be equal after transition in the equilibrium EOS. According to the second law of thermodynamics, the transition leads to an increase of entropy due to the instantaneous transition which isolates the system from outside influence.

The phase transition occurs due to homogeneous nucleation of critical bubbles in the liquid until the fractional volume of all vapour bubbles in the superheated liquid is equal to that following the EOS with the Maxwell construction. The internal energy and the density are constant during the transition for the metastable state to the equilibrium state, see Figure 2.11. It is then argued that the instantaneous transition is accompanied by a jump in pressure, temperature and entropy. The delay in surface expansion due to entrance in the metastable EOS leads to an explosive jump of pressure that

creates a dynamic jet of droplet-vapour mixture [30].

For a laser/target interaction, this phenomenon occurs only if the external pressure is not dynamically adjusted to the pressure vapour at the surface. This only happens if the heating rate is large enough, surpassing the characteristic time of the plasma/ambient pressure at the surface. Therefore, the ejection of high speed droplet-vapour mixture during heating mainly occurs during the leading part of the pulse. However, it only offers temporary relief to the heating of the target, see Figure 2.12, and does not account for a large part of the ablated material [30].

2.1.4.4 Supercritical state

Heating of the target is not stopped due to homogeneous vaporisation and the ejection of vapour-droplet mixture [30]. The trajectories in the thermodynamics diagram present a "saw pattern" along the binodal leading to the critical state [30]. At this point, the distinction between the liquid and the vapour no longer exists. Further investigations close to the critical point have shown that fluctuations of density are important, leading to large scattering at all wavelengths, see Figure 2.13. This is also supported by experimental investigations of thermodynamic anomalies (i.e. jump of specific heat at constant pressure and sound speed) near the critical point [115, 116]. The critical fluid is therefore added to the hydrodynamic domain since it transforms like a weakly ionised plasma which is semitransparent to incoming radiation [23]. The critical fluid experiences large density fluctuation on a micro-scale size which leads to the generation of a jet of degenerate mixture of supercritical fluids with large density fluctuation [117].

The generation of a high pressure/temperature gas over the crater due to equilibrium vaporisation, superheating homogeneous boiling or supercritical phase leads to a shielding of the laser light. In the next section, the interaction

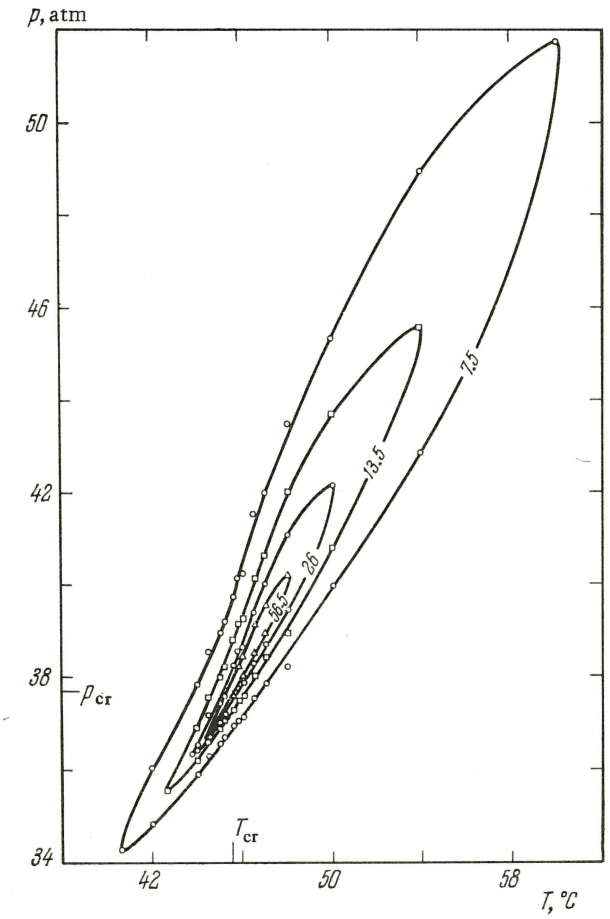

Figure 2.13 : Lines of equal light scattering in SF_6 projected onto the T, p plane [100, p. 249]

between this high temperature gas and the laser are detailed and the related shield/heating phenomena are presented.

2.1.4.5 Plasma generation, interaction with the laser field and the vapour plume

The generation of a plasma from the vapour is a common event during nanosecond pulsed laser ablation. The generation of a strong plasma, which can affect the amount of absorbed laser intensity by the target, occurs for pulses with an energy above the breakdown threshold. Shadowgraphy imaging shows that the laser beam can be the main driver of the vapour plume dynamics, see Figure 2.14. Shadowgraphy is based on light deflection

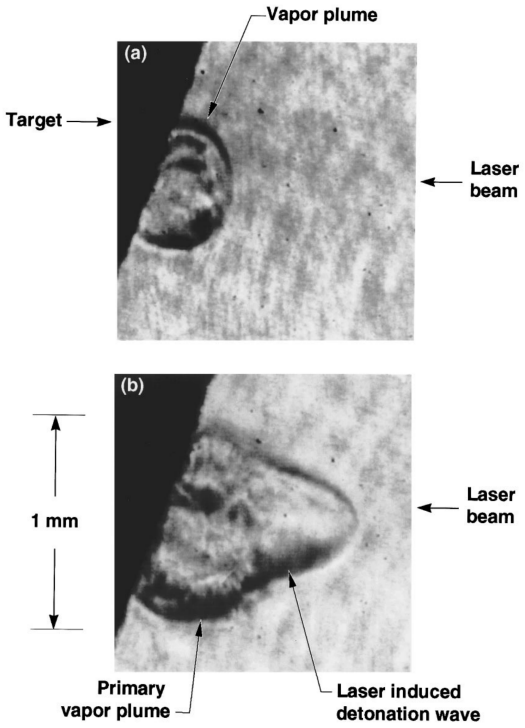

Figure 2.14 : Copper laser produced vapour plume on an aluminium target at laser intensities of (a) 0.93 GW.cm^{-2} and (b) 7.3 GW.cm^{-2} during the end of the 40-ns laser pulse [118].

due to change in refractive index, therefore jumps in density and temperature (shock wave) are easily captured. The shadowgraph presented in Figure 2.14(a) clearly shows the shock wave due to strong ablation at the surface. However, the shock wave geometry is not influenced by the direction of the laser. For higher energy, shown in Figure 2.14(b), the shadowgraph clearly shows a protuberance in the direction of the laser. This strongly suggests that the laser interacts significantly with the vapour plume, changing the energy distribution on the plume. Interestingly, measurement of the speed of the laser-induced detonation front shows that the apparition of the laser-induced detonation saturates the speed of the primary vapour front [118]. The vapour front position is related to the amount of energy stored in the gas [119] therefore a saturation of the front speed is related to a saturation of the amount of energy deposited into the target. This suggests that vapour

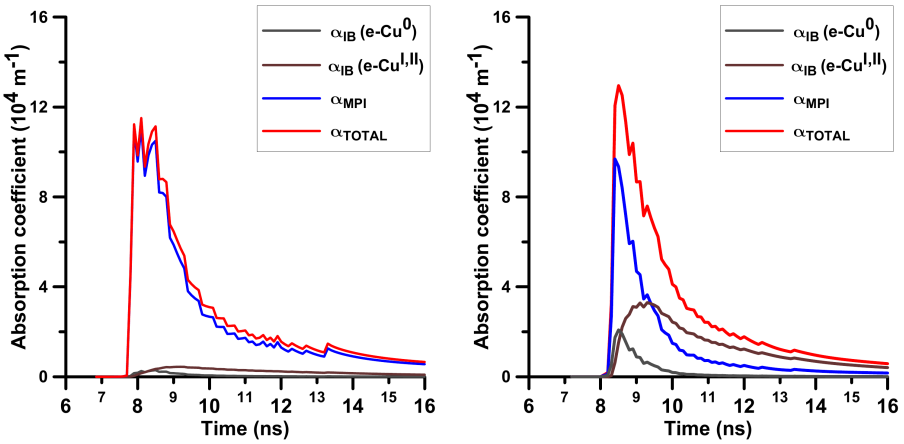

Figure 2.15 : Spatially average absorption coefficient in the plasma over a target of copper with a peak irradiance of 10^{13} W.m^{-2} for (a) UV light (266 nm) and (b) VIS (532 nm) [121].

plume interaction with the laser shields the target from part of the energy available in the laser pulse. Further experimental investigations have shown that the plume has a significant role in the energy balance, absorbing most of the energy that the laser pulse carries during nanosecond ablation [23, 120]. The vapour temperature is high enough to create a consequent amount of excitation of the atomic species in the plume. The vapour then starts to absorb the incident radiation, leading to breakdown and the plasma formation above the crater. The properties of the laser ablation process in this case are strongly influenced by the coupling between the plasma and the laser. The specific kinetics of the plasma will also play a dominant role in the ablation process.

The different mechanisms that lead to absorption of the laser light by the vapour plume are:

i) Inverse Bremsstrahlung: a process involving the absorption of photons by free electrons moving through the electric field induced by neutrals

and ions,

$$\mathrm{C}_{\mathrm{j}}^{\mathrm{k}} + \mathrm{e}^{-}(\epsilon_{\mathrm{e}^-}) + \mathrm{h}\nu_{\mathrm{laser}} \rightharpoonup \mathrm{C}_{\mathrm{j}}^{\mathrm{k}} + \mathrm{e}^{-}(\epsilon_{\mathrm{e}^-} + \mathrm{h}\nu_{\mathrm{laser}}). \tag{2.21}$$

The inverse Bremsstrahlung neutral-electron can be the dominant absorption process at the beginning of the interaction with the laser. However, the ion-electron interaction is usually dominant once the ion concentration in the plasma is large [122]. The inverse Bremsstrahlung is mainly dependent on the density of electrons, the wavelength of the laser, and the temperature. The cross section formulation for the neutral-electron inverse Bremsstrahlung is,

$$\begin{aligned} \varsigma_{IB}^{n,e} = \frac{[\mathrm{C}^0]}{3\ m_{\mathrm{e}^-}\,\mathrm{c}\pi\mathrm{h}\nu_{\mathrm{laser}}^3} \frac{\mathrm{e}^2}{4\pi\varepsilon_0} \sqrt{\frac{2(\mathrm{h}\nu_{\mathrm{laser}} + \epsilon_)}{m_{\mathrm{e}^-}}} \\ \left[(\epsilon_{\mathrm{e}^-} + \mathrm{h}\nu_{\mathrm{laser}})\,\varsigma_{\mathrm{C}}(\epsilon_{\mathrm{e}^-}) + \epsilon_{\mathrm{e}^-}\varsigma_{\mathrm{C}}(\epsilon_{\mathrm{e}^-})\,(\epsilon_{\mathrm{e}^-} + \mathrm{h}\nu_{\mathrm{laser}})\right] \end{aligned} \tag{2.22}$$

and the ion-electron inverse Bremsstrahlung is,

$$\varsigma_{IB}^{n,i} = \frac{4}{3}\sqrt{\frac{2\pi}{3\ m_{\mathrm{e}^-}k_{\mathrm{B}}T_{\mathrm{e}^-}}} \frac{\sum_{k=0}^{k=k_{\max}} \mathbf{Z}^{k+}\left[\mathrm{C}^{\mathrm{k}}\right]}{\mathrm{hc}\nu_{\mathrm{laser}}^3\ m_{\mathrm{e}^-}} G \frac{\mathrm{e}^6}{(4\pi\varepsilon_0)^3} \tag{2.23}$$

Therefore, the inverse Bremsstrahlung is the dominant process for laser within an IR light. For VIS and UV lasers, the inverse Bremsstrahlung is only significant at high temperature and high density of electrons [123], see Figure 2.15.

ii) Photoionisation: an atom or ion absorbs a photon which becomes ionised [124],

$$\mathrm{C}_{\mathrm{i}}^{\mathrm{k}} + k \times \mathrm{h}\nu_{\mathrm{laser}} \rightleftharpoons \mathrm{C}_{\mathrm{j}}^{\mathrm{k+1}} + \mathrm{e}^{-}(k\mathrm{h}\nu_{\mathrm{laser}} - \Delta\mathfrak{E}_{i,j}^{k,k+1}). \tag{2.24}$$

The interaction is highly dependent on the amount of energy that the

photon carries due to the number of electronic levels available for the interaction. In effect, if the energy between the two levels is greater than the energy given by the photon, the interaction cannot occur from these levels. Therefore, interaction is only possible in the thermally (collisional) populated excited electronic levels of the atom or ion for which the energy difference between the initial level and the final level is lower than for the photon energy. Excess energy from the absorption is transferred to the kinetic energy of the free electrons. The absorption coefficient therefore requires consideration of the discrete electronic levels of an atom/ion to accurately simulate the photo-ionisation. Thus, proper understanding of the dynamics of the electronic level requires comprehension of the collisional (excitation, ionisation) and radiative transition (ionisation, spontaneous emission, etc.). The cross section for the interaction between one photon and heavy (ions and neutrals) species is

$$\varsigma_{PI} = \frac{64\pi^4 \mathtt{e}^{10} m_{\mathtt{e}^-}}{3\sqrt{3}\,(4\pi\varepsilon_0)^5\,\mathtt{h}^6\mathtt{c}}\,\frac{1}{\nu_{\text{laser}}^3}\,\frac{\left(\Delta\mathfrak{E}_{i,j}^{k,k+1}\right)^{5/2}}{\sqrt{\mathfrak{E}_0^{k+1}}\left(\mathfrak{E}_{ion}^{\text{H}}\right)^2} \tag{2.25}$$

where $\mathfrak{E}_{ion}^{\text{H}}$ and $\mathfrak{E}_0^{k+1}$ are the ionisation energy of the Hydrogen atom and the ionisation energy of the species at the current level of ionisation, respectively. The cross section for the interaction between k-photon and heavy species is

$$\varsigma_{MPI} = \frac{\varsigma_{PI}}{(k-1)!\nu_{\text{laser}}^{k-1}(\mathtt{h}\nu_{\text{laser}})^k}. \tag{2.26}$$

The photo-ionisation process is effective for UV and VIS lasers since a larger number of electronic states can participate to the interaction [125], whereas IR light does not participate effectively to the photoionisation process due to the low number of electronic states allowed for the transition [121], see Figure 2.15.

Plasma ignition of the plume is a complex phenomenon since it depends on the wavelength of the laser, the temporal profile, target properties, etc. However, several trends are possible to extract from the discussion above:

i) UV plasma absorption is dominated by photoionisation absorption.

ii) VIS plasma absorption is firstly dominated by photoionisation, then after the ignition the neutral/ionic inverse Bremsstrahlung absorption could represent a significant part of the absorption.

iii) IR plasma absorption is dominated by inverse neutral/ionic Bremsstrahlung absorption.

iv) LTE cannot be used if correct ignition start is required, and might underestimate the total absorption by the plasma. Collisional-Radiative (CR) models are used to improve the description of the thermo-optical properties of the plasma. The Boltzmann-Saha is usually used to estimate the plasma properties. However, it has been found that during LIP the electron density is usually higher than the equilibrium value [126], and so caution must be taken when using the Boltzmann-Saha equilibrium to calculate the density of the electrons and electronic levels.

The plasma ignition threshold for UV and VIS lasers should be close to the ablation threshold since absorption occurs mainly through direct photoionisation. However, plasma ignition for IR can present a delay [31] due to low density of electron energy levels that can participate to the direct photionisation. Absorption then occurs through the neutral/ionic inverse Bremsstrahlung, which is dependent on the temperature of the plume before plasma ignition [122].

Plasma ignition has two main effects. Firstly, the laser is partially absorbed by the plasma, potentially shielding the target of a large part of the laser

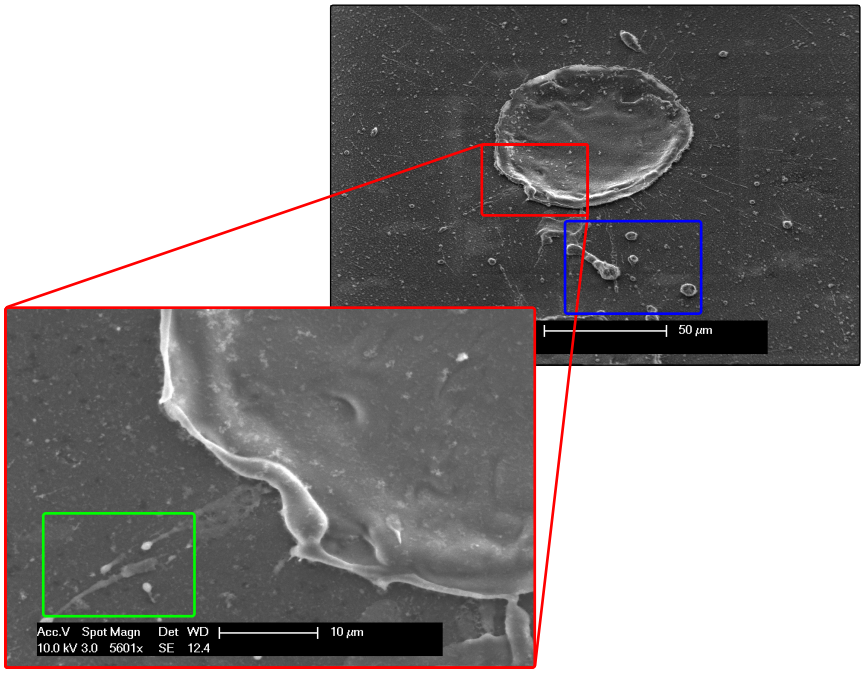

Figure 2.16 : SEM images of an ablation crater using a nanosecond laser with 30 ns (FWHM) at 1061 nm with a fluence of 110 J.cm^{-2}. Within the green rectangle are signs of fast ejection around the crater. The blue rectangle shows an area of large material ejection.

energy. Secondly, the combination of vaporisation at the surface and plasma ignition creates a high pressure field over the crater [127, 128] leading to ejection of matter. In the next section, the material ejection due to the pressure field over the crater is discussed.

2.1.4.6 Material ejection due to recoil and plasma pressure

One explanation for the discrepancy between theoretical and experimental results is the presence of high pressure above the crater due to recoil of the material from the crater [91]. This pressure produces a piston effect on the pool of molten material, pushing the material away from the centre of the crater [129]. In the next section, the interaction between the pool of molten material and the recoil pressure is described in detail.

The increase in temperature due to a poor evaporation process leads to a pressure on the crater surface of up to several Megapascals [127] for low

irradiance levels ($\sim 10^{10}$ W.m^{-2} for Titanium) and up to several hundred Gigapascals for high irradiance levels (10^{15} W.m^{-2} for Silicon) [128]. Experimental results show the presence of small and large droplets on the surface after laser ablation of aluminium using a nanosecond laser with high power, see Figure 2.16. A rim around the crater is also observable. The ejection and the rim can be explained by the presence of high pressure above the crater. Unfortunately, modelling of the melt ejection or the rim formation is not usually studied. Appropriate simulation of the system requires consideration of the 2D/3D phenomena which considerably increases the associated computational costs. The study of Leitz et al. [130] is one example of a simulation of the ablation process using a 3D framework. The ejection of material is predicted by the model and is due to the formation of a high pressure gas over the crater. Experimental work presented in Leitz et al. [130] also confirms that larger amounts of melted material present during longer pulses increase the amount of material ejected during ablation. Another interesting work about melt displacement produced by recoil pressure is the study by Harimkar et al. [131], where the infiltration of the melt into porous alumina grains is studied. Three-dimensional modelling gives acceptable results for the depth of melting of porous ceramics. Both works show that the recoil pressure due to evaporation leads to displacement of the material in the crater and also to ejection of the melt around the crater, as can be seen from the experimentation on Aluminium shown in Figure 2.16.

Furthermore, numerical prediction shows that melt ejection can be the dominant removal mechanism for fluence close to the melting threshold, such as for iron and aluminium [129]. However, it must be noted that this model might not appropriately predict the amount of material ablated because it cannot differentiate between the displaced material inside the crater and the material ejected from the crater. In effect, the model cannot consider surface

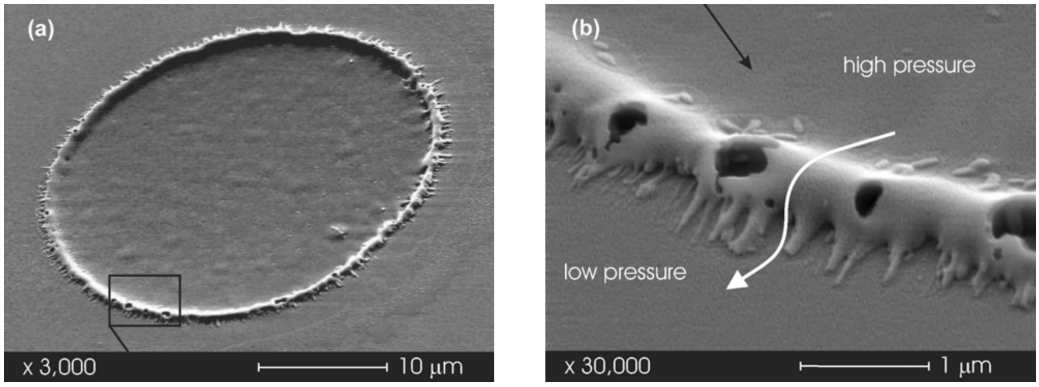

Figure 2.17 : SEM images of the crater using a femtosecond laser with a 100 fs (FWHM) at 800 nm with an average fluence of 34 J.cm^{-2} from the work of Ben-Yakar et al. [82]. Image (b) is a magnification of the area indicated by a black rectangle in image (a).

tension and does not differentiate between the displacement of material from the centre to the edge and pure ejection of material due to high pressure. The simulation of the evolution of melt-air/plasma by Ben-Yakar et al. [82] for an axi-symmetric system provides insight into the ejection of molten material during femtosecond glass ablation. In this study, the pressure is due to plasma excitation above the crater and not the recoil pressure. However, some insights provided about material displacement during ablation are still applicable for longer pulses. The simulation shows that the rim around the crater is due to displacement of the molten material toward the edge of the crater. Furthermore, the pressure at the centre of the crater creates a high speed flow ($\approx$ 2000 m.s^{-1} [116]) that flattens the rims and leads to the ejection of molten material around the crater, see Figure 2.17. The same behaviour is observed during the ablation of an aluminium crater by a nanosecond laser, see Figure 2.16. Consideration of the displacement of material during pulsed laser ablation due to the recoil pressure is important for understanding the crater shape after solidification. However, displacement of the material does not always lead to ejection (and removal) from the target. Therefore, depending on the methods used to measure the amount of material

ablated from the target, it is important to take into account the displacement of material for modelling. In effect, the displacement of material affects the position of the interface but does not always affect weight loss. Therefore, if the change in topography is used to calculate the amount of ablated material, as in the study of Stafe [31], the piston effect must be taken into account. However if the weight loss is used, the amount of material displaced would not change the weight and consideration of the piston effect would overestimate the amount of ablated material. Therefore, the piston effect should not be taken into account as done in the study of Bulgakova and Bulgakov [89]. The amount of ejected material follows:

$$v_{ej} = 4v_m h_m/d, \tag{2.27}$$

where v_{ej}, v_m, h_m and d denote the speed of recession into the material due to ejection, the radial speed of the melt in the crater due to pressure over the crater, the thickness of the melted layer and the diameter of the crater respectively. The radial speed of the melt is equal to

$$v_m = \sqrt{2 * P_{plume}/\rho} \tag{2.28}$$

where P_{plume} and ρ are the pressure of the plume over the crater and the density of the melt respectively. The amount of ejected material is directly proportional to the thickness of the melted layer, thus this effect is more pronounced for longer pulses than for shorter pulses.

The pressure over the crater leads to displacement of the material around the crater and pushes the material from areas of high pressure to areas of low pressure. The material is pushed at the edge of the crater and creates a rim. The material in the rim is then ejected away due to the high speed flow of evaporated material from the centre. This explanation is supported by

experimental investigations on metal thin-film [132]. It has also been found that when the system relaxes (after the main evaporation) and the pressure above the crater is reduced, the flow is driven by the surface tension [132], as occurs for pulsed laser melting [86].

The above phenomena occur only during the leading part of the pulse, however further experimental studies show that the exit part of the pulse can be as important with regards to the amount of material removed [44, 133–136]. In the next section, the removal processes during the exit part of the pulse are discussed.

2.1.4.7 Ejection of material during the exit part of the pulse and after the pulse

It has been found in nanosecond pulsed laser ablation experiments that there exists a jump of material removal for a particular threshold for a wide variety of materials such as Aluminium [134], porous graphite [32], YBaCuO [89], Silicon [133] and fused silica [136], see Figure 2.18. The experiments by Yoo et al. [133] and the following work of Lu et al. [113] demonstrate a good example for the investigation of material ejection. These experimental results, presented in Figure 2.18, show the variation in phenomena that occurs with an increase in deposited energy. The ratio of volume clearly shows two phases:

(i) The first phase is a melting phase and a light ablation. The volume ratio shows that the real amount of vaporised material is low compared to the volume that is displaced by the recoil pressure and the surface tension.

(ii) The second phase for high irradiance, characterised by a dramatic increase in the amount of ablated material. Interestingly, the ratio

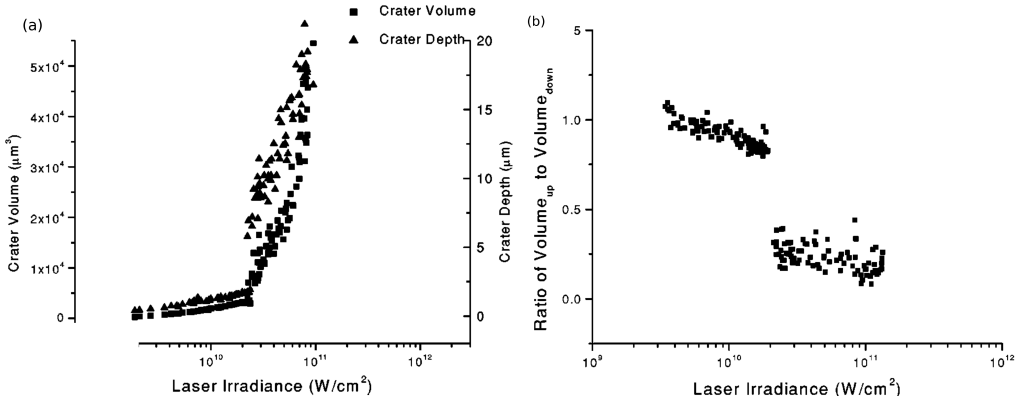

Figure 2.18 : (a) Crater volume and depth, (b) Ratio of the volume over the horizon to the volume under the horizon as a function of laser irradiance for Silicon ablated with pulsed laser ablation (FWHM =3 ns) at 266 nm, [133].

of volume over and under the horizon shows a jump from 0.75 to 0.25. The jump cannot be explained by the evaporation model alone. Furthermore, shadowgraphs show that this threshold correlates with the apparition of a large amount of ejected material after a delay of around 400 ns. It must be noted that the ratio also shows larger variance in the experimental results, suggesting a more chaotic and stochastic process.

In the study by Yoo et al. [133], the final amount of ejected material represents the main removal mechanisms for high irradiance and this occurs largely after the end of the laser pulses (3 ns FWHM), suggesting that relaxation of the target after the heating could be an important part of the process.

Modelling of the ablation of Silicon shows that the plasma over the crater is already fully developed, leading to a high pressure field [97, 113]. Experimental measurements of the explosive boiling for Aluminium also display a high pressure field (0.12 GPa) over the crater [98]. Finally, the plume pressure over the crater drops dramatically due to sonic plume expansion [23, 31]. The characteristic time for the pressure drop is usually lower than the characteristic time for the temperature drop inside the material. It is

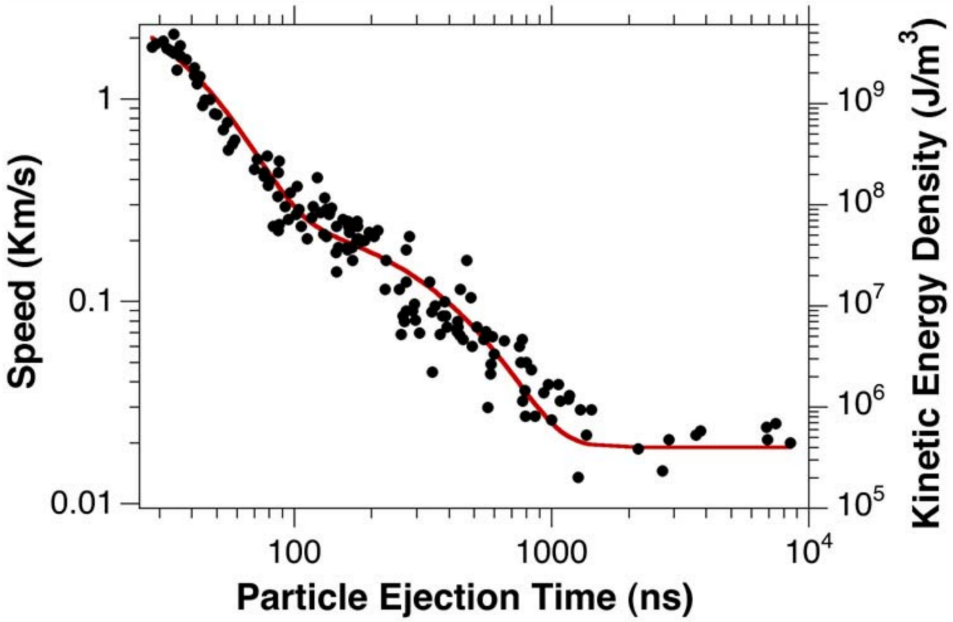

Figure 2.19 : Speed and kinetic energy density of ejected particles as a function of the estimated ejection time delay from the breakdown on the exit surface for the ablation of fused silica with nanosecond pulses (8 ns FWHM) at 355 nm for fluence on the order of 40-60 J.cm^{-2} [136].

therefore likely that the target enters the metastable phase leading to the ejection of a droplet-vapour mixture jet [136]. Existence of a delayed jet of a droplet-vapour mixture was observed decades ago, however there are few studies that systematically study the dynamics of the jet as a function of time. The work of Demos et al. [136] offers particular insight into the processes that lead to the formation of the jet and also their dynamics. The speed of the ejected particles as a function of the delay compared to the start of the breakdown is presented in Figure 2.19. The following equation is used,

$$K = c_0 + c_1 \exp\left[\frac{t - t_0}{\tau_1}\right] + c_2 \exp\left[\frac{t - t_0}{\tau_2}\right] \tag{2.29}$$

where K is the kinetic energy of the particles, t is the time, t_0 is the delay for the onset of the particle ejection, τ_1 and τ_2 are the decay times for the process and c_0, c_1 and c_2 are fitted constants. The best fit for Equation 2.29)

is plotted in red in Figure 2.19 with the parameters

$$\begin{aligned} &c_0 = 4 \times 10^5 \text{ J.m}^{-3}, \quad c_1 = 3.8 \times 10^9 \text{ J.m}^{-3}, \quad c_2 = 9 \times 10^7 \text{ J.m}^{-3}, \\ &t_0 = 30 \text{ ns}, \qquad\qquad \tau_1 = 15 \text{ ns}, \qquad\qquad \tau_2 = 170 \text{ ns}. \end{aligned} \tag{2.30}$$

The values of the fitting parameters suggest that the ejection starts with a 30 ns delay compared to the main evaporation. Furthermore, it is suggested that there are two mechanisms for particle ejection with a large difference of intensity and decay time. It must be noted that the speed of ejection arises directly from the pressure work of the ejected material volume, therefore it is possible to estimate the pressure of the heated material during the particle ejection. The results presented in Figure 2.19 suggest that the pressure at the start of the ejection reaches $\approx$ 3.8 GPa. At the end of the first relaxation process, the pressure drops dramatically to 90 MPa in around 15 ns. Finally, at the end of the second relaxation, the pressure is only four times the atmospheric pressure, around 0.4 MPa. The dramatic fall in pressure is coherent with the entrance of the material in the thermodynamic metastable phase and the onset of explosive boiling. Further experimental results presented in the work of Demos et al. [136] suggest that the ablation and particle ejection for high power nanosecond laser arise in the following manner:

a) The first phase is the supercritical vaporisation of the surface due to the action of the laser. This is supported by shadowgraphy of the shape of the shock wave presenting an elongated shape, which indicates a piston-like action in the direction perpendicular to the surface. It is also confirmed by the experimental and numerical investigations of Galasso et al. [23] and [120].

b) Following the first explosive evaporation, a swelling of the surface appears

[137]. The swelling process is followed by an explosive fragmentation of the surface around 30 ns after the explosive evaporation. This suggests that the second phase of response is due to the superheating of sub-surface material leading to the fragmentation of the liquid surface. This is also confirmed by the shape of the ejecta showing small fragmented particles that were completely melted during ejection, see Figure 2.20(a). The value of 15 ns provided from the fitting of the speed of ejection can be interpreted as the relaxation time for the superheated material. This is the first ejecta visible with shadowgraphy imaging.

c) The material still has a large amount of heat and previous numerical experiments have shown that the matter should be in a metastable state [120], leading to partial ejection of melt until the thermodynamic stable state is reached. This is supported by the shape of the ejecta showing long filaments, see Figure 2.20(d)-(e), suggesting that the temperature of molten glass was low during ejection.

d) Finally, the low speed ejection of particles (over 1 µs) is due to mechanical recoil of the fractured surface. It has previously been reported that large bulks of material are ejected during pulsed laser ablation of glass [137]. This is supported by numerical modelling for graphite [44] which suggests that the pressure due to recoil/plasma could exceed the tensile strength of the material, leading to crack formation. This is confirmed by the shape of the ejecta, see Figure 2.20(b)-(c), that do not present any melted part.

The phenomena occurring at the exit part of the pulse is complex to understand and model due to the interaction between the target and the plasma. In effect, it seems that the material removal passes through several phases with different thermodynamic paths involving metastable state, crack formation and ejection.

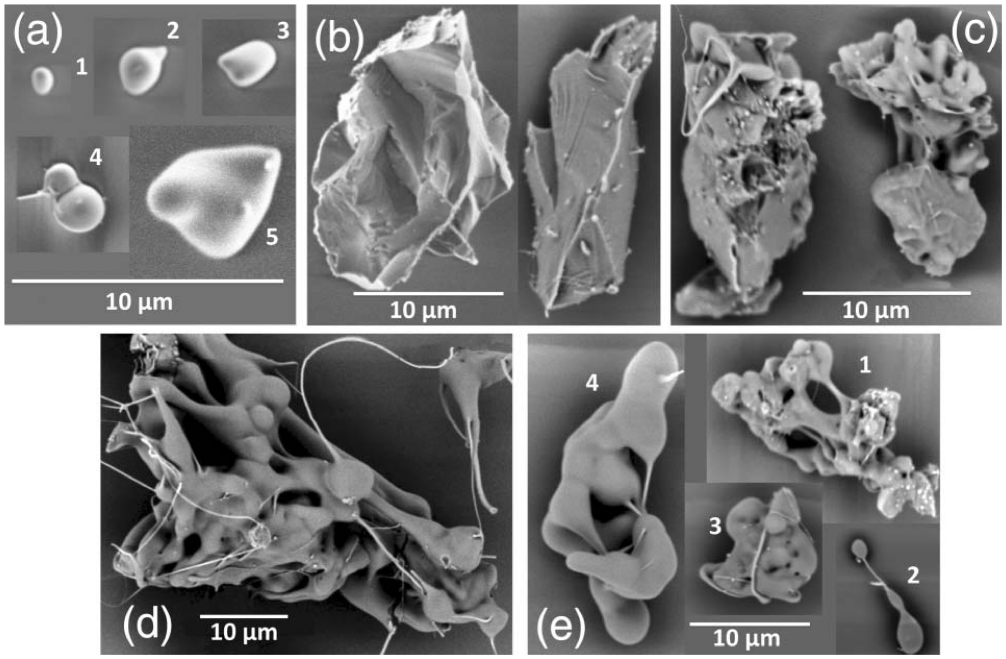

Figure 2.20 : SEM images of particles ejected during pulsed laser ablation of fused silica with nanosecond pulses (8 ns FWHM) at 355 nm for fluence on the order of 40-60 J.cm^{-2} [136]. There are three main types of particles, (i) small and completely melted (a), (ii) melted with small filaments between globular melt (d)-(e) and (iii) presenting fractured material (b)-(c).

2.1.4.8 Discussion of the removal mecanisms

The discussions presented so far have shown that removal mechanisms during pulsed laser ablation are varied (melt ejection, equilibrium vaporisation, superheated explosive boiling, supercritical explosive vaporisation, ejection of mechanically damaged material). Furthermore, a complete description of the phenomena requires understanding of the material interaction with the laser, the plasma generation and properties (optical, collisional and thermodynamic), the thermodynamic properties of the target and mechanical properties. In effect, the evolution of the material along the metastable state that might be the dominant ablation process during high power nanosecond ablation requires a complete description of the pressure field above the crater (plasma) and inside the material.

Finally, two main modes of removal during nanosecond pulsed laser

ablation can be isolated:

(i) For low power, the material is removed following equilibrium evaporation until the critical temperature is reached, leading to an explosive evaporation at the surface. Description of the plasma properties might be necessary should the plasma ignition threshold be crossed. The ejection of melted material could happen if the pressure over the crater is high and the depth of melted material is significant. The model developed by Galasso et al. [23] is a good example for the modelling of low power events without the generation of metastable phase.

(ii) For high power, the material follows the thermodynamic process path during the leading part of the pulse. However, the plasma absorbs most of the pulse energy leading to an interaction between the plasma and the target via the Bremsstrahlung emission [32]. The explosive vaporisation at the surface does not release enough energy, therefore the material moves toward the metastable phase during the pressure drop and this leads to the ejection of a droplet-vapour jet [136]. Finally, mechanically damaged materials are ejected at low speed a long time (≈ 1 µs) after the pulse.

Distinguishing between the two modes is important for reliable modelling. The ablation for low power is mostly related to the equilibrium evaporation with explosive vaporisation of the material reaching T_c that is transferred to the plume domain. The surface cell will then follow a trajectory along the binodal, which simplifies the requirement for the thermodynamic properties. The plume domains can usually be modelled using a perfect gas EOS using a CR model to understand the optical properties.

However, the second model of ablation requires understanding of the metastability of the phase and the production critical nucleus during the

interaction. A complete description of the material properties of the T-ρ plane is required, therefore it is necessary to use an EOS for a complete simulation of the process [30, 107].

2.1.5 Modification of the material properties during pulsed laser ablation

The large variation of temperature from ambient temperature to the critical temperature (and above if the plasma is considered), and of pressure from atmospheric pressure to several GPa, during pulsed laser ablation generates large variation in the material properties [55]. For modelling of PLA, the lack of experimental data on material properties at high temperatures necessitates the extrapolation of data at lower temperatures for high temperatures. In this regard, some studies have attempted to estimate the variation in material properties with temperature using certain general and empirical theories along with available experimental data. The work published by Marla et al. [55] evaluated properties of Aluminium at high temperature and showed a significant variation with temperature. It was found that temperature variation between ambient temperature and near-critical temperature for surface reflectivity varies from 92% to 45%, absorption coefficient reduces by a factor of seven, thermal conductivity becomes fives time smaller, density decreases by a factor of four, and specific heat reduces by a factor two. The use of temperature-dependent material properties for modelling pulsed laser ablation shows a large variation (up to four times the surface temperature) in the response of the target to the incoming laser beam compared to using constant material properties, see Figure 2.21. This suggests that consideration of the temperature variation of material properties is essential to correctly simulate the target response to the laser beam. Despite the large variation of material properties, a number of models published on pulsed laser ablation

are based on constant properties for each phase of the material [31, 32, 54, 73, 138]. In recent years, the increased availability of experimental data at high temperature [139–141] and the derivation of EOS for a wide range of materials [104–107] has facilitated the use of temperature and pressure-dependent material properties. Consequently, several models for nanosecond pulsed laser ablation have been published using temperature-dependent material properties [23, 30, 55]. These studies have shown that the thermodynamic path of the material is along the binodal during heating. In this study, the material properties used are provided by experimental results.

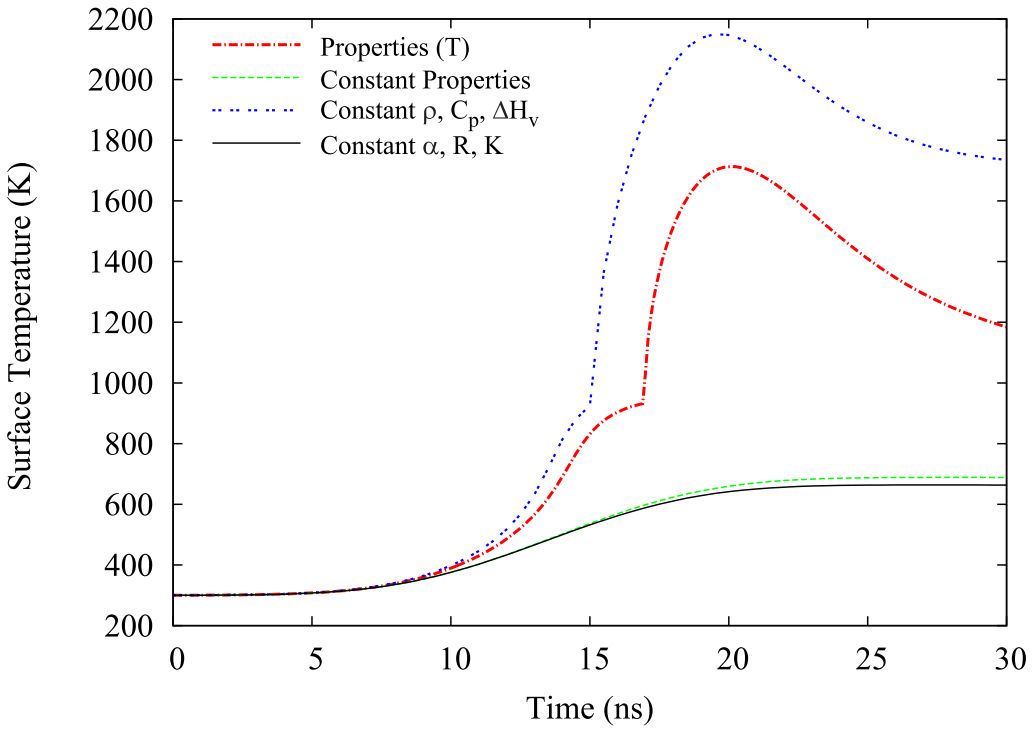

Figure 2.21 : A comparison of the surface temperature using constant properties and temperature-dependent properties of Aluminium [55].

2.2 Study of diamond and related material laser ablation

The unique properties of diamond and related materials compared to conventional materials allow the development of numerous potential applications such as wear resistant coating [142], cutting tools for ceramic materials in oil and gas exploration [143], two-dimensional pixel and strip detectors for UV and X-ray sources [144, 145], charged particle detection systems for high-energy physics experiments [146], heat sinks for power electronics [147], and optical windows [148]. However, "as-synthesised" bulk diamond often requires post-machining of a specific shape to enable functionalities of the product. The shaping of diamond by conventional methods (e.g. grinding, EDM) is complex due to the limited access of the tools to minute part geometries, whilst also being regarded as economically inefficient. The use of laser for through cutting of diamond is already well documented [149] but recently the use of pulsed laser for the shaping of diamond and related materials has been viewed as the next step for the efficient generation of complex 3D shapes [150] with application in the manufacture of cutting and drilling tools [151], grinding pads [36], diamond diffractive optics [28], etc. The use of various laser sources from microsecond to femtosecond (nano [26, 152], pico [138] to femto [153] second) and from infra-red to UV has been reported for the processing of diamond and related materials [28], generating different levels of thermal and mechanical damage to the piece. The employment of shorter pulses (pico-second and femto-second range) shows a tremendous improvement in the cut-quality and reduction of thermal damages [28]. Despite these advantages, ultra-short pulsed lasers are less used industrially due to the advantages of widely used nano-second lasers with their robustness, reliability and increased power per price unit. Nevertheless, the many physical mecha-

nisms involved during nano-second pulsed laser ablation and the generation of defects in the piece remain unclear [23, 136].

2.2.1 Experimental investigations

A profound understanding of the physical phenomena occurring during the pulsed laser ablation of diamond is necessary to predict possible defects or subsurface damage to the target. Thus, thermal and mechanical damages have been investigated for a wide range of laser machining conditions and for a variety of diamond and related materials [29, 36, 37, 154]. Although time consuming and difficult, these studies have shown that there is extensive graphitisation of the laser-irradiated area with the presence of a variety of carbon micro-structures (highly oriented micro-crystalline graphite, nano-crystalline graphite, corrugated graphite, amorphous graphite) on the target surface. These findings are in good agreement with previous studies on annealing of diamond in furnaces showing similar graphitisation [155]. In the annealing studies, the speed of the phase transition is proportional to the furnace temperature [156, 157]; this demonstrates the prevalence of the thermally driven phase transition of diamond. The graphitisation of diamond during pulsed laser ablation is produced along an abrupt transition interface between the diamond and the graphitic or carbon structure which, as expected, suggests that the thermal load is the main driver of the graphitisation of diamond. Thermal phase transition has also been highlighted as a characteristic of pulsed laser ablation in tetrahedral amorphous carbon (ta-C) [138], a form of incomplete diamond for which the amount of carbon-carbon bound sp^3 (diamond like bound) is between 70% and 90%, and CVD diamond [28, p. 394]. In effect, these studies have shown that the thickness of the graphite layer as a function of the temporal length of the pulse follows the same trend as the characteristic length of the heat penetration. Thus, thermally activated

phase transition of diamond is an important mechanism for the growth of a graphite layer near the surface during pulsed laser ablation. Although experimental investigations help to understand the main drivers of diamond graphitisation, there are few studies investigating the thickness of this layer as a function of the pulse fluence. Furthermore, the kinetics of the growth of the graphite layer (as material swelling) and the ablation (as material removal) of diamond structure have never been studied. The graphite layer formed in the initial stages of the ablation process plays a dominant role in the laser absorption due to its high absorption coefficient compared to diamond and related material [28]. Previous experimental investigations have studied the phase transformation when pulsed laser ablation has been performed by overlapping pulses. They therefore provide detailed information about the processes, without separating physical phenomena (melting, vaporisation, plasma creation, condensation, etc.) occurring from different pulses and at levels of energy along the spatial profile of the pulse. Furthermore, the experimental studies of crystalline structure change during pulsed laser ablation using TEM analysis use a constant energy per pulse to create the "trench", hence they cannot investigate the effect of the pulse energy on the micro-structure [29, 36, 37]. Although adequate for quantifying damage of large machining tasks, the observations from these studies might not provide sufficient detail (energetically and due to the overlapping of pulses) to study the fundamental generation of thermal defects during a single pulse laser ablation.

The ablation of diamond by nanosecond laser pulses is of particular interest due to the wide usage of nanosecond laser to machine diamond. It must be noted that the previous discussion about the physical processes leading to the ablation of the target apply also to diamond ablation. However, the carbon allotropes with high sp^3 bound present a specific solid transition

between the thermodynamic metastable diamond form to the stable form, graphite. Hence, the addition of the solid transition occurring during the thermal ablation dramatically changes the material properties at the surface of the target [28]. It is therefore necessary to address the particular challenges of graphitisation during interaction with the laser pulse. A few models about pulsed laser ablation of diamond have been published [138, 158–160].

2.2.2 Modelling and numerical investigations

2.2.2.1 Formulation of direct graphitisation by laser pulses

The work of Strekalov et al. [159] concerns the interaction between pure diamond and nanosecond laser pulses. The study focuses on the estimation of the probability of graphitisation at the surface of the diamond. The study also shows that for the graphitisation energy of pure diamond, the probability of optical transition between graphite to diamond for 30 ns FWHM pulses is extremely low ($< 10^{-26}$ for a given carbon atom) for the early stage of graphitisation. Although this study is interesting for its estimation of the threshold of graphitisation at the beginning of the interaction between the diamond and the laser, it does not address the propagation of a graphitisation front inside the diamond. Thus, the study cannot be used to understand the dynamic propagation of the interface between the diamond and the graphite. Furthermore, the study estimates the reduction in activation energy due to the interaction of the diamond lattice with the photon from the laser. Once the thickness of the graphite layer reaches 140 nm, the laser light is completely absorbed by the graphite. The study is useful for understanding the initial interaction between the laser and the diamond target, however it shows that the probability of transition from a undisturbed pure diamond by optical transition is not likely to occur during nanosecond pulse laser

ablation. It is therefore possible that the main initiation mechanism for the graphitisation of diamond is the presence of surface defects that further reduce the activation energy necessary.

2.2.2.2 Thermal graphitisation estimation at the end of the pulse

Similarly, a model for the graphitisation of diamond like carbon is proposed by Kononenko et al. [138]. The model uses the material properties of tetrahedral amorphous carbon to estimate the maximum extension of a graphitisation temperature during the interaction between the diamond like carbon and the laser. Although the model is in reasonable agreement with experiments, it does not address the transition between the diamond like carbon to graphite in a self-consistent way. The position of the interface is calculated after the end of the simulation, thus the graphitisation does not have an impact on the result of the simulation and the model supposes that the material properties of graphite are the same as the diamond like carbon. Furthermore, the model is calibrated using the graphitisation temperature as a free parameter. The value for the graphitisation temperature from the model is 500 °C. Although this value seems to be correct for the thermodynamic stability of the film, it does not address the dynamic transition from diamond to graphite. Previous studies have shown that the thermal graphitisation of bulk diamond also has an important temporal component [155], and a temperature threshold is not sufficient to describe the transition between graphite and diamond. Hence, this approach is not self-consistent and should be discarded for a deeper understanding of the mechanisms of graphitisation and ablation.

2.2.2.3 Optical graphitisation of diamond

The work of Lin et al. [160] provides a self-consistent formulation for the rate of graphitisation using the formula proposed by Strekalov et al. [159]. The

diamond is considered as transformed into graphite when the total probability of transition is equal or superior to one. However, the model estimates the temperature using a semi-analytical formulation that does not consider the temperature-dependent parameters and the vaporisation at the surface of the target. Furthermore, the pulse shape is a simple rectangular shape which cannot account for the real temporal shape of pulses. The lack of consistent description of the ablation mechanism means that the model depends on an ablation temperature for which the material is considered ablated. The ablation temperature is not a fundamental property of the material, thus the authors estimate the temperature as 3700 K. This is in contradiction with numerical and experimental results for graphite ablation [44, 89], for which an ablation temperature cannot be defined during nanosecond ablation. Although the model is in good agreement with experimental results for the thickness of the graphite layer, the position of the surface is not calculated in a consistent manner, thereby invalidating the results from the simulation. It must be noted that although the model considers the optical graphitisation of diamond, it does not consider the thermal graphitisation occurring during the heating of the diamond target. Thus, the graphitisation in the model cannot extend over the absorption length of graphite for the laser. This is not in agreement with experimental investigations of thermal damage induced by laser during diamond machining that observe graphite layer extending 20 times the absorption length. Therefore, the optical graphitisation alone cannot explain the observed thickness of the graphite layer.

2.2.2.4 Conclusion

Finally, previous models for the nanosecond ablation of diamond do not address essential phenomena occurring during pulsed laser ablation of diamond such as the variation of material properties with the diamond transition and

the temperature-dependent material properties. The models are mostly not self-consistent for the graphitisation threshold or the ablation threshold. Accurate description of the processes leading to the graphitisation and ablation of diamond during nanosecond laser pulse requires the development of a novel model for diamond ablation using the modelling tools developed for the ablation of pure materials. The study by Strekalov et al. [159] shows that optical graphitisation is unlikely to occur during nanosecond ablation, hence thermal graphitisation is the main graphitisation mechanism.

2.3 Kinetic methods for pulsed laser ablation modelling

With its capability to generate small features, pulsed laser ablation (PLA) offers new possibilities for microprocessing/structuring of a large variety of difficult-to-cut materials such as high strength Ti/Ni based superalloys (e.g. Ti6Al4V [39], Inconel 718 [161]), ceramics (e.g. SiC [162], Al_2O_3 [163]) and super-hard materials (e.g. diamond [164], cubic boron nitride [43]). This, in conjunction with the decrease in capital cost for high power lasers, makes pulsed laser ablation a viable machining method for high value-added industries (e.g. medical, aerospace, defence, microelectromechanical systems). PLA has the capability to machine parts with complex geometries (e.g. cutting insets [165], dressing/truing tools [166], micro-grinding wheels [27], ink-jet holes [167], etc.) for which conventional (turning, grinding and milling) and other non-conventional (e.g. abrasive water jet, electrical discharge) machining processes might not be appropriate due to the small size of the feature to be generated or limitations caused by the hardness/strength of the workpiece material or other part quality related issues (e.g. heat affected zones).

Although PLA has some significant advantages in micro-machining, it also faces some major challenges: (i) apart from the beam characteristics (pulse energy, temporal profile of the pulse and spatial profile of the pulse) and kinematic parameters (vector of propagation of the beam and feed velocity), it is a time dependent process; the accelerations and decelerations caused by the machine stages/optics (i.e. galvanometric mirrors) dynamics result in non-uniformity of the ablation process, thus leading to inherent variation of the machining quality; (ii) because PLA occurs in a small area (spot size $<$ 50 µm) [36] and a short time ($<$200 ns) [168] while generating molten debris and noise (e.g. plasma emission, electron generation etc.) [135, 169], the process is difficult to monitor online; (iii) the material removal mechanisms are diverse and complex as they depend on the wavelength and temporal profile of the laser pulse; furthermore some removal mechanisms (i.e. explosive boiling, homogeneous vaporisation, etc.) are not entirely understood [23, 44]. Thus, not surprisingly, PLA has been a significant research subject for micro-machining in the last two decades.

Despite the ever-increasing use of lasers for micro-machining, lengthy and costly experimental studies are often required to estimate the optimum beam path and process parameters for the generation of specific micro-features [170]. The development of a beam path strategy is not a trivial task for free-form structures and normally involves a number of iterations, with measurements being done on the resulting part at each iteration to enable the optimisation of the process parameters and beam path. This can be a barrier for some potential users of laser machining, especially those who need to create innovative free-form structures.

The development of physical models to describe the conservation of heat, mass and momentum, using the finite difference/element/volume methods to solve the system of equations, requires HPC computational power to calculate

the three dimensional solution in a realistic time period [85]. Therefore, most of the models presented in the literature are one [23] or two [47] dimensional systems of equations, hence not covering the full 3D information needed for the simulation of free-forms to be generated by PLA. These models have mainly been developed to provide useful insight into the phenomena occurring during pulsed laser ablation for the interaction of a single or low number of pulses with the target surface. However, following this approach, the simulation of one laser pulse interacting with the target requires several minutes with a standard computer. Since the simulation of a surface generated by PLA can require tens of thousands of pulses, this would last at least several days. Thus, physical modelling of PLA cannot be applied for optimisation of the beam path and process parameters for micro-machining of complex geometry surfaces. In this context, the avoidance of a "trial and error" experimental approach requires the development of a computationally inexpensive mathematical model for PLA, which will enable a step-change in the process control. However, little attention has been given to this issue and there are few examples in the literature on modelling of PLA for large scale machining tests.

2.3.1 Modelling based on simplified assumptions

A modelling approach based on simplified assumptions leads to a simple model with low computational cost [171, 172], enabling rapid calculation of the amount of material removed by an individual pulse. This approach has been widely used to reduce the computational cost for the study of drilling using several thousands of pulses [172]. This modelling approach provides predictions with reasonable agreement with experimental results, however it is often impractical or impossible to consider temperature dependent material properties such as the thermal conductivity, reflectivity, specific heat, etc. Although these methods can be useful to understand the main

factors influencing the accuracy of numerical predictions, they cannot be used to provide accurate predictions for pulsed laser ablation since temperature-dependent parameters are essential [33].

2.3.2 Modelling based on learning/genetic algorithms

Another kind of modelling approach is based on the generation of machine learning algorithms [41, 42, 171]. These methods rely on the availability of a large dataset of experimental results from which the model is trained to reproduce the experimental results for a given condition. The use of machine learning can be advantageous if experimental results do not show a clear correlation with experimental conditions (fluence, pulse length, laser wavelength, etc.). However, since the models are simply reproducing experimental results, they are not able to reveal the physical processes occurring during pulsed laser ablation. Furthermore, these models work only within the range of conditions for which they have been trained and cannot be modified to capture experimental observations made during the process. Finally, this method is ill-formulated for the physical understanding of pulsed laser ablation due to (i) the cost of producing large datasets of experimental data; (ii) the experimental conditions usually being well controlled, producing relatively well reproducible experimental results; (iii) the lack of physical meaning. Although the method provides accurate results for single pulses [171], it cannot be modified to predict overlapping pulses and cannot be applied to the machining of large surfaces by pulsed laser ablation.

2.3.3 Modelling based on the calibration of parameters with a pulse-by-pulse evaluation of the resulting surface

The calibration of models that is informed by experimental results has produced fast and accurate prediction of single pulses [39, 40, 173]. The method is similar to models based on learning or genetic algorithms, however relations between the conditions (fluence, feed speed, pulse length) and the predictions are derived from experimental data and hence the physical meaning is preserved. Modification of the model to consider new physical phenomena is then facilitated, such as the method presented by Holmes et al. [173]. The model is computationally inexpensive and can simulate large machining works (above 10^4 pulses) in around 10 seconds. Interestingly,

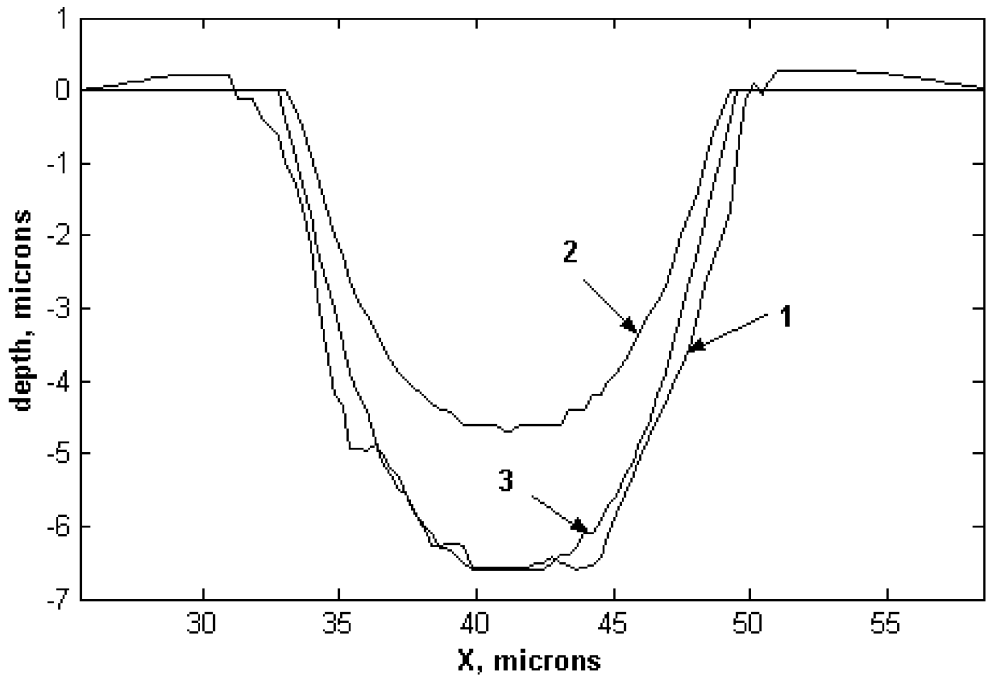

Figure 2.22 : Cross section for a machined trench using a nanosecond pulsed laser in SU8 [173]. Curve 1 is the experimental profile, curve 2 is the simulated profile using the single crater for the calibration of the model, and curve 3 is the simulated profile using single craters and trenches for calibration of the model with a delay in the ablation term.

the model does not usually require material properties such as specific heat, absorption coefficient, etc., therefore the model is applicable for a wide range of materials and conditions. The main drawback of this method is the loss of accuracy during the machining of large surfaces by overlapping pulses [39, 40, 173], see Figure 2.23.

These models are usually based on the Beer's law to characterise the influence of the local fluence on the amount of material removed. The model is then calibrated using the maximum depth at the centre of the crater, neglecting any interaction inside a single crater. Finally, the model considers that the target is instantaneously ablated. The model is proven to be accurate for single crater and relatively low overlapped pulses [39, 40], however an increase in the overlapping of pulses leads to poor prediction of the average profile, see Figure 2.22. This might be due to the change of material properties after the first few pulses, which is commonly found in pulsed laser ablation [173]. One might add a delay in the ablation term until the material reaches "maturity" with constant properties. The work of Holmes et al. [173] shows that this approach proves effective for improving the agreement between experimental results and the model, see Figure 2.22, however it seems that the method is inextensible to free-form topography such as the example presented in Figure 2.23. Modification of the modelling framework is therefore hardly justifiable since the machining of the free-form surface is only a direct extension of the trench machining. The modelling framework for the simulation of free-form surfaces thus requires a step change in the consideration of the impact of the overlapping of pulses on the material removal that the single pulse models cannot take into account.

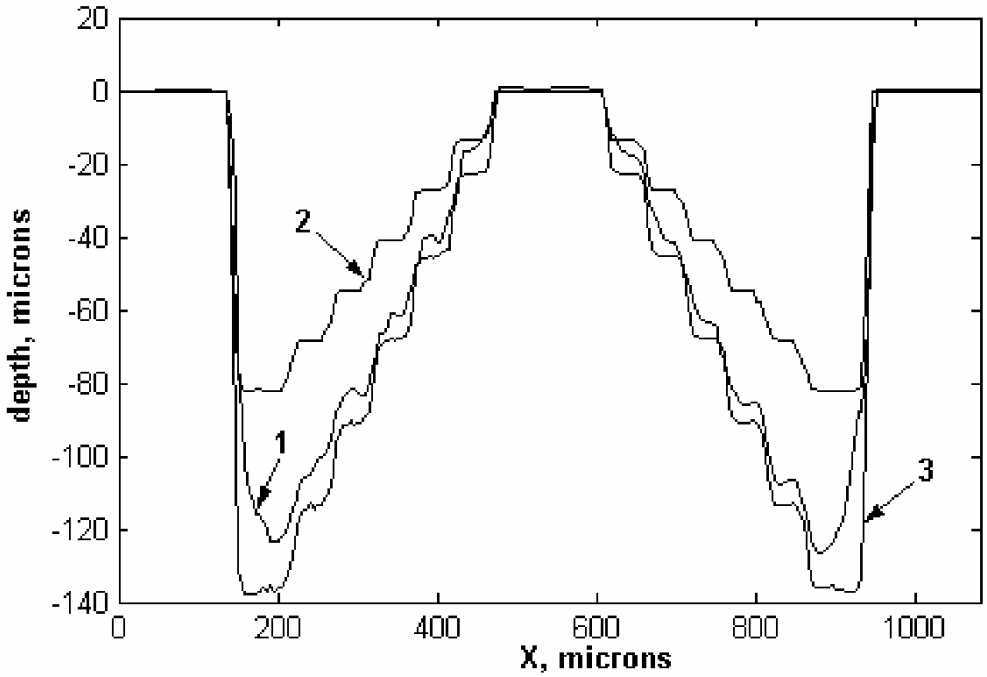

Figure 2.23 : Cross section for a machined pyramid structure using a nanosecond pulsed laser in SU8 [173]. Curve 1 is the experimental profile, curve 2 is the simulated profile using the single crater for calibration of the model, and curve 3 is the simulated profile using single craters and trenches for calibration of the model with a delay in the ablation term.

2.3.4 Example of the abrasive water jet machining with a continuous modelling of the abrasive wear by multiple grid impacts

The use of calibrated continuous models for apparently discrete processes has proven to be a successful avenue for accurate prediction of material removal for AWJ [174–176]. The erosion process during AWJ is mainly due to the impact of the grit onto the surface, generating plastic deformation and cracks. These two mechanisms are due to the high frequency impact of abrasive particles randomly distributed in the water jet [177]. Although the model does not compare the erosion process due to individual grit, continuous models have proven to be valuable due to their wide applicability and good agreement with experimental results, see Figure 2.24. Continuous modelling

to predict the material removal from discontinuous and stochastic processes has been shown to be particularly effective at improving the model to consider an increasing number of experimental conditions such as feed speed variation, stand off distance [178], angle of incidence, forward/backward milling [175] and overlapping of trenches [174]. Recent work on the continuous modelling of AWJ considers the stochastic variation of the trench profiles [176].

Finally, the main advantages of the simplified model for AWJ are the use of a reduced amount of experimental results to calculate the model parameters and the possibility of modification of the framework to account for new experimental conditions.

2.4 Summary of the literature

A detailed literature review on previous research into PLA processes and phenomena has been presented. A large group of researchers have focused on improving understanding of the physical phenomena occurring during pulse laser ablation by experimentally studying the ablation mechanisms and

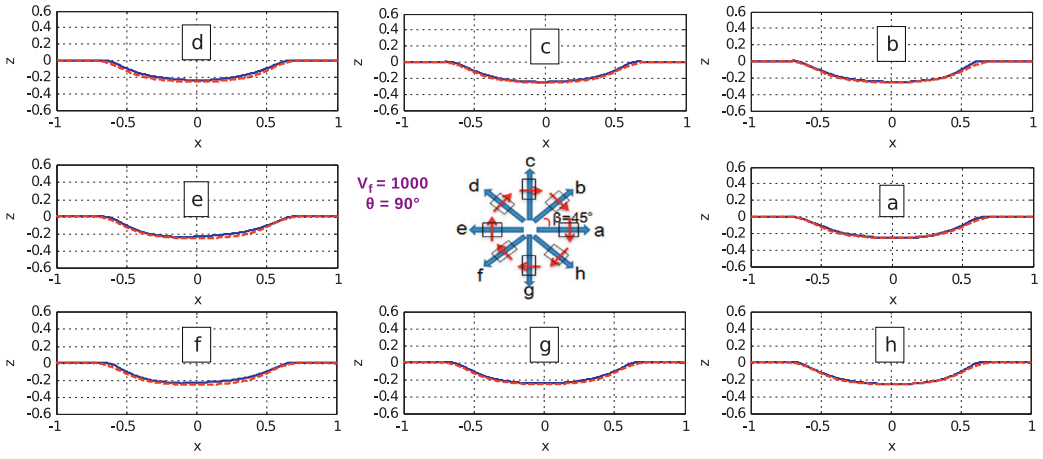

Figure 2.24 : Examples of model-predicted footprint profiles (red dotted lines) against experimental profiles (blue solid lines) for abrasive water-jet. [Note: the unit for x and z is millimetres and the "eight-spoked asterisk"(*) in the middle represents milled trenches (blue arrows) at different jet trajectory angles and their directions of scanning (red arrows)].

resulting damage to the surface. The difficulty in experimentally capturing the ablation mechanisms during the short space and time frame of the ablation has led to the development of numerous models to simulate the physical phenomena occurring during nanosecond pulse laser ablation. These models have shown that the thermodynamic path of the material is highly dependent on the energy input of the laser, however several other conclusions can also be drawn:

- Temperature dependent parameters are critical for accurate prediction of the amount of ablated material, the heat distribution and the plume break down into a plasma.
- Entrance of the material in the thermodynamic metastable area during heating does not significantly affect the amount of material ablated during pulsed laser ablation. Experimental results exist which suggest that it might be significant for the ejection of particles during the cooling phase of the ablation.
- Plasma absorption, which occurs only after the break down of the plume into a fully ionised plasma, can play a major role in the saturation of the amount of ablated material.
- Volumetric evaporation due to heating of the material above the critical temperature can be a major ablation mechanism, especially for short nanosecond laser pulses.

The development of physical models is the main area of research for the study of the ablation mechanisms during nanosecond PLA. However due to the high computational cost of physical simulation, they cannot be used to predict the amount of material removed during the machining of large workpieces. Some researchers have therefore developed models that rely on

simplified modelling or are built on empirical modelling using experimental data. The advantages and limitations of each approach have been discussed.

An improved physical model for diamond associated with a fast semi-analytical model would be highly beneficial for computing the optimum tool-path with a CAD/CAM system and providing information about the thermal damage associated with the machining. The development of such models is critical, since this would enable the development of new machining strategies without costly and lengthy experimental trials.

2.5 Research challenges emerging from the literature review

Extensive review of previous research has shown that new frameworks to investigate the ablation of diamond using physical and simplified models are key to the development of controlled machining of diamond by laser. This work addresses several difficulties that arise when studying this issue.

2.5.1 Research challenges – Physical model for the graphitisation of diamond

- Although there has been previous research on physical modelling for nanosecond pulsed laser machining, the ablation of diamond is not well understood due to the thermal graphitisation of the target when exposed to laser pulses. It is therefore necessary to construct a new model specifically adapted to the study of the dynamic of the graphitisation front.

- When building a physical model, the change in density of the material is usually not taken into account for the spatial position of the interfaces.

However, if such phenomena is discarded during the simulation of pulsed laser ablation, it is possible to overestimate the amount of material removed by breaking the conservation of mass at the transition between the two materials.

- Consistency of the model is particularly important to accurately predict the amount of material removed. Since the temperature varies over a large range, it is necessary to consider temperature dependent parameters.

- Graphitisation occurs during the laser ablation of diamond and diamond like carbon. For the model to be widely applicable to graphitisation occurring during PLA of diamond and related material, it is necessary to validate the modelling framework for at least two different types of high sp^3 content carbon allotropes.

2.5.2 Research challenges – Simplified model

- There are no previous attempts at constructing a simplified model that addresses the PLA in a continuous framework. Therefore, a new methodology for the model and its calibration must be developed and tested based on existing models currently applied for other energetic beams.

- Previous simplified models have used a reduced amount of experimental data to estimate model parameters. The new framework must be developed such that experimental tests for calibration of the model are kept to a reasonable amount of experimental data.

- Previous simplified models have usually used only one type of target material. The scope of this work is to provide a general framework for

which the model can be applied for a wide range of materials, hence the model framework must be tested for several materials.

- The aim of the simplified model is to be integrated into a CAD/CAM system to design tool-path strategies using optimisation algorithms. A computationally inexpensive model is therefore required and simplicity of the framework is key for wide acceptance and usability.

- The model will be applied for the simulation and path optimisation of large surfaces. It is therefore necessary to test the model for the machining of large surfaces, including several tens of thousands of pulses as well as simple tests to quantitatively calculate the model accuracy.

- The novel approach presented in this work for the prediction of target ablation is the first step toward the generation of a simplified model aimed at CAD/CAM integration. However, since the model will be tested on a relatively small number of materials, it is necessary for the new modelling framework to be capable of accounting for more complex phenomena that might occur for a wider range of materials.

2.5.3 Research challenges – Ablation mechanisms during PLA

- The literature review has shown that there is a need for further understanding of the processes leading to the ablation of material from the target. To address this point, it is necessary to develop a model for which the plume break down into a plasma is connected to the target domain. This provides a comprehensive model which is consistent from the heating of the target to the plume break down into a plasma.

- The thermal damage occurring during PLA can be investigated to

provide additional information about the processes leading to graphitisation and ablation of the target. It is necessary to use advanced characterisation methods to observe the material below the surface of the crater. It must be noted that previous works have focused on the amount of material ablated or the amount of energy absorbed by the plasma. Deeper understanding of the thermodynamic path the material follows has not been investigated due to the laborious work necessary. The transformation of carbon allotropes from diamond to nano-crystalline carbon is not well understood at a fundamental level for a single pulse.

- Allotropes of carbon have been widely studied using Raman spectra, and this work presents an interesting opportunity to use the literature on Raman spectra of carbon material to understand the effect of thermal ablation of the microstructure.

The work presented in this thesis addresses the limitations observed in the literature, with the aim to enhance current understanding of PLA and in particular the ablation of diamond, and to develop a simplified approach with wide usability in CAD/CAM packages.

Chapter 3

Methodology

The experimental equipment used for this work is described in this chapter. This includes the detailed explanation of the experimental set-up, the different techniques that have been used to analyse the samples and the methodology used to extract the experimental results from the empirical measurements. In addition, the limitations and disadvantages of the imaging and measurement methods are also detailed.

3.1 Pulsed laser ablation apparatus

This section describes the lasers and optical setups used in this study.

3.1.1 Laser used in this study

The laser used is the SPI G3 20W-ST. The active medium is a Yb-doped fibre, and GTWave™ technology [179] is used, see Figure 3.1, producing a pulse centred at 1061 nm ± 3 nm. The active medium is pumped by a series of diodes producing a continuous laser light around 900-1000 nm. Laser seeds are generated by a laser diode. The seed is amplified and transmitted through a optic fibre. At the end of the fibre, the pulse is collimated and expanded. It is possible to change the temporal profile of the pulse ad hoc. The waveform can be chosen between 32 pre-programmed "states". From the data shown in Figure 3.2(a), the profiles of the pulses may be expressed as a function of the "states" or waveforms. The temporal profile of the pulse can

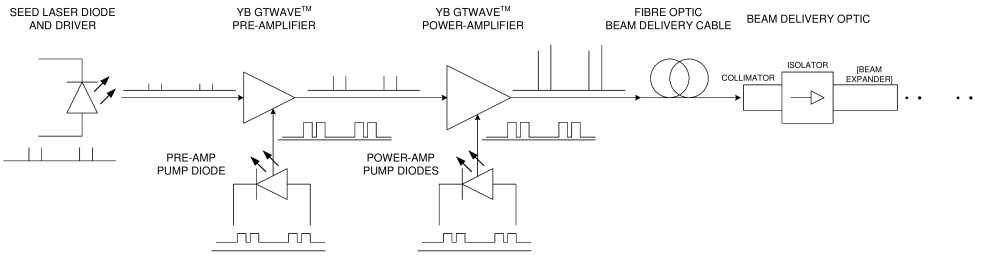

Figure 3.1 : A scheme of optical configuration for the generation of pulses with the SPI G3 [180]

be varied from 250 ns (Waveform 0) to 9 ns (Waveform 5). Energy per pulse decreases with shorter temporal profile. The maximum power for all the waveforms is 20 W, and the reduction of energy is therefore counterbalanced by increasing the switching frequency. In Figure 3.2(b), the variation of power and energy per pulse is given as a function of the pulse repetition frequency. The energetic and temporal characterisation of the pulses are highly dependent on the waveform and the pulse repetition frequency. It must be noted that the pulses' temporal profile and energy are constant over the range of 1 kHz to $\mathbf{PRF}_0$.

Proper understanding of the pulse properties dependent on laser parameters is essential for consistency of experimental data and reliable interpretation of experimental results. The use of a laser system may span several years, therefore its optical properties can change over time due to slow deterioration of optical and electronic components. Moreover, the temperature variation can induce small, but not negligible, variation of the optical properties. The laser energetic response must therefore be carefully characterised before each experimental session. Due to the limitation of the optical design of the laser, the first few pulses will have significantly less energy than the typical pulse energy over a time interval. The simmer current of the power amplifier can be modified to reduce this effect but it cannot be completely eliminated.

The laser is controlled through RS232 DE-9 communication standard. It

is possible to control the pulse repetition frequency, simmer current of the power amplifier, the level of the power amplifier, and the pulse waveform. It must be noted that the level of the power amplifier can be changed inline, whereas the pulse waveform and pulse repetition frequency require the laser

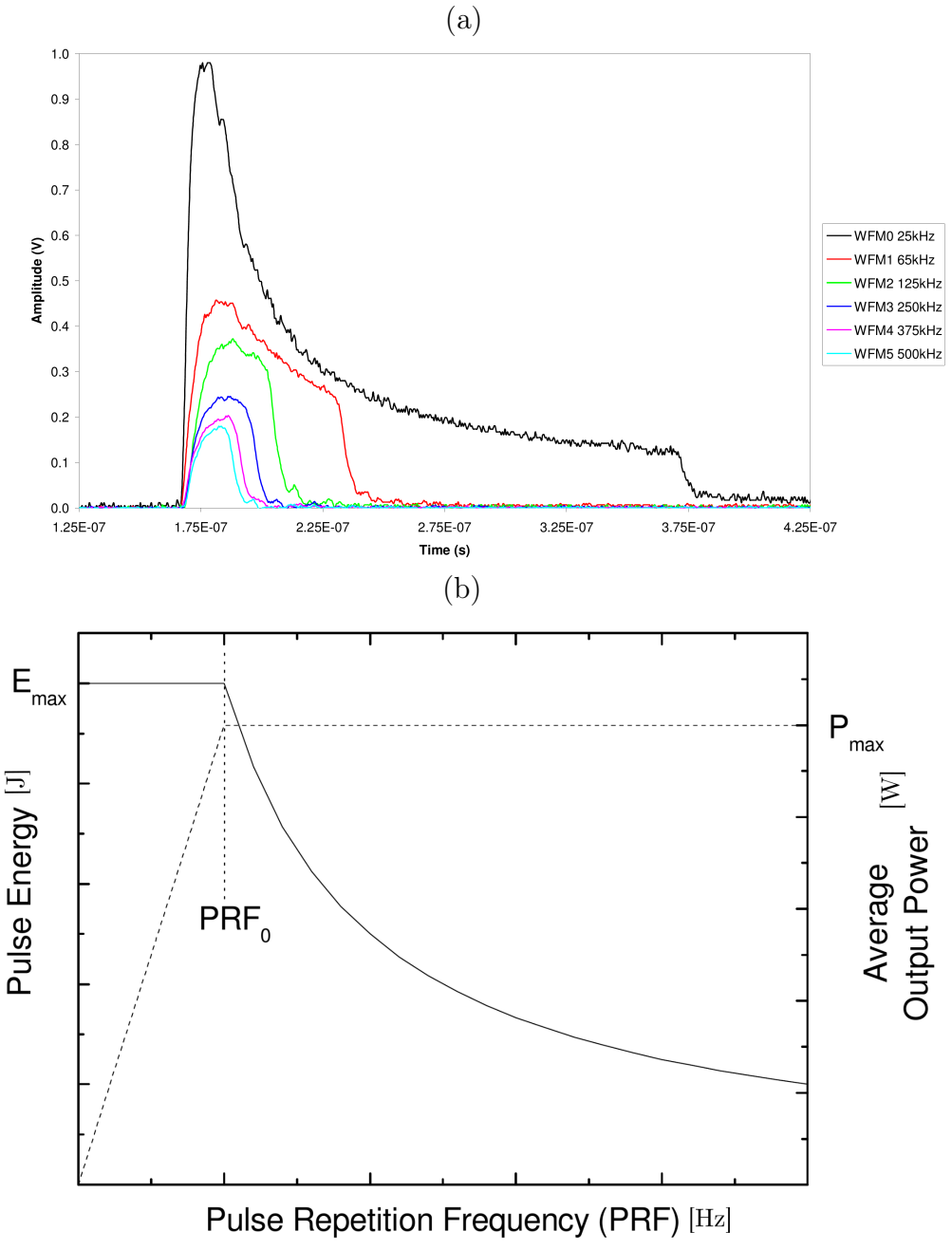

Figure 3.2 : (a) Temporal profile of the pulses for 5 Waveforms produced by the SPI G3 [180]. (b) Variation of power and energy per pulse with pulse repetition frequency.

state to be "READY". In the next section, the equipment used to measure the power and spatial profile is presented.

3.1.2 Measurement techniques for pulse characteristics

3.1.2.1 Optical power meter

The optical power meter used during the experiments is a S350C from Thorlabs, and is designed for high-peak-power pulsed laser sources around 1064 nm. This power meter is based on the conversion of the laser light to heat and utilises the generation of a voltage when a conductor is subject to a thermal gradient [181] (also known as the Seebeck Effect). The difference in temperature between the absorber (a Schott Glass) and the mount is measured using a thermopile and converted into a power measurement. Such instruments are useful for average measurement of the power and are relatively slow (1 second response time to a power variation). At 1064 nm, the measurement uncertainty is around ± 5% of the real power. The instrument is fairly independent of the wavelength and should give the real total power in the spectrum range of the pulses. The system is fairly robust but cannot be used if the laser is tightly focused, as damage may be caused to the absorber.

Since the sensor can be used anywhere along the beam path, it is possible to monitor loss due to the mirror and the accumulation of dust on the mirror. Unless otherwise specified, experimental power measurements are taken at the end of the beam path just after the last optical element (usually the f-θ lens of the 2D galvanometer scanner head). The total power is equal to

$$\mathcal{P} = E_p f_l \tag{3.1}$$

with $\mathcal{P}$, E_p and f_l being the power of the laser, the energy per pulse and the repetition frequency of the laser pulse respectively. Considering that the pulse

repetition frequency is accurately set by the laser, the power measurement is used to retrieve the energy per pulse. From the temporal profile of the pulse (taken from the literature, the constructor manual, or experimental measurement), it is possible to extract the peak power and therefore obtain all the energetic parameters of the pulses and laser. The peak power can be calculated using the relation below,

$$\mathcal{P}_{\mathrm{p}} = \frac{E_p}{\int_{t_{\mathrm{start}}}^{t_{\mathrm{end}}} \mathfrak{i}(\mu) d\mu}, \tag{3.2}$$

with $\mathcal{P}_{\mathrm{p}}$ and $\mathfrak{i}(t)$ being the peak power and the instantaneous intensity respectively. Measurement of the temporal energetic parameters is not sufficient to fully characterise the pulse, therefore the spatial profile is as important as the pulse energy.

3.1.2.2 Beam profiler

In effect, assuming a Gaussian profile at a wavelength of 1061 nm, it is found that a pulse focused by a lens of 100 mm focal length has a beam diameter, ω_0, at the focal plan equal to,

$$\omega_0 = \frac{67.545}{D}, \tag{3.3}$$

with D and ω_0 respectively in millimetres and microns. This simple equation explains one of the most interesting properties of a Gaussian beam. The beam can be focused to a very small size. Using Equation (3.3), a 6.5 mm width Gaussian beam will produce a beam radius at a focus of 10.4 µm. This is a reduction of the beam size by 312 times and an increase of energy by area of almost 5 orders of magnitude. Thus, the beam radius at the focus plan is critical for accurate determination of the energy balance during the interaction between the laser and the material. The beam size at the

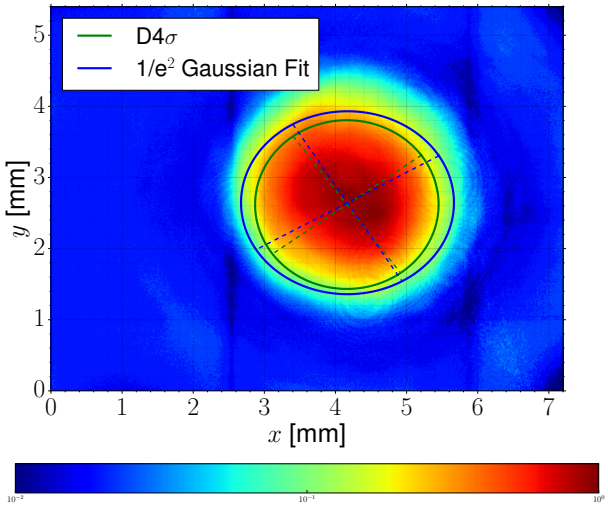

Figure 3.3 : Measurement of the laser beam profile out of the laser head of the SPI-G3, the size of the laser beam measured using the $1/e^2$ Gaussian width definition in solid blue and the D4σ definition in solid green. The spatial distribution of the power is plotted in normed logarithm.

focal plan can be retrieved by calculation, such as the one presented above, but due to the non-perfect Gaussian beam (M^2 >1) and optical aberrations the real beam size is not equal to the calculated value. A camera based beam profiler is used to accurately measure the beam size. The system is a CMOS-1203 from Cinogy Technologies. It uses a CMOS based light sensor with a pixel size of 4.5 µm, assuring accurate measurement of the beam width as low as 30 µm. Each pixel has an 8-bit bit depth for the measurement of the power at the pixel. The sensor is calibrated before each measurement in the range of the dynamics of the camera to take account of the external light sources (lighting, computer screen, etc.). An attenuator is used to attenuate the laser light and protect the sensor from overexposure. The measurement of the spatial profile is taken over at least 100 frames, or 10 seconds. Various definitions of the beam width can be found in the literature such as D4σ, knife-edge, $1/e^2$, FWHM, D86, etc. The D4σ and $1/e^2$ definitions have been used in this study, see Figure 3.3. For the D4σ definition, the calculation of the beam is based on the first and second moment of the

power density distribution for stigmatic beam [182] and astigmatic beam [183]. This definition is sensitive to the baseline value of the measurement since the baseline value is subtracted from the image before calculation of the moment using proprietary algorithms from Cinogy Technologies. This definition is the ISO 11146 international standard for beam width. The second definition consists of fitting an elliptical Gaussian to the measurement of the laser beam. The beam width is equal to the distance between the two points on one axis of the ellipse that are $1/e^2$ times the maximum value of the Gaussian. For an arbitrary stigmatic Gaussian beam, the width measurement using the two definitions gives the same result. However if the beam diverges from a perfect Gaussian distribution, the two methods give different values. The D4σ definition gives more importance to the "wing" of the distribution whereas the $1/e^2$ definition gives more importance to the centre of the beam. The $1/e^2$ definition cannot be used for multi-mode laser beam or beams with a spatial profile too dissimilar to an elliptical Gaussian distribution, for which only the D4σ definition is suitable. In practice, the spatial profile of the laser beam is similar to an astigmatic Gaussian beam, therefore the $1/e^2$ definition is used to measure the beam width along the axis of propagation. In this way the focal plan of the optical system is determined. The beam size is fitted to

$$\omega(z) = \omega_0 \sqrt{1 + \left(\frac{z - z_0}{z_\mathrm{R}}\right)^2}, \tag{3.4}$$

where z_0, ω and z_R are the position of focal plan, the radius of the laser beam and the Rayleigh length of the laser beam. The Rayleigh length is equal to

$$z_\mathrm{R} = \frac{\pi {\omega_0}^2}{4\nu_\mathrm{laser}}. \tag{3.5}$$

with z_R and ν_laser being the Rayleigh length and the laser frequency respectively. It is possible to extract the position of the focal plan and the

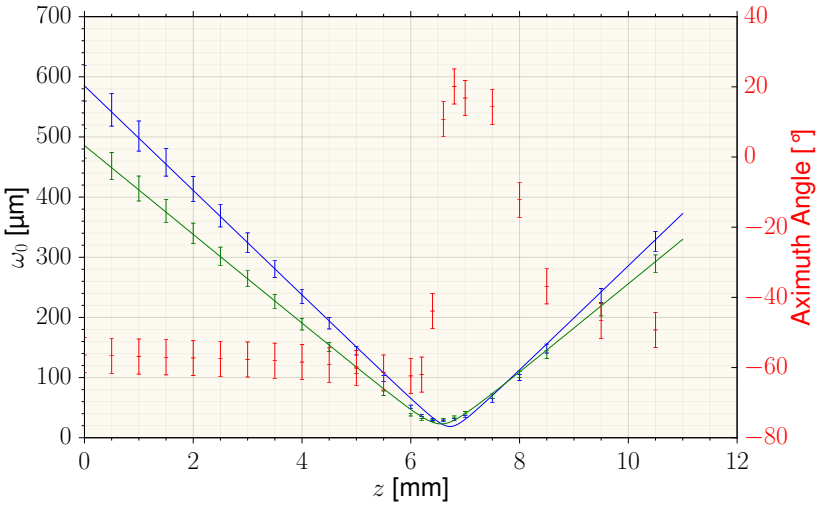

Figure 3.4 : Beam width of the laser as a function of the distance along the propagation axis. The origin of the propagation axis is arbitrarily chosen. The beam width has been measured using an f-θ lens of 100 mm focal lens with the SPI G3 laser. The width of the beam at the entrance of the galvanometer head is around 6.5 mm. The beam is astigmatic, the two beam axes are shown in green and blue.

divergence of the beam. The exact position of the focal plan of the optical system is crucial for determining the correct placement of the workpiece for the machining test, see Figure 3.4. For the system used in this study, the Rayleigh length is around 0.64 mm. This means that 1 mm away from the focal plan, the fluence is reduced by 3.44 times.

The attenuator placed in the beam path to reduce the incident of the beam is not neutral. In the configuration chosen for the camera, an attenuator is always placed in front of the CMOS. The refractive index of the attenuator is different to that of air, which induces an error in the position of the focal plan. The same effect can be observed for pulsed laser ablation in water and laser assisted plain water jet machining [184]. This effect can be quantified and corrected for any attenuator used, for example the attenuator provided with the camera introduced a 0.7 mm offset of the focal plan. If other attenuators are placed in front of the camera in the focusing area, the offset is

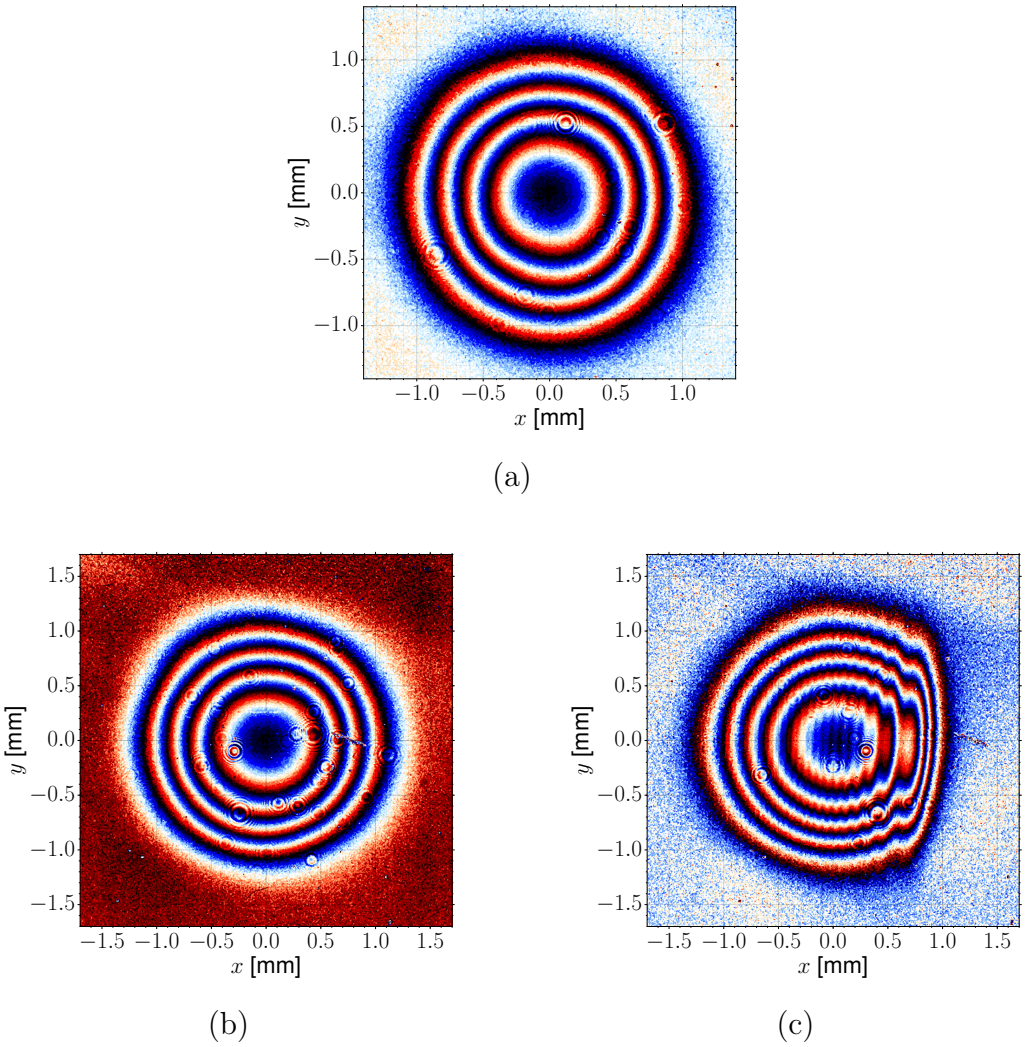

Figure 3.5 : Interferogram of (a) Beam profile with little dust, (b) Beam profile with high level of dust, (c) Beam profile with a wall clipping the beam from the right with the Atlantic-HE of Ekspla.

the sum of all attenuator offsets. When the beam is collimated, the placement of an attenuator in the beam path does not induce an offset of the focal plan. Another defect to consider is the presence of dust on the optics which creates interference patterns in the power of the beam, see Figure 3.5(b). The beam can be clipped if the beam is not correctly aligned or wider than the optical/optomechanical component's aperture, an example of clipping by a vertical wall is given in Figure 3.5(c). Clipping induces a loss of energy and interference pattern that reduces the beam quality. In Figure 3.6, the

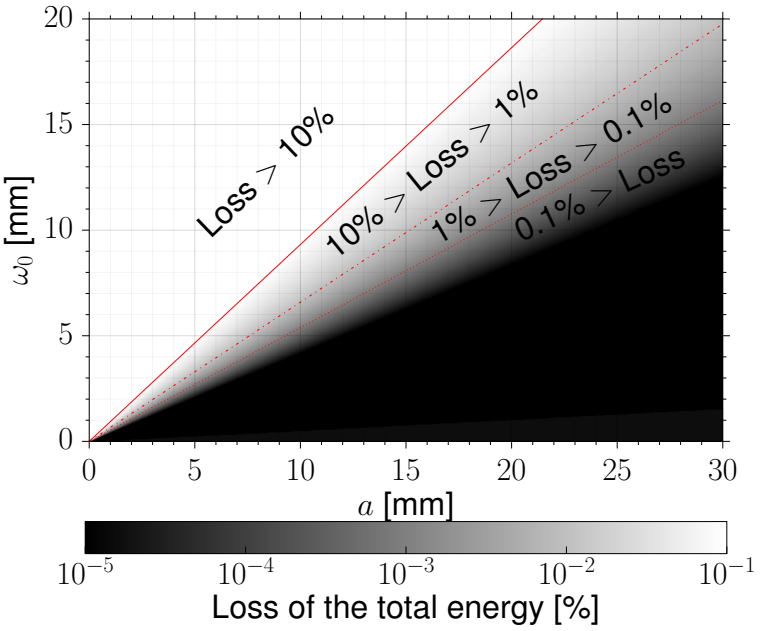

Figure 3.6 : The energy loss due to the clipping of a beam with radius ω_0 passing through a circular aperture of diameter a. The red line represents the iso-loss, solid line 10%, the dashed-dotted line 1% and the dotted line 0.1%.

loss due to the clipping of a circular aperture is calculated. Usually, the loss due to the clipping of the beam must be lower than 1% of the total energy of the beam to avoid degradation of the beam quality. In this study, the galvanometers used have an aperture of 10 mm diameter therefore the beam radius cannot exceed 3.25 mm.

3.1.3 Optical setup

The optical setup has been designed and implemented to satisfy the specific needs of the experimental study. The laser beam must be correctly aligned between the consequent optical elements. This is challenging for several reasons: (i) the laser beam (1061 nm) used is invisible to the human eye, thus requiring specific fluorescent card and imaging equipment, (ii) the position of the beam is highly sensitive to an error in beam pointing, a misalignment of

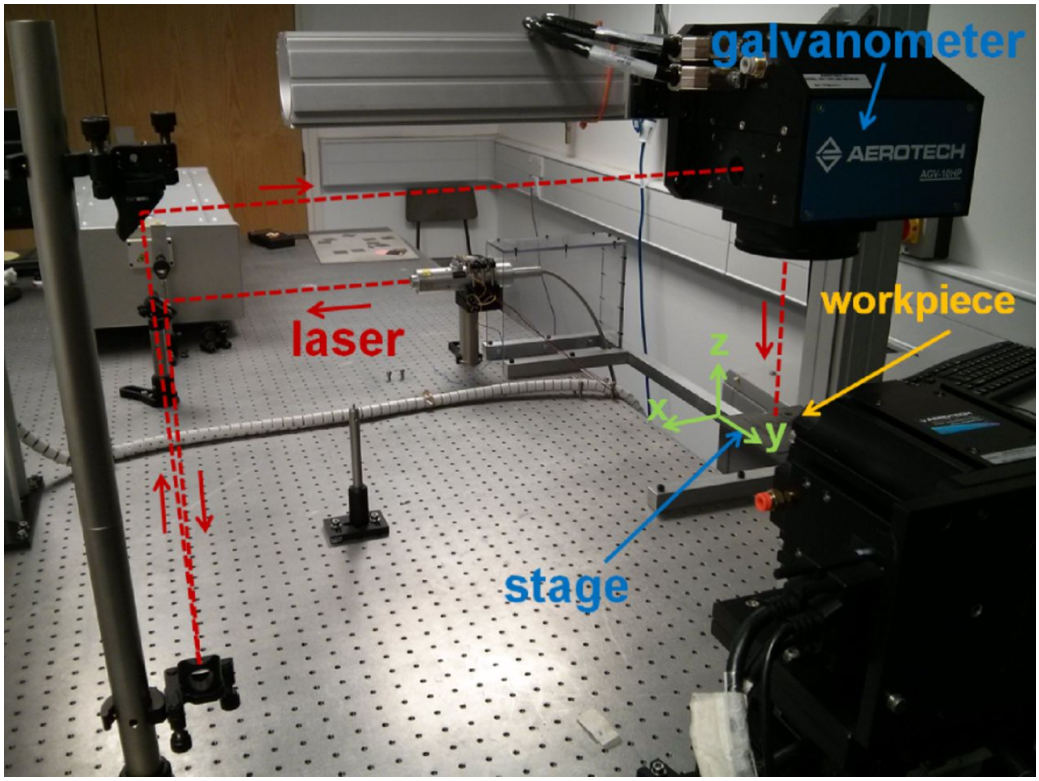

Figure 3.7 : Experimental set-up for the PLA system [185].

1 mrad creates a displacement of the beam of 1 mm after 1 m of propagation, (iii) requires a simultaneous change in angle with the kinematic mirror mount and position of the mirror on the table to reach good alignment. A model of the optomechanical/optical setup is made using a CAD software. The CAD model enables the verification that the equipment will fit on the table and ease the alignment task by placing the element and the clamp to the best position. The alignment of the laser beam is done using the beam profiler, the measurement of the beam position has an error lower than 10 µm.

For the beam expander made directly from 2 lenses in the Galilean telescope design, the relative distance between the two lens needs to be adjusted to collimate the beam. Afterwards, the collimation of the beam is checked by measuring the width of the beam along the path. The beam is then fed into a galvanometers scanner head and focused through a f-θ lens, see Figure 3.7.

3.1.4 Motion control during machining test

The motion of the stages and the galvanometers is controlled by a custom Aerotech System. The system is a compound of a stage for the positioning of the parts/samples and a 2D galvanometer head AGV-10HP (axes C and D). The positioning stage has four axes: three of translation and one of rotation. The translation axes are two ALS130H-025 for the planar translation normal to the axis stage–galvanometer head (axes X and Y) and one AVS125 for the translation of the sample in the direction of the axis stage–galvanometers (axis Z). The rotation axis assured by an ACS-150-135 (denoted by A) has the direction of the axis X. The system is controlled by the software-based machine controller A3200 connected to a Npaq Drive Rack. The amplifiers used for the Npaq are DP32010E. The axes X, Y, Z and A have respectively an accuracy of ± 1 µm, 1 µm, 1.5 µm and 72.7 µrad. The axes C and D provide an accuracy of ± 1.2 µm. A minimal working example of the programming language for the Aerotech system is presented in the Listing A.1. Initialisation of the variable and mode for the control of the stages is set at the beginning of the program, lines 1–22. Subsequently, the laser parameters are set, lines 24–31. Afterwards, the commands for the position of the C axis are executed, lines 33–51. The position of each axis and the laser activation are measured by the system. The command and feedback position for each axis can be saved.

It is possible to control up to two positions and two speeds in synchronisation. The command for a synchronous movement to a specific position is,

$$G41\,\underbrace{C\,1.}_{\text{Master Axis: Next position}}\quad\underbrace{D\,2.5}_{\text{Secondary Axis: Next position}}\quad\underbrace{F\,355.}_{\text{Global speed: Global Speed}},$$

This defines the next position for the two axes and the global speed to reach the position. The control always pre-computes the path to generate an achievable

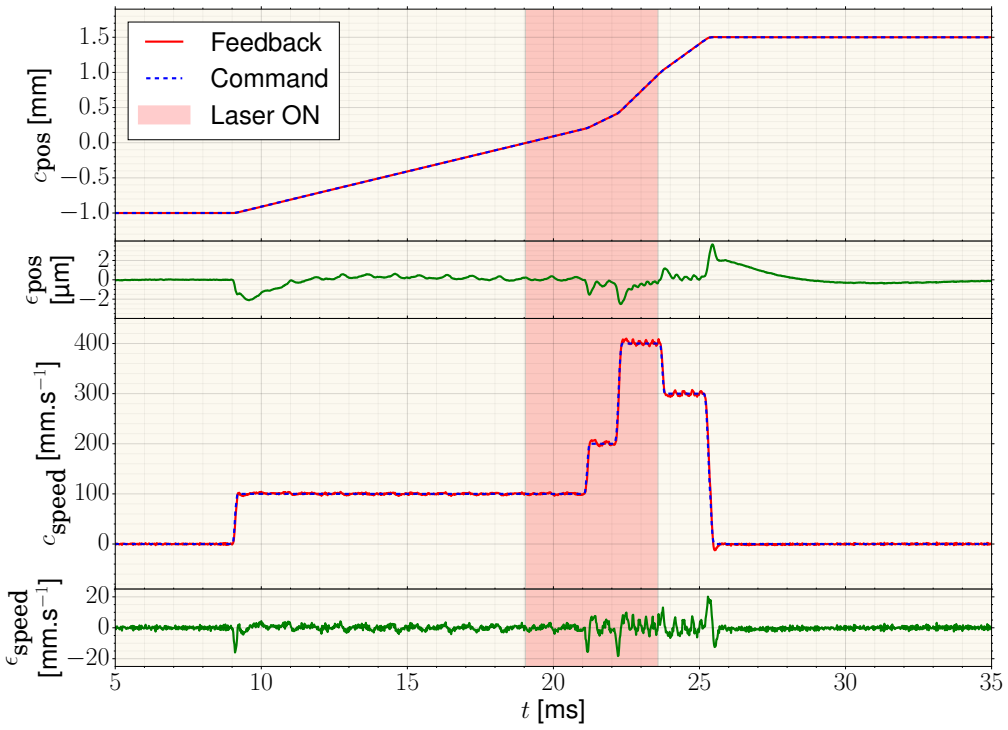

Figure 3.8 : The controller response to the program presented in the Listing A.1. The top, second, third and bottom plots are respectively the position, position error, speed, speed error as a function of the time.

command. The process can be tuned using software parameters, therefore the command and the resulting movement can be improved. However, the tuning of the parameters is challenging since it is done iteratively and the results are difficult to predict due to the complex control system of the Aerotech system. Tuning therefore cannot be done for large scale machining for which a program consists of tens of thousands of lines.

A review of the feedback compared to the command position is done, thus improving the reliability of the system for experimentation. In Figure 3.8, the axis movement resulting from Listing A.1 is presented. The controller accurately reproduces the position command, with an error below 4 µm. From Figure 3.8, it is apparent that the feedback position is always delayed compared to the command position. This is coherent with a closed-loop control and the reaction of a non-infinitely stiff system (jerk limitation).

Clearly visible at the deceleration after 25 ms in Figure 3.8, the inertia of the axis is higher than expected by the controller, and the last position is overshot by around 4 µm for 2 ms. The quality of the control directly affects the quality of the resulting piece. The feedback speed of axis C is in good agreement with the command speed. It must be noted that oscillations appear after high acceleration of the system. It seems that the system does not succeed to dampen these oscillations even after hundreds of microns of travel. Oscillations affect the machining quality and are inherent to the control system.

The system is limited by the processing power of the computer and the internal memory of the controller. In effect, a synchronous movement cannot exceed a certain number of positions, typically 300, that can be extended but at a cost to the memory available. The test presented in Figure 3.8 is typical of the speed and size of real machining tests. The total time of the machining is in the order of tens of milliseconds, therefore the number of control points to compute per timestep can outstrip the computer capacity and limit precision of the movement for high speed.

The laser is controlled via a positive 5V gate with a BNC cable. During the machining of pockets, it has been found that the start and stop of the laser is not perfectly synchronised with the position of the laser on the surface. The error in position (around 5–10 µm) cannot be explained by an inaccuracy in the control of the axis. This effect can only be explained by the absence of synchronisation between the clock of the SPI G3 laser and the Aerotech system, introducing a delay in the start/stop time of the laser that can result in poor machining quality. A delay of several 10 µs creates a displacement of several µm. This effect is particularly visible during large machining tests of pockets or trenches.

3.2 Surface characterisation and measurement techniques

Surface characterisation and measurement is key to the validation of the model. They offer a means to evaluate the results of the tests and to investigate the physical processes occurring during PLA. In this section, several instruments for the measurement and the characterisation of the surface and subsurface are presented. For each instrument, the operation principle is presented and the limitations of the technique are explained.

3.2.1 Surface Imaging techniques - Scanning Electron Microscopy

Optical microscopy is limited by the size of the observable features by the Abbe diffraction limit [186]. The minimum size of observable feature is around 250 nm, which is not sufficient for accurate imaging of the features that are produced by PLA (crack, micro-droplet, etc.). Scanning electron microscopy offers a resolution lower than 1 nm (using De Broglie wavelength for the

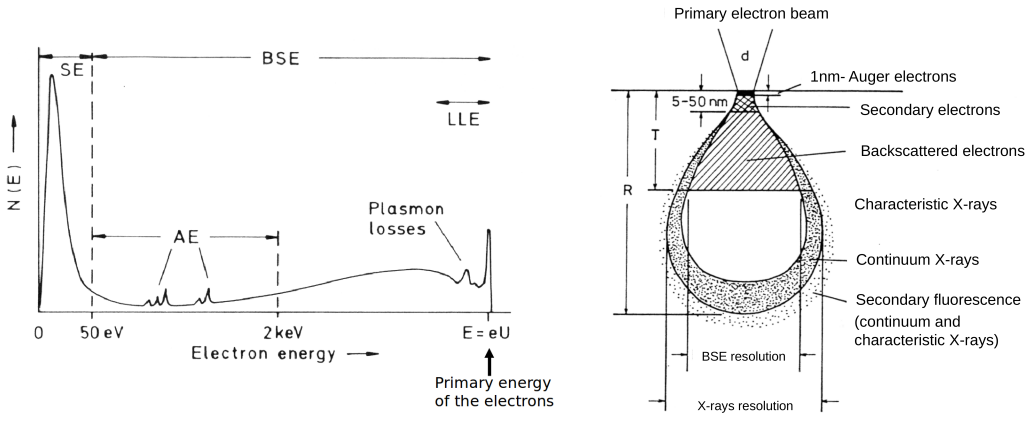

Figure 3.9 : (a) the energy distribution of the electron population as measured by an electron detector in a SEM. (b) the typical interaction volume of an electron beam with the sample.

electron) that decreases with an increase in acceleration voltage. SEM uses a beam of accelerated electrons that is tightly focused on a sample to produce signals [9] (particles emission, X-Rays emission, cathode-luminescence). An image of the signals is reconstructed from the strength of the signal over the scanning range of the electron beam. The beam of electrons, called Primary Electrons (PE), interacts with the sample and produces a series of emissions that can be used to obtain information about the topological surface, material composition and density of the sample. SEM signals are often the super-imposition of several effects that cannot be separated, therefore proper understanding of the signal generation is essential for interpretation of the images produced by SEM. The PE meet the sample surface and penetrate the sample, see Figure 3.9. The PE are scattered due to elastic and inelastic collision with the electrons and nuclei of the sample. The PE do not lose much energy during these interactions, and after one or several collisions the electrons can be scattered outside of the sample again. This family of electrons is called BSE. The inelastic collisions occur during the interaction between the PE and the electron shells. The PE lose part of their energy to the sample (ionisation of the atom, generation of phonons, plasmons or inter band transition). Consequently, the PE penetrate the sample by only a specific range (between 10 nm until 10 mm depending on the sample and the acceleration voltage). The resulting low energy PE no longer interact with the sample (due to a dramatic reduction of the cross section with a decrease of the electron kinetic energy) and the electrons close to the surface (5–50 nm) can escape. These electrons are called SE. Afterwards, they are accelerated towards the detector due to the suction current between the sample and the detector. The inelastic collisions produce X-rays due to the interaction with the nuclei Coulomb field. The inelastic collisions can also ionise the inner layer of an electron shell and produce an X-ray or an

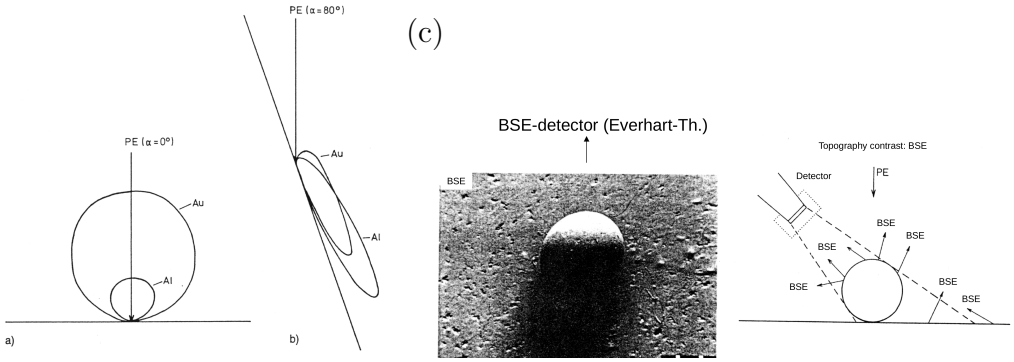

FIGURE 3.10 : (a) the angular dependency of the BSE for a normal interaction for Au and Al and (b) the angular dependency of the BSE for a 10° interaction for Au and Al [9].(c) the shadowing effect due to the specific path of the BSE to the detector [187]

Auger-electron. The emission of photons in the visible and infra-red range due to the recombination with a hole and a SE is also observable in certain materials. In Figure 3.9(a), the energetic distribution of the electron from the surface shows a broad range of energy, with two orders of magnitude between the SEs and the PE. This is key in the determination of the surface characteristic because the two populations of electrons (SE and BSE) are emitted following very different processes and retain distinct information about the sample, see Appendix B for additional information.

At University of Nottingham, the SEM used is a Philips XL30 system. The electron source is a tungsten filament which is heated to provide a supply of electrons. The SE signals are measured by a standard Everhart-Thornley SE detector and a solid-state BSE detector. The microscope operates at a beam acceleration voltage of 0.2-30 kV. The X-Ray detector signal is measured using an Oxford instrument Link ISIS EDX microanalysis system with a Si(Li) detector.

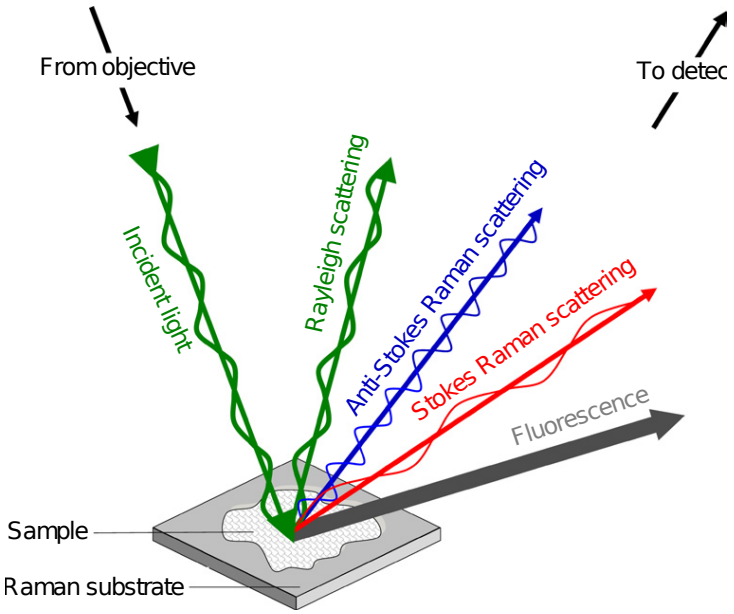

Figure 3.11 : Schematic representing the different types of light emitted/scattered from the sample. There are 4 types of signal produced: Rayleigh scattering, Stokes, anti-Stokes scattering, and fluorescence. Rayleigh scattering (green emitted light on the schematic) is when photons are elastically scattered to the detector without losing energy. Stokes (red emitted light) and anti-Stokes (blue emitted light) scattering is when photons are emitted with lower and higher energy respectively due to inelastic interaction with the phonons in the material and is usually called Raman scattering. Fluorescence can occur when exited electrons fall to the ground states by emitting a photon at a longer wavelength than the incident light. The image is from the work of Butler et al. [188]

3.2.2 Raman Spectroscopy

Raman spectroscopy is a non-invasive, local and fast diagnostic tool for the determination of the chemical and structural composition of the sample surface. It is commonly used to analyse biological samples [189], carbon materials [190, 191], etc. Raman spectroscopy relies on inelastic scattering of the stimulating light (usually a monochromatic laser source) that interacts with the molecular vibrations (phonons, or system excitation) of the material, see Figure 3.11. Thus, the spectrum obtained (from the scattered light) gives information about the specific vibrational modes occurring inside the materials. The spectrum is equivalent to a fingerprint of the materials, and

depends on several factors such as temperature[192], strain[193], doping rates [194], impurities [195], micro-structures [196], etc. These characteristics mean that Raman spectroscopy is widely used for the analysis of carbon composites such as diamond like carbon [196], doped diamond [191] and graphite [197]. Raman spectra are usually complex to interpret and require an understanding of the electronic band structure and phonon dispersion. Thus, practical interpretation of the Raman spectrum is usually done using a database of spectra acquired from the literature [188]. For the studies presented in this thesis, the Raman spectra analysis will be limited to the interpretation of the spectra in relation to the microstructural composition and doping of the carbon composites produced during pulsed laser ablation. The material used is a spectroscope measuring a Raman shift between 200 cm^{-1} and 2560 cm^{-1}. The excitation laser is a -type- at 562 nm.

Raman spectra usually present several defects that overlay the Raman fingerprint such as fluorescence background, cosmic spikes, Gaussian noise, etc [189]. These defects must be removed in order to produce reliable and stable results for the analysis of the isolated Raman spectra, see Figure 3.12.

3.2.2.1 Pre-processing of Raman spectra

In this section, the pre-processing of Raman spectra for each defect will be discussed. The removal of defects from the spectra is done step by step:

1. Fluorescence background and Charge-coupled device (CCD) Baseline, see Figure 3.12(a)–(b): the fluorescence background is due to the stimulated excitation of electrons in material by the laser source. The emission is produced during the fall from an electronic excited state to the ground state. It must be noted that VIS lasers are particularly susceptible to background fluorescence, whereas UV and Near-IR are free from it. In this study, the estimation of the background is done using

a polynomial fit of a spectra that does not present Raman scattering [198].

2. Cosmic spikes, see Figure 3.12(b): Raman instrumentations using CCD for the recording of the spectra suffer from occasional spikes caused by cosmic rays [199]. The removal of cosmic ray is problematic as some Raman features present similar characteristics. The cosmic rays are manually removed for analysis.

3. Gaussian Noise, see Figure 3.12(b): the Raman spectra presents uncorrelated noise that is removed using Savitzky-Golay methods.

4. Scaling: the intensity can vary considerably from one measurement to another due to variation of the focal volume or the intensity of the laser source. Thus, the extractable information is carried by the shape and the relative intensity of the peaks in the Raman spectra. All the spectra are normalised using the min-max-normalisation method [189].

The resulting spectra after pre-processing are clean from any apparent defects. Raman spectra analysis is firstly done qualitatively using the shape of the Raman spectra. It is possible to obtain information about the variation of the Raman spectra for a range of conditions. Then, a quantitative analysis of Raman spectra is performed using multivariate calibration of a generic model for the spectra of carbon material.

3.2.2.2 Analysis of Raman spectra

The Raman spectrum is a vibrational density of states modified by various resonances thus there is no *a priori* function to fit the spectra [196]. Experimentally, it has been found that carbon materials exhibit specific features that occur across a various micro-structural and doping rate/type carbon materials, see Figure 3.13. The range of Raman shift used in the study is

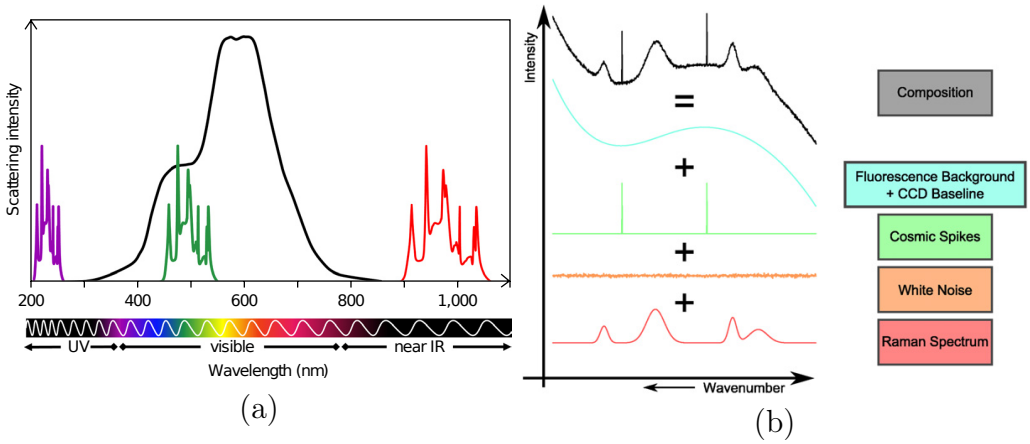

Figure 3.12 : (a) Raman induced fluorescence spectral range from Butler et al. [188]. (b) Diagram showing the main different side effects of Raman spectra measurement such as fluorescence background, cosmic spikes and white noise from the work of Bocklitz et al. [189].

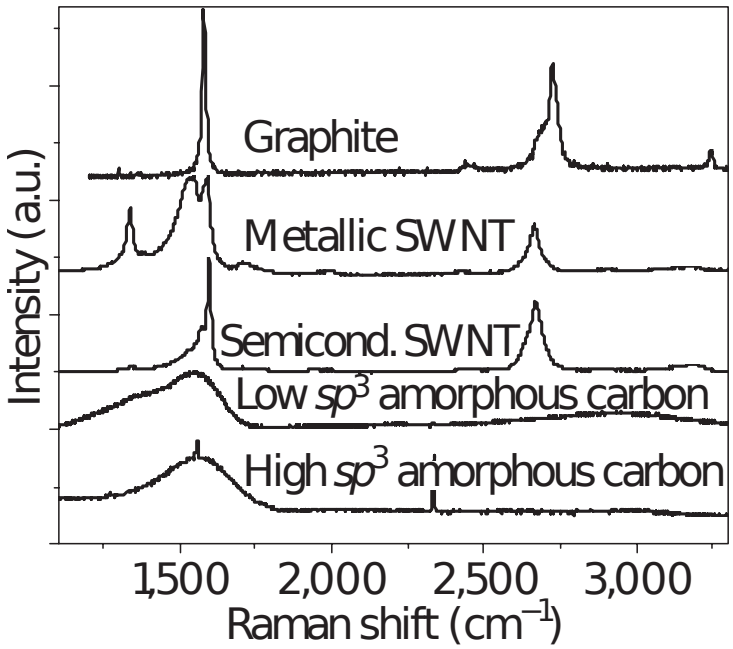

Figure 3.13 : Raman spectra of graphite, metallic and semiconducting carbon nanotubes, low and high sp^3 amorphous carbons [200].

between 200 cm^{-1} and 2560 cm^{-1}. In the literature, the 1000 cm^{-1} – 1800 cm^{-1} range has been widely studied for carbon materials [196, 201, 202]. In this range, there are one or two prominent features ($\simeq$ 1350 cm^{-1} and $\simeq$ 1590 cm^{-1}) with possibly some minor modulations (at $\sim$ 1100 cm^{-1} and $\sim$ 1400 cm^{-1}). It is common for Raman spectra to present background peaks that

could influence the intensity in the range studied (between 1000 cm^1 and 1800 cm^{-1}), therefore the Raman spectrum outside this range is fitted to the series of background peaks presented in [201], to remove their influences from the region studied. The two main features of the Raman spectra between 1000 cm^{-1} and 1700 cm^{-1} are commonly called G-band, for the peak at 1590 cm^{-1}, and D-band, for the peak at 1350 cm^{-1}. The G-band arises from the breathing mode E_{2g} of sp^2 bound between pairs of C atoms [196, 200], see Figure 3.14(a). The D-band arises from the A_{1g} breathing mode. The mode is forbidden in perfect graphite, see Figure 3.13 graphite, but is active in the presence of disorder in the graphite lattice [196, 200], see Figure 3.14(d-f).

The fitting of the Raman spectra in the 1000 cm^{-1} to 1700 cm^{-1} region is done using different types of peaks:

1. Gaussian model: the Gaussian model is widely used to fit a scattering peak. This shape is expected for a random distribution of phonon lifetimes occurring in disordered materials [196]. The formula used for the Gaussian model is

$$I(\omega) = I_0 \exp\left[-\frac{(\omega-\omega_0)^2}{2\sigma^2}\right] \tag{3.6}$$

   where I_0 is the peak intensity, ω_0 is the peak position and σ is the peak dispersion.

2. Lorentzian model: the Lorentzian model is also widely used to fit a scattering peak. This shape is expected for a distribution of phonons with a finite lifetime broadening that arises crystalline materials. The formula used for the Lorentzian model is

$$I(\omega) = I_0 \frac{\sigma}{(\omega-\omega_0)^2+\sigma^2}. \tag{3.7}$$

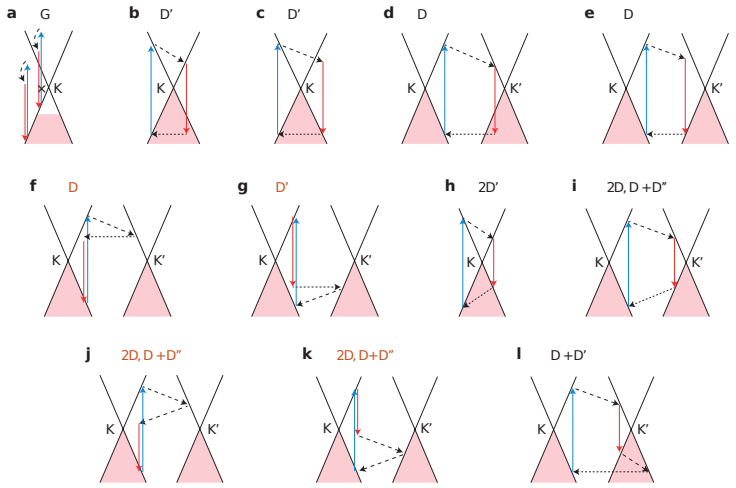

Figure 3.14 : Photon-Phonon processes for a variety of Raman scattering peaks (G, D', D, 2D', 2D and second order combinations) occurring in carbon material. Electron dispersion (solid black lines), occupied states (red shaded area), inter-band transitions neglecting the photon momentum, accompanied by photon absorption (blue arrows) and the emission of a photon (red arrows), intra-band transitions accompanied by phonon emission (dashed arrows) and electron scattering on a defect (horizontal dotted arrows).

3. Breit-Wigner-Fano (BWF) model: the BWF model is used for a non-symmetric peak that arises from the coupling of a discrete mode to a continuum cite. The BWF line shape is given by

$$I(\omega) = I_0 \frac{\left[1 + \frac{(\omega-\omega_0)}{(Q\sigma)}\right]^2}{1 + \frac{(\omega-\omega_0)^2}{\sigma^2}} \tag{3.8}$$

where Q is the BWF coupling coefficient. The Lorentzian line shape is recovered from the BWF line in the limit $Q \to \infty$.

Modelling of the region of interest depends on the visual examination of the Raman spectra (qualitative information). In effect, the Lorentzian and BWF model both correspond to spectra with "sharp" peaks whereas the Gaussian line is more suited to "round" peaks. For example, the graphite spectrum presented in 3.13 will be fitted with the Lorentzian or BWF model and the low sp^3 amorphous carbon with the Gaussian model.

The quantitative interpretation of the spectra is done using the peak fitting. There are several features (FWHM, peak position, ratio of maximum intensity or total intensity of two different peaks) that can be used to quantitatively analyse the spectra.

It must be noted that Raman scattering is usually dependent on the excitation wavelength [203]. The influence of the excitation wavelength has been characterised by Ferrari and Robertson [203] for amorphous carbon and related materials. It shows that the main features (D and G band) occur for all wavelengths tested. However, their shapes and positions change noticeably with the wavelength. It is also possible that certain bands appear for specific wavelengths such as the T-band ($\sim$ 1060 cm^{-1}) present during UV excitation [192].

Micro-Raman spectra were acquired using a confocal setup (NT-MDT, Russia) with a 532 nm laser excitation source and an integration time of 60 s. The laser power at the sample surface was maintained at approximately 80 µW through the use of neutral density filters. The use of a 100ÃŮ objective (NA 0.95, Olympus) allowed for a focused spot size of approximately 1 micron. The collected micro-Raman spectra were post-processed by removing the background signal and cosmic radiation events using the methodology proposed by Bocklitz et al. [189]. The main features of the Raman spectra followed here are: diamond band at 1332 cm^{-1}, D-band for microcrystalline graphite at 1350 cm^{-1} and G-band for graphite at 1580 cm^{-1} [196, 200, 201]. The Raman spectra were recorded in the range of 300–2590 cm^{-1} in order to allow reliable fitting of the full spectral bans. The Raman feature used to study the micro-structural state of carbon allotropes are in the range between 1150 and 1700 cm^{-1}. The bands outside the range of 1150–1700 cm−1 (background bands) are fitted to Gaussian peaks using the peak described by Schawn et al. [201] (at 1950 cm^{-1} and 2420 cm^{-1}) and Szirmai et al. [191].

The Raman feature in the range between 1150-1700 cm^{-1} after the removal of the background bands are fitted using a combination of Breit-Wigner-Fano (BWF) and Gaussian peaks for the diamond band, D-band and G-band [203]. The fitting parameters such as FWHMs, positions and intensity are allowed to vary to obtain a good fit. It must be noted that the G-band can present a secondary feature corresponding to the C=O functional groups at 1760 cm^{-1} that is fitted to a Gaussian peak.

3.2.3 X-Ray Diffraction

X-ray diffraction is a non-invasive, local and fast diagnostic tool for the determination of the phase of a crystalline material. It is also possible to extract the local stress of the material, the crystal orientation and the purity [204]. The high degree of periodicity and order in the lattice is a series of parallel planes for which each has a specific direction in space, see Figure 3.15(a). The incident x-ray beam causes each atom to re-emit a small portion of its intensity as a spherical wave. The high periodicity of the crystal creates constructive interferences for specific angles that depend on the distance between the planes and the common direction. The Bragg equation determines the specific angle for which the intensity is maximum (when $2d \sin\theta$ is equal to a multiple of the wavelength of the incident beam). The XRD diffraction pattern is a fingerprint of the material crystalline structure. Usually, the diffraction pattern is compared to available databases. For the studies presented, XRD diffraction was used to analyse the proportion of crystal in a specific orientation. The database usually provides the position of the peak and the ratio of the peak in the case of a random distribution of the crystal orientation. Thus, it is possible to obtain a preferential orientation of the crystalline structure in the material.

The crystal orientations of the Boron doped diamond are investigated

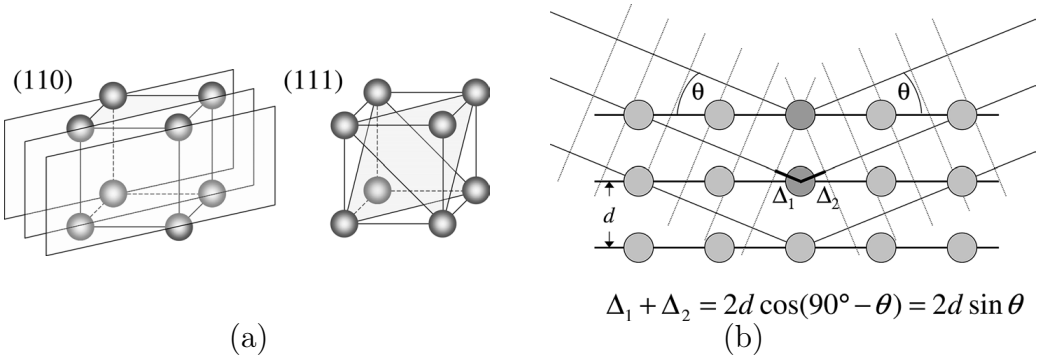

Figure 3.15 : (a) Example of the lattice planes in a simple cubic lattice [204, p. 8]. (b) Schematic of the interaction between the X-ray and the plane of the lattice with the Bragg equation below [204, p. 9].

using a D8 Discover diffractometer with a Cu K_α radiation source over a 2θ range from 40°to 95°and scanning velocity of 0.0625°/min for a beam size of 1 mm at the target interaction. The step size for the XRD measurement is 0.020°and the dwell time is around 0.4 seconds per data points.

3.3 Subsurface Characterisation - Transmission Electron Microscope

The methods presented previously only characterise the sample on the surface or a thin layer. Although these methods carry information about the material characteristics in a layer from a few hundred nanometres to several microns, it is not usually possible to extract information at a specific depth. The signal is usually encompassed informations about the whole volume that interacts with the source (electron, X-ray, laser source), thus cannot be directly attributed to a specific depth. Thus, subsurface characterisation is done using other techniques such as FIB pocket milling and lamellae preparation with TEM imaging. The use of FIB pocket milling has been investigated for the characterisation of the subsurface carbon microstructural composition, however the image does not resolve the microstructure well

Figure 3.16 : SEM of a crater with Platinum deposited on the area used for the lamella.

enough for analysis. In effect, the FIB pocket milling is particularly useful to study a change of elemental composition in the depth of the material or the grain size and orientation via the channelling effect. These effects are not dominant in carbon material in this study. Thus, the lamellae preparation with TEM imaging has been used to study the microstructural composition in the depth of the crater. It must be noted that lamellae preparation is a destructive process and a part of the sample will be removed for analysis. The appropriate lamellae preparation is critically important for TEM imaging. In the following paragraph, the steps used to prepare the lamellae are described. Then, a discussion about TEM imaging is presented.

3.3.1 Lamellae preparation

The preparation of a TEM lamella requires many steps to achieve the quality necessary to obtain accurate TEM imaging. In this section, the methodology used in this work for the preparation of lamellae is detailed.

3.3.1.1 Deposition of Pt on the area of interest

The first step is the deposition of a layer of Platinum to protect the area of interest. The deposition is done in two steps:

1. The electron beam is used to deposit a layer ($\simeq$ 100 nm) of Platinum carried by a gas in the region surrounding the area of interest. The area of interest is thus not damaged by the electron beam. Furthermore, the Platinum is heavier than the Carbon and Boron so the protective layer is clearly distinguishable compared to the sample. The electron beam deposition is slow and cannot provide a thick layer to protect the sample during rough milling.

2. FIB with a low current and low acceleration voltage is used to deposit a thick layer ($\simeq$ several microns) of Platinum. The sample is appropriately protected for the next steps and should not be damaged. An example of a crater at the end of the Platinum deposition is presented in Figure 3.16.

3.3.1.2 Milling and rough polishing of lamellae

After the deposition of the protective coating, the lamella undergoes rough milling and polishing. The first step produces two pockets along the lamella, see Figure 3.17(a). There are two important parameters for the milling to be successful:

1. The milling around the lamella must be of the required depth. This is not straightforward as the milling rate depends on the material and the redeposition rate. Thus, SEM imaging (with a 33° compared to the FIB imaging) is used to control the depth of the milling.

2. The milling pockets must be wide enough for the bottom of the lamella

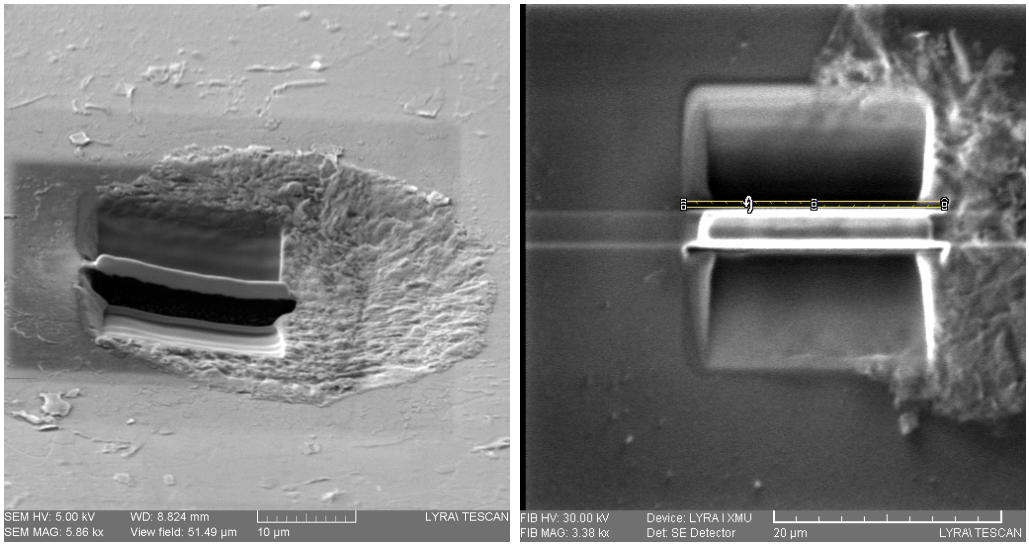

(a) (b)

Figure 3.17 : (a) SEM image of milling of the side of a lamella. (b) FIB imaging of the rough polishing of a lamella.

to be reached on the side by FIB for the undercut in the following stages.

After the pocket milling, three sides of the lamella are roughly polished, see Figure 3.17(b). In this study, the width of the lamella after the rough polishing is around 4 µm.

3.3.1.3 Undercut and in situ lift-out of lamellae

The sample is rotated such that the side of the lamella is visible with the FIB. Afterwards, a thin layer of material is removed under the lamella, see Figure 3.18(a) at the bottom of the lamella, at one side of the lamella, see Figure 3.18(a) on the left of the lamella, and almost removed at the other side, see Figure 3.18(a) on the right of the lamella. The lamella is held by a small amount of material (on the right side for the example given) and should not be connected to the sample by any other parts. The undercut milling is critical due to the possible redeposition of material inside the undercut that is impossible to detect before lift-out.

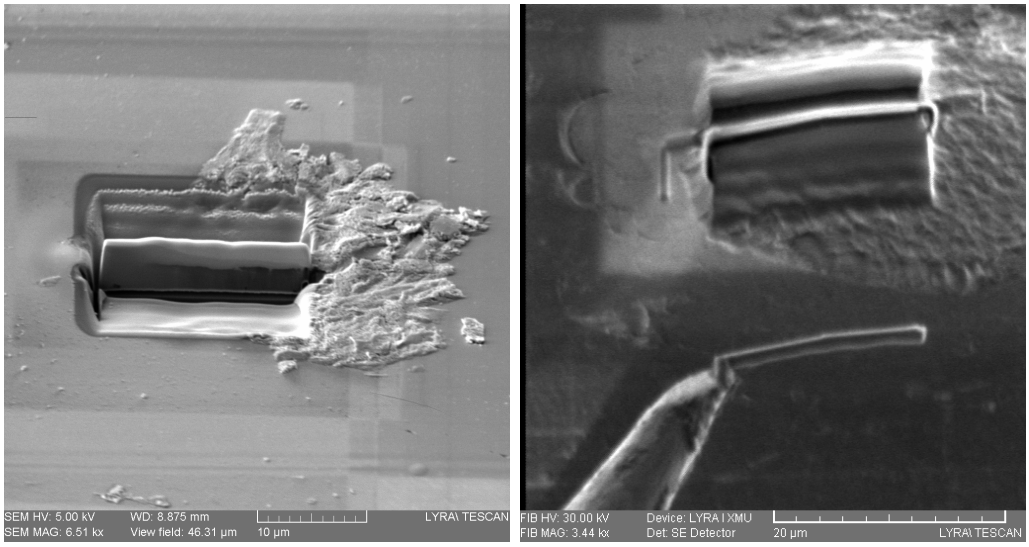

(a) (b)

Figure 3.18 : (a) SEM image Undercut of a lamella. (b) SEM image of the in situ lift-out of a lamella.

After the undercut milling, the needle is carefully positioned close to the lamella. The lamella is welded to the needle using Platinum deposition with the FIB deposition. The needle is welded to the part of the lamella that is not connected to the sample (the right side in the example, see Figure 3.18). Then, the other side of the lamella is disconnected from the rest of the sample using the FIB. Finally, the lamella is carefully lifted out of the site. The whole procedure needs to be done swiftly to avoid any shift of the sample or needle that might knock out the lamella from the site or the needle.

3.3.1.4 Attachment to the TEM grid and further polishing of lamellae

Finally, the lamella is welded to a copper TEM grid, see Figure 3.19. Then, the lamellae are thinned to around 100 nm.

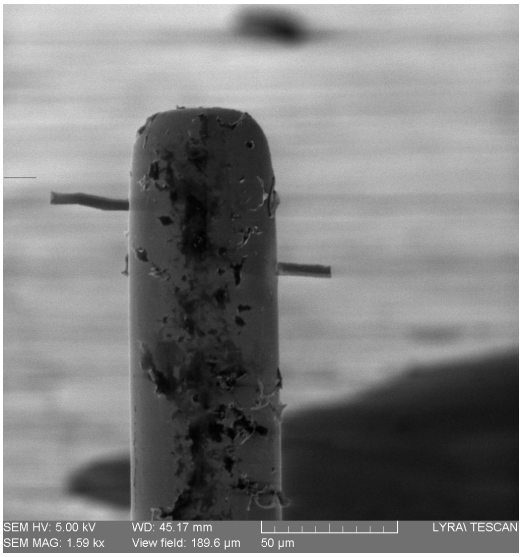

Figure 3.19 : Extracted lamella of a TEM grid.

3.3.2 Imaging principles

The system used in TEM imaging is similar to SEM imaging, however whereas the SEM imaging system uses the electron interaction with the sample to retrieve information, TEM imaging measures the transmitted electron through the sample without using the BSE or SE used in SEM imaging. The image that is formed at the back of the sample by the transmitted electron is focused on a CCD by electromagnetic lenses. It is also possible to image the diffraction pattern from the sample by shifting the focal length. There are two apertures to control the signal from the sample. The objective aperture is used to improve contrast, decrease lens aberration, depth of field and allow for signal selection (between bright field and dark field imaging) from the imaging mode. The selected area diffraction (SAD) aperture is used in diffraction mode to control the portion of the sample from which the diffraction pattern arises. The TEM imaging mode is separated into three modes:

1. Bright-field mode: the bright field mode is the imaging mode for which

the transmitted beam and low angle scattered electrons are used for the imaging of the sample, see 3.20(a). Thus, the image presents a high contrast between the higher density and thicker materials such as the difference of intensity between the Platinum and graphite areas.

2. Dark-field mode: the dark field mode is the reverse of the bright-field model. The high angle scattered electrons are used for the imaging, see 3.20(b), therefore the image is bright for high density areas and thicker materials.

3. Phase-contrast imaging: the phase contrast mode is the imaging mode for which the transmitted beam and high angle scattered electrons are used for the imaging of the sample, see 3.20(c). Although phase-contrast mode offers higher resolution imaging compared to bright and dark field imaging, the contrast arises from the interferences due to the shift in phase between the scattered and unscattered electrons rays in different parts of the image. The signal is therefore more complex to interpret and is not a direct representation of the sample crystallographic structure [206], however it carries qualitative information about the order of the

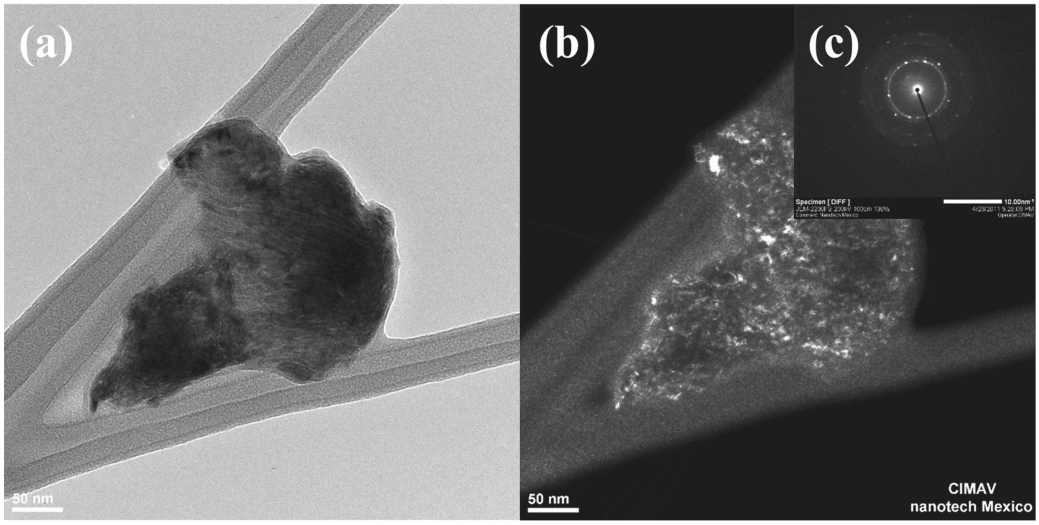

Figure 3.20 : (a) Bright-field, (b) Dark-field and (c) corresponding diffraction mode [205].

crystallographic structure in the sample [206].

A dual-beam FIB-SEM Tescan Vela is used to make the TEM cross section of the two samples. The area of interest is protected with a Platinum layer deposited using a gas injection system. The FIB is used to cut out cross sections from the area of interest and to thin the cut out down to the electron transparency. The lamellae used in the TEM are protected by a layer of Platinum. The lamellae are investigated using a JEOL LEM-2200FS operating at 200 kV for the bright-field TEM (BFTEM) and High Resolution TEM (HRTEM). The HRTEM micrographs includes a 2D Fourier spectra on the bright-field images to highlight the local orientation of the lattice.

3.4 Surface topography measurement systems

3.4.1 White light interferometers for surface topography measurements

A WLI consists of a Michelson illuminated by a broadband light source. The measured object is placed in one arm of the Michelson and the other arm is a reference mirror. The object is moved in the direction of the Michelson as indicated in Figure 3.21(a). The surface of the sample is imaged onto a CCD using a telecentric optical system. A series of images is acquired during the movement of the object in the longitudinal direction. The optical system produces interference fringes in the surface such as a Michelson. For each pixel, the interference fringes are localised close to the sample focus due to the low temporal coherence of the source or the high numerical aperture of the microscope objective. A correlogram is produced, see Figure 3.21(b), and the pixel height is unambiguously retrieved at the peak of the fringe envelope. Although simple in principle, determination of the surface

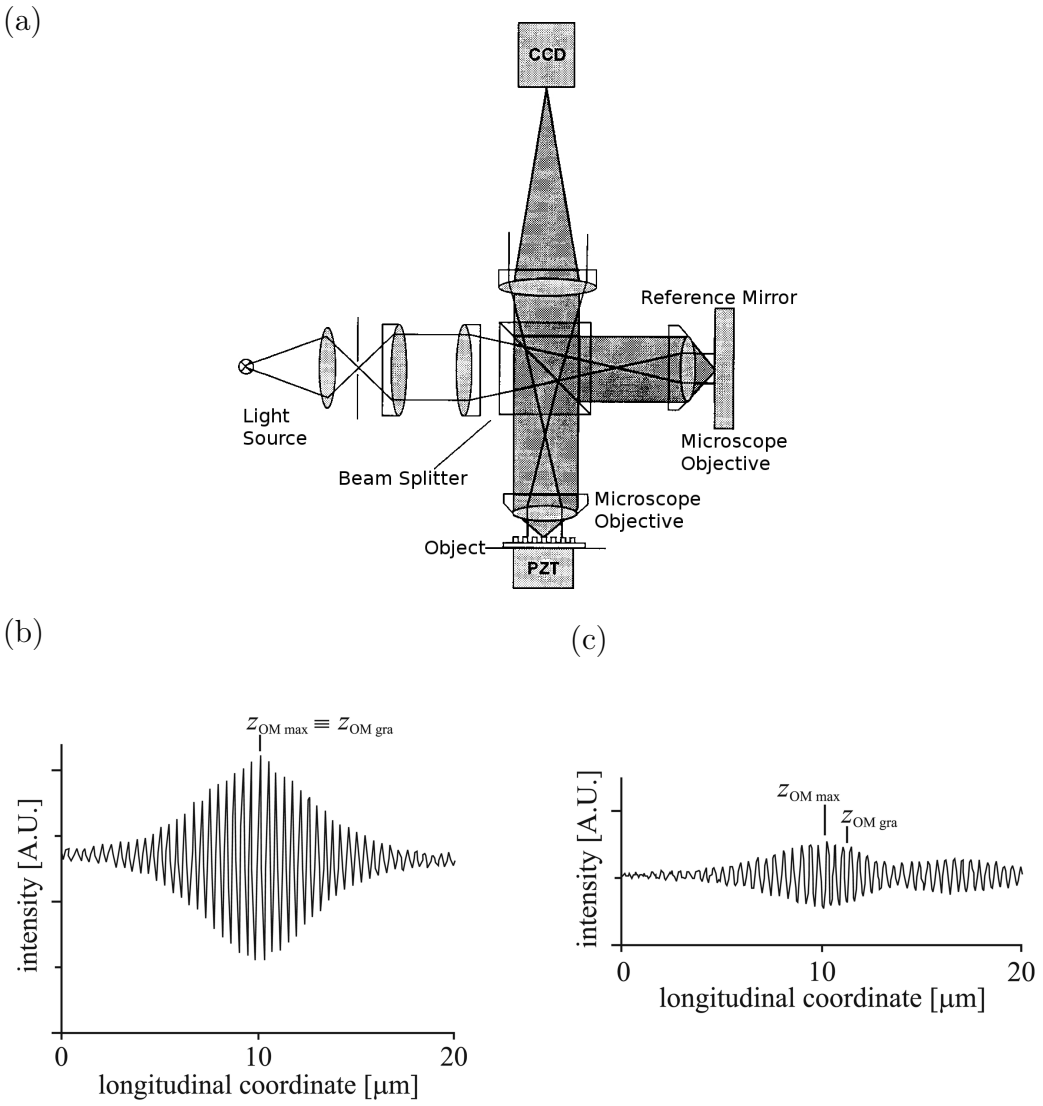

Figure 3.21 : (a) Scheme of a WLI [209] (b) Typical white-light interferogram (c) Distorted interferogram due to the surface roughness and the spectral width of the light [207]

topography is hindered due to the generation of systematic errors which decrease measurement accuracy. Nevertheless, these systematic errors are usually corrected but correction artefacts can still be present on the surface. It has been shown that the surface roughness introduces a systematic uncertainty of the position of the peak of the fringe envelope [207]. Furthermore, an evaluation of several WLI has shown that the system is still sensitive to a 2π phase jump in the measurement of the fringe order [208] which introduces a "ghost step" in the measured topography.

Improvement of the correction algorithms is still the subject of ongoing research [210]. It has been found experimentally and proved numerically that the surface slope influences the generation of errors in the surface measurement [211, 212]. Several conclusions can be drawn from the literature regarding the accuracy of the topography measurement using white light interferometers, (i) interpretation of the measured surface must be done with caution, where there is doubt the surface topography should be verified using imaging techniques such as SEM, Atomic Force Microscope (AFM), etc.; (ii) although the general shape is likely to be correct the measurement of highly sloped surfaces is prone to inaccuracies; (iii) the centre of the field of view is resilient to errors due to chromatic aberration. Finally, WLI offers a fast and globally accurate measurement technique. If doubt exists about the surface topography, SEM, AFM or a stylus profilometer is used to validate WLI measurements.

3.4.2 Profilometer for surface topography measurements

A surface profilometer consists of a stylus in contact with the sample connected to a beam, see Figure 3.22(a). The angle of the beam is measured using an electronic system and converted into a height measurement. Unlike the WLI, the profilometer can only measure along a straight line, so the surface is reconstructed by measuring a series of profiles using a raster path over the area of interest. The profilometer is particularly useful for measuring samples with low surface reflectivity for which the WLI is not suitable. Furthermore, the topography measurement is almost free of errors (white noise).

However, the size and shape of the stylus limits the range of surfaces that may be measured, see Figure 3.22(c). The stylus used in this study has a radius of 5 µm, thus providing accurate measurement for large craters ($>$ 50 µm) or large surfaces. It must be noted that the stylus cannot be used

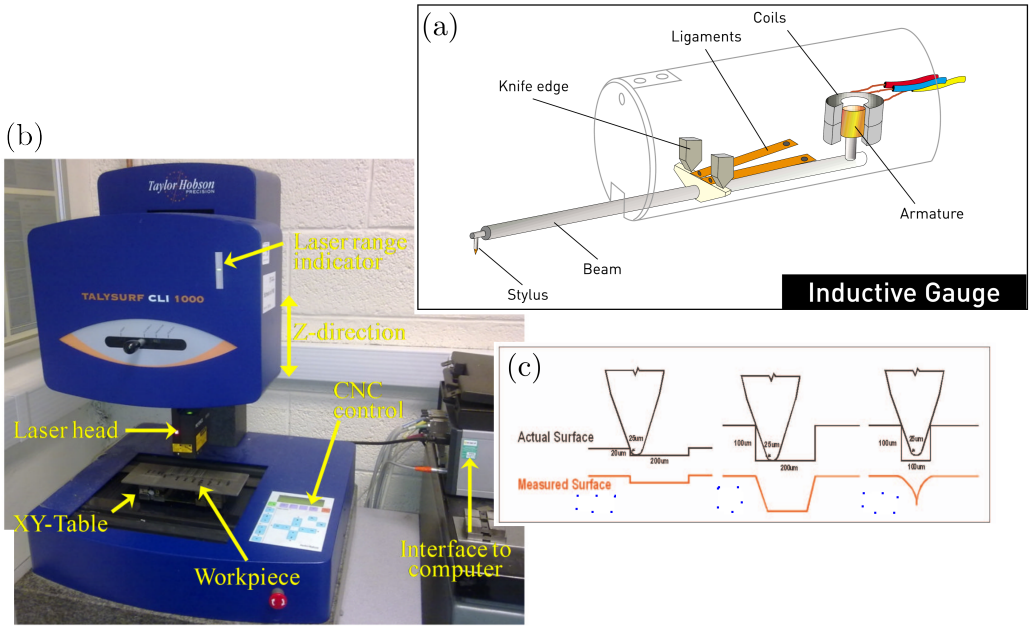

Figure 3.22 : Talysurf CLI 1000 system and scheme of the inductive gauge [213, 214].

for the measurement of trenches due to the high aspect ratio. The system must be used with caution as it produces a measurement for surfaces that it cannot measure accurately. Furthermore, the minimum lateral accuracy is 0.5 µm.

Chapter 4

A study of surface swelling caused by graphitisation during pulsed laser ablation of carbon allotrope with high content of sp^3 bounds

This chapter provides a description of the development of a modelling framework capable of predicting the surface swelling occurring during nanosecond pulse laser ablation of diamond and related material. The model is constructed using the conservation of mass and heat in the target. Then, an overview of the methodology to process the experimental results and compare them with experimental data is given. It must be noted that the model is validated for boron doped diamond then the model is used to estimate the activation energy of Tetrahedral amorphous carbon (ta-C). The calculation of the activation energy for ta-C using the model offers an improve accuracy over previously published results. The description of this work is accompanied by a discussion of the insight obtained with the model and how those results can provide further understanding of the ablation processes in general.

4.1 Introduction

In most advanced applications, "as-synthesised" bulk diamond requires post-processing to generate 3D (micro) features that add specific functionalities to the product. However, the generation of $2\frac{1}{2}$D or 3D functional features in diamond structures by mechanical methods (e.g. grinding) is difficult due to the limited access of the cutting tools to minute part geometries while generally not being regarded as economically efficient. With this in mind, a material removal method that is not based on mechanical interaction between the tool and the workpiece would be much more appropriate for the shaping of diamond and related materials at a high level of geometrical detail while resulting in less mechanical damage to the diamond based structure [36]. The use of lasers for diamond through cutting is well documented [149] but recently Pulsed Laser Ablation (PLA), i.e. controlled depth material removal, has been recognized as one of the most efficient and suitable methods for the 3D shaping of diamond [150] with unique capabilities to generate micro-features/textures to support the development of advanced products made of this unique material.

Considering the above, it seems that for industrial applications, machining with nanosecond lasers offers a good compromise between the removal rate and the quality of the detail achieved through ablation [215]. In most cases, the generation of features using PLA is done based on experimental knowledge of the material removal, i.e. beam footprint against a particular target material. Some attempts at using geometrical modelling (convolution of a known footprint along the laser beam path) of PLA to predict the surface micro-geometry have been reported [1]; although these can predict the ablated surface and incorporate various laser characteristics (e.g. power, repetition rate), these geometrical models suffer from not taking into account

the physical phenomena that lead to material removal [30]. Therefore, they are not suitable for understanding thermal damage or possible phase change during the laser-workpiece interaction that is critical to assess the possible uses of processed diamond.

To address the research gaps presented in the Chapter 2, a new model is developed to study the kinematics of the graphitisation of diamond during nanosecond PLA. The proposed model and investigation methods aim at providing better insight into the kinematics of the graphite layer formation in the diamond structure thereby predicting the thickness of the graphite layer as a function of the fluence. The model is one-dimensional, and consists of the conservation of heat and mass during the interaction; radial heat diffusion can be neglected because the thermal penetration depth is at least one order of magnitude smaller than the diameter of the laser spot. This provides a flexible framework within which to study the influence of the optical and thermal properties of the diamond on graphitisation. The dynamic positions of the interfaces (graphite/diamond and graphite/vacuum) are simulated, but cannot be measured experimentally, so the final position of the surface (graphite /vacuum) is used to validate the model for two types of diamond: boron-doped diamond and tetrahedral amorphous carbon.

4.2 Graphitisation model for nanosecond laser pulse ablation

The ablation process for diamond and related material can be separated into three phases:

1. Diamond heating: the laser interacts with the pristine diamond phase. The heat distribution is governed by the thermal diffusivity and the laser penetration depth inside the diamond [89]. The saturated vapour

pressure is negligible due to the low surface temperature, so vaporisation does not occur during the diamond heating. This phase ends when the total thickness of graphite calculated using the Arrhenius law at the surface of the diamond is equal to two layers of graphene ($\sim$ 0.7 nm). The surface temperature is used to calculate the graphitisation rate of the diamond.

2. Graphitisation and ablation: the total thickness of the layer of graphite reaches 2 layers of graphene and the laser interacts with the graphite and diamond layer. A thin-layer (a few Ångström) of diamond is numerically transformed into graphite at the surface of the diamond [216]. At first, this layer does not have a strong influence on the temperature distribution as its thickness is too small to absorb a significant part of the laser energy. However, the graphite layer quickly grows and, due to its high absorption coefficient, the heat distribution is dramatically changed. The dynamic position of the interfaces is critical for the determination of the heat distribution during this phase. A new modelling framework has therefore been used to correctly describe it, which represents the key element of this chapter and is described in this section.

3. Relaxation of the system: graphitisation stalls due to a lack of heat propagation inside the target. However, the surface temperature can still be above the ablation threshold resulting in the vaporisation of a part of the graphite layer. The new modelling framework can also be used to simulate this phase.

The model for the diamond heating phase has already been described elsewhere [89]. The physical phenomena are modelled to improve understanding of the ablation process during the graphitisation and ablation phase.

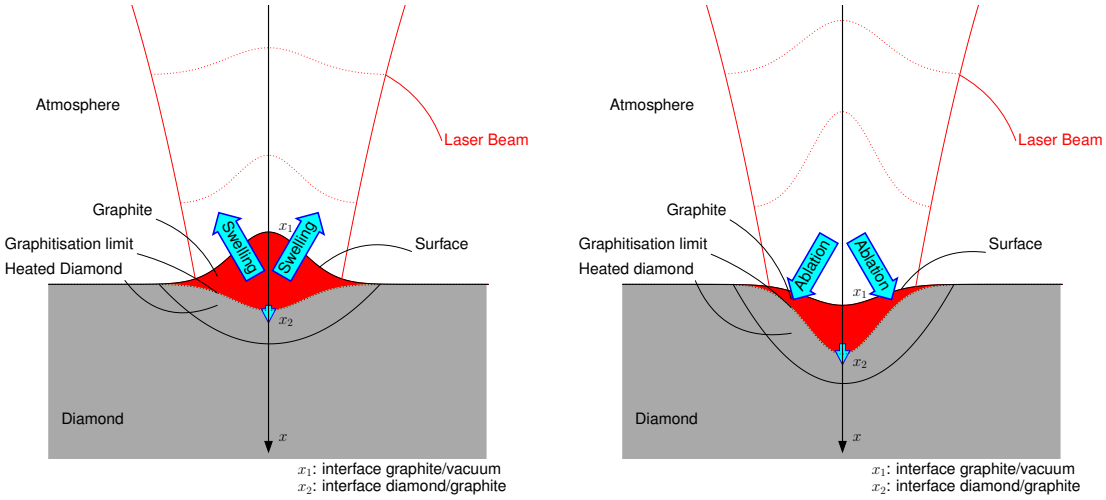

Figure 4.1 : a) Scheme of diamond ablation at low fluences. b) Scheme of diamond ablation for high fluences.

Nanosecond laser ablation, that is to be considered in this chapter, is a thermal process that is induced by the absorption of the laser pulse by the electrons in the target followed by a rapid (< 10 ps) thermalisation between the electrons and the lattice. The resulting heat then diffuses within the target. The thermal penetration depth, defined as $d_{Thermal} = \sqrt{2D\tau_{pulse}}$ (where D is the diffusivity and τ_{pulse} is the temporal length of the laser pulse), is at least one order of magnitude smaller than the diameter of the laser spot on the target. Thus, the heat distribution within the target workpiece can be determined using a 1D model. In this approach, the two layer (graphite and diamond) system is modelled (based on mass and energy conservation) to take into account graphitisation during the irradiation. In the following equations the subscripts d and g are used for the thermo-physical and optical properties of diamond and graphite respectively. The vacuum/graphite and graphite/diamond interfaces are at $z = z_1$ and $z = z_2$ respectively.

The density difference between graphite and diamond leads to an outward displacement of the graphite, or swelling, of the graphitised surface as shown

in Figure 4.1. Mass conservation at the diamond-graphite interface leads to

$$v_{\text{swelling}} = \frac{\rho_g - \rho_d}{\rho_g} \partial_t \{z_2\}, \tag{4.1}$$

where ρ is the density of the material and v_{swelling} is the speed induced in the graphite due to the graphitisation. The heat equation for the graphite is, using Equation (4.1),

$$\mathtt{d}_t \{H_g\} = \partial_x \{[v_{\text{swelling}} H_g + \mathrm{D}_g \partial_x \{H_g\}]\} + S_g, \tag{4.2}$$

with H, D and S being enthalpy of the material, thermal diffusivity and the heat source induced by the laser respectively. The enthalpy is generically calculated as

$$H(T) = \int_{T_0}^{T} \rho(T) c_p(T)\, dT, \tag{4.3}$$

with c_p and T being the specific heat and temperature respectively. The source term S from the laser beam is

$$S_g = (1 - R_g(T_{\text{surface}}) \alpha_g \exp\left[-\alpha_g (z - z_1)\right] \mathfrak{i}(t), \tag{4.4}$$

with R, α, T_{surface} and $\mathfrak{i}(t)$ being reflectivity, absorption coefficient for the laser wavelength, surface temperature, and the temporal profile of the laser pulse respectively. It has been shown that the absorption of a significant fraction of the laser energy by the plasma that is created above the surface is an important phenomenon during nanosecond laser ablation [89], [217]. Including plasma absorption can lead to significant improvement of model predictions [46, 54, 113, 218]. In this context, using the method developed for graphite ablation by Bulgakova et al. [219], the plasma absorption is

estimated using the total optical thickness of the ablation plume Λ such that

$$\Lambda(t) = az_a(t) + bE_a(t), \tag{4.5}$$

with $E_a(t)$ and $z_a(t)$ being the energy in the plasma and the depth ablated respectively. Here a and b are free parameters usually determined by fitting the model to experimental data. This simple model for the optical thickness is based on the hypothesis than an increase in the plasma energy, $E_a(t)$, or the plasma density increases the absorption. Thus, the plasma shielded heat source is

$$S_g = (1 - R_g(T_{\text{surface}}))\alpha_g \exp\left[-\alpha_g(z - z_1))\right] \exp[-\Lambda(t)]\mathfrak{i}(t). \tag{4.6}$$

The heat equation for the diamond is

$$\mathfrak{d}_t\left\{H_d\right\} = \partial_z\left\{\mathrm{D}_d\partial_z\left\{H_d\right\}\right\} + S_d, \tag{4.7}$$

where the source term S_d is

$$\begin{aligned} S_d =& (1 - R_g(T_{\text{surface}}))\alpha_d \exp\left[-\alpha_d(z - z_2) - \alpha_g(z_2 - z_1)\right] \\ & \exp[-\Lambda(t)]\mathfrak{i}(t). \end{aligned} \tag{4.8}$$

The system is completed by the Stefan condition,

$$\mathrm{D}_g\partial_z\left\{H_g|_{z=z_2}\right\} - \mathrm{D}_d\partial_z\left\{H_d|_{z=z_2}\right\} = \partial_t\left\{z_2\right\}\rho_d\Delta h_{d-g}, \tag{4.9}$$

with Δh_{d-g} the heat of graphitisation and the jump of enthalpy at the

graphite-diamond interface

$$h_g|_{z=z_2} - h_d|_{z=z_2} = h_g(T_{\text{interface}}) - h_d(T_{\text{interface}}), \tag{4.10}$$

where $T_{\text{interface}}$ is the temperature at the interface between diamond and graphite. Note that the Stefan condition has been modified to take into account the fact that graphitisation is irreversible and follows Arrhenius law, (unlike melting or solidification phase changes) thus the speed of the interface between the graphite and the diamond cannot be negative and is calculated using the following equation,

$$\partial_t \{z_2\} = C_r \exp\left[\frac{-\mathtt{E}_a}{\mathfrak{R} T_{\text{interface}}}\right], \tag{4.11}$$

with C_r and $\mathtt{E}_a$ being respectively a constant representing the rate of transformation between graphite and diamond, and the activation energy for the transition between diamond and graphite. The domain of the solution is finite, and an adiabatic boundary condition is applied at the bottom, $z_{\max}$, so that

$$\mathrm{D}_d \partial_z \{H_d\}|_{z=z_{\max}} = 0. \tag{4.12}$$

We always choose $z_{\max}$ large enough that the temperature there does not change significantly during the simulation. At the top of the domain, the boundary condition is controlled by evaporation. Thus, the energy balance at the irradiated surface is

$$\mathrm{D}_g \partial_z \{H_g\}|_{z=z_1} = v_a \Delta H_{\text{vap}}, \tag{4.13}$$

with v_a and ΔH_{vap} being the speed of ablation and the enthalpy of vaporization [220] respectively. The relation between the rate of evaporation and

vapour pressure is [88],

$$m = \sqrt{\frac{M}{2\pi\mathfrak{R}T_{\text{surface}}}}P_v, \tag{4.14}$$

with M, $\mathfrak{R}$, T_{surface} and P_v being molar weight, the gas constant, surface temperature and the saturated vapour pressure respectively. The saturated vapour pressure is estimated using the Clausius-Clapeyron equation,

$$\mathtt{d}_T\{P_v\} = \frac{\Delta H_{\text{vap}}}{T\Delta v}, \tag{4.15}$$

with Δv the change in specific volume during the evaporation. The vapour is considered to behave like an ideal gas and the latent heat of vaporization is regarded as a constant over the range of temperatures encountered [221]. Since it has been shown that a certain proportion of the atoms from the vapour are reflected to the surface [95], a sticking coefficient β is included in (4.16) to account for this phenomenon. Using (4.14) and (4.15), it is possible to obtain the ablation velocity of the graphite,

$$v_a = (1-\beta)\sqrt{\frac{M}{2\pi\mathfrak{R}T_s}}\frac{P_0}{\rho_g}\exp\left[\frac{H_{\text{vap}}}{\mathfrak{R}}\left(\frac{1}{T_0}-\frac{1}{T_s}\right)\right], \tag{4.16}$$

where T_0 is the reference temperature under the reference pressure P_0. The saturated pressure for carbon is tabulated for a range of temperatures [222] with reference pressure and temperature $P_0 = 100$ kPa and $T_0 = 3908$K. The position of the interface between graphite and vacuum is determined by

$$\partial_t\{z_1\} = v_{\text{swelling}} + v_a. \tag{4.17}$$

Finally, a front fixing method [223] is used to map the domain of solution to a field domain which is more convenient for numerical solution.

At the start of the simulation, the temperature of the diamond is set at 300 K. Initially, the laser interacts directly with the diamond, so just the equation for the flow of heat in the diamond is solved. The surface temperature in the diamond increases until the total thickness of the graphite layer calculated using the Arrhenius relation reaches twice the thickness of graphene layer. Once this thickness of the graphite layer is attained, the diamond is numerically transformed into graphite. Numerically, graphitisation is initialized by instantaneously replacing a small layer of diamond (two layer of graphene thickness) with graphite. Afterwards, the two heat equations are solved simultaneously and the interfaces (graphite/diamond and graphite/vacuum) evolve according to (4.17) and (4.9).

The system of equations is discretised using Taylor series and finite volume methods. Temporal discretisation is achieved using the implicit Euler method. The solver uses an adaptive time step dependent on the value of the ablation speed. A high ablation speed means a small time step. The matrix resulting from the discretisation is inverted using the library SUPERLU [224]. The solver is second order in space and first order in time. At each time step, the material properties are evaluated using the enthalpy from the previous time step. The simulation is carried out until the system is not subject to vaporisation and graphitisation, usually about 2μs. The size of the simulated sample is around 2 µm for tetrahedral amorphous carbon and 20 µm for boron doped diamond. The temperature of the sample at the end of the simulation typically is around 20 K over the initial value.

4.3 Methodology for material properties used in the simulation

In this study, the model has been tested against two types of diamond: boron doped diamond (BDD) and tetrahedral amorphous carbon (ta-C). These materials are chosen because they present dissimilar optical and thermal properties, as well as a notable difference in microstructure. BDD is a microcrystalline diamond exhibiting a high diffusivity and low absorption coefficient at the wavelength of the laser used in the experimental investigations (1061 nm). In contrast, ta-C is an amorphous diamond like carbon having a low diffusivity and high absorption coefficient at the laser wavelength used during the experimental tests (248 nm) [28]. Previous studies show that the temperature dependence of the material properties (thermal and optical) has a strong influence on the predictions of models for nanosecond pulsed laser ablation [55]. Thus, it is critical for the accuracy of the model results to employ material properties as close as possible to the real ones. The methodology for the determination of the material properties (optical and thermal) for the two target materials and graphite will be presented below. The thermal properties used in the model are the specific heat capacity, the density, the thermal diffusivity, the specific enthalpy of graphitisation and the temperature of graphitisation for the diamond material. The optical properties used in the model are the reflectivity and the absorption coefficient.

4.3.1 Optical and thermal properties for boron doped diamond (BDD)

The optical [194, 229–231] and thermal [232, 233] properties of boron doped diamond have been widely reported in the literature. However, there is little data for the sample used in this study (a micro-crystalline diamond with a

Table 4.1: Thermal and optical data for boron doped diamond produced by Element Six

Density [225], $g.cm^{-3}$	3.5
Absorption coefficient @1061 nm [226], m^{-1}	4.3×10^5
Reflectivity @1061 nm [227],	0.16
Specific enthalpy of graphitisation [228], $J.g^{-1}$	-158.2
Rate of graphitisation [157], $m.s^{-1}$	9.00×10^{19}
Activation Energy [157], $J.mol^{-1}$ / eV	1.06×10^6 / 11.0
Specific heat, Manufacturer's data sheet	See Figure 4.3(a)
Thermal diffusivity, Manufacturer's data sheet	See Figure 4.3(b)

boron doping rate of $\sim 3 \times 10^{20}$ cm^{-3}), due to the wide range of microstructural composition (single crystal, micro-crystalline and nano-crystalline) and doping rate (10^{16} to 10^{21} cm^{-3}) available. Furthermore, previous studies have shown that boron doping rate influences the optical properties and some thermal properties. The thermal and optical properties used in the simulation are:

- Specific heat: previous studies show that the specific heat of boron doped diamond is not dependent on the boron doping rate [146][p. 476]. Furthermore, the specific heat of diamond does not depend on its microstructure (single-crystalline, micro-crystalline, nano-crystalline) [234]. Thus, the specific heat of single crystal diamond is used in the model for the specific heat of boron doped diamond [225].

- Thermal conductivity: the boron doping rate in diamond affects the thermal conductivity [235, 236] by up to one order of magnitude. This is due to the increase of point defects and boron concentration in the grain boundaries which increases the phonon dispersion. The thermal conductivity reported in the manufacturer data sheet[225] is used in the model. Although, the thermal conductivity should decrease with an increase of temperature, the reported data only includes the value at 300 K. Thus, the thermal conductivity is considered as constant over

the range of temperature studied.

- Density: the density of boron doped diamond is considered to be equal to the density of pure diamond [236].
- Specific enthalpy of graphitisation: the specific heat of graphitisation has been experimentally measured in the work of Rossini et al. [228].
- Activation energy and rate of graphitisation: the graphitisation rate as a function of temperature for pure diamond has been previously reported [156, 157].
- Reflectivity: the complex part of the refractive index is relatively small compared to its real part [231]. Thus, the real part of the refractive index alone is meaningful for the calculation of the refractive index. Experimental studies show that the refractive index has a negligible dependence on the boron doping rate [231]. Furthermore, the reflectivity of a micro-crystalline boron doped diamond with a doping rate at 1.3 $\times$ 10^{20} cm^{-3} has been reported in the literature [237] and is used in the model.
- Absorption coefficient: the absorption coefficient at 1061 nm (the laser wavelength used in the experimental tests) is highly dependent on the boron doping rate [229, 230], and is approximately 6 $\times$ 10^5 m^{-1} at 300 K for the BDD sample used in this study. Furthermore, Hall mobility and carrier concentration measurements show that the absorption coefficient should decrease with an increase of temperature [229].

The thermal and optical properties for the boron doped diamond used in the model are summarised in Table 4.1.

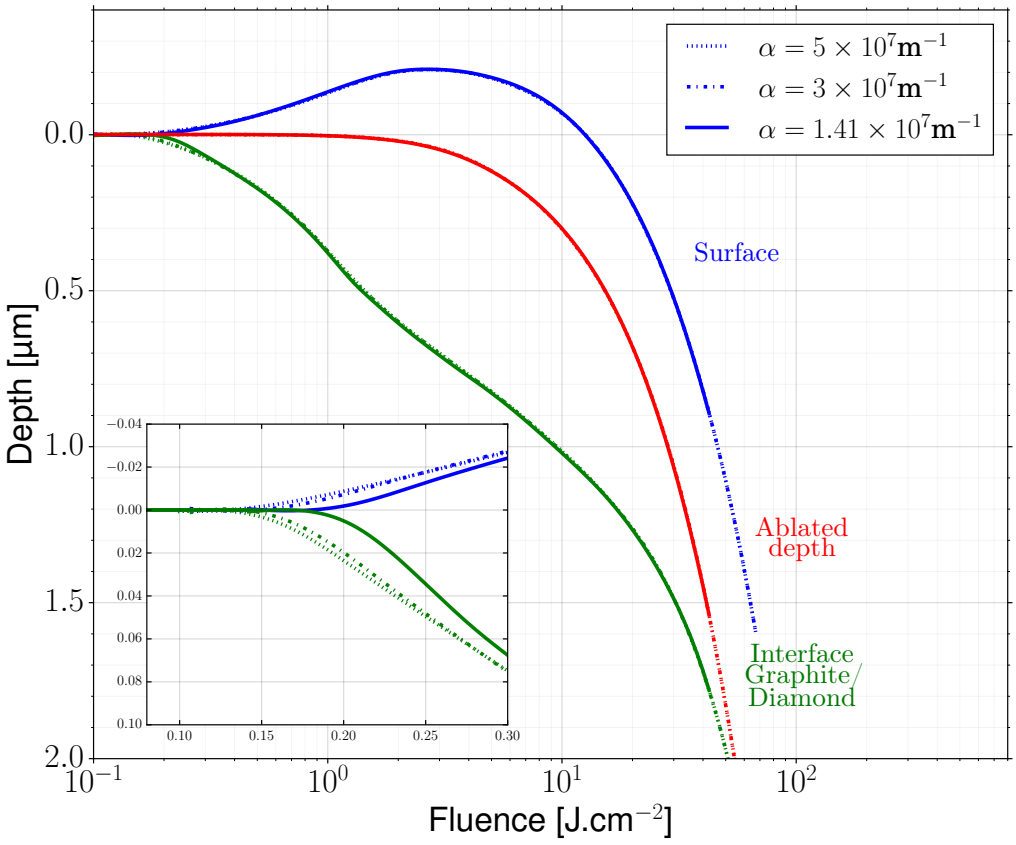

Figure 4.2 : Position of the interfaces for ta-C with a constant reflectivity (R = 0.45) for the graphite at 248 nm without considering the plasma absorption. The red, blue and green lines are respectively the ablated depth, the interface position of graphite/vacuum and interface position of diamond/graphite.

Table 4.2: Thermal and optical data for ta-C DLC

Density [238], g.cm^{-3}	3.0
Ratio sp3/sp2 [239], %	80
Absorption coefficient 1024x768 [240], m^{-1}	3× 10^7
Reflectivity @248 nm [240]	0.22
Specific enthalpy of graphitisation [228], J.g^{-1}	-126.6
Rate of graphitisation, optimized see 4.13, m.s^{-1}	1.99 × 10^8
Activation Energy, optimized see 4.13, J.mol^{-1} / eV	3.04 × 10^5 / 3.15
Specific Heat [241],	See Figure 4.3a)
Thermal diffusivity [242],	See Figure 4.3b)

4.3.2 Optical and thermal properties for tetrahedral amorphous carbon

The thermal and optical properties of tetrahedral amorphous carbon are not commonly reported in the literature since their measurement is difficult in the thin films that are typically deposited [8, p. 158–162]. However, it has been established that the fraction of sp^3/sp^2 carbon-carbon bond is linked to the density [238], the thermal conductivity [242], the specific heat [241] and the optical properties [243]. The thermal and optical properties are usually measured at 300 K [28, 239]:

- Specific heat: the work of Hakovirta et al. [241] suggests that the specific heat of diamond like carbon films can be calculated using the specific heat of the graphite and diamond, the ratio of sp^3/sp^2 and the hydrogen concentration in atomic percentage. Thus, the specific heat used for this study is

$$c_{p_{\mathrm{taC}}}(T) = r_{sp^3/sp^2} c_{p_d}(T) + (1 - r_{sp^3/sp^2}) c_{p_g}(T), \tag{4.18}$$

  with r_{sp^3/sp^2} the ratio of sp3/sp2 bond, $c_{p_d}(T)$ the specific heat of diamond and $c_{p_g}(T)$ the specific heat of graphite.

- Thermal conductivity: a previous study demonstrates that the thermal conductivity is linearly dependent on the ratio of the sp^3/sp^2 bond and weakly dependent on the temperature around 300 K [242]. Thus, the thermal conductivity is considered as constant over the range of temperature used.

- Density: the film density is linearly dependent on the ratio of the sp^3/sp^2 bond [238].

- Specific enthalpy of graphitisation: since the change of enthalpy between

graphite and diamond is the energy released from the sp3 carbon-carbon bond, the specific enthalpy of graphitisation depends linearly on the ratio of sp3/sp2 bond [228].

- Activation energy and rate of graphitisation: the activation energy for ta-C has been previously reported [244, 245] however due to the thickness of ta-C the most accurate value available is 3.5 ± 0.9 eV. Furthermore, the rate of graphitisation has not been measured. Thus, the activation energy and the rate of graphitisation are free parameters that are determined by fitting the experimental results and the calculated data on the surface position. In this work, the model is validated for boron doped diamond, then the same model is applied for ta-C. It is then possible to obtain accurate values for the activation energy and rate of graphitisation for ta-C.

- Reflectivity: Tay et al. [243] have measured the optical properties of ta-C film for a ratio of sp^3/sp^2 bond around 80-85% and found a weak dependence of refractive index at 250 nm on the ratio of sp^3/sp^2 bond. The reflectivity measured by Larruquert et al. [240] is used in the model for the reflectivity of the ta-C film at 248 nm.

- Absorption coefficient: the absorption coefficient at 248 nm for ta-C is highly dependent of the ratio of sp^3/sp^2 bond[243]. Numerical experiments has been performed showing that the model predictions are not noticeably influenced by the absorption coefficient of ta-C, see Figure 4.2. Thus, a good accuracy for the absorption coefficient is not necessary to provide accurate numerical results.

The thermal and optical properties for the ta-C used in the model are summarised in the Table 4.2.

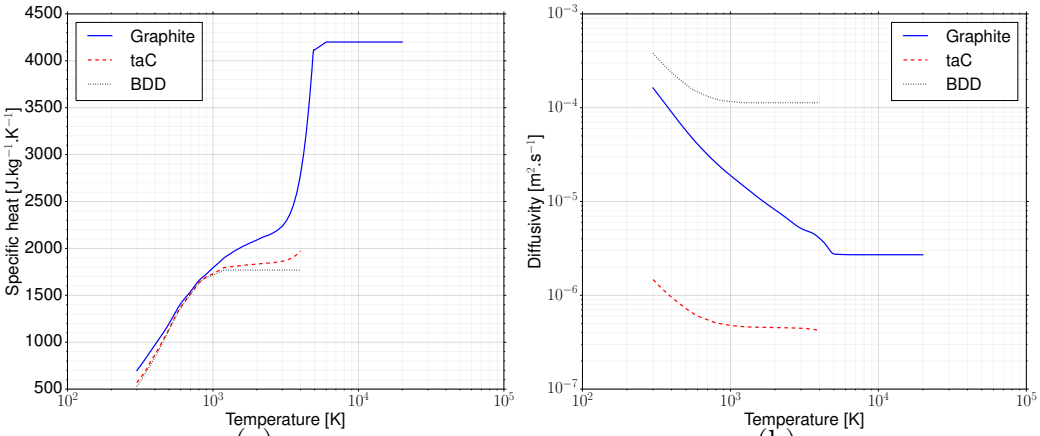

Figure 4.3 : Material properties as a function of the temperature for the three materials used in the model for (a) the specific heat and (b) the diffusivity.

4.3.3 Optical and thermal properties for graphite

The optical and thermal properties of graphite are commonly reported in the literature. In this study, the graphite is considered to be non-porous during the ablation process [154] and polycrystalline [**Butler-smith2013**].

- Specific heat: the specific heat of graphite has been reported in numerous works for many varieties of graphite (pyrolytic, porous, etc.) [89, 140, 250]. The specific heat reported in the different studies are in fairly good agreement from 300 K to 4800 K. Thus, the value of the

Table 4.3: Thermal and optical properties of graphite

Density [246], g.cm^{-3}	2.2
Temperature of reference [222], K	3635
Latent heat of vaporization [89], kJ.mol^{-1}	713
Absorption coefficient [247] @1061, m^{-1}	2.4×10^7
Absorption coefficient [247] @248, m^{-1}	1.12×10^8
Reflection coefficient [89] @1061 nm	
	0.21 -2.83×10^{-5}(T-300) for $T \leq$ 7000 K
	0.02 for $T >$ 7000 K
Reflection coefficient [247, 248] @248 nm	
	0.45 -5.22×10^{-5}(T-300) for $T \leq$ 7000 K
	0.10 for $T >$ 7000 K
Specific Heat, [140]	See Figure 4.3a)
Thermal diffusivity, [89, 249]	See Figure 4.3b)

specific heat used in the model for graphite is the one reported in [140]. For a temperature over 4800 K, experimental measurements suggest that the specific heat of graphite is constant, [251].

- Thermal conductivity: the thermal conductivity of porous graphite (16%) was reported in [89]. For non-porous material, the thermal conductivity is calculated using the Maxwell Garnett model [252]. The thermal conductivity used in the model for graphite is 25% higher than thermal conductivity reported by Bulgakova et al. [89].

- Density: the density of non-porous graphite has been reported to be 2.2 $g.cm^{-3}$, [246].

- Reflectivity at 1061 nm: the reflectivity of graphite at 1061 nm has been previously reported [89], see Table 4.3.

- Reflectivity at 248 nm: the reflectivity of graphite at 248 nm has been measured at 300 K [247]. Furthermore, pump and probe experiments show that the reflectivity of graphite for three different wavelengths decreases with temperature [248]. It is likely that the reflectivity at 248 nm follows the same trend, so it is assumed that the reflectivity decreases with temperature down to 0.10 at 7000 K. It is believed that a reduction of the reflectivity with temperature represents a closer approximation to reality than a constant reflectivity. The value of the reflectivity taken for graphite at 248 nm is given in Table 4.3. Furthermore, numerical experiments are presented in the Subsection 5.4.5.2 to understand the relationship between the reflectivity and the position of the interfaces (graphite/vacuum and graphite/diamond).

- Absorption coefficient at 248 nm and 1061 nm: Djurišić et al. have measured the absorption coefficient of graphite at 248 nm and 1061 nm

at 300 K [247]. It must be noted that pump and probe experiments demonstrate a decrease of the absorption coefficient with temperature. For the sake of simplicity, the absorption coefficient is considered to be constant.

The optical and thermal properties used in the model for graphite are given in Table 4.3.

4.4 Experimental Methodology

The model developed in this study is used to simulate the phase transition between diamond and graphite under high thermal load. This effect is particularly important during the first interaction between the laser and the diamond target (single pulse ablation). In effect, the creation of a graphitic layer over the diamond leads to a large variation of material properties, which dramatically changes the heat distribution inside the target. Subsequent interactions between the laser and the diamond target (multi-pulse ablation) do not create such a dramatic change in the heat distribution since a graphite layer is already present on top of the diamond. Single pulse ablation tests are the most stringent, and are therefore used to investigate the capabilities of the model for the two dissimilar diamond and related materials.

The methodology and experimental results for tetrahedral amorphous carbon have been reported previously [28, 253]. Therefore, the experimental setup is briefly described in the following paragraph and the reader is referred to the previously published studies for further information. However, the results for boron doped diamond have not been previously published, and the experimental methodology used in this study is detailed below.

4.4.1 Tetrahedral amorphous carbon (ta-C)

A KrF excimer laser producing 20 ns (FWHM) pulses at 248 nm is used to study the ablation of 2 μm thick ta-C. The height and depth of the crater is measured for a range of fluence between 0.1 and 600 J.cm^{-2}. The 2μm ta-C film is produced by pulsed arc deposition, using a technique described in the study by Schulz et al. [239].

4.4.2 Boron doped diamond (BDD)

The experimental tests for the model validation are conducted with a fibre laser at constant pulse repetition rate of 35 kHz. The temporal profile is characterised by a full-width at half-maximum of 30 ns with a long trail after the maximum that lasts approximately 200 ns. The exact temporal profile of the laser pulse is obtained from the manufacturer data sheet and an example is provided in Figure 4.5. Laser pulses are fed into a galvanometers head mounted with a 100 mm focal length f-θ. The resulting spatial profile is Gaussian with a diameter around 38 µm (using the 1/e^2 definition). The maximum power achievable at the focal plane is 18.48 W and the maximum energy per pulse is 0.53 mJ. Thus, it is possible to obtain fluences between 0.2 and 93.5 J.cm^{-2}. The boron doped samples are produced by Element Six Ltd. The samples are polished on both sides (Ra $<$ 30 nm) and have a thickness around 0.5 mm. The beam moves on the target surface with a high speed ($>$ 4000 m.s^{-1}) so that two consecutive pulses do not overlap and at least ten craters are produced and averaged in order to reduce the error arising from variability of the laser parameters. Each crater is measured using a white light interferometer, Br uter GT-i, that provides accurate measurement (error $<$ 10 nm) of the surface after the ablation. Afterwards, the radial profile and depth at the centre of the crater is extracted, see Figure 4.9.

4.5 Results and discussions

The model is tested for two dissimilar diamond and related materials, a tetrahedral amorphous carbon and a boron doped diamond. For tetrahedral amorphous carbon, the influence of the graphite reflectivity on the position of the interfaces is discussed. The numerical predictions are then compared to the experimental results. Finally, the discrepancies between predictions and experimental results are discussed. For boron doped diamond, the experimental results are presented and reviewed. Then, the influence of the absorption coefficient of boron doped diamond for the position of the interfaces is presented. Finally, the discrepancy between the numerical and experimental results is investigated.

4.5.1 Boron doped diamond

In the case of boron doped diamond at low fluence, the swelling is clearly visible in Figure 4.4(a). SEM imaging (Figure 4.4(a)) suggests that the swelling occurs following the preferential direction and that the microstructure has a small influence on the final topography. Previous investigation shows that a variation in the doping rate over the surface exists [254]. This creates local variability in the amount of absorbed energy during pulsed laser ablation, leading to variation in the amount of swelling. Thus, this explains the higher variability observed for the depth/height of the crater for low fluence. SEM imaging for high fluence does not show such variability in the shape of the crater, see Figure 4.4(b). For high fluence, the graphitisation occurs earlier, see Figure 4.5, thus a larger part of the laser pulse interacts directly with the graphite for which boron doping rate does not affect the absorption coefficient of the graphite. This leads to a lower variation of ablation/swelling over the surface at high fluence.

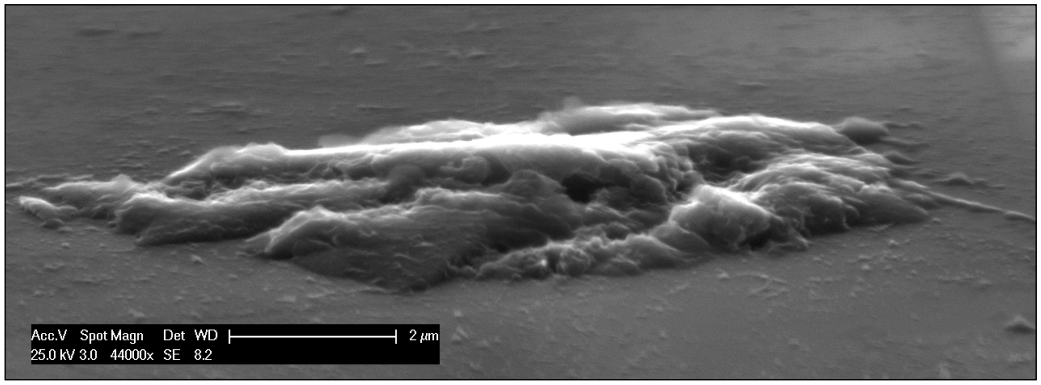

(a)

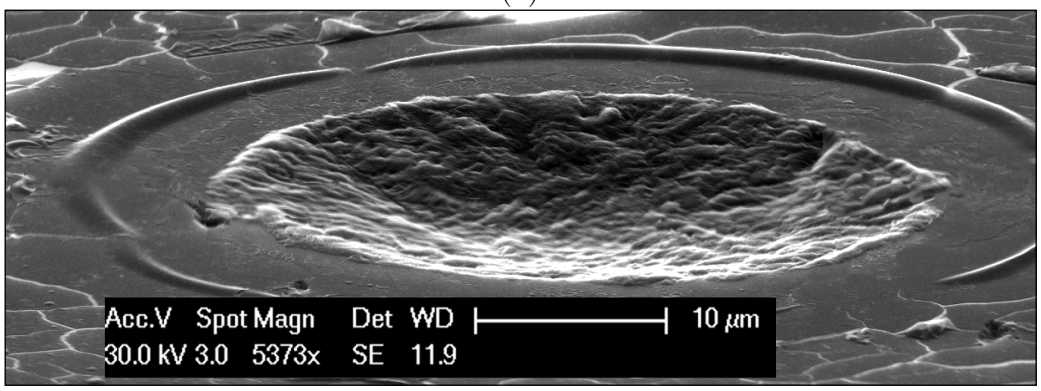

(b)

Figure 4.4 : SEM collage imaging of crater for a fluence of (a) 12.48 J.cm^{-2} and (b) 65.9 J.cm^{-2} with an angle of 75°.

As mentioned previously, the absorption coefficient of boron doped diamond has a strong influence on the results of the simulation. The influence of the absorption coefficient on the simulation cannot be estimated easily because the moment the graphitisation starts the properties of the surface material change dramatically, see Figure 4.5. The absorption coefficient for square diamond is two orders of magnitude lower than the coefficient for graphite, which leads to a steep increase of temperature after the start of the graphitisation at the surface, see Figure 4.5. Therefore, numerical experiments have been performed to quantify the influence of the absorption coefficient on the simulation, see Figure 4.6.

The numerical results show a marked influence of the absorption coefficient on the position of the interfaces for the whole range of fluence studied, see

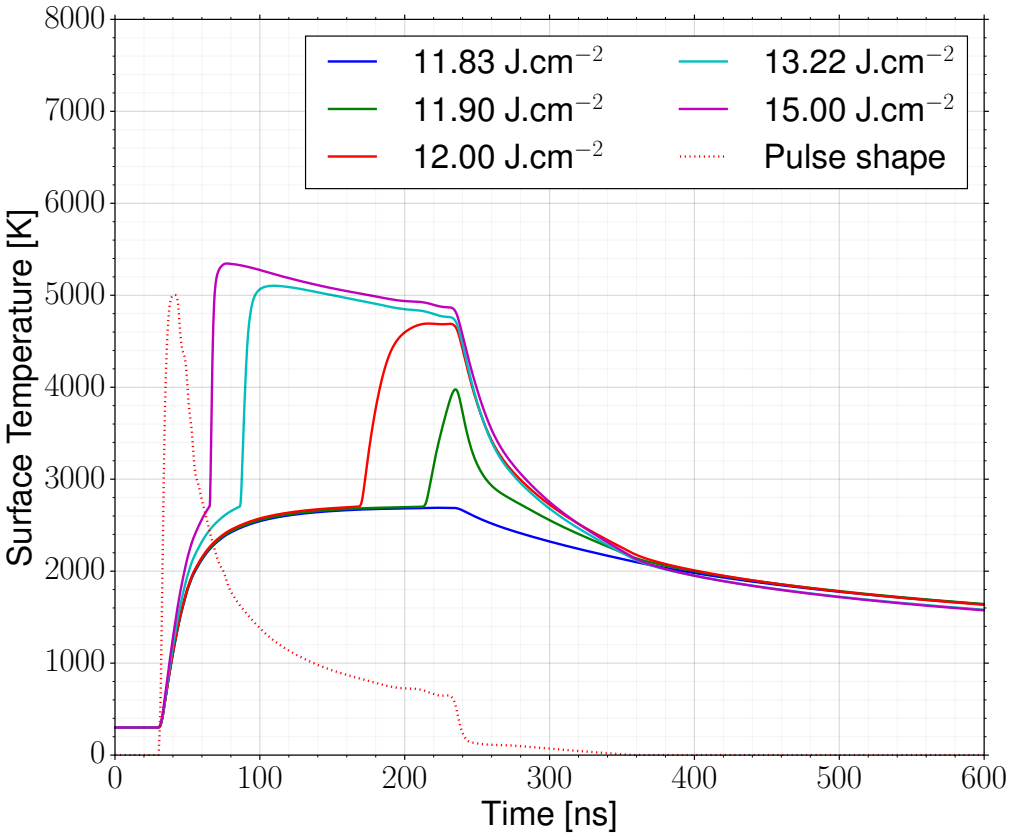

Figure 4.5 : Surface temperature as a function of time for several fluence and the pulse shape for the SPI-G3.

Figure 4.6. First of all, the time at which graphitisation begins is highly dependent on the absorption coefficient of square diamond, and the final position of the interfaces is highly dependent on this time. The jump of absorption coefficient of the surface material leads to a dramatic change in the heat distribution, with a significant fraction absorbed in the first 42 nm of the graphite layer. The large amount of heat generated at the surface quickly diffuses inside the graphite, leading to a rapid swelling of the surface by tens or hundreds of nanometres. Furthermore, the diamond graphitisation is accompanied by a strong vaporisation at the surface of the graphite. Thus, the start of graphitisation will affect greatly the distribution of the heat. Interestingly, the position of the interface between the graphite and the diamond converges to one curve for high fluence, which suggests that the BDD absorption coefficient mostly affects the amount of energy used to

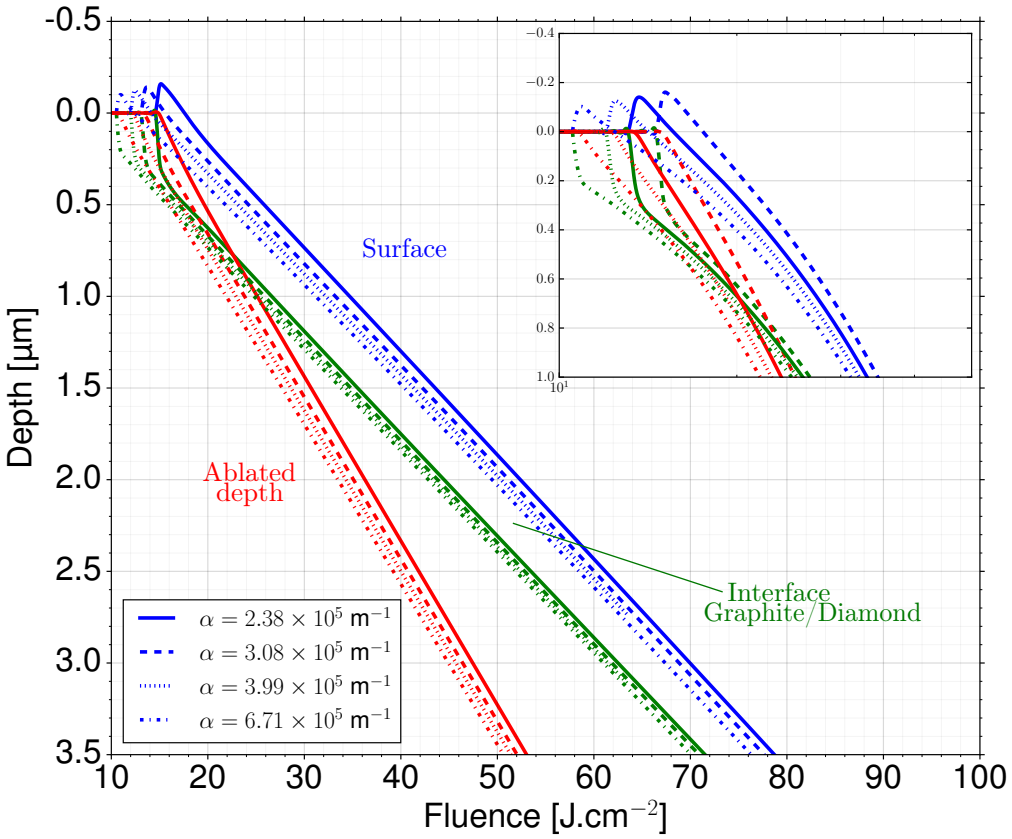

Figure 4.6 : Interfaces position as a function of the fluence for 3 different values of the boron-doped diamond absorption coefficient. The blue, red and green line are the position of the graphite/vacuum interface, the depth of ablated graphite and the position of the graphite/diamond interface respectively.

evaporate the graphite.

In the results presented in Figure 6.21, the absorption coefficient is determined by fitting the experimental results and the calculated position of the interface graphite/vacuum. It has been found that an absorption coefficient for the boron doped diamond of 5.18×10^5 m^{-1} gives good results, see Figure 6.21. It is close to the value measured at 300 K (approximately 7×10^5 m^{-1}, [229]). Furthermore, it has been shown that the absorption coefficient should decrease with an increase of temperature[230], so the value found is consistent with the available experimental data. The experimental results show that the amount of ablated material increases linearly up to a

fluence of 50 J.cm^{-2}, which suggests that the energy of the laser beam is totally coupled to the target and that the amount of energy absorbed by the plasma over the crater is small, see Figure 6.21. This is substantiated by the good agreement between the model without plasma absorption and the experimental results.

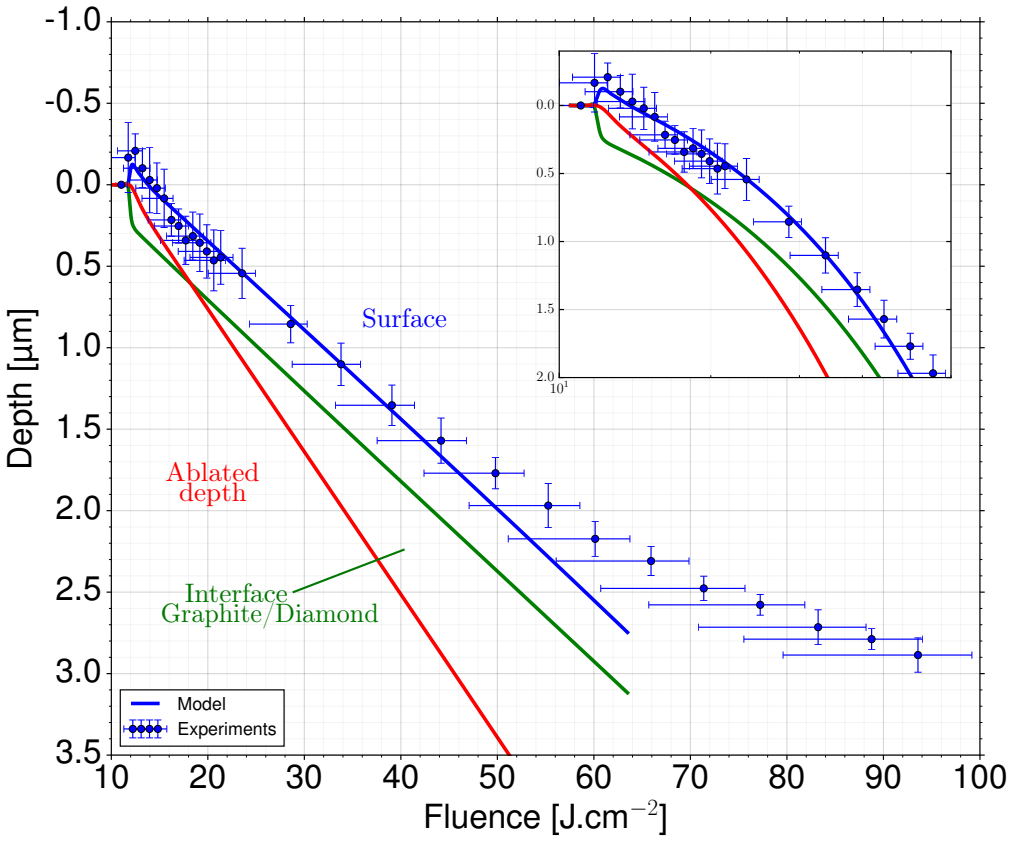

Figure 4.7 : Position of the interfaces for the model and the experiments for BDD. The red, blue and green lines are the ablated depth, the interface position of graphite/vacuum and interface position of diamond/graphite respectively. The inset show a subset of the data in a logarithm scale for the fluence.

At higher powers, when plasma absorption is neglected the amount of ablated material is lower than the model prediction. This suggests that a part of the energy is shielded from the target by the plasma. However, when the method presented above was used to estimate the plasma absorption, (4.5), no values of the parameters a and b could be found to reproduce the

experimental results. The failure of the plasma model to correctly predict the amount of energy absorbed is due to several factors. The main absorption mechanism during infrared pulsed laser ablation is via inverse Bremsstrahlung, which is highly dependent on the temperature and density of electrons [125]. Thus, the plasma absorption will present an ignition threshold for which the amount of energy absorbed offers positive feedback, leading to a large increase in the amount of energy absorbed [125]. For the same pulse energy, the shorter pulses have a high intensity overcoming losses due to the three body recombination, de-excitation, photon recombination, Bremsstrahlung emission and plasma expansion [120, 125] and reach the ignition threshold. However, longer pulses requires more pulse energy to reach the same intensity and overcome the ignition threshold. The model for the plasma absorption implicitly considers that the plasma absorption occurs at the same time as the start of the ablation. The experimental results presented in Figure 6.21 show that it is not the case for the present experimental setup as the linear coupling between the fluence and the amount of ablated material stops around 50 $J.cm^{-1}$. Furthermore, previous modelling work has found similar behaviour for the plasma ignition [31]. Thus, it is likely that a better description of the plasma will improve the prediction of the model for a fluence over 50 $J.cm^{-2}$.

Finally, the good agreement between the experimental results and the model for boron doped diamond validates the methodology for the prediction of the thermal stability of diamond during pulsed laser ablation. In the following section, the same methodology is applied for tetrahedral amorphous carbon thus providing further information about the thermal stability for diamond-like carbon thin films that cannot be directly obtained [245, 255].

4.5.2 Tetrahedral amorphous carbon

As mentioned previously, the value of the reflectivity for graphite at 248 nm is not precisely known as a function of the temperature. However, previous pump and probe experiments show that the reflectivity decreases at higher temperature [248]. The error in the model prediction due to the uncertainty of the reflectivity value cannot be estimated analytically and therefore, several values for the reflectivity have been tested numerically. For this investigation, plasma absorption is not taken into account to simplify the discussion. The free parameters used in the implementation of the plasma model are calculated using the experimental results, see (4.5), which could counterbalance the influence of the reflectivity on the amount of energy reaching the target (by changing the free parameter values) and biasing the discussion about the reflectivity. The position of the interfaces for four cases is shown in Figure 4.8. It is clear that the reflectivity has a significant influence on the position of the interfaces (graphite/diamond and graphite/vacuum) over the whole range of fluence. For fluence lower than 2.5 J.cm^{-2} (fluence for the maximum swelling), the influence of the reflectivity is not strong; an error of 50% in the value of the reflectivity only introduces around 50 nm error in the position of the interface between the graphite and vacuum and around 100 nm for the position of the interface between graphite and diamond. However, for fluence over 10 J.cm^{-2}, the error increases proportionally with the fluence. Several points explain these results. For low fluence, a large part of the energy is absorbed when ta-C is the top material, so changes in the reflectivity of the graphite phase will not change the amount of energy absorbed. As the fluence increases, the start of graphitisation occurs earlier, which means that a large part of the pulse is absorbed when graphite is the surface material. For fluence over 10 J.cm^{-2}, most of the energy is absorbed when the graphite is the surface material, which leads to a large variation in the position of the

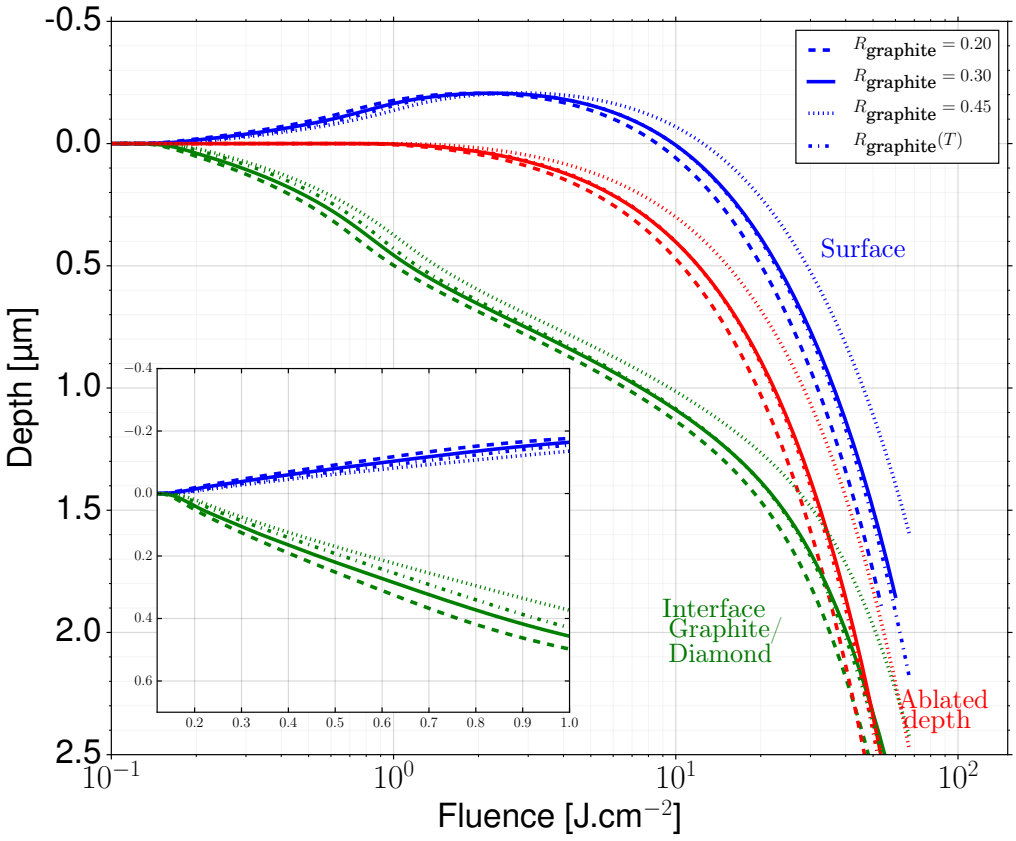

Figure 4.8 : Position of the interfaces and the amount of ablated material for different value of the reflectivity for the graphite phase and for the function given in Table 4.3. The red, blue and green lines are the ablated depth, the interface position of graphite/vacuum and interface position of diamond/graphite respectively.

interfaces, see Figure 4.8.

The value of the graphite reflectivity has a notable influence on the value of the position of the interfaces especially for high fluence. However, it does not change the trend presented by the numerical experiments. The graphitisation starts at 0.2 J.cm^{-3} and increases until the surface reaches 0.2 µm at approximately 2.1 J.cm^{-3}. For higher fluence, ablation overcomes the swelling and the surface recedes. However, the model results for high fluence cannot be used to estimate the variation of the reflectivity due to the ignition of the plasma, which decreases the amount of absorbed energy. It must be noted that the numerical results using these four reflectivity values

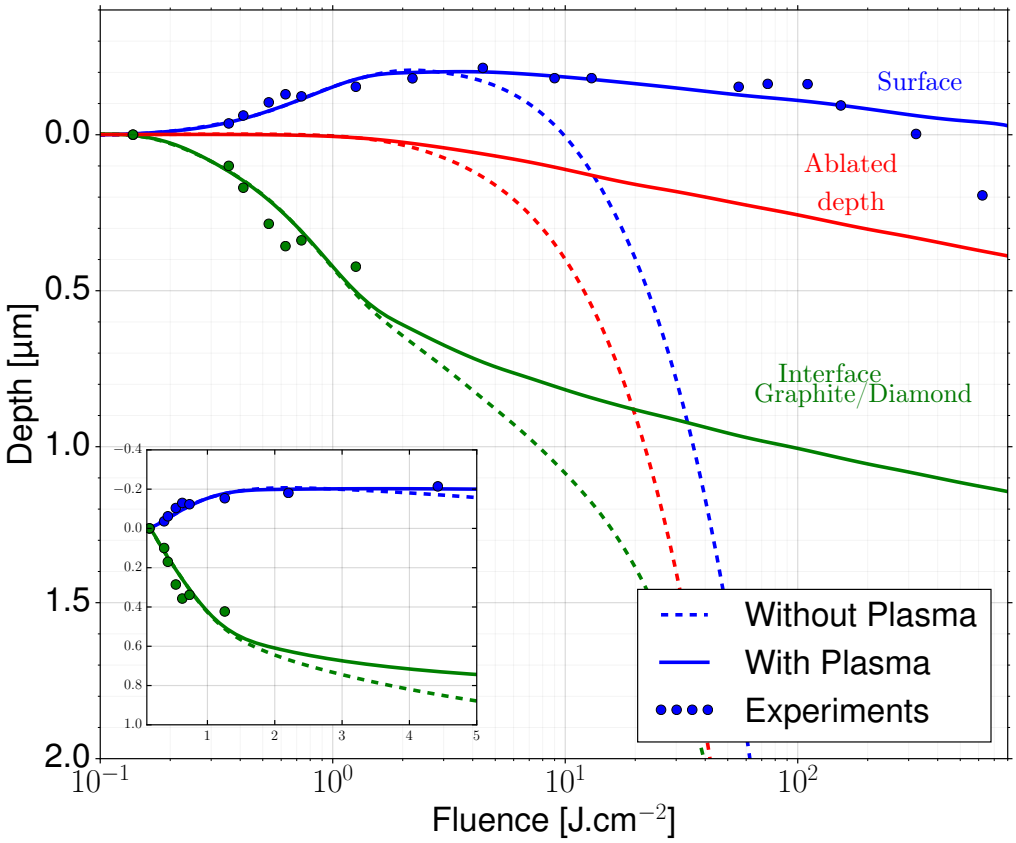

Figure 4.9 : Blue circles are the experimental data from [28]. Green circles are the position of the graphite-ta-C interface estimated using the relation (6.1). The red, blue and green lines are the ablated depth, the interface position of graphite/vacuum and interface position of diamond/graphite respectively calculated using the model.

are all in fairly good agreement with the available numerical results for low fluence. Thus, it does not give us enough information to distinguish between the different cases. In the following simulations, the reflectivity is dependent on the temperature (see Table 4.3) [248], which leads to better agreement with the experiments.

The experimental and numerical position of the surface for ta-C ablated as well as the numerical results for the position of the interface between diamond and graphite and the amount of ablated material by 20 ns pulsed laser at 248 nm are presented in Figure 4.9. It must be noted that the experimental position of the interfaces between graphite and diamond, presented in Figure

4.9, has been calculated using the mass conservation, Equation (6.1), until the start of the material ablation at around 2.1 J.cm^{-2}.

Without considering the plasma shielding, the model is in excellent agreement with the experiments for fluence lower than 3 J.cm^{-3}. The model is used to simulate the interaction between the diamond and the graphite during pulsed laser ablation. Therefore, it is particularly interesting that the predictions are accurate for low fluence and shows that the modelling framework chosen can correctly predict the surface graphitisation of diamond during pulsed laser ablation. Using the simple description of the plasma absorption, (4.5), it is possible to estimate the amount of energy absorbed by the plasma and extend the range of validity of the model. The parameters a and b have been evaluated using the experimental data and are respectively equal to 5×10^8 m^{-1} and 0 J^{-1}.cm^2. These values are consistent with the literature for the ablation of graphite previously done with laser pulses at 532 nm with a FWHM of 7 ns [32] and at 1064 nm with a FWHM of 13 ns [89]. The value of a increases with a decrease of the wavelength (3×10^5 m^{-1} at 1064 nm and 2×10^6 m^{-1} at 532 nm) suggesting that plasma ignition occurs with a lower amount of material ablated. Furthermore, it has been shown that at 532 nm, the free parameter b is equal to zero, suggesting that the plasma absorption is almost independent of the amount of energy inside it. These observations are consistent with the main absorption mechanisms of laser pulses at 1064 nm and 248 nm. For infrared lasers, plasma absorption occurs mainly through inverse Bremsstrahlung with the ion and neutral [120, 125], which requires a large electron density and temperature to ignite, so that the parameter b should not be zero. In contrast. for UV lasers, plasma absorption is dominated by photo-ionisation processes that does not require a large electron population generated by an increase of temperature [120, 124] so the parameter b should be small. It must be noted that the variation of the

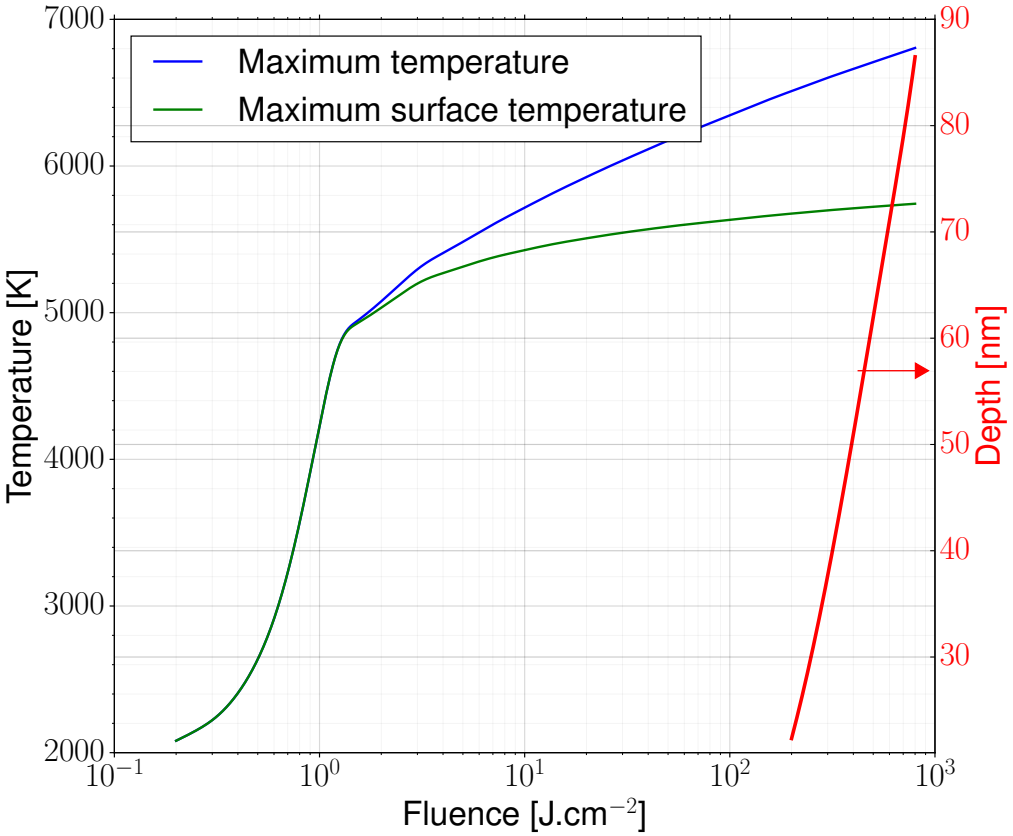

Figure 4.10 : Maximum surface temperature and maximum temperature during the simulation of the interaction between the laser and ta-C as a function of fluence. The red solid line represents the maximum depth such as the temperature is equal to 6500 K.

parameter a is also consistent with the absorption mechanisms at VIS and UV wavelength. In effect, a decrease of laser wavelength increases the number of atomic electronic levels (especially so that those levels are generally more densely populated) that participate in photo-ionisation, which leads to a step increase in the plasma absorption coefficient [256]. The plasma absorption increases the range for which the model is in good agreement with the experiments and suggests that the inclusion of the plasma in a more detailed manner could provide additional insight into the ablation mechanisms.

[b] The plasma absorption increases the range for which the model is in good agreement with the experiments and suggests that the inclusion of the plasma in a more detailed manner could provide additional insight into

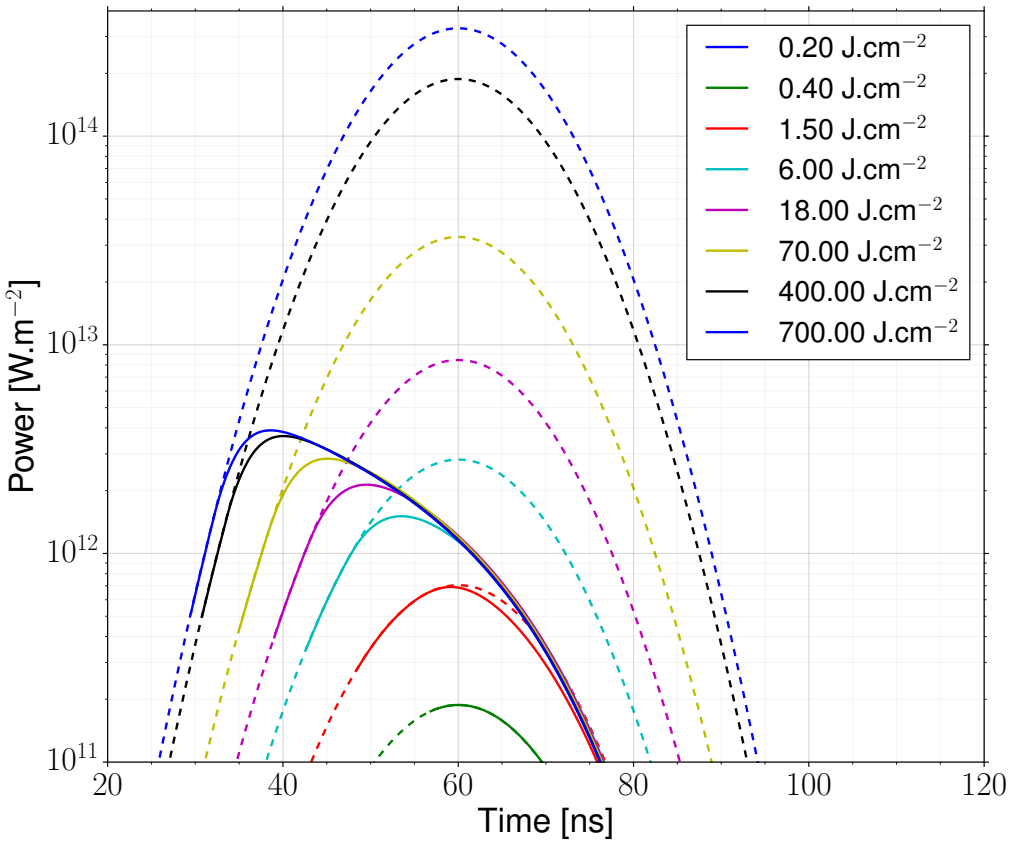

Figure 4.11 : Instantaneous intensity for several fluence of the laser pulses. The solid curve (–) is the instantaneous intensity reaching the target and the dashed curves (- -) is the instantaneous intensity that is emitted by the laser.

the ablation mechanisms. The instantaneous intensity reaching the target is greatly reduced by the plasma absorption reaching 1 order of magnitude for 700 J.cm^{-2}, see Figure 4.11.

For fluence higher than 150 J.cm^{-2}, the experimental data shows a steep increase in the amount of ablated material that the model presented here cannot explain. This discrepancy for high values of fluence is often found in the literature for pulsed laser ablation modelling [31] and can be explained by explosive boiling/volumetric mass removal, as presented in the work of Demos et al. [136]. The numerical experiments show that the maximum temperature reaches around 6500 K for fluence over 150 J.cm^{-2}. This is close to the widely accepted critical temperature of graphite [140] and is consistent

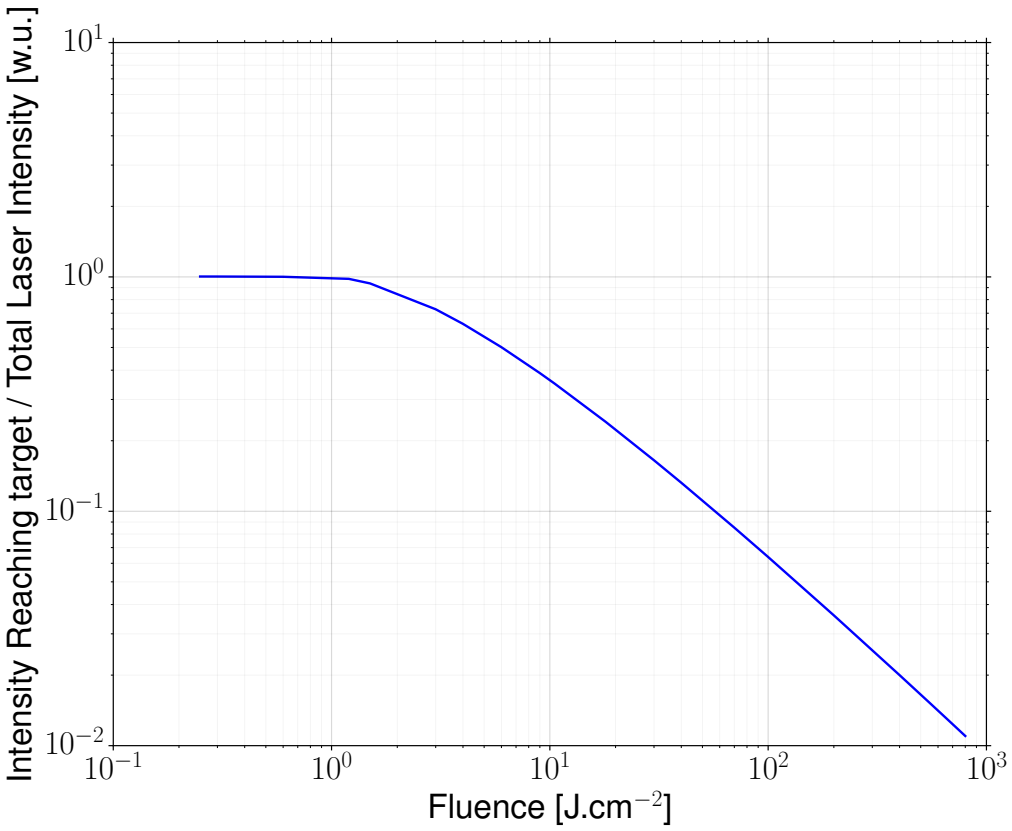

Figure 4.12 : The ratio of energy reaching the target over the amount of energy coming from the laser pulse.

with the beginning of explosive/volumetric mass removal. It has been found that the thickness of material in a thermodynamic state close to the critical is less than 100 nm, see Figure 4.10. Therefore, the model might not be able to explain the 250 nm difference between the model and the experiments for a fluence of 622 J.cm^{-2}. However, the amount of energy reaching the target is around 1% of the total energy expenditure from the laser source, see Figure 4.12. Thus, it is likely that the amount of energy emitted by the plasma via bremsstrahlung or photo-recombination processes should be of the same order than the transited amount of energy that reaches the target. It has been found in a previous study that the emission of energy by the heated plasma over the crater causes deeper heating without affecting the amount of ablated material [32]. This effect has not been taken into account for this

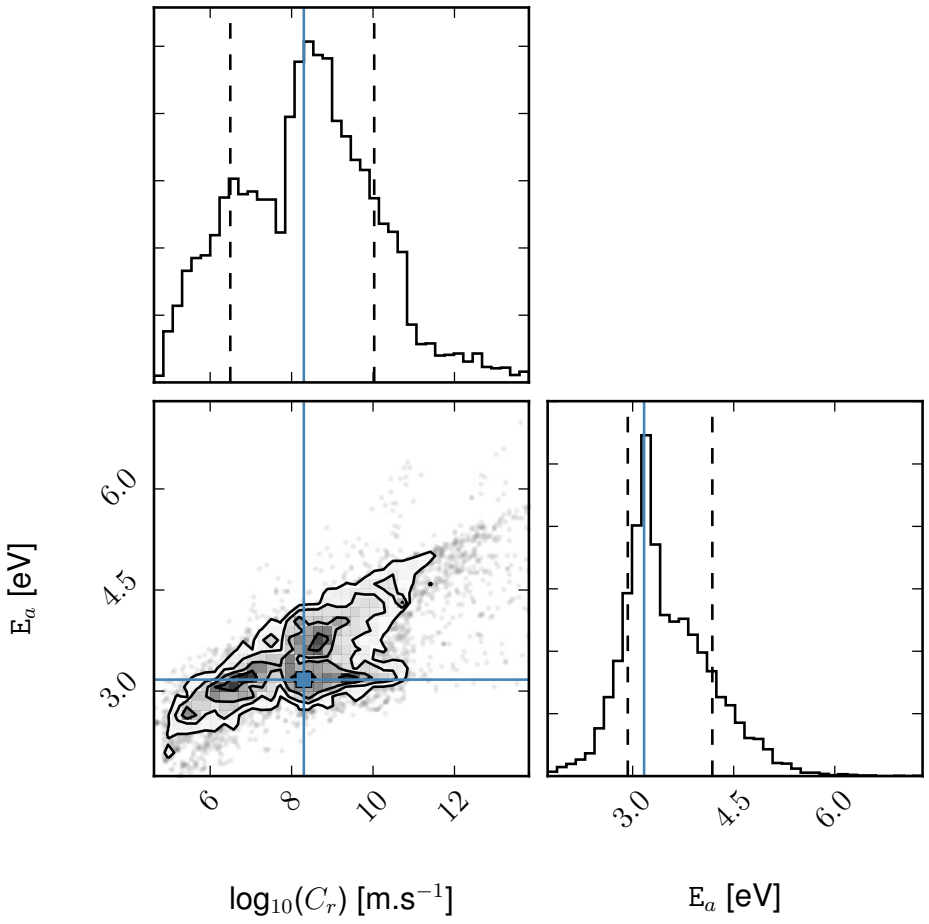

Figure 4.13 : Affine Invariant Markov chain Monte Carlo (MCMC) Ensemble sampler [255] for the the fitting of the surface position predicted from the model to the experimental results using activation energy and the rate of graphitisation as free parameters [257]. The blue line represents the result for the activation energy and the rate of graphitisation from the optimisation using the maximum likelihood method.

study but it would suggest that the plasma absorption is overestimated or that the amount of energy emitted by the plasma reaches level comparable to the energy coming directly from the laser. In effect, deeper heat absorption should lead to a larger swelling that should be counterbalanced by an increase of ablation at the surface. It should also lead to a larger layer of material heated over the critical temperature and explain the difference between the experiment and the model for high fluence. Further investigation of the

interaction between the plasma and the laser needs to be carrier out to understand the discrepancy at high level of fluence.

The estimation of the parameters used in Arrhenius law for the graphitisation of ta-C provides further information about the thermal stability of diamond-like carbon films, see Figure 4.13. The activation energy for ta-C has previously been determined experimentally at 3.5 ± 0.9 eV [196, 244]. The present study provides improved accuracy for the activation energy ($3.15^{+1.0}_{-0.22}$ eV) and also provides an estimation for the rate of graphitisation ($\exp\left[\log[10] \times 8.3^{+1.72}_{-1.8}\right]$ m.s^{-1}), see Figure 4.13.

4.6 Conclusion

Theoretical and experimental results have been used to investigate the ablation of diamond and related materials with nanosecond laser pulses. The dependence of the ablation rate on laser fluence has been analysed for a wide range of values of laser fluence and two dissimilar types of diamond and related material. The experimental data shows a swelling of the surface for low fluence and an ablation of the surface for high fluence, see Figure 4.4.

Furthermore, the behaviour of the diamond during laser ablation has been addressed theoretically within a one dimensional modelling framework. The model takes into account the transition between graphite and diamond/ta-C, the jump of density, the plasma absorption and the evaporation of the material during nanosecond pulse ablation. By solving the system of equations numerically, the space-time distribution of temperature is obtained from the model within the diamond/graphite target. The positions of the interfaces are also obtained from the model. The model shows excellent agreement with the experimental data until the onset of the explosive/volumetric mass removal for ta-C and plasma absorption for boron doped diamond. Model

presented in this study is the first one to address the particularity (phase change with change of density) of the interaction between the diamond and related materials with a pulsed laser beam. In effect, previous studies only reported the thickness and the position of the surface without providing a complete modelling framework taking into account the transition of the optical and thermal properties and the dynamic position of the interfaces (diamond/graphite and graphite/vacuum). Interestingly, the model provides insights into the ablation process. It shows that using the quasi-stationary annealing threshold for the graphitisation of diamond and related material does not give accurate results. This work shows that the Arrhenius law provides accurate predictions for the rate of graphitisation during pulsed laser ablation for two allotropes of carbon with a large amount of sp^3 bonds. The present study provides a new method to obtain the activation energy and the graphitisation rate for diamond-like carbon, and provides numerical estimations for a ta-C with around 80% sp^3 bonds with an improved accuracy.

In recent years, the interaction between the material ablated from the surface and the laser has been investigated in detail, which demonstrates the importance of accurately modelling the temperature dependence of key physical properties, [23, 30, 55], an aspect that has been strongly emphasised in this chapter. The behaviour of the subsurface during ablation has not been heavily studied due to the difficulty of measuring the microstructure inside the material and relating it to the processes that created it. Diamond ablation presents an interesting case for which the maximum position for the graphitisation temperature can be measured after the removal of the graphite layer (using acidic solutions [138] or a furnace in an oxidising atmosphere [28]) putting further constraint on the results of the model. Future studies should provide additional information about the phenomena occurring inside the material during pulsed laser ablation.

This study is encouraging for the development of an alternative approach that could address the main issue of this framework for the modelling of large machining task, such as the long computation time required and the lack of flexibility for the capture of 3D removal rate. The prediction of the footprint profile in very short times in order to embed these models into CAD/CAM systems enabling tool-path generation in real time for PLA machining.

Chapter 5

Modelling of pulsed laser ablation by continuous trench

A novel approach to predict the surface topography change during PLA machining of large surface is describe in this chapter. The framework is a geometrical model that enables the fast prediction of the resulting surface topography that use a relatively small amount of experimental data for its calibration. The new model is accompanied by a detailed methodology for the accurate calibration of the model using empirical data. This new methodology provides a fast method to implement optimisation methods into CAD/CAM system to support the generation of tool-path strategies to manufacture innovative 3D geometry using PLA.

5.1 Introduction

The development of mathematical framework for PLA machining is essential for the development of this technology as a feasible manufacturing process, and recently more consideration has been given to computationally inexpensive approaches [39, 40, 42, 43, 173] as discussed in the section 2.3. Those methods, unlike the physical models as the model presented in Chapter 4, focus on the estimation of the footprint of PLA as a function of the variable parameters during the machining process, see Figure 5.1.

In order to address the drawbacks presented in the section 2.3, this chapter

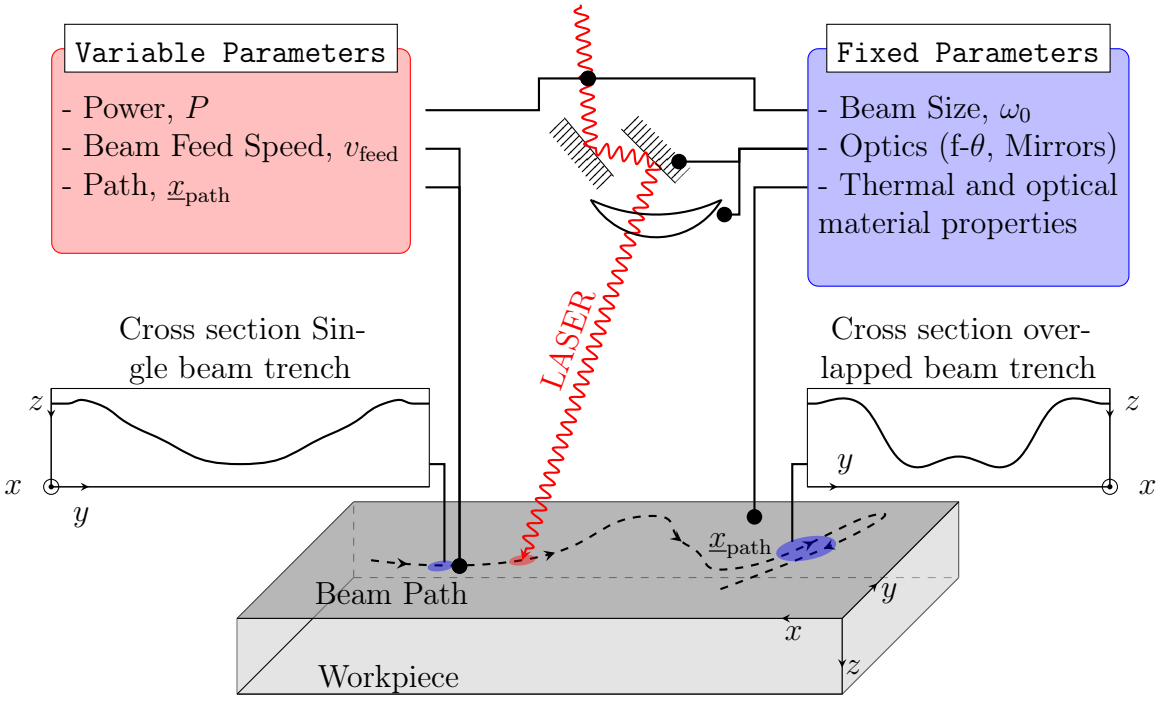

Figure 5.1 : Variable and fixed parameters used in the model for PLA machining.

presents an innovative model in which the ablation of the surface by the pulsed laser is treated as a continuous process, so that the interaction between two pulses is implicitly taken into account in the values of the calibrated parameters. Unlike, previous modelling approach, the framework enables the modelling non-linear interaction between pulses, it also requires the little experimental data for an accurate calibration of the model and opens the way for continuous optimisation of the machining parameters to generate specific topography. The model does not have any inherent restriction on the material or lasers used and can easily be calibrated with a few experimental tests. This model for micro-machining takes into consideration the following aspects:

- Beam feed speed: the variation of the trench depth with the degree of overlapping of the pulses. This takes implicitly into account heat conservation between pulses, material ejection and surface property

modification.

- Position of the beam on the surface: allowing the prediction of the 3D surface resulting from the machining process.
- Beam Power: the variation of the width and depth of the trench with the power.

The modelling approach is validated for three materials (POCO graphite AF-5, metal-matrix diamond CMX850 and a polycrystalline diamond, PCD) as an example of its accuracy, for both single and overlapped trenches, thus making the first step towards controlled and predictable micro-machining by PLA of truly complex geometries.

5.2 Modelling of continuous trench PLA for an arbitrary moving beam

This section provides the mathematical framework used to model the interaction between the laser beam and the workpiece.

5.2.1 Model of a single footprint of an arbitrary moving beam

The variation in the depth, Z_s, at the point $\underline{x} = (x, y)$, due to the impact of the laser beam moving on the tool path, $\underline{x}_{\text{path}} = (x_{\text{path}}, y_{\text{path}})$, is expressed by a general relation,

$$\partial_t \{Z_s\} = \mathcal{A}\left(\mathcal{P}, v_{\text{feed}}, \sqrt{(x - x_{\text{path}})^2 + (y - y_{\text{path}})^2}\right). \tag{5.1}$$

The ablation rate, $\mathcal{A}$, is calculated from experimental data. The following calculation shows that the ablation rate can be expressed using the profile

of a trench, $p(y, \mathcal{P}, v_{\text{feed}})$. From experiments presented in the chapter, it has been found that the profile of a trench at constant feed speed, v_{feed}, and power, $\mathcal{P}$, can be expressed as

$$p(y, \mathcal{P}, v_{\text{feed}}) = \left[\frac{\Upsilon(\mathcal{P})}{v_{\text{feed}}} + \chi(\mathcal{P})\right] \bar{p}\left(\frac{y}{r^*(\mathcal{P})}\right), \tag{5.2}$$

with $\Upsilon(\mathcal{P})$ the factor for the variation of the depth with the inverse of the feed speed, $\chi(\mathcal{P})$ the factor for the effect of the pulse interaction on the profile depth, $r^*(\mathcal{P})$ the width of the trench profile (that is not directly related to the spot size), y the position along the profile of the trench and $\bar{p}$ the generic profile of the trench. Using (5.1) and changing the integration with respect to the time to an integration with respect to the beam path arc length, s_{path}, so that

$$\mathtt{d}_t \{s_{\text{path}}\} = v_{\text{feed}}. \tag{5.3}$$

with s_{path} is the equivalent arc length between the start (t_{start}) and the end (t_{end}) of the machining time defined by the path of the beam, $\underline{x}_{\text{path}}$, such as

$$s_{\text{path}} = \int_{t_{\text{start}}}^{t_{\text{end}}} \sqrt{(\partial_t \{x_{\text{path}}\})^2 + (\partial_t \{y_{\text{path}}\})^2} dt. \tag{5.4}$$

Using the notation r as the distance between the centre of the beam, $\underline{x}_{\text{path}}$, and a point on the surface, $\underline{x}$

$$r = \sqrt{(x - x_{\text{path}})^2 + (y - y_{\text{path}})^2}. \tag{5.5}$$

It is possible to express the depth, Z_s, as a function of the ablation rate assuming that $Z_s(x, y, t) = 0$ when $t = 0$, as

$$Z_s(x, y, \mathcal{P}, v_{\text{feed}}) = \int_{s_{\text{start}}}^{s_{\text{end}}} \frac{\mathcal{A}\left(\mathcal{P}, v_{\text{feed}}, r\right)}{v_{\text{feed}}} ds_{\text{path}}, \tag{5.6}$$

where s_{path} is the beam path arc length. Remarking that the position of the centre of the beam in the y direction is constant, the path ds_{path} can be expressed as,

$$ds_{\text{path}} = \sqrt{1 + \left(\frac{dy_{\text{path}}}{dx_{\text{path}}}\right)^2} dx_{\text{path}} = dx_{\text{path}}, \tag{5.7}$$

and since the ablation rate, $\mathcal{A}$, has a compact support and the beam is moving with a constant feed speed in the x direction, it is possible to simplify this equation as the depth does not depend on x to give,

$$v_{\text{feed}}\ Z_s(x, \mathcal{P}, v_{\text{feed}}) = \int_{-\infty}^{\infty} \mathcal{A}\left(\mathcal{P}, v_{\text{feed}}, r\right) dx_{\text{path}}. \tag{5.8}$$

Assuming that the beam path is centred on the y axis thus $y_{\text{path}} = 0$. It gives,

$$dx_{\text{path}} = \frac{r dr}{\sqrt{r^2 - (y - y_{\text{path}})^2}}, \tag{5.9}$$

and using the Abel transform [258], the ablation rate is,

$$\mathcal{A}(P, v_{\text{feed}}, r) = -\frac{v_{\text{feed}}}{2\pi} \int_r^{\infty} \frac{\partial_y \left\{p(y, \mathcal{P}, v_{\text{feed}})\right\}}{\sqrt{y^2 - r^2}} dy. \tag{5.10}$$

Using Equation (5.2), the ablation rate, $\mathcal{A}$, is equal to,

$$\mathcal{A}(\mathcal{P}, v_{\text{feed}}, r) = \left[\frac{\Upsilon(\mathcal{P}) + \chi(\mathcal{P}) v_{\text{feed}}}{r^*(\mathcal{P})}\right] \left[-\frac{1}{2\pi} \int_{\bar{r}}^{\infty} \frac{\partial_{\bar{y}} \bar{p}\,(\bar{y})}{\sqrt{\bar{y}^2 - \bar{r}^2}} d\bar{y}\right], \quad (5.11)$$

with,

$$\bar{y} = \frac{y}{r^*(\mathcal{P})} \text{ and } \bar{r} = \frac{r}{r^*(\mathcal{P})}, \quad (5.12)$$

with $\bar{r}$ the normed radiation distance with respect to the width of the trench. Equation (5.11) can be rewritten as:

$$\mathcal{A}(\mathcal{P}, v_{\text{feed}}, r) = \left[\frac{\Upsilon(\mathcal{P}) + \chi(\mathcal{P}) v_{\text{feed}}}{r^*(\mathcal{P})}\right] \bar{\mathcal{A}}(\bar{r}), \quad (5.13)$$

with the generic ablation rate, $\bar{\mathcal{A}}$, only dependent on the generic profile, $\bar{p}$,

$$\bar{\mathcal{A}}(\bar{r}) = -\frac{1}{2\pi} \int_{\bar{r}}^{\infty} \frac{\partial_{\bar{y}} \bar{p}\,(\bar{y})}{\sqrt{\bar{y}^2 - \bar{r}^2}} d\bar{y}. \quad (5.14)$$

Equation (5.13) is particularly interesting. It shows that the ablation rate can be expressed using two factors showing that the power and feed speed can be separated to the influence of the beam size and material properties. The first factor represents the variation of the ablation rate with the power and feed speed of the beam. The second factor, $\bar{\mathcal{A}}(\bar{r})$, represents the constant shape of the material removal rate. This separation makes it possible to isolate the influence of each parameter and therefore, calibrate each part of the ablation rate separately.

5.2.2 Calibration of the model

The ablation rate presented above, (5.13), needs to be calibrated. A simple method to calibrate the ablation rate is to produce a series of trenches over

a range of feed speed (i.e. overlapped pulses) and power; this requires a large data set of profiles to calibrate each function accurately. To ease the constraint on the amount of experimental data required to correctly calibrate the model, a new calibration method has been developed that greatly reduces the amount of experimental data necessary.

Using the formulation of the ablation rate, (5.13), and the standard formulation for the calculation of the surface after the ablation from the laser, (5.1), it is possible to calculate the effect of the laser on the surface for a given power and a beam path as

$$Z_s(x,y) = \frac{1}{r^*} \int_{t_{\text{start}}}^{t_{\text{stop}}} [\overbrace{\Upsilon(\mathcal{P})}^{\text{Term } I} + \overbrace{\chi(\mathcal{P}) v_{\text{feed}}(t)}^{\text{Term } II}] \bar{\mathcal{A}} \left(\frac{r}{r^*} \right) dt. \tag{5.15}$$

The term II is equal to,

$$II = \frac{1}{r^*} \int_{t_{\text{start}}}^{t_{\text{stop}}} \chi(\mathcal{P}) v_{\text{feed}}(t) \bar{\mathcal{A}} \left(\frac{r}{r^*} \right) dt. \tag{5.16}$$

The value of the term II can be easily simplified, using Equations (5.3), (5.7), (5.9) and (5.14), as,

$$II = \chi \bar{p}(\bar{y}) \tag{5.17}$$

If the variation of the feed speed along the path is chosen such that

$$v_{\text{feed}}(t) = \frac{a}{b - x_{\text{path}}(t)}. \tag{5.18}$$

since the ablation rate is symmetric with respect to the y axis and defined over a compact domain,

$$I = \Upsilon r^* \frac{(b-x)}{a} \bar{p}(\bar{y}), \tag{5.19}$$

for x in the support of the ablation rate. Finally, the surface after the test is equal to

$$Z_s(x,y) = \left[\Upsilon\frac{(b-x)}{a} + \chi\right]\bar{p}(\bar{y}) = \left[\frac{\Upsilon}{v_{\text{feed}}(x)} + \chi\right]\bar{p}(\bar{y}), \tag{5.20}$$

This shows that by using the feed speed variation, (5.18), along a straight path, the feature produced on the surface can be used to calibrate the whole model for a chosen power. In effect, the surface presents the exact same profile and depth that a trench machined at a constant feed speed and power should generate for a given feed speed. Thus, the profile of the trench for a particular x and y is directly related to Υ, χ and the feed speed of the beam through

$$p(x,y) = \left[\frac{\Upsilon}{v_{\text{feed}}(x)} + \chi\right]\bar{p}(\bar{y}). \tag{5.21}$$

Therefore, it greatly reduces the number of trenches needed for an accurate calibration of the model.

5.3 Methodology

The model described above ultimately needs to be integrated into laser machining CAD/CAM systems. Consequently, the agreement of the model only with single trenches is not a full test for its use in machining environments, for which a feed speed variation and the overlapping of trenches is fundamental to the manufacturing of 2.5D/3D free-form parts. Thus, additional tests have been conducted to characterise the performance of the model in the following distinct conditions: (i) arbitrary moving beam, (ii) overlapped trenches. The two sets of tests are not real-life machining tests but are arguably closer to real machining conditions for generating free-forms They have been chosen for the simplicity of their implementation but mostly because it is possible to

precisely monitor the process, accurately calculate the error and find possible deficiencies from the modelling perspective. In this chapter, many conditions for constant feed speed single trenches are tested for the three materials. Afterwards, tests for a reduced number of cases with a feed speed variation and overlapping trenches are performed to demonstrate that the model is accurate for a large set of kinematic conditions. Thus, the combination of the two sets of tests offers a comprehensive view of the model's capabilities.

The methodology for the calibration and the validation of the model consists of the following steps.

Step 1, Calibration: generate a series of trenches for a range of feed speeds and powers. The resulting trenches are measured using a white light interferometer (WLI); then, the depth at the centre of the trench and profiles of the trench are extracted and used to calibrate the model as per the work-flow presented in Figure 5.2.

Step 2, Validation and error quantification for the proposed model for constant feed speed single trench. A series of trenches with constant feed speed and power are produced and then measured. Afterwards, the cross-section (2D) of the surface (3D) is calculated by averaging the profile along the beam path over at least 150 µm. Then, the cross-sections are compared with simulations and the errors are evaluated.

Step 3, Evaluation of the model error for a single trench with a continuous feed speed variation. A series of trenches for a range of powers and varied feed speed is produced for each material. The depth at the centre of the trench is extracted from the experimental set and compared to the numerical one.

Step 4, Evaluation of the model for overlapped trenches. The feed speed and power are kept constant for both trenches and the distance between the centres of the two trenches (i.e. step-over) is varied. The cross-sections (by

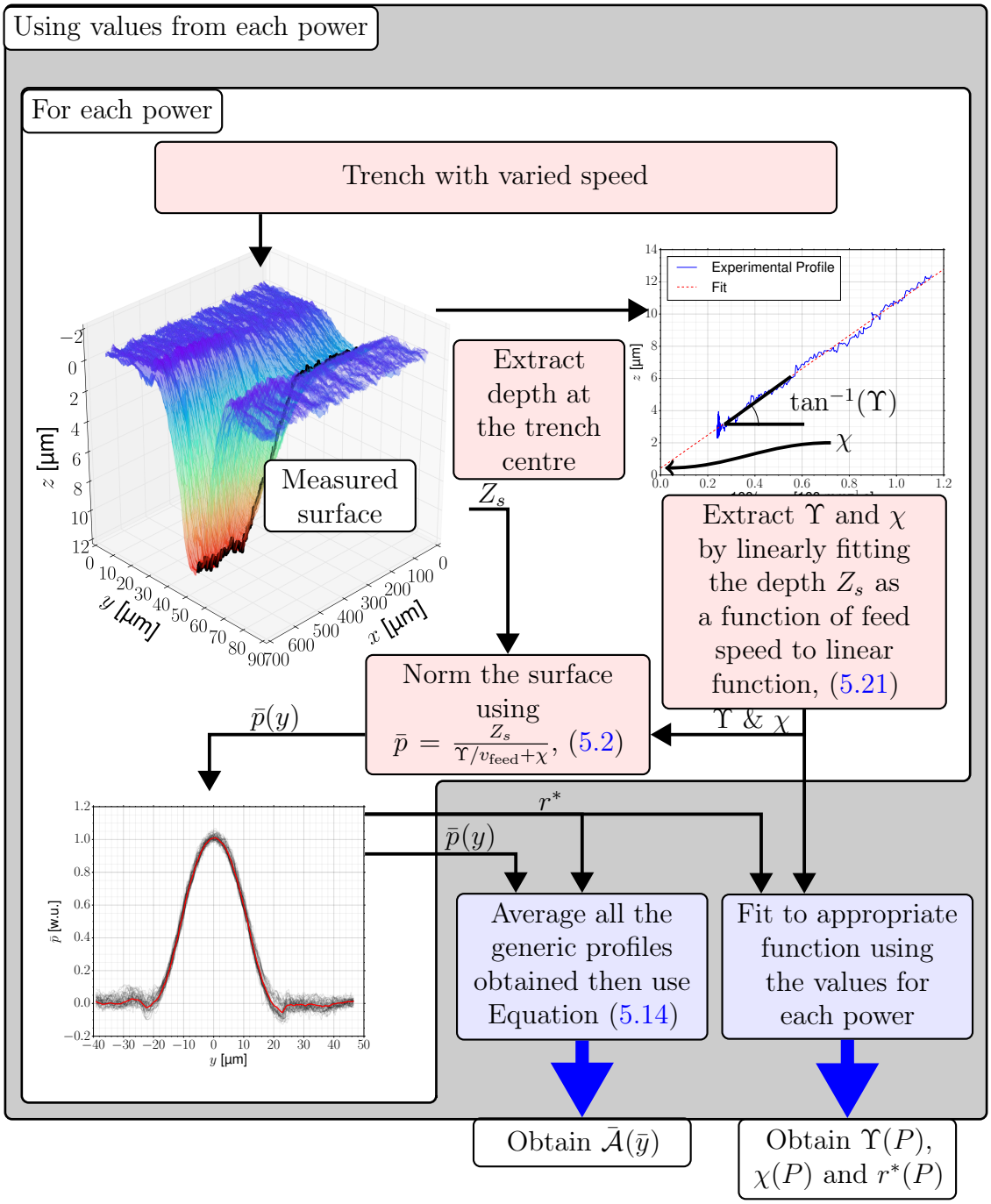

Figure 5.2 : Diagram of the calibration work-flow, the plot presented are an example of the calibration process for CMX850 at 8.07 W.

averaging the profile over 150 µm) extracted from the surfaces are analysed, compared with the simulations and the errors are calculated.

The errors have been evaluated as the relative error of the area of the

simulated cross section compared to the experimental value. One should bear in mind that, even if the feed speed is kept constant, there is variability in the material removal process along the trenches due to several factors: (i) variation of the pulse to pulse energy (ca. 5%); (ii) the feed speed variation along the path (ca. 3%); (iii) distribution of side-effect/surface defects (e.g. graphitic material for mechanical PCD, tungsten and cobalt for CMX850 and void distribution for graphite); (iv) errors in the flatness of the initial surface and roughness variation. Thus, the evaluation of the errors must be interpreted with caution because it is believed that a significant part of the error could be associated with the above-mentioned variabilities.

5.4 Experimental setup and measurement methods

The experimental setup used in the calibration and following tests for the model is the one presented in the Chapter 3.

For the purpose of validating the modelling framework, the model is calibrated and tested on three materials. The first material is an isotropic graphite, POCO AF-5, exhibiting small grain size of 1 µm and a void quantity of 20%. This material presents low recast material at the rim of the trench making it a good candidate for the validation of the modelling approach. The second material is a metal-diamond composite CMX850, with high wear resistance and strength due to the small diamond grain size and is widely used in micro-tooling [36]. CMX850 has a diamond grain (<10 µm) in a metal matrix of tungsten and cobalt. The last material is a CVD mechanical grade polycrystalline diamond (referred as mechanical PCD) used for manufacturing insets for turning [259] or for micro-tooling [29]. This material has a large grain size with graphitic phase present at the grain boundaries.

In order to avoid noise in the PLA trenches to enable accurate validation of the model, a smooth initial target surface is needed, so the roughness of the samples have been reduced by polishing if possible. For the graphite POCO AF-5, the samples have been manually polished; an R_a value of 50 nm has been achieved. In the case of CMX850 and mechanical PCD, the samples could not be manually polished due to the hardness of the materials; an R_a of 200 nm has been observed for these samples.

5.5 Results and discussion

The first subsection presents the calibration process step by step using the graphite POCO AF-5 as an example. Each step of the calibration is critically evaluated and the possible errors are discussed. Then, the model errors for each test are evaluated for the three materials and discussed in detail. Several examples of the machined surface are presented. The error tables offer a comprehensive view of the ability of the model to predict the resulting topography of PLA micro-machining.

5.5.1 The calibration method: example of graphite POCO AF-5

Calibration of the model requires a series of trenches with a specific feed speed variation along the trench at different levels of powers. The resulting trenches are scanned and then the depth at the centre of the trench is extracted, see Figure 5.3(a). As demonstrated, the depth measured at a certain position along the axis x, see Figure 5.1, is equal to the depth that a single trench at a constant feed speed will produce for a given power. The parameters Υ and χ of the linear fit are extracted by matching the depth and the feed speed using Equation 5.21, see Figure 5.3(b). This process is challenging

because the depth at the centre of the trench exhibits variation due to the errors of the process (as discussed in subsection 5.3); this is especially visible at constant feed speed when the depth at the centre of the trench has a near constant depth, see Figure 5.3(a). It should be noted that an error of 10-20µm in the positioning of the feed speed profile compared to the depth profile can introduce uncertainties of up to 5% in the value of linear fit. Once the positions of the two profiles are correctly aligned, it is possible to extract the values of Υ and χ at a particular power level, see Figure 5.3(b).

The calibration process can be repeated for as many power levels as necessary over the range studied; for graphite POCO AF-5, 8 different powers were used to calibrate Υ, χ and r^*. The values of Υ and χ as a function of the power are shown in Figure 5.4(b), 5.4(c). The next parameter to calibrate is the variation of the width of the profile, r^*, with respect to the power, see Equation 5.13. It is possible to extract the generic profile, $\bar{p}(y)$, of the trench once Υ and χ have been calibrated. The surface, shown in Figure 5.5, is obtained by normalising the depth of the trench along the path by $\Upsilon/v_{\text{feed}}(x) + \chi$ using Equation (5.21). It is apparent from Figure 5.5 that the calibration has been done correctly since the value at the bottom of the

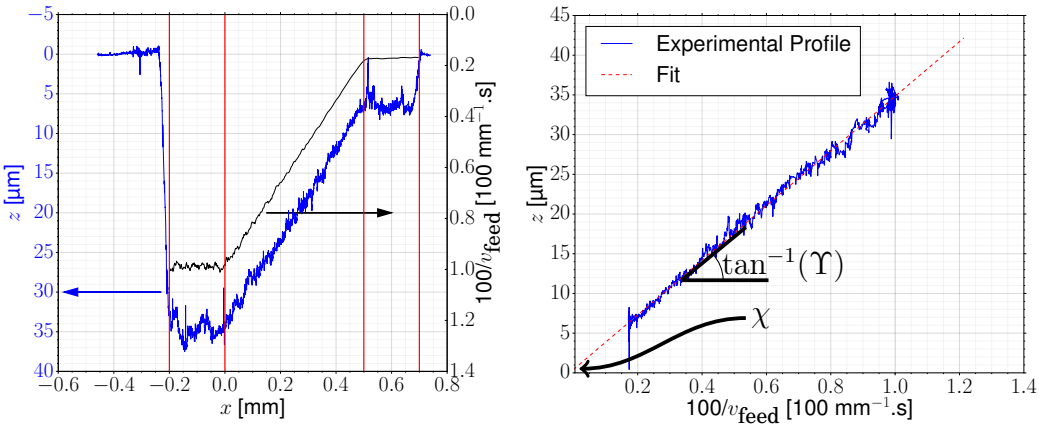

(a) (b)

Figure 5.3 : Calibration for graphite POCO AF-5 at 10.24 W; (a) Extracted profile along the trench, (b) fit of the depth as a function of the inverse of the feed speed by a linear function.

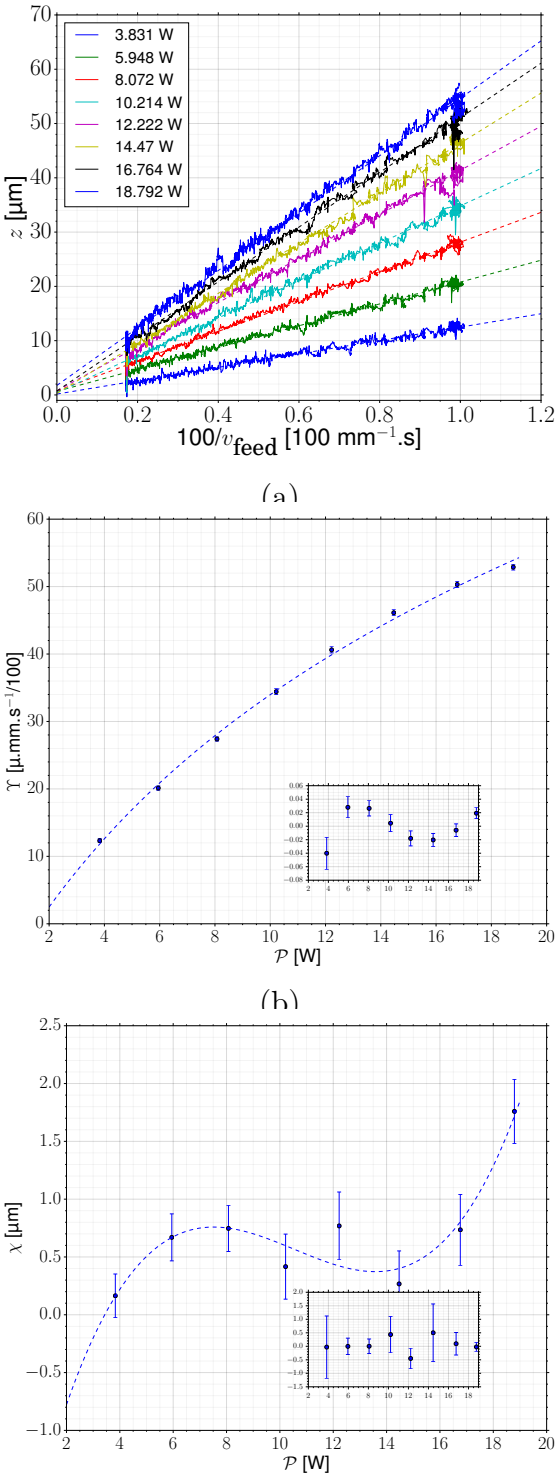

Figure 5.4 : (a), extracted profile along the trench for a range of power used in the calibration; (b), fit for Υ (the inset is the relative error of the fit in percentage); (c), fit for χ (the inset is the relative error of the fit in percentage).

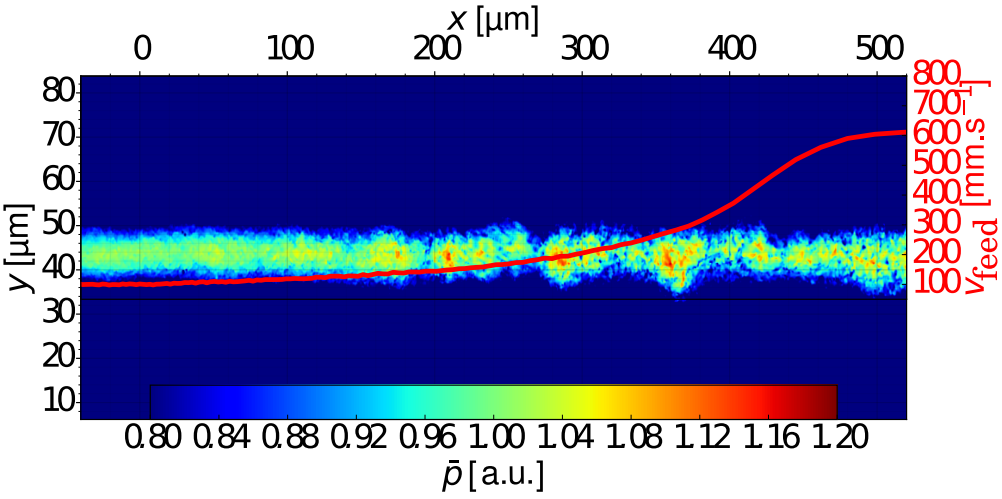

Figure 5.5 : Normalised surface using Υ and χ, see Figure 5.4 at 14.47 W on Graphite POCO AF-5.

profile along the trench is close to 1. The generic profile of the trench for this power is extracted by averaging the profiles along the path. This process is repeated for each power level.

The characteristic width of the profile, r^*, is obtained by measuring the distance from the centre of the profile to the position such that the value of the depth is less than 20% of the maximum depth. This threshold is chosen as a good trade-off between the noise caused by the initial surface roughness of the part and the acceptable measurement accuracy of the generic profile width.

In Figure 5.6, the width of the profile as a function of the power is presented. The profile extracted from the normalised surface, Figure 5.5, is presented in 5.7. It is clear that the shape of the generic profiles of the trenches for all powers and feed speeds are close and justifies the assumptions made in Equation 5.2 for the modelling of the PLA. The most striking observation to emerge from the Figure 5.7 is that, with the ranges of the tested parameters, the ablation rate does not depend on the slope of the profile. One might expect that the slope highly affects the ablation on the

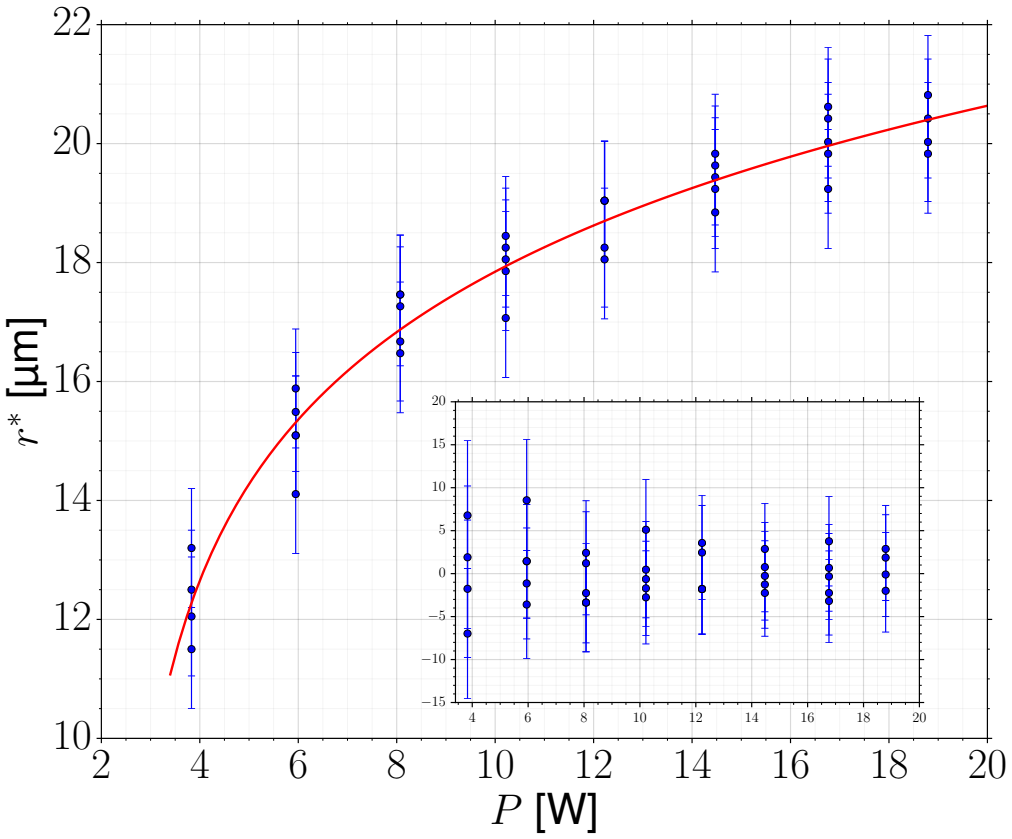

Figure 5.6 : Fit for r^* as a function of the power (the inset is the relative error of the fit in percentage)

side of the profile due to the increased surface of interaction leading to a reduction of the fluence. It is not the case for the ablation of trenches of the materials studied (graphite POCO AF-5, CMX850 and mechanical PCD), at least for a slope of the side of the trench lower than 75 °.

The simulation of the machining process for a laser beam requires the calculation of the generic ablation rate; this relates to Equation (5.1) and Equation (5.13). Knowing the generic profile, it is possible to obtain the generic ablation rate using Equation (5.14). A numerical inverse Abel transform [260] is used to calculate the generic ablation rate from the mean of the generic profile presented in Figure 5.7. The generic ablation rate, for graphite POCO AF-5, is presented in the Figure 5.8.

For graphite POCO-AF5, the model has been calibrated for a range of

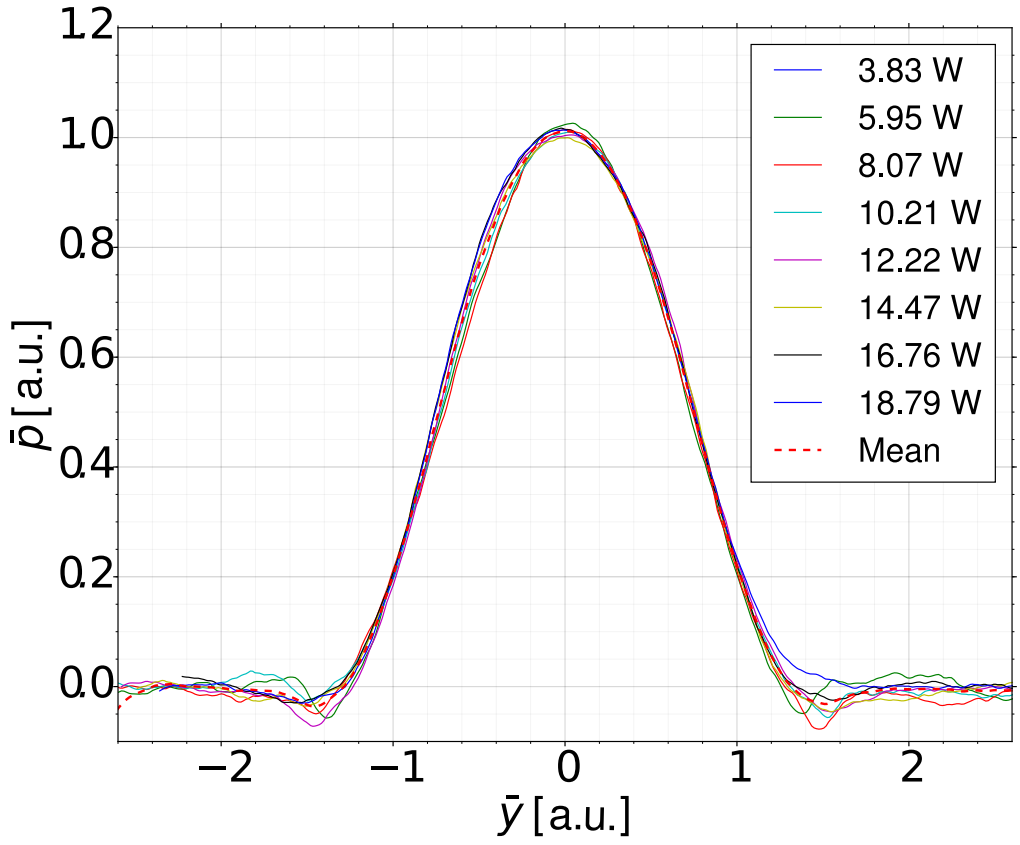

Figure 5.7 : Generic profiles of the trench for all the powers used in the calibration.

powers [4, 18.8] W and a range of beam feed speeds [100, 600] mm.s^{-1}. The model has also been calibrated for CMX850 and mechanical PCD for the power in a range of respectively [6, 18.8] W and [8, 18.8] W, for the beam feed speed in a range of respectively [100, 400] mm.s^{-1} and [100, 300] mm.s^{-1}.

The maximum range of calibration depends on the material properties and is determined by two criteria: (i) the feed speed cannot exceed a critical value for which separate pulses are observable; hence, not obtaining a trench (such that the bottom of the trench has a constant depth); (ii) a low feed speed generates a large amount of debris and thermal damage to the surface/target and should be avoided furthermore the slope of the trench ($> 70°$) and depth are too large for the measurement system used thus prone to measurement errors; (iii) the lower limit of the power is the ablation threshold of the

material. Thus, the model is aimed at the generation of acceptable micro-machining surfaces.

5.5.2 Single trenches with constant direction and beam feed speed

The error calculations are made using the method described in section 5.3. For graphite, CMX850 and mechanical PCD, the error tables are respectively presented in Table 5.1, 5.2 and 5.3. The maximum (Δ_{Max}) and average (Δ_{Avg}) errors are: Δ_{Max}=10% and Δ_{Avg}=4.11% for graphite, Δ_{Max}=8% and Δ_{Avg}=3.69% for CMX850 and Δ_{Max}=7% and Δ_{Avg}=4.81% for mechanical PCD. For the three target materials studied, the error values are scattered from 10% to less than 1% without revealing any evident pattern which

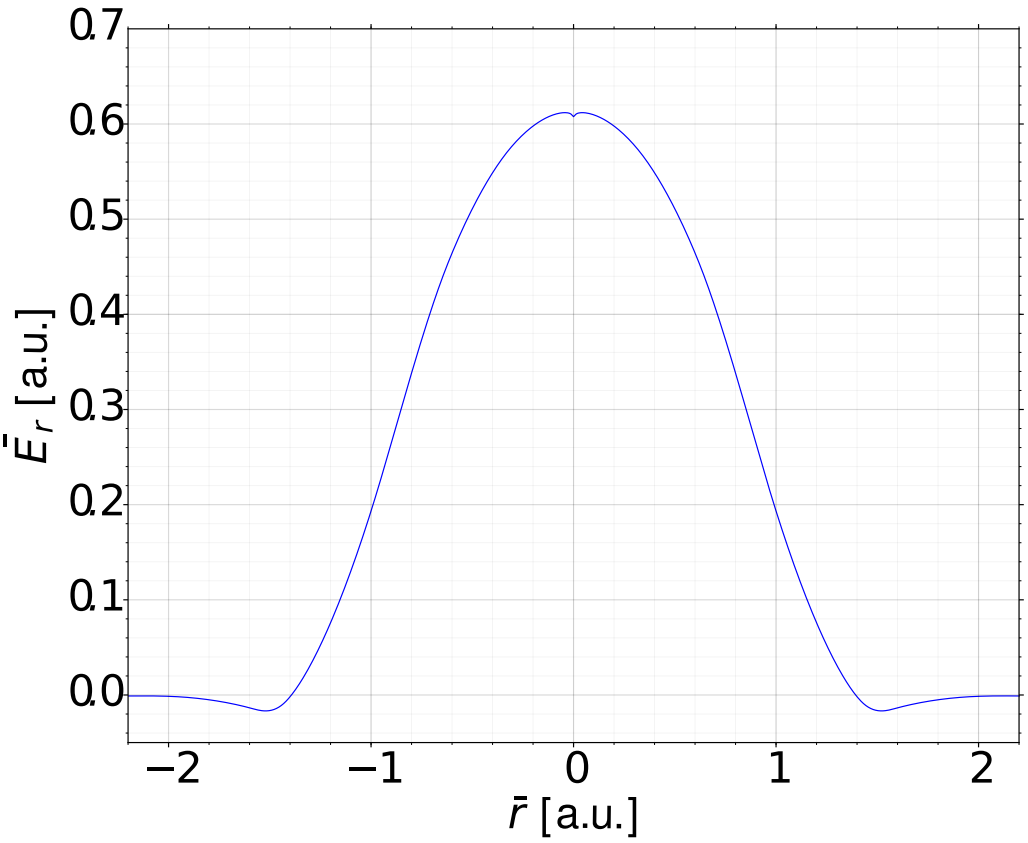

Figure 5.8 : The normalised ablation rate $\bar{\mathcal{A}}$ for the Graphite POCO AF-5.

suggests that their origin is variability in the process such as power variation, speed variation and porosity. Average error values for each material are lower than 5% giving a good indication that the model is in good agreement with the experimental results. Studying in detail the performance of the model for single trenches is key to ensuring the consistency of the following tests that show the performance of the modelling framework for real machining tests.

Table 5.1: Relative error in the area of the trench cross section for the Graphite POCO AF-5 for single trenches with a constant direction and value of the beam feed speed

Feed Speed [mm·s^{-1}]	Power [W]									
	2.6	3.77	5.04	6.27	7.45	8.62	9.85	11.1	12.02	15.95	17.97
	Relative Error [%]										
150	3.71	2.56	7.12	5.16	5.06	6.00	4.06	8.13	8.29	9.12	9.65
200	2.38	2.01	0.60	7.22	5.20	6.43	5.41	2.95	1.29	1.23	1.88
300	2.35	1.89	3.36	1.20	1.11	2.24	1.38	1.18	1.49	4.23	3.38
400	3.27	6.52	1.85	6.72	4.49	6.69	9.81	7.17	6.87	7.78	1.97
500	6.77	2.28	3.49	2.58	3.69	1.48	1.14	1.40	1.78	3.41	4.95
600	—	7.85	2.22	2.26	1.53	1.82	2.05	1.05	3.84	2.81	7.35
700	—	7.67	2.90	4.03	6.45	8.24	4.07	3.91	4.99	4.45	8.41

Table 5.2: Relative error in the area of the trench cross section for CMX850 for singles trenches with a constant direction and value of the beam feed speed

		Power [W]						
		5.95	8.07	10.12	12.22	14.47	16.76	18.79
		Relative Error [%]						
Feed Speed [mm.s^{-1}]	100	4.70	5.46	7.81	5.91	3.62	3.00	2.18
	150	3.82	2.98	1.27	1.49	3.45	3.02	1.79
	200	7.28	1.97	1.04	3.64	1.22	1.38	7.37
	300	2.28	1.23	2.37	5.18	2.64	1.69	8.69
	400	4.60	1.92	6.5	2.82	5.32	2.21	3.54

Table 5.3: Relative error in the area of the trench cross section for Mechanical PCD for single trenches with a constant direction and value of the beam feed speed

		Power [W]					
		8.07	10.12	12.22	14.47	16.76	18.79
		Relative Error [%]					
Feed Speed [mm.s^{-1}]	100	3.21	1.93	3.8	5.02	4.30	3.23
	128	5.89	5.60	5.49	6.07	3.39	4.13
	200	4.85	3.58	3.02	4.94	4.37	3.39
	300	—	3.5	2.71	2.46	1.87	1.55

5.5.3 Single trenches with constant direction and variable beam feed speed

The feed speed variation during laser machining affects the removal rate, therefore controlling the depth of the profile. To compare the model and experimental results, the depth at the centres of the profiles along the path are shown in Figure 5.9 and 5.10.

It is apparent from Figure 5.9 and 5.10 that the model is in excellent agreement with experimental tests for the three workpiece materials. The model does not take into account the variability of the process and therefore it predicts the local average depth that will be found without the roughness.

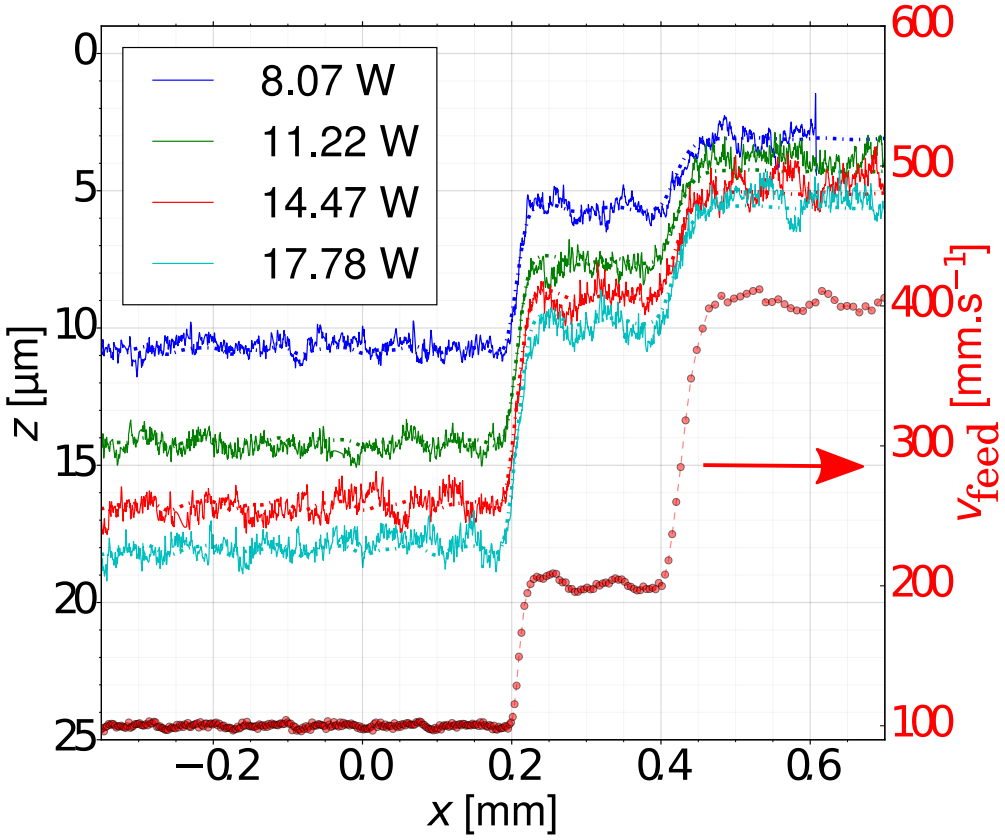

Figure 5.9 : Feed speed variation tests for CMX850. Solid line (-) experimental depth, dashed line (- -) simulation and red (-o-) measured feed speed.

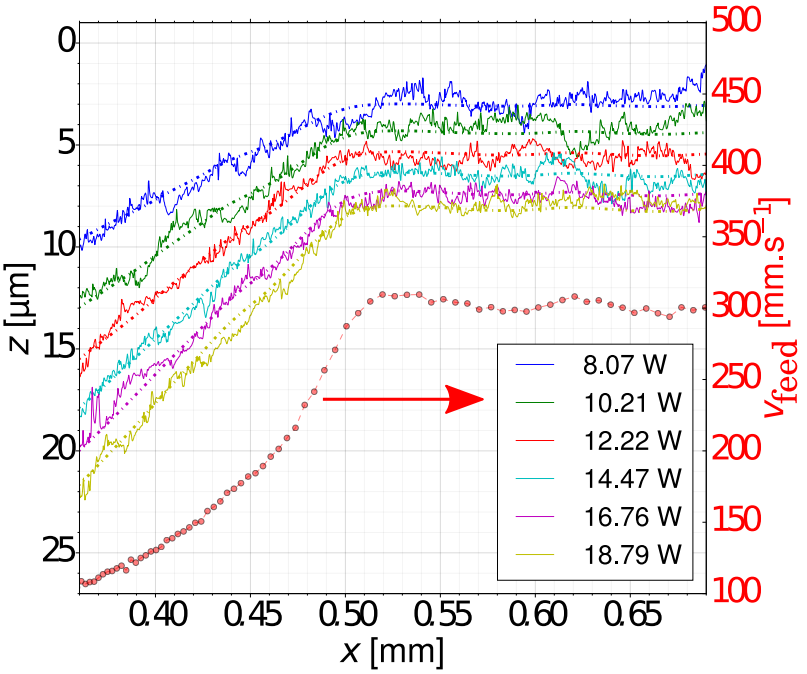

(a)

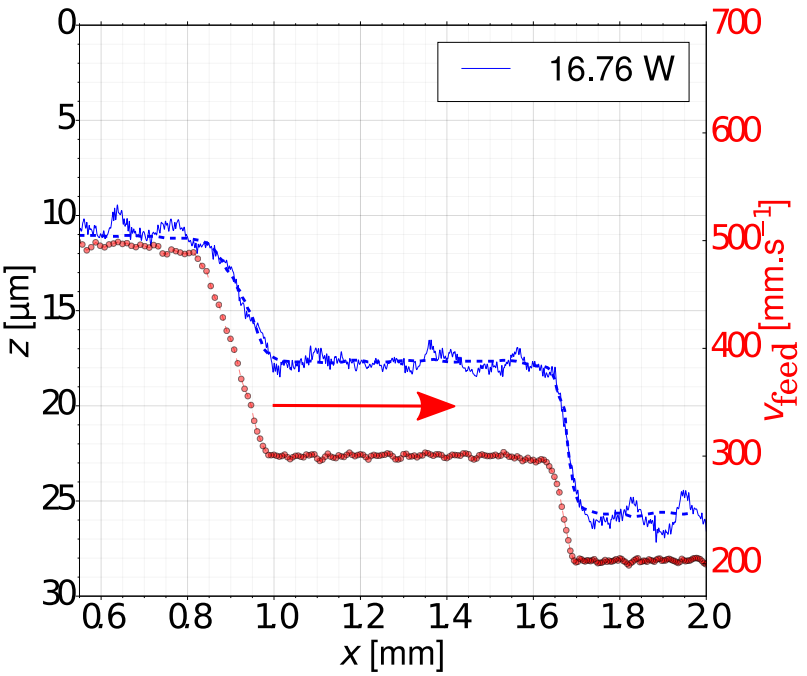

(b)

Figure 5.10 : Feed speed variation tests for (a) Mechanical PCD and (b) graphite POCO AF-5. Solid line (-) experimental depth, dashed line (- -) simulation and red (-○-) measured feed speed.

Interestingly, the experimental depths present some larger scale (depth $\geq$ 500 nm and length $\geq$ 100 µm) fluctuations along the trench. This suggests that the error variations, presented in Tables 5.1, 5.2 and 5.3, might come from intrinsic variability of from the process parameters and macro-micro geometry of the initial workpiece surfaces.

5.5.4 Overlapped trenches with constant direction and beam feed speed

Experiments to validate the model for overlapped trenches at normal beam incidence were carried out for several powers and feed speeds by varying the distance between the centre of the two trenches from 0 µm to a maximum of 60 µm while keeping feed speed and power constant. In Figure 5.11, four tests on CMX850 are presented at 14.47 W and 300 mm.s^{-1}.

The relative errors between the model and the experimental results are presented in Table 5.4. The model accurately predicts the results of overlapping trenches for graphite POCO AF-5, CMX850 and mechanical PCD. The results are particularly good for graphite POCO AF-5 and CMX850, with an error usually less than 5%.

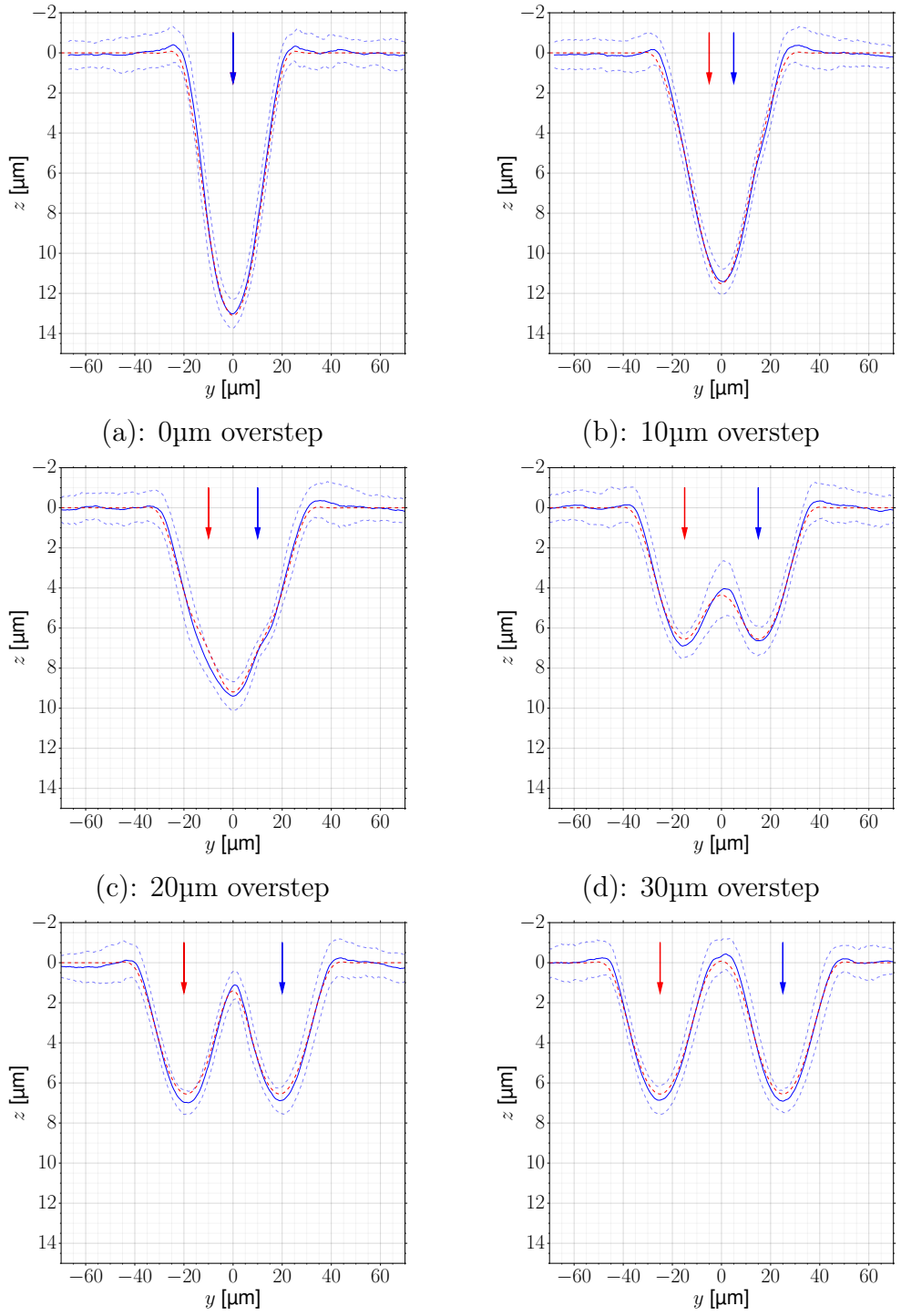

(a): 0µm overstep

(b): 10µm overstep

(c): 20µm overstep

(d): 30µm overstep

(c): 40µm overstep

(d): 50µm overstep

Legend:

Centre of the first trench
Centre of the second trench
Model Profile
Experimental profile
2σ variance of the experimental profile

Figure 5.11 : Overlapping cross sections for CMX850 for trenches at 14.47W and 300 mm.s^{-1} feed speed.

In the case of the mechanical PCD, the errors increase for high level overlapping (overstep $\leq$ 30 µm). This might be caused by variability of the laser operating parameters or inaccuracies in the measurement of the surfaces, but it is likely that a great part of them is related to non-linear effects that are not presently taken into account by the model. In this respect, it could be noted that for mechanical PCD, the absorption of the laser relies mainly on the presence of impurities, such as amorphous carbon, which exists between the diamond grains [261]. In effect, the absorption coefficient of pure diamond is lower than 1 m^{-1} whereas the graphite absorption coefficient is around 10^8 m^{-1}. Previous studies of pulsed laser ablation of diamond [28, 138] have shown that diamond ablation is always accompanied by the transformation of a diamond layer into graphite. Hence, diamond is metastable at ambient pressure and temperature; above 2000 °C diamond is transformed into graphite [155]. The creation of a thin graphite layer, after the first trench is machined, dramatically changes the optical properties of the superficial layer. Thus, the graphitised layer absorbs the energy of the laser much more efficiently and therefore, it reduces the fluence necessary to ablate the surface, see

Table 5.4: Relative error in the area of the trench cross section for overlapped trenches for the three materials

		Overstep distance [µm]						
		0	10	20	30	40	50	60
		Relative Error [%]						
AF-5	18.97 W 200 mm.s^{-1}	3.78	4.15	2.77	1.58	4.56	5.89	4.73
CMX850	14.47 W 300 mm.s^{-1}	4.38	4.03	3.16	5.18	2.52	5.78	—
CMX850	18.79 W 200 mm.s^{-1}	2.68	4.83	4.91	7.87	3.02	5.14	—
Mech. PCD	18.79 W 150 mm.s^{-1}	—	3.92	9.8	6.79	7.74	4.83	—
Mech. PCD	14.47 W 300 mm.s^{-1}	9.4	9.8	7.11	6.36	5.87	1.36	—

Figure 5.12. After the first few pulses, a thin graphite layer is created and maintained by the subsequent ablation.

The model takes into account the low absorption of the first pulses and does not exhibit significant errors for single trenches. However, when mechanical PCD is the workpiece material, if the beam passes over an area already ablated, the first few pulses will be much more effective than a surface free of graphite, see Figure 5.13. Currently, the model does not take into account changing material properties after the first pass and consequently, it under-predicts the removal of material. However, the side of the trench is accurately predicted and proves that the model is still behaving correctly outside of the affected area, see Figure 5.13. This phenomenon will only occurs at the start of the machining process; once the laser has passed over the whole workpiece the ablation should be homogeneous. Therefore, it is possible to develop a two steps machining (i) ablate lightly the whole workpiece with the near infra-red laser and (ii) carry out the machining task

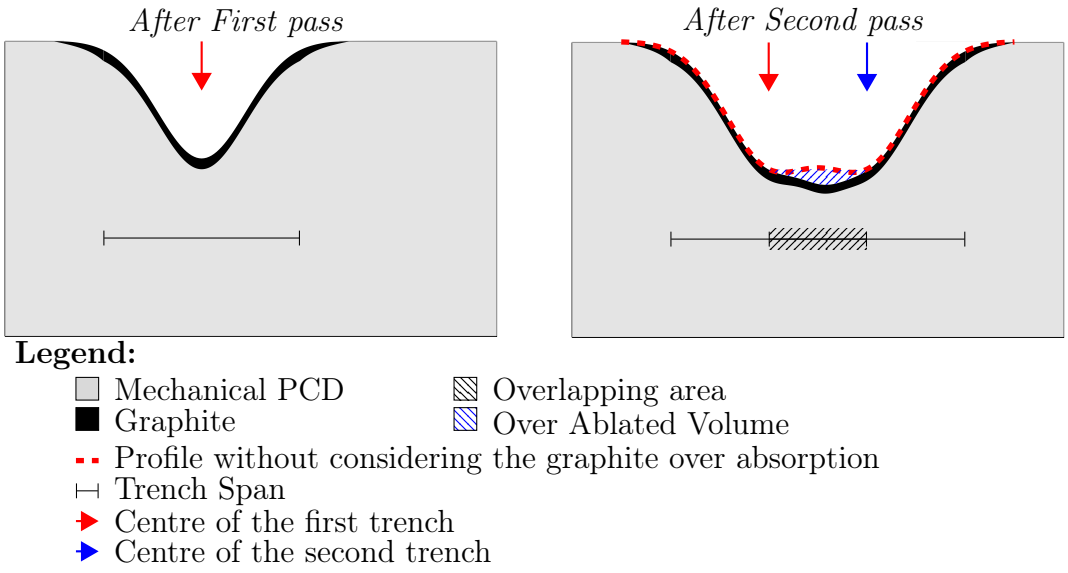

Figure 5.12 : Scheme of the ablation pattern (creation of a small graphite layer) in the case of mechanical PCD during the overlapping of two trenches.

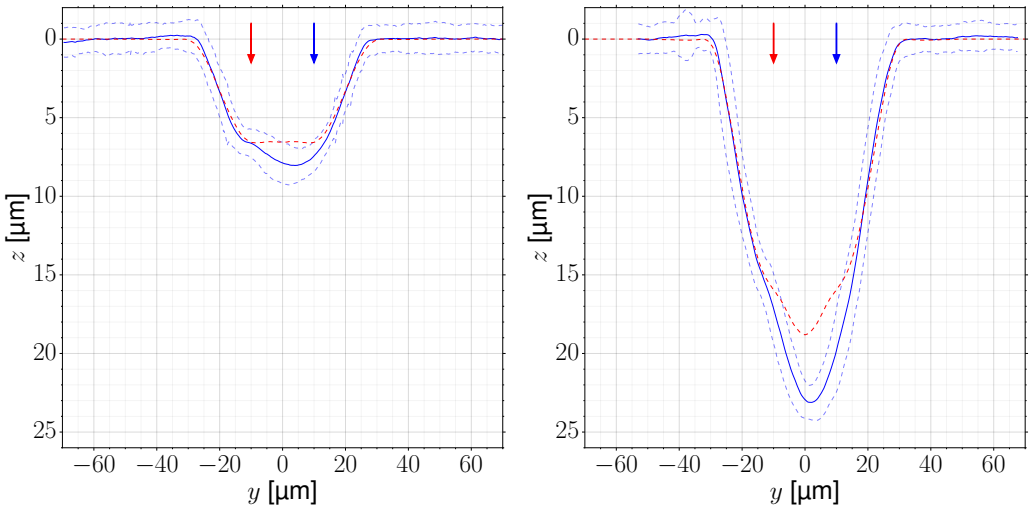

Figure 5.13 : Overlapping test for mechanical PCD:(a) cross section at 14.47 W and 300 mm.s^{-1} with 20 µm between the centre of the two trenches. (b) cross section at 18.79 W and 150 mm.s^{-1} with 20 µm between the centre of the two trenches.

on the uniformly ablated surface. The model will have to be recalibrated for the lightly ablated surface but should give good results. This method is currently being investigated.

5.6 Free-form surface with constant overlapped between two trenches

Finally, the model is tested against three free-form shapes. The three different free-form shapes have been chosen to test different aspect of the model. The first free-form surface is a "simple" pattern consisting of several pillars with different gradient for each direction, see Figure 5.14. The second tests is a free-form surface with continuous slope variation. Furthermore, the results does not present any specific pattern that can be average, thus representing a closer results of the real machining result for free-form surfaces, see Figure

5.16. The last tests is designed to test the model against step variation of the depth in the direction of the laser machining and perpendicular to the laser machining, see Figure 5.18. The choice of beam path for the generation of the free-form surface use the classical raster paths technique is parallel straight line paths in the x-direction with constant overlap in the y-direction with a variation of the speed along the x-direction to vary the amount of material removed. The generation of complex surfaces with an optimization algorithm is a hard optimization problem. For the examples provided in this section, the speed used for the machining is directly interpolate from the maximum depth of the trench for a chosen power. The power of the laser is kept constant during the whole machining.

5.6.1 Simple 3D shapes

The "simple" free-form surface is made of several pillars next to each other. The result of the simulation and the experimental result for the "simple" 3D shape is presented in Figure 5.14 (a) and Figure 5.14(b) respectively. The numerical model is closely following the experimental results, see Figure 5.15. Similarly to the error from the previous tests, the error is mainly generating do to variation of the material removal or material internal variation. Interestingly, the model and the experimental results present errors around high variation of depth in the x-direction suggesting that the error is coming from a poor control of the speed.

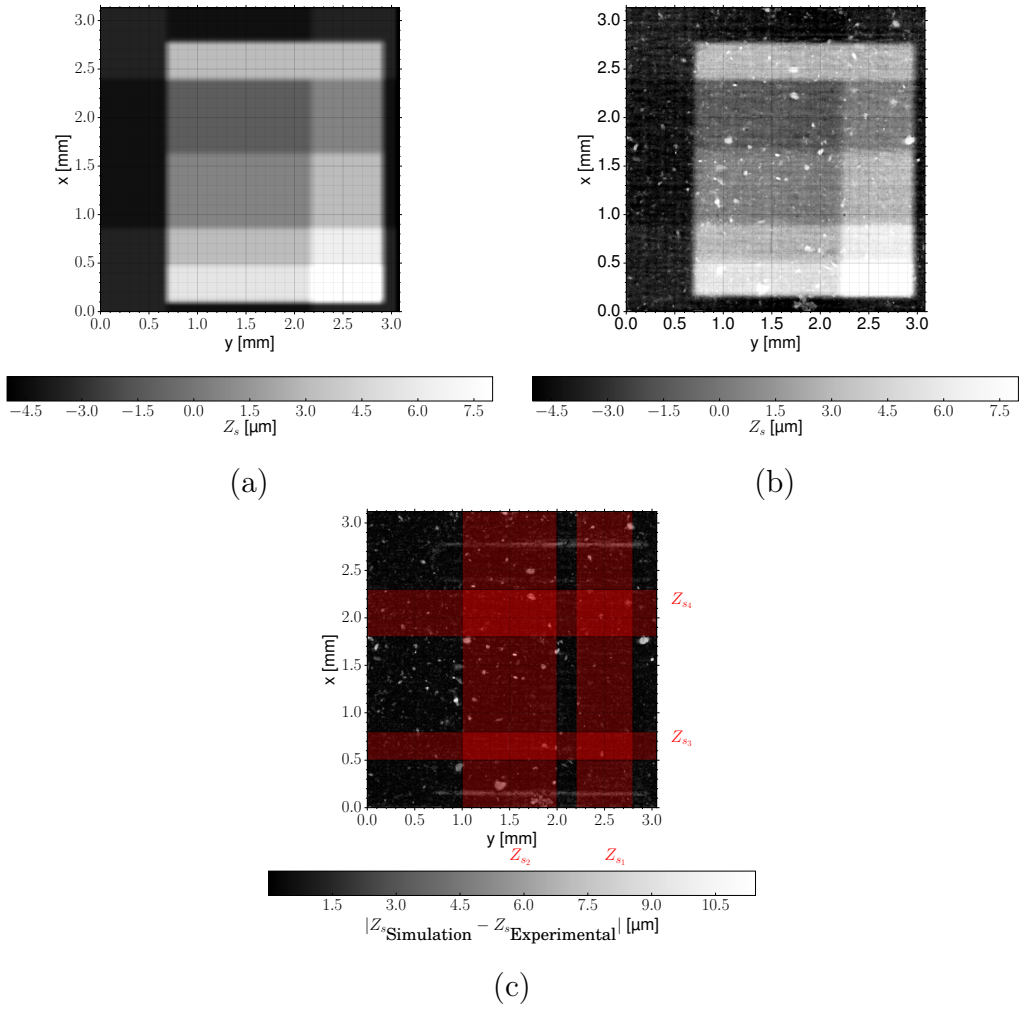

Figure 5.14 : The simulated depth (a), the experimental depth (b) and the absolute error between the experimental and simulated results (c).

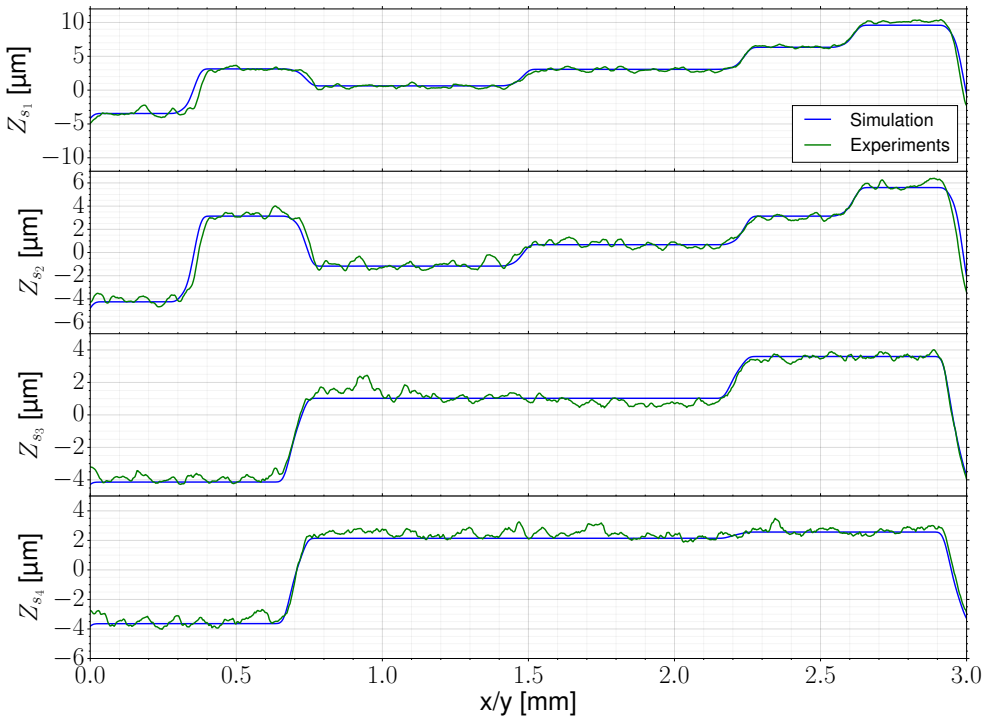

Figure 5.15 : The depth from the simulation and the average of experiments over different sections of the surface presented in the Figure 5.14 (c)

5.6.2 Freeform with smooth transition

The following test is made from a picture converted to depth using the intensity value, see Figure 5.16. The comparison between the model results and the experimental result shows that the model predicts correctly the depth, see Figure 5.17. The error for each profile is mainly coming from the roughness generated in the ablation process.For the free-form tests, the error is mainly due to the presence of dust or uncontrolled variation of the machining parameters (e.g. pulse-to-pulse energy, feed speed) and the presence of dust. Without considering the area affected by previously described defects, the model shows good agreement with the experimental results. The variation in the surface depth are properly predicted, see Figure 5.17.

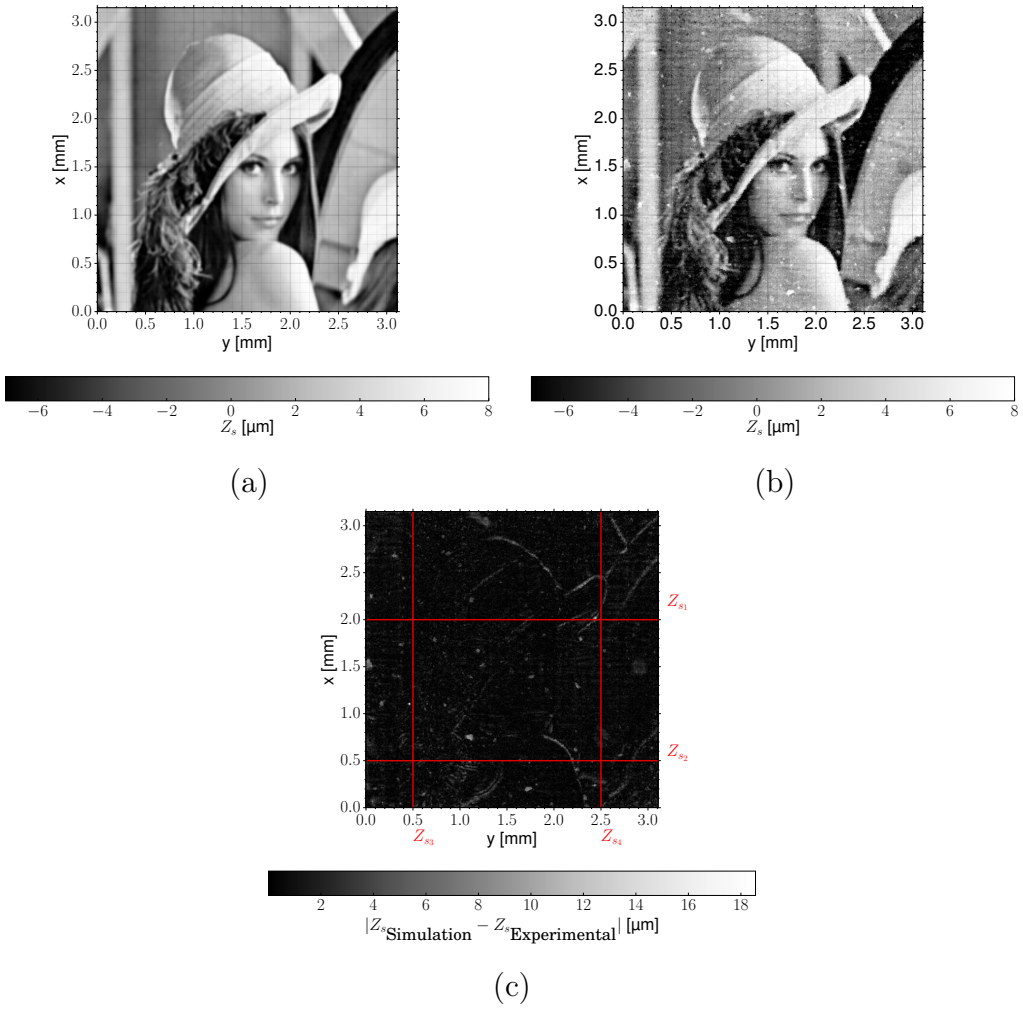

Figure 5.16 : The simulated depth (a), the experimental depth (b) and the absolute error between the experimental and simulated results (c).

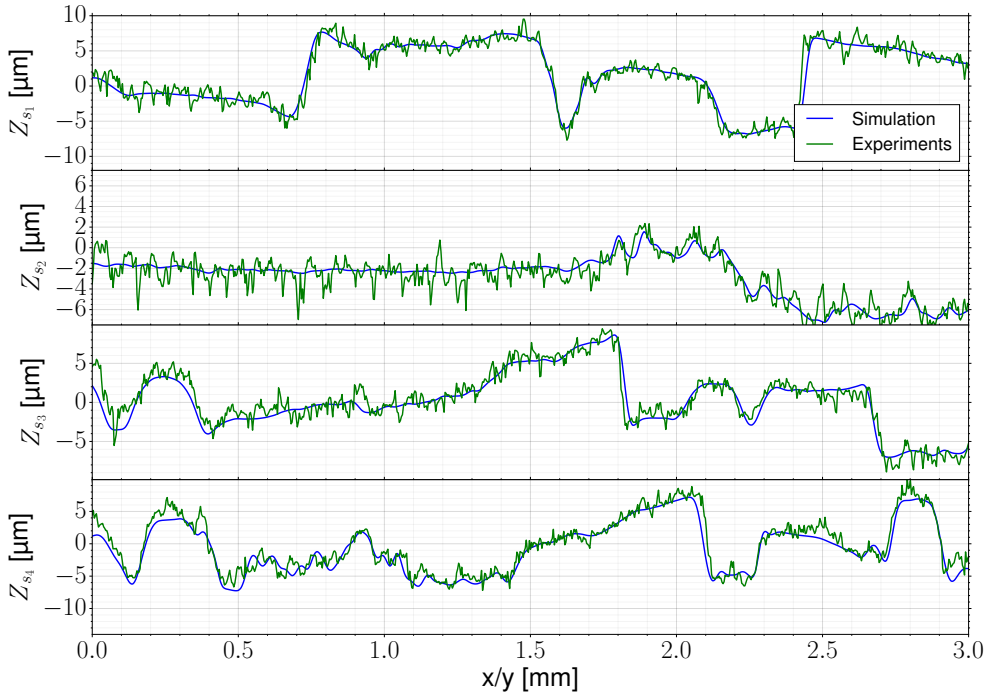

Figure 5.17 : The depth from the simulation and the experiments for different sections presented in the Figure 5.16

5.6.3 Freeform with discontinuous transition

The following test is made from a picture converted to depth using the intensity value, see Figure 5.18. The same conclusion for the previous test can be drawn. It must be noted that error is also present around high slope areas, suggesting that the error is due to reliability of the galvanometers to control the speed correctly during high accelerations. It is also interesting that the profile can follow pattern that have a similar size or lower than the size of the laser spot, see Figure 5.19 for the profile Z_{s_1}.

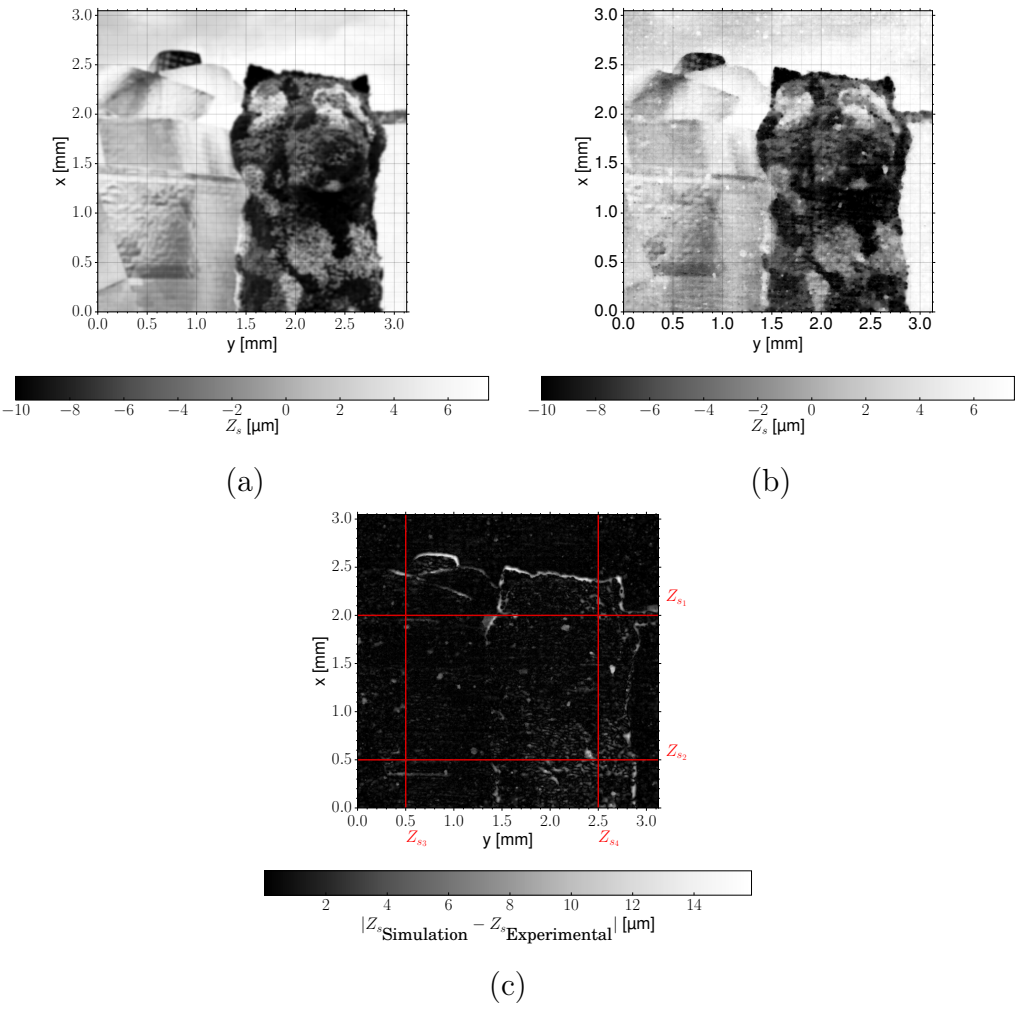

Figure 5.18 : The simulated depth (a), the experimental depth (b) and the absolute error between the experimental and simulated results (c).

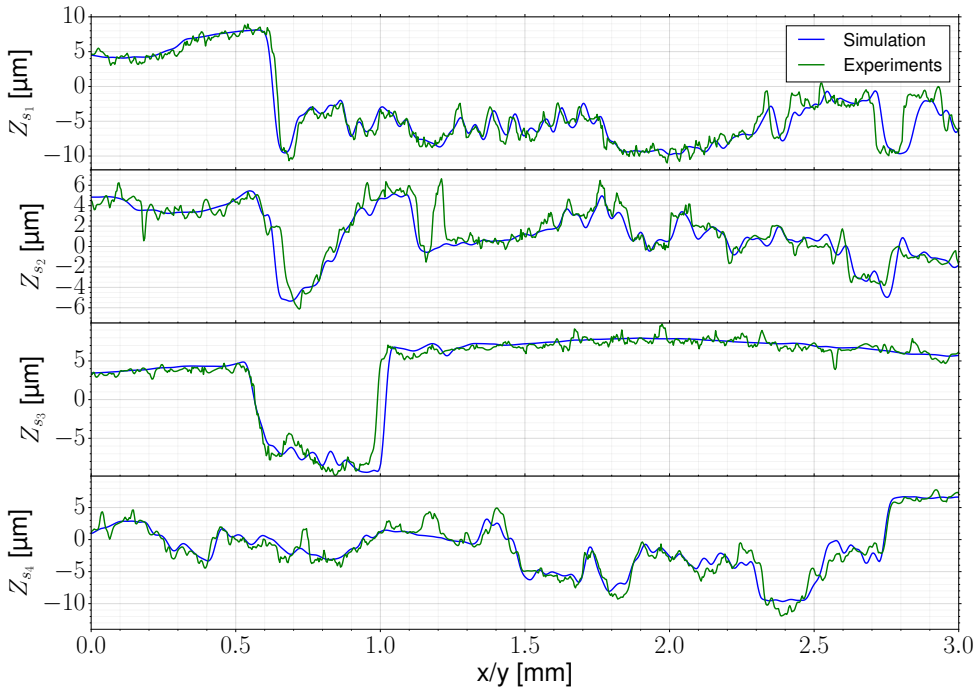

Figure 5.19 : The depth from the simulation and the experiments for different sections presented in the Figure 5.18

5.6.4 Discussion on the source of errors

There are multiple sources of error associated with the experimental data and modelling results. Experimental results show high frequency variation compared to the modelling results, see Figure 5.17. The high frequency variation might be due to the porosity of the material used in the tests (graphite POCO AF-5) which is not taken into account in the model. This also presents large positive errors that span several laser passes, see Figure 5.16(c), Figure 5.14(c) and Figure 5.18(c). It is likely that errors are due to the redeposition of ablated material and dust over the already ablated material. Finally, errors are also present in areas of large depth variation. In this case, the error is due to failure of the galvanoscanner to follow the speed profile accurately, leading to a delay in the depth jump.

5.7 Conclusion

This chapter has proposed and validated a new modelling framework for pulsed laser ablation. The comprehensive and innovative research approach used in this study allows the characterisation of the material removal (i.e. prediction of the single/overlapped trenches) for the pulsed laser ablation process, a crucial first step on the path to support the generation of free-form surfaces. In this respect, the main contributions of the chapter are as follows:

- The model distinguishes itself by being able to be calibrated using trenches thus, contrasts with previous modelling approaches use single craters and the calibration is therefore prone to error for a few pulses, due to variability in the crater shape and depth. Furthermore, the interaction between consecutive pulses is implicitly taken into account as the proposed model uses continuous trenches for its calibration. The depth variation of the trenches with feed speed shows that consecutive

pulses interact with each other and slightly enhance the ablation. This work presents conclusive evidence of the model capability to predict the shape of overlapped trenches and large scale machining of several millimetres, with average error lower than 5% for a wide range of machining conditions. Finally, the use of trenches for the model calibration leads to a simpler and more accurate calibration procedure compared to previous approaches.

- The modelling framework also highlights interesting ablation mechanisms. The evaluation of the spreading of the pulse (and a reduction of the fluence) due to the slope of the surface is a common feature added to pulse-by-pulse previously developed models. Experimental results presented in this work show that the profile of all the trenches has the same shape for the same power (they are related by a linear function that is proportional to the amount of dwell time at the local position). Therefore, the local slope does not seem to be important (up to a certain angle) during the ablation process. A quick calculation shows that for an angle higher than 40°, the spot spreading reduces the amount of fluence received at the local surface by around 40%. If the local angle during the ablation process is important, the trench should present a clear variation in the profile, especially for the high power and low speed. However this is not the case, therefore one can rule out a simple direct relation between the local fluence and the amount of ablated material for the tested materials. It must also be noted that the amount of ablated material during the ablation throughout the trench is not perfectly linear due to the interaction between pulses ($\chi \neq 0$). The amount of material ablated during the overlapping of trenches is linear and the local angle (up to a certain angle) does not seem to affect the amount of ablated material. It is possible to understand these results

by taking into account that the evaporation of the material is a purely superficial phenomenon. Therefore, an increase in the surface area facilitates the evaporation of the material. The previous approaches (pulse-by-pulse evaluation) failed to take into account the increased surface area available for evaporation and underestimated the depth after the ablation especially for steep slope.

- The model enables the generation of free-form features in a controlled and repetitive manner without lengthy and costly experimental trials. The model is computationally inexpensive, less than 10 seconds to simulate the processing of one mm^2 surface, and accurate, less than 5% error on average; it can be used as a tool to pre-compute and optimise the beam path and also as an online prediction tool in association with inline measurement systems. It represents a significant development in pulsed laser machining and allows the development of specialised CAD/CAM software for the automatic planning and optimisation of the beam path and processing parameters such as presented for abrasive water-jet machining [262].

- This modelling framework is the first step towards a numerically inexpensive generic model for pulsed laser ablation because it requires only a limited number of experimental trials to calibrate the model for any material and machining system. Furthermore, the modification of the ablation rate by various correction factors driven by experimental observations could further enhance the accuracy of the prediction and introduce the variability of the machining process [176].

The findings reported in this chapter suggest that the framework can be applied to a wide range of materials. Further experimental investigations are needed to establish the capability of the model for a broader range of

materials such as metals or ceramics.

Chapter 6

Experimental investigation of crystalline structure due to phase transition

This chapter provides a detailed description of the work carried out to investigate the effect of the pulse laser on the crystalline structure of the target. For this purpose, Raman spectroscopy and TEM analysis are used to experimentally characterise the micro-structure of the diamond transformed into graphite. Furthermore, a plasma model is developed to improve the understanding of the melting process during the ablation with an extensive discussion of the implications of the observed finding with the modelling results. The chapter provides an understanding of the material response to the laser informing the material damage induced by the graphitisation.

6.1 Introduction

The study of pulsed laser ablation using single pulses would be able to provide an insight into the graphitisation and the growth of the graphitic layer with the possible melting or disorder generation of the material at the surface. However, studies focussing on the crystalline structure of the carbon for a wide range of laser fluence seem to be scarce, see Chapter 2.2. Although the investigation of the micro-structure resulting from the ablation could provide insights into the phase transition and the thermal balance during pulsed laser ablation of diamond, it does not provide enough information about the temporal behaviour of the material to the pulsed laser. The profound understanding of the physical phenomena during nanosecond pulse laser ablation is usually done using model due to the complex and intertwined phenomena that are difficult to observe experimentally.

Thus, in this chapter micro-structure investigations are used to further constrain the model that is used to simulate the behaviour of the material to the thermal load. There are few studies modelling the graphitisation of diamond. Previous studies of pulsed laser ablation of diamond demonstrate that graphitisation is mainly a thermal process for nanosecond pulsed laser ablation [28, 138]. The Chapter 4 presents the dynamics of the interfaces (graphite and diamond and graphite and air) have been taken into account in the pulsed laser ablation of boron doped diamond. This study provides particular insight into the generation of the graphite layer for low fluence. Although accurate for the position of the surface for a wide range of fluence, the study does not provide experimental information about the position of the interface between graphite and diamond. Furthermore, the plasma absorption is not taken into account and the model has limitation to accurately predict the position of the surface for fluence higher than 60 J.cm^{-2}.

The work described in this chapter is focused on the investigation of the carbon crystalline structure resulting from the nanosecond ablation of Boron doped diamond. To support the understanding of the observed phase transformation phenomena, a model for the laser ablation of diamond is developed considering the heating of the diamond, the graphitisation and the vaporisation at the surface coupled with collisional-radiative model for the plasma absorption of the laser pulse. The predictions are validated against the position of the interfaces (vacuum/graphite, graphite/diamond and position of the melting line) and the allotropes of carbon observed experimentally.

6.2 Theoretical Background

During the pulsed laser ablation, the target material is heated from a solid at ambient temperature to a plasma with a temperature above the critical temperature. Thus, the full system requires the consideration of the conservation laws of mass, momentum and energy within one single computational domain for all phases involved. This can be accomplished using an equation of state (EOS) to properly close the system of equations describing the conservation laws which connects the thermodynamic state functions of the material such as the pressure, temperature, density or internal energy. However, this method is often cumbersome due to a lack of appropriate equations of state covering the whole range of density and temperature [23] occurring during the ablation of material using nano-second pulsed laser ablation [30]. Therefore, the plume part (the vapour and plasma phase) of the model is usually split from the solid and liquid phases due to the plasma ionisation and non-local thermal equilibrium of the plasma. The plasma is commonly considered to follow an ideal gas-like law EOS [23, 30, 125]. Typically, the plasma is assumed to Boltzmann-Saha equilibrium and making use of the

local thermodynamics equilibrium (LTE) hypothesis [30, 263] which assumes that locally the species possesses the same temperature and the electronic level distribution is dominated by the collisional processes. It has been shown that this assumption does not properly describe the initial non-equilibrium plasma formation, for which the radiative processes dominate [23, 120]. In this study, the plasma processes are described using a Collisional-Radiative model that considers the elemental interactions between electrons and heavy species [23], thus the collision radiative model enables a detailed description of the atomic processes. In this work, the solid (diamond and graphite) and liquid (liquid carbon) phases are considered as a one dimensional target while the plume is treated as an expanding cell using spatial average properties. The solid and liquid phases are well approximated by a one dimensional target since the thermal penetration depth is at least one order of magnitude smaller than the laser spot size on the target [2]. The temporal evolution of the target can be separated into distinct phases. The first phase is governed by the heat diffusivity of the diamond and the heat input from the laser. The diamond surface is heated over the graphitisation threshold, thus a thin layer of graphite is transformed into graphite. This layer greatly reduces the light absorption coefficient of the target, thus most of the energy is deposited at the surface. The surface layer is quickly heated above the ablation threshold, and evaporation starts once the vapour pressure reaches ambient pressure. A plume of hot carbon gas is formed over the crater and, if the laser intensity is large enough, the plume breaks down into an ionised plasma leading to the total absorption of the laser energy into the plasma. The target is shielded from the laser intensity, however the large energy input into the plasma generates a highly ionised, hot plasma that emits energy back to the target via radiative recombination and thermal Bremsstrahlung. Finally, the plasma expands rapidly, losing the capability to emit via radiative recombination

significantly. The target also cools down due to internal heat diffusivity.

6.2.1 Target modelling

The target is modelled as a two layer system based on the conservation of mass an energy to take into account graphitisation during laser irradiation. The subscripts d and g are respectively used for the material properties belonging to the graphite and the diamond, while the position of the surface is denoted as z_1 and the position of the graphitisation front is denoted as z_2.

The density jump at the graphitisation front interface induces an outward displacement, or swelling, of the graphitised surface. Mass conservation at the graphitisation front interface leads to:

$$v_{\text{swelling}} = \frac{\rho_g - \rho_d}{\rho_g} \partial_t \left\{ z_2 \right\}, \tag{6.1}$$

where ρ is the density of the material and v_{feed} is the speed induced in the graphite due to the density jump at the graphitisation front. The conservation of energy in the graphite leads to, using (6.1),

$$\rho_g c_{p_g} \left(\partial_t \left\{ T_g \right\} - v_{\text{feed}} \partial_z \left\{ T_g \right\} \right) = \partial_z \left\{ \kappa_g \partial_z \left\{ T_g \right\} \right\} + S_g, \tag{6.2}$$

with c_p, κ, T, and S being specific heat of the material, thermal conductivity, temperature and the heat source induced by the laser respectively. Similarly, the energy conservation for the diamond leads to

$$\rho_d c_{p_d} \partial_t \left\{ T_d \right\} = \partial_z \left\{ \kappa_d \partial_z \left\{ T_d \right\} \right\} + S_d. \tag{6.3}$$

The system is closed by the Stefan condition at the graphitisation front,

$$\kappa_g \partial_z \left\{ T_g \right\} |_{z=z_2} - \kappa_d \partial_z \left\{ T_d \right\} |_{z=z_2} = \partial_t \left\{ z_2 \right\} \rho_d \Delta h_{d-g}, \tag{6.4}$$

with Δh_{d-g} the creation of enthalpy at the graphite-diamond interface

$$T_g|_{z=z_2} - T_d|_{z=z_2} = 0 \tag{6.5}$$

where $T_{\text{interface}}$ is the temperature at the interface between diamond and graphite. The graphitisation front unlike phase change is not reversible with a decrease of temperature thus it has been modified to account for this fact and follows Arrhenius law [157], hence the speed of graphitisation front cannot be negative and is calculated using the Arrhenius law,

$$\partial_t \{z_2\} = C_r \exp\left[\frac{-\mathtt{E}_a}{\mathfrak{R} T_{\text{interface}}}\right], \tag{6.6}$$

with C_r and $\mathtt{E}_a$ being respectively a constant representing the rate of transformation between graphite and diamond, and the activation energy for the transition between diamond and graphite. The domain used to calculate the solution is finite, and an adiabatic boundary condition is applied at the end of the domain, $x_{\max}$, so that

$$\left[\kappa_d \partial_z \{T_d\}\right]|_{z=z_{\max}} = 0. \tag{6.7}$$

The value of $z_{\max}$ is chosen such that the temperature at the end of the simulation does not exceed 350 K. At the surface, the boundary condition is controlled by evaporation coupled with the plasma model. Thus, the energy balance at the irradiated surface is

$$\kappa_g \partial_z \{T_g\}|_{z=z_1} = F_{\rho e,\text{surface}}, \tag{6.8}$$

where $F_{\rho e,\text{surface}}$ is the flux of energy at the interface between the target and the plume. The relation between the rate of evaporation and vapour pressure

is calculated using the Knudsen-Knight jump relation [90]. The position of the interface between graphite and vacuum is determined by

$$\partial_t \{z_1\} = v_{\text{feed}} + v_a. \tag{6.9}$$

with v_a being the speed of ablation. Finally, a front fixing method [223] is used to map the domain of solution to a field domain which is more convenient for numerical solution.

with v_a being the speed of ablation.

The initial temperature for the target domain is 300 K. At the start of the interaction, the laser deposits energy directly into the diamond, so only the equations for the diamond is solved. Then, the surface temperature in the diamond increases until the total thickness of the graphite layer calculated using the Arrhenius law reaches the thickness of two graphene layer and a thin layer of diamond is numerically transformed into graphite [2]. Afterwards, the system of equations for the target is solved and the surface and graphitisation front position evolve according to Equation (6.4) and Equation (6.9). The material properties used to simulate the response of the target to the incoming laser pulse are as in Chapter 4.

6.2.2 Boundary conditions at the surface and Knudsen layer

The rapid evaporation or condensation during the nanosecond pulsed laser ablation leads to a strong vapour motion that is not in equilibrium. The phase transformation at the interface between the liquid and vapour depends on surface temperature and ambient pressure. It occurs in a thin layer (a few mean free paths) known as the Knudsen layer that describes the transition from a thermal and kinetic non-equilibrium to a Maxwell-Boltzmann equilibrium

distribution for the vapour particles. Thus, a consistent connection between the target surface under high thermal load (vaporisation/condensation) and the plume domain is ensured. The Knudsen layer can be described using a variety of models [90–93]. The approach developed by Knight et al. [90] is particularly adapted to the present study since it treats the evaporation in an ambient environment. The Knudsen layer is treated as a gas dynamic discontinuity [90] for which analytical expressions are derived that link the temperature, pressure, density and velocity along both sides of the Knudsen layer. The equations governing evaporation are:

$$\frac{T_K}{T_{\text{surface}}} = \left[\sqrt{1+\frac{\pi \mathsf{m}^2}{4}\left(\frac{\gamma-1}{\gamma+1}\right)^2} - \frac{\mathsf{m}\sqrt{\pi}}{2}\frac{\gamma-1}{\gamma+1}\right]^2 \tag{6.10}$$

with T_K, m, γ being the temperature outside of the Knudsen layer, the reduced Mach number and the ratio of specific heats (for a mono-atomic gas $\gamma = 5/3$). The ratio of density at the Knudsen discontinuity is equal to,

$$\begin{aligned}\frac{\rho_K}{\rho_S} =& \sqrt{\frac{T_{\text{surface}}}{T_K}}\left[(\mathsf{m}^2+1/2)\exp\left[\mathsf{m}^2\right]\operatorname{erfc}\left[\mathsf{m}\right] - \frac{\mathsf{m}}{\sqrt{\pi}}\right] \\ &+ \frac{1}{2}\frac{T_{\text{surface}}}{T_K}\left[1-\mathsf{m}\sqrt{\pi}\exp\left[\mathsf{m}^2\right]\operatorname{erfc}\left[\mathsf{m}\right]\right].\end{aligned} \tag{6.11}$$

The speed of the gas outside of the Knudsen layer is equal to

$$v_k = \mathsf{m}\sqrt{\frac{2\mathfrak{R}T_K}{\mathsf{M}}} \tag{6.12}$$

with $\mathfrak{R}$ and M being the gas constant and the molar mass of the carbon gas respectively. The pressure at the entrance of the Knudsen layer is equal to the vapour pressure for carbon that is calculated using the Clausius-Clapeyron

equation considering the gas to behave like an ideal gas,

$$\partial_{T_{\text{surface}}} \{P_{\text{surface}}\} = \frac{\Delta H_{\text{vap}} P_{\text{surface}}}{\Re T^2_{\text{surface}}}, \tag{6.13}$$

with ΔH_{vap} and P_{surface} being the enthalpy of the vaporisation and the vapour pressure respectively. The gas at the surface behaves like an ideal gas, thus the density is equal to,

$$\rho_S = \frac{P_{\text{surface}} M}{\Re T_{\text{surface}}} \tag{6.14}$$

with ρ_S and M being the density of the gas at the surface and the molar mass of the gas respectively. It must be noted that the ratio of the pressure at the surface and the pressure outside of the Knudsen layer governs the process evaporation or condensation. The pressure at the surface P_{surface} is equal to the vapour pressure at the surface temperature T_{surface} whereas the pressure outside the Knudsen layer, P_K, is equal to the ambient pressure of the plume. As soon as the vapour pressure exceeds the plume pressure P_K, evaporation starts and the speed at the exit of the Knudsen layer follows the following relation, [263, 264]:

$$\mathsf{M}_K = \frac{1 - [P_K / P_{\text{surface}}]^{-0.275}}{1 - P_0^{-0.275}}, \tag{6.15}$$

with P_0 being the sonic pressure ratio. The Knight relations are developed for subsonic evaporation, thus the supersonic evaporation, for which no disturbance propagates from the Knudsen to the gaseous phase, is not possible [90, 265]. The Mach number is equal to

$$m = \begin{cases} \sqrt{\frac{\gamma}{2}} \mathsf{M}_K & \text{if } \mathsf{M}_K < 1, \\ \sqrt{\frac{\gamma}{2}} & \text{if } \mathsf{M}_K \geq 1, \end{cases} \tag{6.16}$$

During the interaction between the laser and the plasma, the plume pressure over the Knudsen layer can exceed the vapour pressure. As a result, the evaporation of the target stops. Thus, it is possible to properly close the system of equations (6.11)–(6.16) that governs the Knudsen discontinuity. The recession velocity of the target due to the evaporation or condensation is derived,

$$v_a = \frac{v_k \rho_K}{\rho_g}. \tag{6.17}$$

The boundary conditions for the plume domain from Knudsen layer are defined as:

$$F_{\rho,K} = v_k \rho_K \tag{6.18}$$

$$F_{\rho e,K} = (\rho_K e_K + P_K) v_k \tag{6.19}$$

with e_K is the specific energy density, which is composed of the specific kinetic and internal energy density [23],

$$e_K = \frac{1}{2} v_k^2 + e_{\text{internal}}. \tag{6.20}$$

The vapour exiting the Knudsen layer is considered to be in local thermal equilibrium with the distribution of the energy level density respecting the Saha and Boltzmann distributions. The density in the j-th level and k-th charge state is calculated via the Boltzmann equation,

$$\left[\mathrm{C_j^k}\right] = \left[\mathrm{C^k}\right] \frac{g_j^k}{Z^k\left(T_K\right)} \exp\left[-\frac{\mathfrak{E}_j^k - \mathfrak{E}_0^k}{k_\mathrm{B} T_K}\right], \tag{6.21}$$

and the Saha equation,

$$\begin{gathered} \frac{\left[\mathrm{C^{k+1}}\right]\left[\mathrm{e^-}\right]}{\left[\mathrm{C^k}\right]} = \frac{2}{\Lambda^3} \frac{Z^{k+1}\left(T_K\right)}{Z^k\left(T\right)} \exp\left[-\frac{\mathfrak{E}_0^{k+1} - \mathfrak{E}_0^k}{k_\mathrm{B} T_K}\right], \\ \text{with } \Lambda = \sqrt{\frac{\mathrm{h}^2}{2\pi m_{\mathrm{e^-}} k_\mathrm{B} T_K}} \end{gathered} \tag{6.22}$$

with $\left[\mathrm{C}_{\mathrm{j}}^{\mathrm{k}}\right]$, $\left[\mathrm{C}^{\mathrm{k}}\right]$, $[\mathrm{e}^{-}]$, g_j^k, $Z^k\,(T)$, $\mathfrak{E}_j^k$, k_{B}, m_{e^-} and k_{B} being the density for the j-th electronic level of the k-th charge state, the total density for the k-th charge state, the electronic density, the statistic weight for the j-th electronic level of the k-th charge state, the partition function of the k-th charge state, the energy level for the j-th electronic level of the k-th charge state, the Boltzmann constant, the electron mass and the Plank constant respectively. The partition function is calculated using the following expression [124],

$$Z^k\,(T) = \sum_{0}^{j_{\max}} g_j^k \exp\left[-\frac{\mathfrak{E}_j^k - \mathfrak{E}_0^k}{k_{\mathrm{B}} T_K}\right]. \tag{6.23}$$

with $j_{\max}$ being the energy level for the k-th charge state. Finally, the energy flux exiting the target is the sum of the energy flux leaving the Knudsen layer and the energy flux due to the jump of enthalpy during the vaporisation such as,

$$F_{\rho e,\mathrm{surface}} = F_{\rho e,K} + F_{\rho,K}\Delta H_{\mathrm{vap}}. \tag{6.24}$$

The mass and energy transfer between the target and the plume is calculated using equations (6.17)–(6.24), enforcing the mass and energy conservation across the Knudsen layer.

6.2.3 Plasma formation: collisional-radiative model

The plume or plasma evolution above the Knudsen layer is usually described assuming local thermal equilibrium and the Boltzmann-Saha distribution [31, 124]. The Boltzmann-Saha distribution holds true only for dense plasma for which the collisional processes (electrons-heavies collisions) dominate over the radiative processes (photo-ionisation, radiative recombination, spontaneous emission) [266]. This assumption should be true inside the Knudsen layer, however it has been shown that it does not hold during the initial plasma formation that should be regarded as an highly non-equilibrium process [23,

120, 267]. The Boltzmann-Saha equilibrium approach should therefore be avoided in the description of the plasma during nanosecond pulsed laser ablation and instead a collisional-radiative approach is employed [125]. The collisional-radiative model consists of a set of equations describing the atomic processes occurring between the electrons and the various electronic levels in the atomic species. It allows the description of particular collisional and radiative processes on the population of electrons and electronic levels. The complete description of the electronic processes leads to an unpractical model since the computational cost increases dramatically with the description of the full set of electronic levels. Instead, the number of electronic levels considered within each charge state has been reduced into a smaller amount of fictitious electronic levels. The full set of electronic levels are retrieved from the NIST database [268], then the levels are lumped together such that the azimuthal quantum number and the total angular momentum are preserved and the energy separation between the high level and the lowest level is not more than 0.31 eV. It must be noted that the energy criteria correspond to the kinetic energy for a gas at $\approx$ 3000 K thus the lumped level should be close to equilibrium from the initial plasma formation [266]. The present lumping procedure allows detailed description of the most populated levels as well as considering the optically allowed and (parity or spin) forbidden electronic excitation transitions [256]. It is then possible to observe the low-lying metastable states which might delay the plasma breakdown [126]. The fictitious level parameters are calculated as for the equivalent weight

$$g^k_{eq,j} = \sum_{i=0}^{i=n(j)} g^k_i, \tag{6.25}$$

the equivalent level energy,

$$\mathfrak{E}^k_{eq,j} = \frac{\sum_{i=0}^{i=n(j)} g^k_i \mathfrak{E}^k_i}{g^k_{eq,j}}. \tag{6.26}$$

Finally, the lumping procedure results in the ground charge state being described using 54 levels and the first ionised state is described using 62 levels. The numerical tests presented in this study and previously published works [122, 125] show that the doubled ionised state is not excited to a significant density thus only the ground level is used. The following collisional and radiative processes are considered in this study: inverse Bremsstrahlung, thermal Bremsstrahlung, electron impact excitation/de-excitation, electron impact ionisation/three body recombination, photo-ionisation, spontaneous emission and the radiative recombination, see Table 6.1.

Table 6.1: Collisional (c) and radiative (r) processes and corresponding atomic reactions with $\Delta\mathfrak{E}_{i,j}^{k,l} = \mathfrak{E}_i^k - \mathfrak{E}_j^l$.

(c)	Inverse Bremsstrahlung	$\mathrm{C_j^k} + \mathrm{e}^-(\epsilon) + \mathrm{h}\nu_{\mathrm{laser}} \rightharpoonup \mathrm{C_j^k} + \mathrm{e}^-(\epsilon + \mathrm{h}\nu_{\mathrm{laser}})$
(c)	Electron impact exc./deexc.	$\mathrm{C_i^k} + \mathrm{e}^-(\epsilon) \rightleftharpoons \mathrm{C_j^k} + \mathrm{e}^-(\epsilon - \Delta\mathfrak{E}_{i,j}^{k,k})$
(c)	Electron impact ion./tb.rec.	$\mathrm{C_i^k} + \mathrm{e}^-(\epsilon) \rightleftharpoons \mathrm{C_j^{k+1}} + \mathrm{e}^-(\epsilon') + \mathrm{e}^-(\epsilon'')$ with $\epsilon = \epsilon' + \epsilon'' + \Delta\mathfrak{E}_{i,j}^{k,k+1}$
(r)	Photo-ionisation	$\mathrm{C_i^k} + n_{\mathrm{photon}}\mathrm{h}\nu_{\mathrm{laser}} \rightleftharpoons \mathrm{C_j^{k+1}} + \mathrm{e}^-(n_{\mathrm{photon}}\mathrm{h}\nu_{\mathrm{laser}} - \Delta\mathfrak{E}_{i,j}^{k,k+1})$
(r)	Bremsstrahlung	$\mathrm{C_i^k} + \mathrm{e}^-(\epsilon) \rightharpoonup \mathrm{C_j^k} + \mathrm{e}^-(\epsilon - \mathrm{h}\nu) + \mathrm{h}\nu$
(r)	Spontaneous emission	$\mathrm{C_i^k} \rightharpoonup \mathrm{C_j^k} + \mathrm{h}\nu$ with $\mathrm{h}\nu = \Delta\mathfrak{E}_{i,j}^{k,k}$
(r)	Radiative recombination	$\mathrm{C_i^{k+1}} + \mathrm{e}^-(\epsilon) \rightharpoonup \mathrm{C_j^k} + \mathrm{h}\nu$ with $\mathrm{h}\nu = \epsilon + \Delta\mathfrak{E}_{i,j}^{k+1,k}$

The effective cross section for the inverse Bremsstrahlung has been obtained by Weyl et al. [269]. for the absorption of photons by neutral,

$$\varsigma_{IB}^{n,e} = \frac{[\mathrm{C}^0]}{3\ m_{\mathtt{e}^-}\mathtt{c}\pi\mathtt{h}\nu_{\mathrm{laser}}^3}\frac{\mathtt{e}^2}{4\pi\varepsilon_0}\sqrt{\frac{2(\mathtt{h}\nu_{\mathrm{laser}}+\epsilon_{\mathtt{e}^-})}{m_{\mathtt{e}^-}}} \\ \left[(\epsilon_{\mathtt{e}^-}+\mathtt{h}\nu_{\mathrm{laser}})\,\varsigma_{\mathrm{C}}(\epsilon_{\mathtt{e}^-})+\epsilon_{\mathtt{e}^-}\varsigma_{\mathrm{C}}(\epsilon_{\mathtt{e}^-})\,(\epsilon_{\mathtt{e}^-}+\mathtt{h}\nu_{\mathrm{laser}})\right]. \tag{6.27}$$

with $m_{\mathtt{e}^-}$, $\mathtt{e}$, $\mathtt{c}$, $\mathtt{h}$, ε_0, $\epsilon_{m_{\mathtt{e}^-}}$, ς_{C} being the electron mass, the electron charge, the speed of light, the Planck constant, the vacuum permittivity, the kinetic energy of the electrons, and the cross section of elastic collision between electrons and neutrals. The absorption of photon by ionised species is taken from the work of Zel'dovich and Raizer [270],

$$\varsigma_{IB}^{n,i} = \frac{4}{3}\sqrt{\frac{2\pi}{3\ m_{\mathtt{e}^-}k_{\mathrm{B}}T_{\mathtt{e}^-}}}\frac{\sum_{k=1}^{k=k_{\max}}\mathbf{Z}^{k+}\left[\mathrm{C}^{\mathrm{k}}\right]}{\mathtt{hc}\nu_{\mathrm{laser}}^3\ m_{\mathtt{e}^-}}G\frac{\mathtt{e}^6}{(4\pi\varepsilon_0)^3}. \tag{6.28}$$

with $\mathbf{Z}^{k+}$ and G being the charge of the heavy species and the Gaunt factor, which is equal to 1.2 for collision similar to this study, respectively. The cross section for the electron impact ionisation and excitation (optically allowed and forbidden) are calculated using the hydrogen-like cross section proposed by Drawin [271] using the coefficient proposed by Morel et al. [272]. The effective cross section for the electron impact ionisation and excitation of optically allowed excitation is

$$\varsigma_{\mathrm{EI}} = \varsigma_{\mathrm{EE,oa}} = 4\pi a_0^2\left(\frac{\mathfrak{E}_{ion}^{\mathrm{H}}}{\Delta\mathfrak{E}_{i,j}^{k,\{k,k+1\}}}\right)^2\alpha_i\frac{\bar{\epsilon}-1}{\bar{\epsilon}^2}\ln\left(\frac{5}{4}\beta_i\bar{\epsilon}\right). \tag{6.29}$$

with a_0, $\mathfrak{E}_{ion}^{\mathrm{H}}$, $\bar{\epsilon}$, α_i and β_i being the Bohr radius, the energy of hydrogen ionisation, the kinetic energy normalised to the energy for the transition considered ($\bar{\epsilon}=\bar{\epsilon}/\Delta\mathfrak{E}_{i,j}^{k,\{k,l\}}$) and two parameters for the electronic ionisation and electronic excitation cross section respectively. The two parameters, α_i and β_i, are equal to 0.05 and 4 respectively in this model [266]. The effective

cross section for the electron impact excitation of spin forbidden transition (such that $\Delta J \neq 0,\ \pm 1$ and $J = 0 \rightarrow J = 0$) is

$$\varsigma_{EE,sf} = 4\pi a_0^2 \alpha_e^S \frac{\bar{\epsilon}^2 - 1}{\bar{\epsilon}^5} \tag{6.30}$$

with $\alpha_e^S = 0.05$ chosen for the carbon plasma [266]. The effective cross section for the electron impact excitation of parity forbidden transition (such that $\Delta l \neq \pm 1$) is

$$\varsigma_{EE,pf} = 4\pi a_0^2 \alpha_e^P \frac{\bar{\epsilon} - 1}{\bar{\epsilon}^2}, \tag{6.31}$$

with $\alpha_e^P = 0.05$ chosen for the carbon plasma [266]. The effective cross section for the one photon ionisation is taken from the work of Zel'dovich and Raizer [270],

$$\varsigma_{PI} = \frac{64\pi^4 \mathtt{e}^{10} m_{\mathtt{e}^-}}{3\sqrt{3}\left(4\pi\varepsilon_0\right)^5 \mathtt{h}^6 \mathtt{c}} \frac{1}{\nu_{\text{laser}}^3} \frac{\left(\Delta \mathfrak{E}_{i,j}^{k,k+1}\right)^{5/2}}{\sqrt{\mathfrak{E}_0^{k+1}} \left(\mathfrak{E}_{ion}^{\text{H}}\right)^2} \tag{6.32}$$

with $\mathfrak{E}_{ion}^{\text{H}}$ and $\mathfrak{E}_0^{k+1}$ are the ionisation energy of the Hydrogen atom and the ionisation energy of the specie at the current level of ionisation respectively. The formula used to calculated the effective cross section from multi-photon ionisation is given by Müsing et al. [273]. The cross section for the interaction between k-photon and heavy species is

$$\varsigma_{MPI} = \frac{\varsigma_{PI}}{(k-1)! \nu_{\text{laser}}^{k-1} (\mathtt{h}\nu_{\text{laser}})^k}. \tag{6.33}$$

The model only considers the single and two photo-absorption since the cross sections for three and over photo-ionisation are too small for an IR pulse. The effective loss due to thermal Bremsstrahlung is calculated using the formula proposed by Morel et al. [125]. The energy loss by the electrons with the

neutral carbon atoms via Bremsstrahlung is

$$\Theta_{n,\mathrm{e}^-}(TB) = \frac{16}{3\ m_{\mathrm{e}^-}\mathtt{hc}^3} v_{\mathrm{e}^-}^- \frac{\mathtt{e}^2}{\pi\varepsilon_0}\left[\mathrm{C}^0 \varsigma_{\mathrm{C}}(\epsilon) k_{\mathrm{B}} T_{\mathrm{e}^-}^2\right], \tag{6.34}$$

The energy loss by the electrons with the ionised carbon species via Bremsstrahlung is

$$\Theta_{i,\mathrm{e}^-}(TB) = \frac{32}{3\ m_{\mathrm{e}^-}\mathtt{hc}^3} v_{\mathrm{e}^-}^- \left(\frac{\pi}{3\sqrt{3}k_{\mathrm{B}}} G \frac{\mathtt{e}^6}{(4\pi\varepsilon_0)^3} \sum_{k=1}^{k=k_{\max}} \mathbf{Z}^{k+}\left[\mathrm{C}^{\mathrm{k}}\right]\right). \tag{6.35}$$

The spontaneous emission oscillator strength has been obtained using the NIST database for spectroscopic line [268]. It must be noted that the Stark-broadening is not considered in this work [274] thus the plasma is considered optically-thin. The effective transfer rate for the spontaneous emission is equal to

$$\Xi_{\left[\mathrm{C_i^k}\right]}(SE) = -A^*_{\mathrm{C_i^k}\to\mathrm{C_j^l}} \text{ with } A^*_{\mathrm{C_i^k}\to\mathrm{C_j^l}} = \frac{\sum_{m=0}^{m=n_{\max}} g_m^k \sum_{n=0}^{n=n_{\max}} A^*_{\mathrm{C_m^k}\to\mathrm{C_n^k}}}{g_{eq,i}^k}. \tag{6.36}$$

The radiative recombination cross section is calculated according to the Kramer formula [270, 275] using the correction for the effective charge proposed by Kim and Pratt [276, 277]. The cross section of the radiative recombination

$$\varsigma^{RR} = \pi a_0^2 \frac{32\mathbf{Z}_{\mathrm{eff}}^{+\,4} Ry^2}{3\sqrt{3}n^3\,(137)^3\,(\Delta\mathfrak{E}_{i,j}^{k,k+1} + \epsilon_{\mathrm{e}^-})\epsilon_{\mathrm{e}^-}} \tag{6.37}$$

with $\mathbf{Z}_{\mathrm{eff}}^+$ and n being the effective charge and the principal quantum number of the level in the which the electron recombines. The effective charge is

$$\mathbf{Z}_{\mathrm{eff}}^+ = \sqrt{\mathbf{Z}_C^+ \mathbf{Z}^{k+}} \tag{6.38}$$

where $\mathbf{Z}_C^+$ is the nuclear core charge and $\mathbf{Z}^{k+}$ is the ionic charge before the electron capture [277]. The principal quantum number is estimated for species for which the hydrogen-like approximation is not suitable,

$$n = \sqrt{\frac{\mathfrak{E}_0^{k+1}}{\mathfrak{E}_0^{k+1} - \mathfrak{E}_i^k}}. \tag{6.39}$$

The rate equation for each fictitious level is trivial [23], thus the term arising from the atomic processes is noted as $R^k_{[\mathrm{C_j^k}],j}$ for the j-th fictitious level on the k-th charge state. The rate equation for the j-th fictitious level on the k-th charge state is

$$\partial_t \left\{ \left[\mathrm{C_j^k} \right] \right\} = R^k_{[\mathrm{C}],j} + \frac{F_{\rho,K} x^k_{j,K}}{m_\mathrm{C} z_p} + \frac{v_p}{z_p} \left[\mathrm{C_j^k} \right], \tag{6.40}$$

with $x^k_{j,K}$, m_C, v_p and z_p being the fraction of particle exiting the Knudsen layer belonging to the j-th fictitious level and the k-th charge state, the atomic mass of carbon atom, the plasma front speed and the plasma front position respectively. The electron density is obtained by enforcing the charge conservation principle. The rate equations for all the fictitious levels (6.40) are closed by the energy balance for the heavy [23, 266],

$$\begin{aligned} \partial_t \left\{ E_\mathrm{heavy} \right\} = & \sum_{j,k=0}^{j,k=max} R^k_{\epsilon,j} + \frac{3 v_k}{2 z_p} k_\mathrm{B} \sum_{j,k=0}^{j,k=max} \left[\mathrm{C^k_{j,K}} \right] T_K \\ & - \frac{v_p}{z_p} E_\mathrm{heavy} + 3 \frac{m_{\mathsf{e}^-}}{m_\mathrm{C}} \left[\mathsf{e}^- \right] \nu_\mathrm{elastic} \left(T_{\mathsf{e}^-} - T_\mathrm{heavy} \right), \end{aligned} \tag{6.41}$$

and for the electrons

$$\begin{aligned} \partial_t \left\{ E_{\mathsf{e}^-} \right\} = & - \sum_{j,k=0}^{j,k=max} R^k_{\epsilon,j} + \frac{3 v_k}{2 z_p} k_\mathrm{B} \left[\mathsf{e}^- \right]_K T_K + S_{IB} \\ & + S_B + \frac{v_p}{z_p} E_{\mathsf{e}^-} - 3 \frac{m_{\mathsf{e}^-}}{m_\mathrm{C}} \left[\mathsf{e}^- \right] \nu_\mathrm{elastic} \left(T_{\mathsf{e}^-} - T_\mathrm{heavy} \right), \end{aligned} \tag{6.42}$$

with E_{heavy}, T_{heavy}, E_{e^-}, $[\mathsf{e}^-]$, T_{e^-}, m_{e^-}, $R^k_{\epsilon,j}$ and ν_{elastic} being the energy stored in the heavy, the energy stored in the electrons, the electron density, the electron temperature, the electron mass, the reaction rate energy transfer between the electrons and the heavies for all the considered atomic reactions, see Table 6.1, and the elastic collisional frequency between the electrons and the heavies. The elastic collision between the electrons and heavies is composed of two terms; the term for the ionic collision is given by Huba [278] and the term for the neutral collision is derived by Cooper and Martin [279, 280]. The electrons and heavies behave like an ideal-gas [97, 123] so the temperature of the electrons is calculated using,

$$T_{\mathsf{e}^-} = \frac{E_{\mathsf{e}^-}}{\frac{3}{2}\left[\mathsf{e}^-\right] k_{\text{B}}}, \tag{6.43}$$

The temperature of the heavies is obtained using the following equation [122],

$$T_{\text{heavy}} = \frac{E_{\text{heavy}} - \sum_{j,k=0}^{j,k=max} \mathfrak{E}^k_j \left[\text{C}^{\text{k}}_{\text{j}}\right]}{\frac{3}{2}\left[\text{C}\right] k_{\text{B}}}, \tag{6.44}$$

with n_{heavy} being the total density of heavies in the plasma ($[\text{C}] = \sum_{j,k=0}^{j,k=max} \left[\text{C}^{\text{k}}_{\text{j}}\right]$). The plume pressure P_K is given by

$$P_K = k_{\text{B}} \left([\text{C}]\, T_{\text{heavy}} + \left[\mathsf{e}^-\right] T_{\mathsf{e}^-} \right) \tag{6.45}$$

and the plume expands at sonic speed. Its velocity is calculated as,

$$v_p = \sqrt{\frac{\gamma P_K}{\rho_p}} \tag{6.46}$$

with ρ_p being the plume density. The value of intensity absorbed by the

plasma is given by

$$\mathfrak{i}_p(t) = \frac{\mathfrak{i}(t)}{\left(1 + \frac{\alpha_{p,II}\mathfrak{i}(t)}{\alpha_{p,I}}\right)\left(e^{\alpha_{p,I}z_p} + \frac{\alpha_{p,II}\mathfrak{i}(t)}{\alpha_{p,I}+\alpha_{p,II}\mathfrak{i}(t)}\right)} \tag{6.47}$$

where $\mathfrak{i}(t)$, $\alpha_{p,I}$ and $\alpha_{p,II}$ are the intensity of the laser, the absorption coefficient for the linear absorption (inverse Bremsstrahlung and one photon ionisation) and the absorption coefficient for the second order absorption (two photon ionisation) respectively. The plasma absorption is inserted back into for the source term of the target heat equations, Equations (6.2) and (6.3).

The radiative recombination and thermal Bremsstrahlung have previously shown to be of importance for the coupling of the plasma radiation to the target during graphite nanosecond ablation with plasma breakdown [32]. A significant fraction of the plasma energy is re-emitted in the UV range (around 950 Å) [32] during the main laser-plasma interaction and coupled back to the irradiated target. Hence, a new source term is constructed and added to the source term [32].

The source term S_g from the laser beam is

$$\begin{aligned} S_g = &(1 - R_l(T_{\text{surface}}))\alpha_{g,l} \exp\left[-\alpha_{g,l}(z - z_1)\right] I_p(t) \\ &+ (1 - R_p(T_{\text{surface}}))\alpha_{g,p} \exp\left[-\alpha_{g,p}(z - z_1)\right] \mathfrak{i}_{em}(t) \end{aligned} \tag{6.48}$$

with R_l, R_p, $\alpha_{g,l}$, $\alpha_{g,p}$, T_{surface} and $\mathfrak{i}_{em}(t)$ being the reflectivity at the laser wavelength, the reflectivity at 950 Å , absorption coefficient at the laser wavelength for graphite, absorption at 950 Å for graphite, surface temperature, and the re-emitted intensity from the plasma. The source term S_d is

$$\begin{aligned} S_d = &(1 - R_l(T_{\text{surface}}))\, \alpha_{d,l} \exp\left[-\alpha_{d,l}(z - z_2) - \alpha_{g,l}(z_2 - z_1)\right] \mathfrak{i}_p(t) \\ &+ (1 - R_p(T_{\text{surface}}))\, \alpha_{d,p} \exp\left[-\alpha_{d,p}(z - z_2) - \alpha_{g,p}(z_2 - z_1)\right] \mathfrak{i}_{em}(t) \end{aligned} \tag{6.49}$$

with $\alpha_{d,l}$ and $\alpha_{d,p}$ being absorption coefficient at the laser wavelength for diamond and absorption at 950 Å for diamond. The re-emitted intensity from the plasma is calculated using the effective cross section of the thermal Bremsstrahlung and radiative recombination integrated over the plasma size. The re-emitted intensity reaching the target is only half of the total intensity re-emitted [264]. The initial values for the plume parameters are taken at the Knudsen layer boundary values [23].

6.2.4 Numerical implementation

For the target domain, a front fixing method [223] is used to map the domain of solution to a field domain which is more convenient for numerical solution. The spatial discretisation of the target is achieved using Taylor series and finite volume methods. Temporal discretisation is achieved using an implicit Euler method. Furthermore, it must be noted that the stiffness of the system of equation for the plasma requires a smaller time step, thus the time step for the target and the plasma are different to enable computational efficiency. The matrix representing the linearised system of equations are inverted inverted using the library SUPERLU [224]. The simulation is carried out until the evaporation stops and the position of the interfaces are stabilised.

6.3 Methodology

The methodology for the ablation experiments have been previously described in detail elsewhere, see Chapter 4 and Chapter 3. In brief, a Boron doped diamond samples of 0.5 thickness (produced by Element Six Ltd.) with polished surfaces (Ra $<$ 30 nm) are exposed to nanosecond pulses (using SPI-G3 SM laser) with a fluence between 0.2 and 93.5 J.cm^{-2}. The Gaussian spot diameter is 38 µm using the $1/e^2$ definition. The micro-structure

investigations are being carried out using XRD, Raman spectroscopy and TEM analysis.

The surface topography after the ablation is investigated using a white light interferometer (WLI) with a 247 nm pixel size and 1 nm accuracy for the depth position. The position of the surface at the centre of the crater is measured for 10 craters providing an improved accuracy of the surface position. The position of the interface between the graphite and diamond is measured using the same methodology. The graphitic layer is etched using a hot acidic bath of $K_2Cr_2O_7$:H_2SO_4 during 10 h at 100 °C [138]. This method has been previously used to etch graphitic material without affecting the diamond [138] thus enabling the measurement of thickness of the graphite layer.

Thus, these experimental investigations provide detailed information about the phase transformations and the positing of the interfaces occurring during the laser-target interaction enabling validation of the proposed model.

6.4 Results and Discussion

6.4.1 XRD analysis

For polycrystalline boron doped diamond, the boron concentration is dependent on the orientation of the crystal during its crystal growth; the (111) crystallographic orientation has the highest boron uptake [281]. The variation in boron concentration greatly affects the light absorption coefficient of this doped diamond [229, 230], thus it affects the initial interaction between the target and the laser. However, the experimental results have shown small variation of the ablation threshold that is influenced by the variation of the absorption coefficient, suggesting that the sample possesses a preferential directional growth.

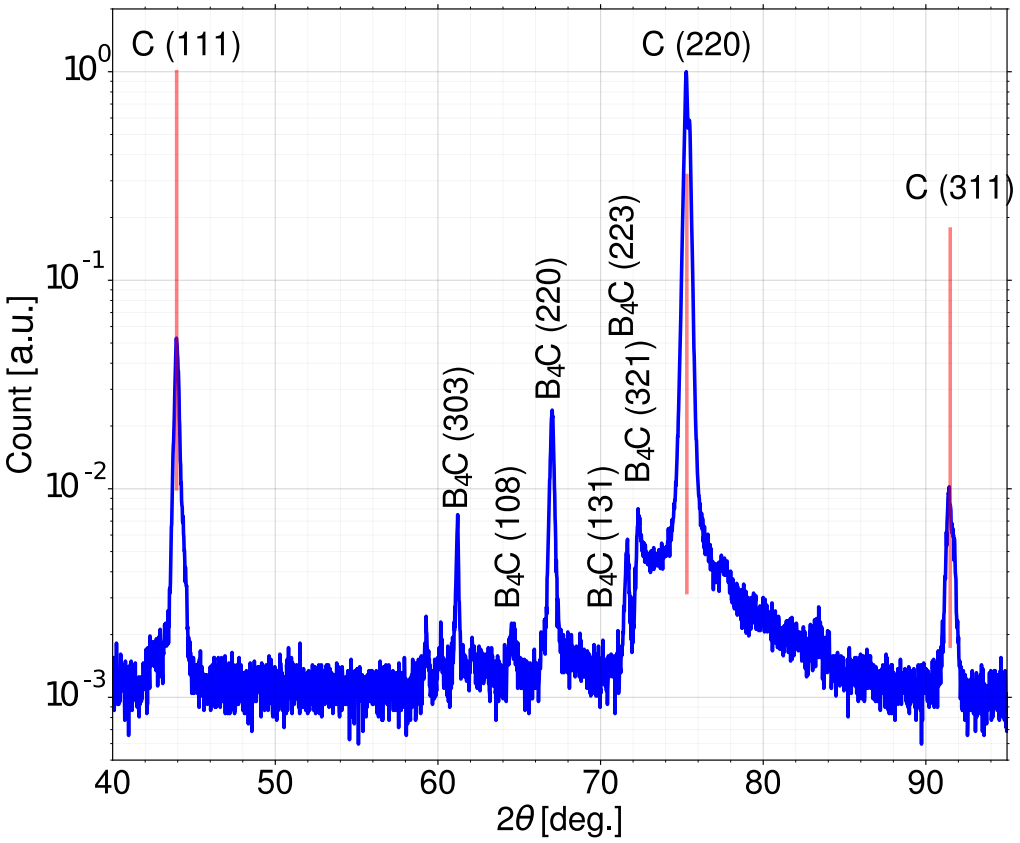

Figure 6.1 : 2-θ XRD measurement of the boron doped diamond sample.

For this, the XRD patterns of the sample is measured to confirm the preferential crystallographic direction of the Boron doped diamond, see Figure 6.1. The XRD spectrum is dominated by three intense peaks located at $2\theta \sim$ 43.92°, 75.27°and 91.44°that are identified with the reflections from (111), (220) and (311) plane of pure diamond respectively [282]. There is also XRD peaks for boron carbide (B_4C) at 61.8°, 65°, 67.5°, 70.8°, 71.8°and 73°from the plane (303), (108), (220), (131), (223) and (321) respectively [283]. The expected peak intensities for these three diamond peaks are presented in Figure 6.1 for equal repartition of the plane from which a strong preferential crystallographic direction (220) for the crystal growth can be observed, thus confirming the mainly homogeneous boron doping of the sample.

6.4.2 Raman Analysis

The intense heat from the laser pulse transforms the diamond into a variety of carbon allotropes [28, 138] that can be identified using Raman spectroscopy. This is a tool widely used to identify different carbon allotropes such as graphite [190, 197], diamond [191, 284] and amorphous carbon [196, 203] as well as the amount of disorder in a graphite based system [285]. Thus, it is possible to understand the micro-structural and crystalline state of the carbon allotrope at the surface for a range of conditions.

6.4.2.1 D-band and G-band at the centre of the crater for a range of fluence

The Raman spectra at the centre of the crater over a range of fluences is presented in Figure 6.2. The spectra present two distinct peaks around 1380 cm^{-1} and 1580 cm^{-1}.

For low power, the Raman spectra presents two distinct peaks suggesting that the graphite is composed of large clusters with limited disturbance of the crystalline structure. This is confirmed by the low FWHM of the D-band and G-band, see Figure 6.3. The increase of the FWHM for the D-band and G-band from 10 $J.cm^{-2}$ to 30 $J.cm^{-2}$ suggests that the number of defects in the crystal lattice increases with an increase of fluence [192].

With a further increase of fluence, the shapes of the Raman spectrum change dramatically at around 30 $J.cm^{-2}$, with a widening of the D-band suggesting a substantial increase of the disorder in the graphite lattice. The ratio of the integrated intensity of the G-band over the D-band is used to the estimate the size of carbon cluster L_a interacting with the laser [190, 286] (as discussed later relative to see Figure 6.10). The ratio of the maximum intensity for the band-D and band-G suggests cluster size around 100 nm for low power. Similarly, the ratio of the integral of the D-band and G-band,

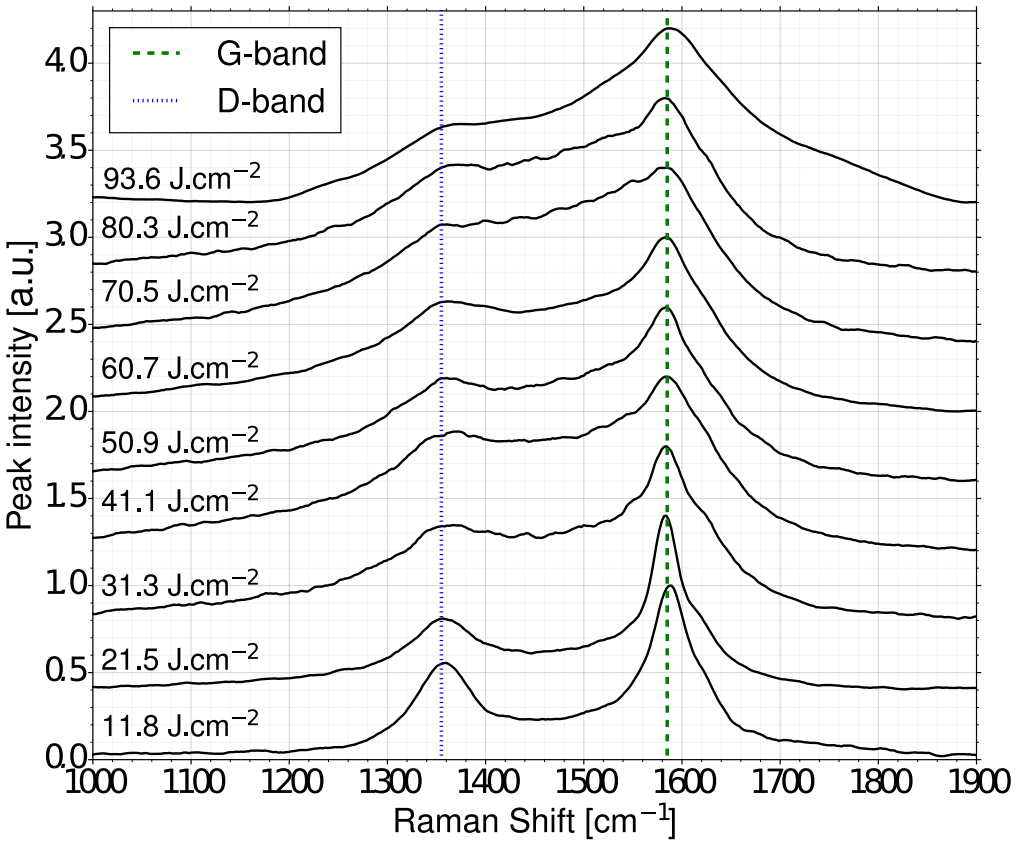

Figure 6.2 : Raman spectra at the centre of the crater for several fluences. The dotted lines are to guide the eye.

see Figure 6.5, jumps from ∼0.6 to ∼ 1 further confirming the increase in disorder with an increase of fluence. The sudden increases in disorder in the graphite lattice at 30 J.cm^{-2} suggests that the material is following different thermodynamic path than for a lower fluence. The loss of order could be due to the sudden melting of the upper layer of the graphite previously shown to occur during the interaction with the laser beam using controlled atmospheric pressure [141]. These experiments show that the melting occurs only for pressure above ∼ 10^7 Pa, which suggests the plume pressure over the crater is this threshold. The peak position the D-band and G-band does not move to lower shift whereas the FWHM widen suggesting that the surface layer does not become fully amorphous, see Figure 6.4 [192].

Indeed, the widening of the G-band after 30 J.cm^{-2} suggests an increase

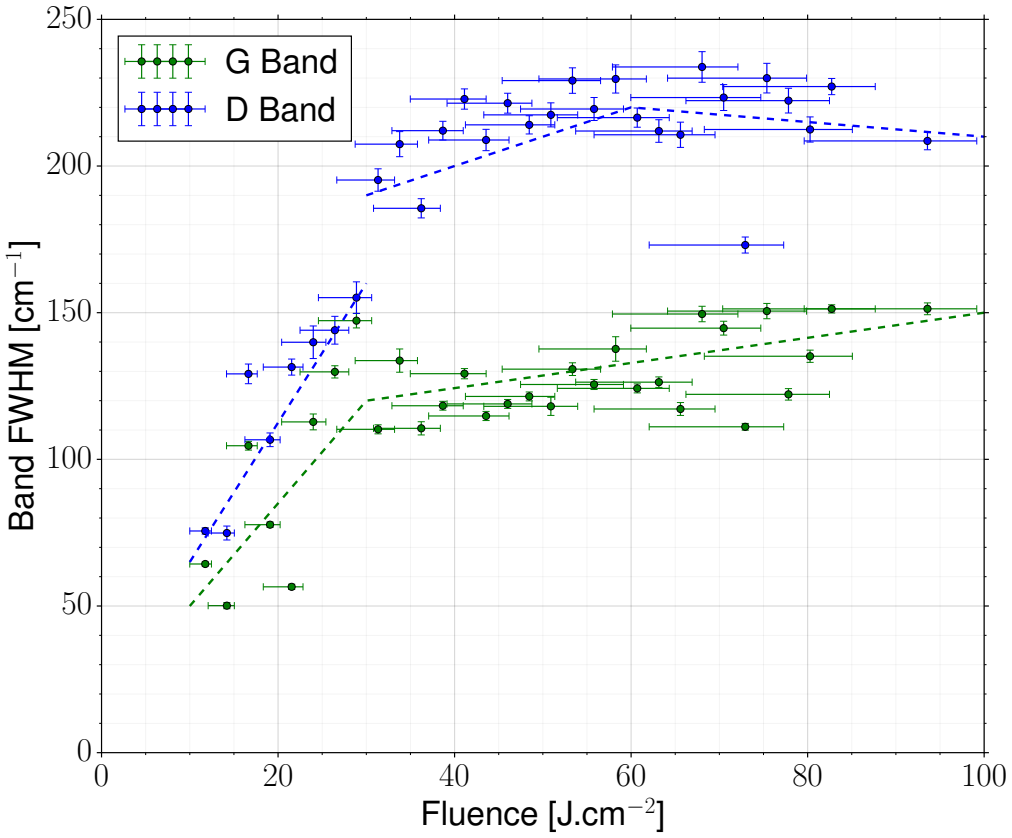

Figure 6.3 : Band Dispersion for the characteristic band of carbon D and G. The dotted lines are guide to the eye.

of the disorder with an increase in fluence, see Figure 6.3. However, the peak position for the G-band is broadly constant over 30 J.cm^{-2} around 1580 cm^{-1}, see Figure 6.4. This is in contradiction with the trajectories for the amorphisation of graphite [192] that should present a decrease of the position of the G-band accompanied by an increase in the FWHM. It suggests that the Raman spectra is composed of spectra from several allotropes of carbon. Previous experiments have shown that the ablation of diamond is accompanied by the deposition of a thin layer ($<$ 100 nm) of the amorphous layer from the condensation of the carbon vapour [36, 37, 154]. The spectra observed after 30 J.cm^{-2} are then a superposition of the spectra coming from a solidified carbon layer that presents a nano-metric cluster size and a thin layer of amorphous layer above it. It is possible to estimate the thickness

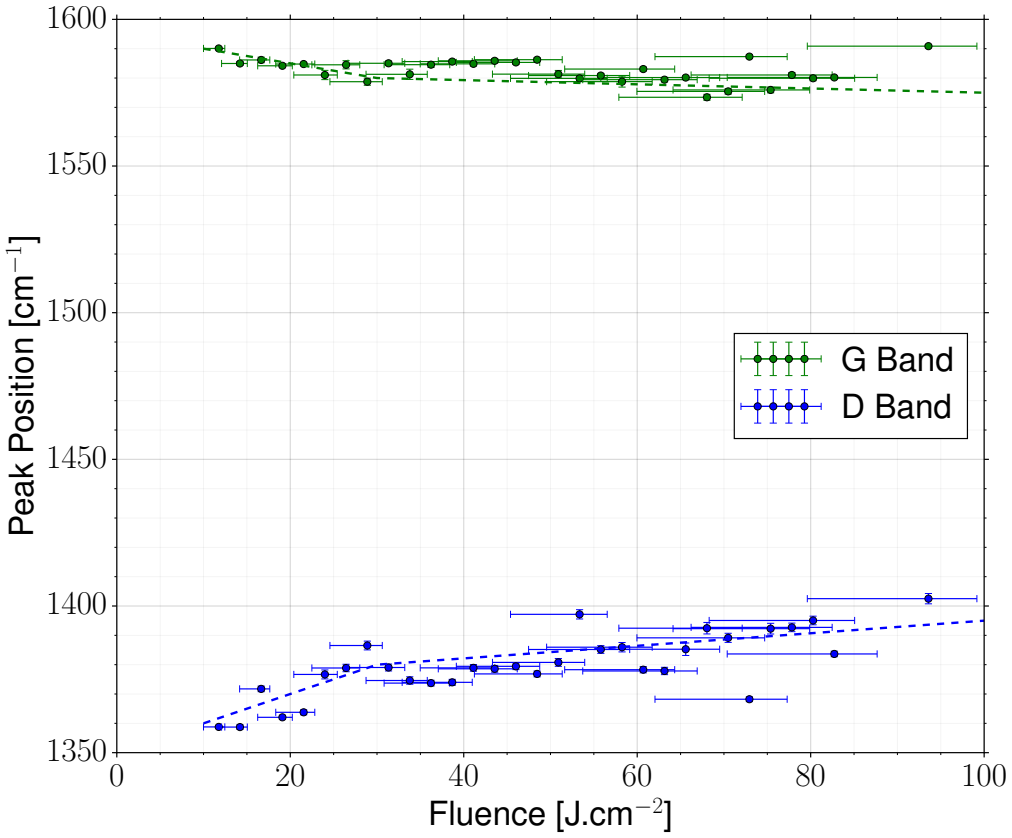

Figure 6.4 : Position of the band D, G and the diamond peak. The dotted lines are guide to the eye.

of the amorphous layer using the the absorption length of the incident light, and this provides a maximum thickness of 145 nm ($5 \times \alpha^{-1}_{g,532\text{ nm}}$). Otherwise, the nano-metric carbon under the amorphous layer will not be excited by the incident light, hence could not be detectable in the Raman spectra. The increase of FWHM for the G-band can be interpreted as an increase of the thickness of the amorphous layer leading to a partial blockage of the light from the Raman laser to the underlying layer. It must be noted that the D-band should disappear for highly amorphous carbon [190] due to the lack of carbon rings that generate the D-band scattering. Thus, the D-band is only generated by the layer below the amorphous carbon and can be used to understand changes in the crystalline structure of the base material. The FWHM of the D-band is constant above 30 J.cm^{-2}, suggesting that the

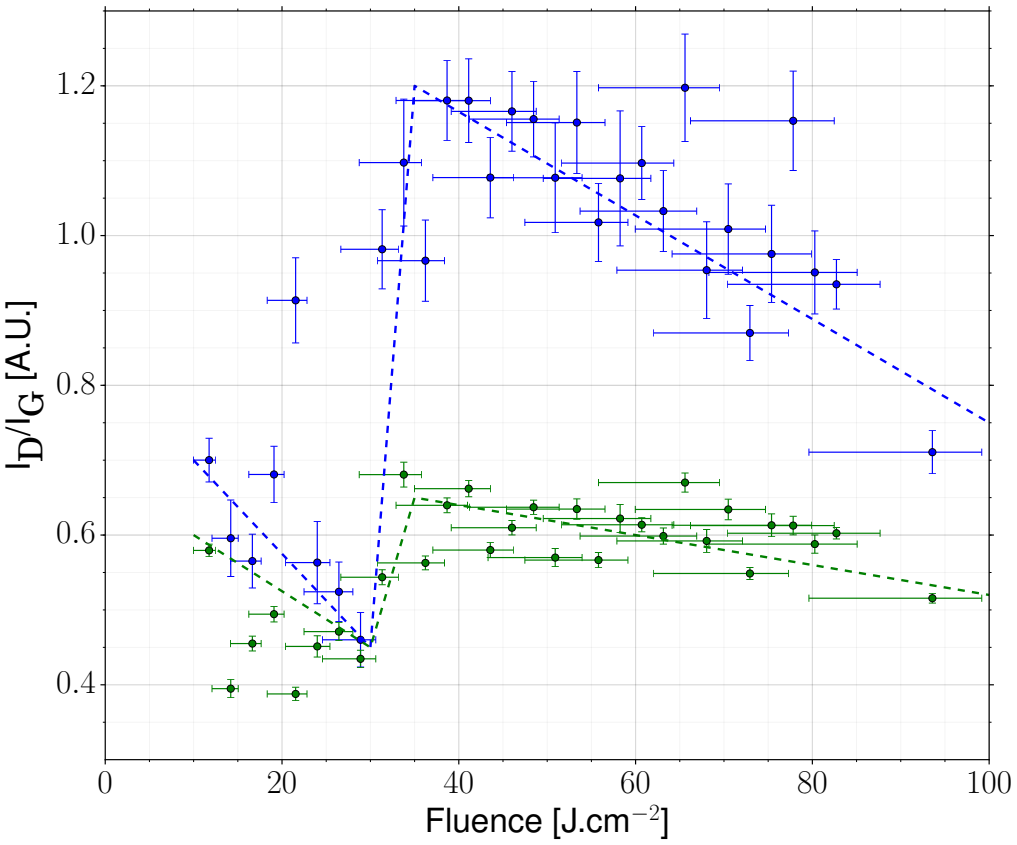

Figure 6.5 : Ratio of the maximum of the peak intensity for the band D and G in green and the Ratio of the integral of the peak intensity for the band D and G in blue. The dotted lines are guide to the eye.

crystalline structure of the base material is similar in the range of fluence investigated.

6.4.2.2 D-band and G-band variation along the profile of the crater for a fluence of 93 J.cm^{-2}

The Raman spectra along the radial profile of a crater for a fluence of 93 J.cm^{-2} is presented in Figure 6.7. The spectra present three distinct peaks around 1335 cm^{-1}, 1380 cm^{-1} and 1580 cm^{-1}.

The position of the D-band and G-band and the width of the bands along the profile of the crater are plotted in Figures 6.8 and Figure 6.9. At the centre of the crater, the diamond band is not present, suggesting the existence

of a thick layer of graphite obstructing the laser/Raman emission from the based material. The Raman band for diamond is present for radial distance larger than 20 µm, suggesting that the diamond is not damaged faraway from the interaction area.

The FWHM and the peak position of the G-band are usually used to describe the micro-structural disorder of the system [190, 196, 203]. At the centre of the crater, the peak position of the G-band is equal to 1590 cm^{-1} and its FWHM is around 150 cm^{-1}. In accordance with the previous measurements of the Raman spectra as a function of the fluence, the spectra

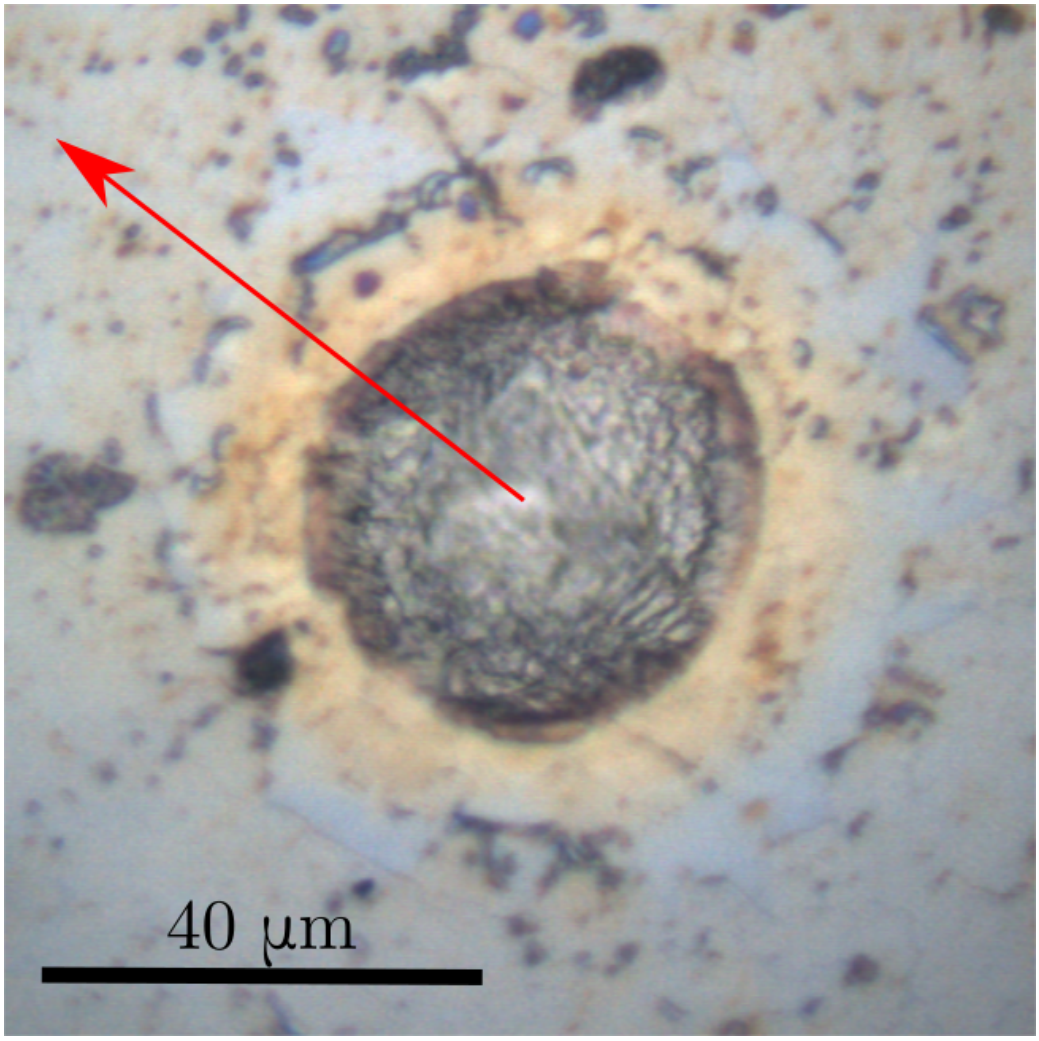

Figure 6.6 : Image of the crater used to perform Raman spectroscopy. The red line highlight the profile used for the Raman measurement.

is composed of a nano-crystalline diamond with a thin layer of amorphous carbon. Interestingly, the peak position of the G-band decreases to around 1550 cm^{-1} with a gradual increases of the FWHM 300 cm^{-1} with an increase of the radial distance between 20 µm and 30 µm, see Figure 6.9 and Figure 6.8. This is showing that the carbon crystalline structure is becoming amorphous for a radial distance over 30 µm. The gradual increases in disorder in the redeposited layer suggests that the diamond around the crater is slightly hotter than the ambient temperature compared to the diamond over 30 µ. The higher temperature of the diamond is due to the "wing" of the Gaussian pulse and the high diffusivity of diamond around the crater. The appearance of the diamond band at 20 µm radial distance shows that the thickness of the graphite layer and amorphous carbon is becoming thinner with an increase

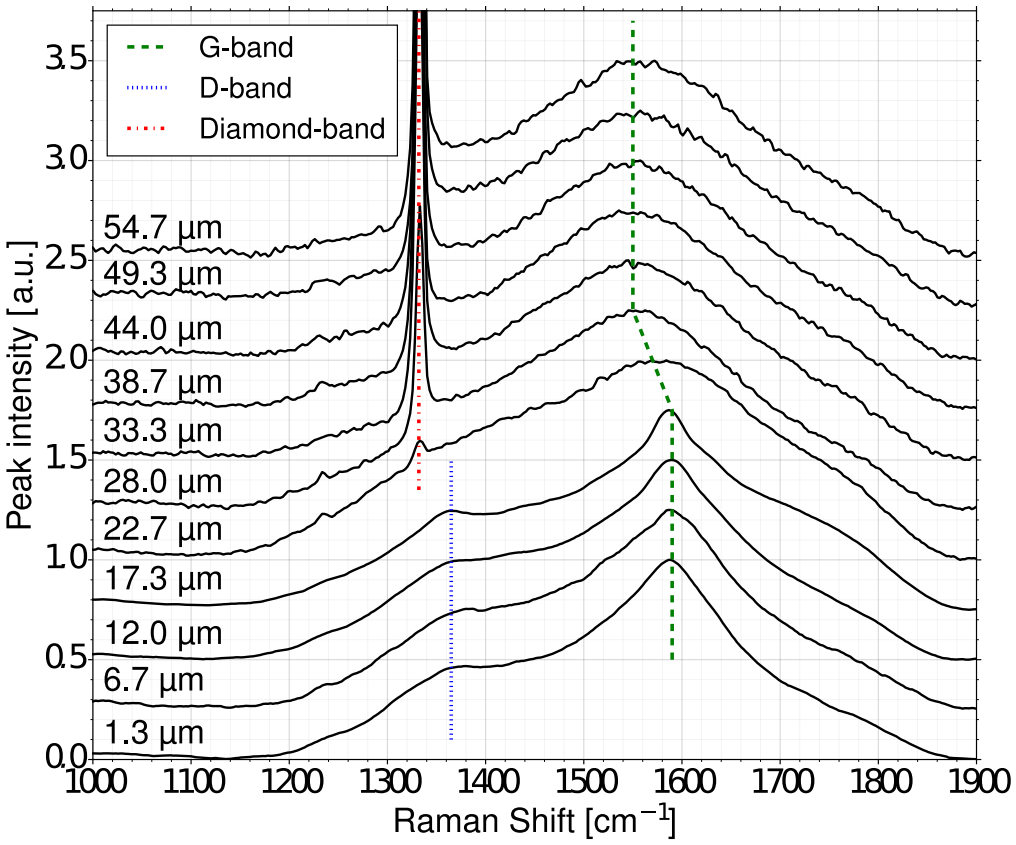

Figure 6.7 : Raman spectra along a radial profile of a crater for a fluence of 93 J.cm^{-2} [190]. The dotted lines are to guide the eye.

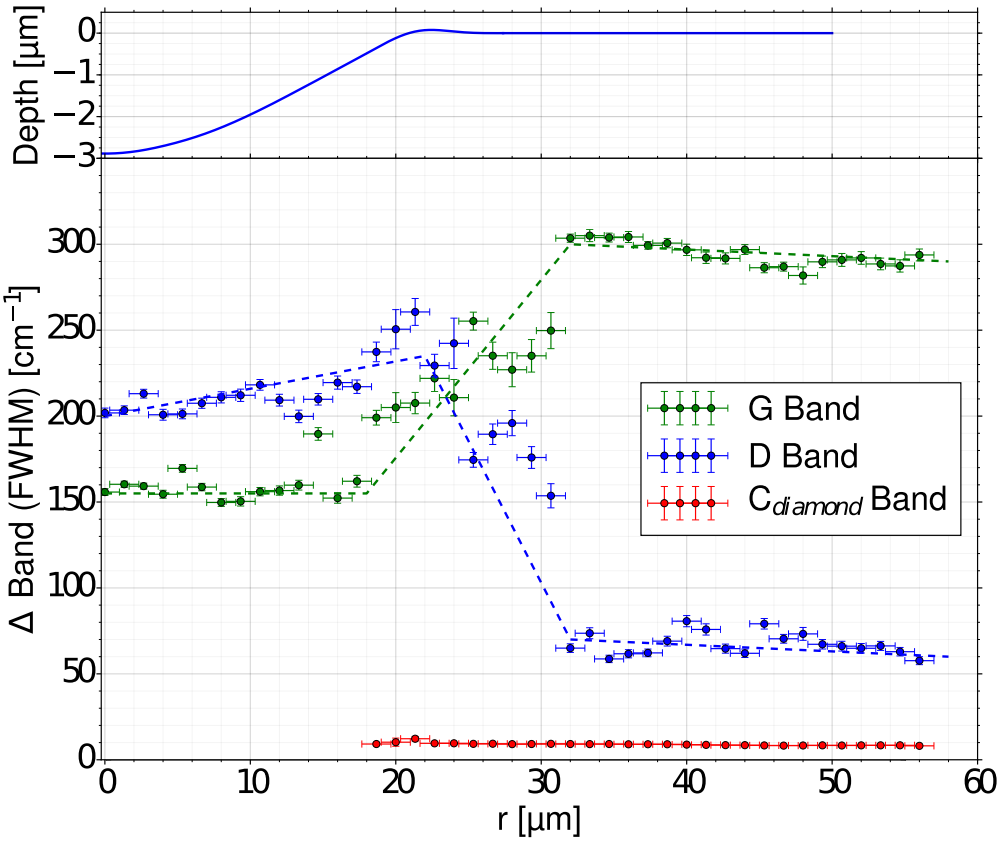

Figure 6.8 : Band Dispersion for the characteristic band of carbon D, G and diamond peak. The dotted lines are guide to the eye.

of radial distance.

Furthermore, the increase influence of the amorphous layer on the Raman spectra is coherent with the deposition/condensation of carbon vapour on the crater and around the crater (> 30 µm) at which nano-crystalline carbon features are not observed on the Raman spectra. The value of the ratio outside the crater zone (~ 0.3) indicates a 5–10 nm graphitic cluster size [190, 286], providing further evidence of the deposition of carbon vapour at the surface of a cold and highly thermally conductive material such as diamond. It must be noted that larger G-band is also associated with higher stress levels in amorphous carbon, suggesting a highly stressed ($\sim$ several GPa) thin layer of carbon [201]. The investigation of the G-band shows that the surface material at the centre of the crater is a highly disturbed nano-crystalline

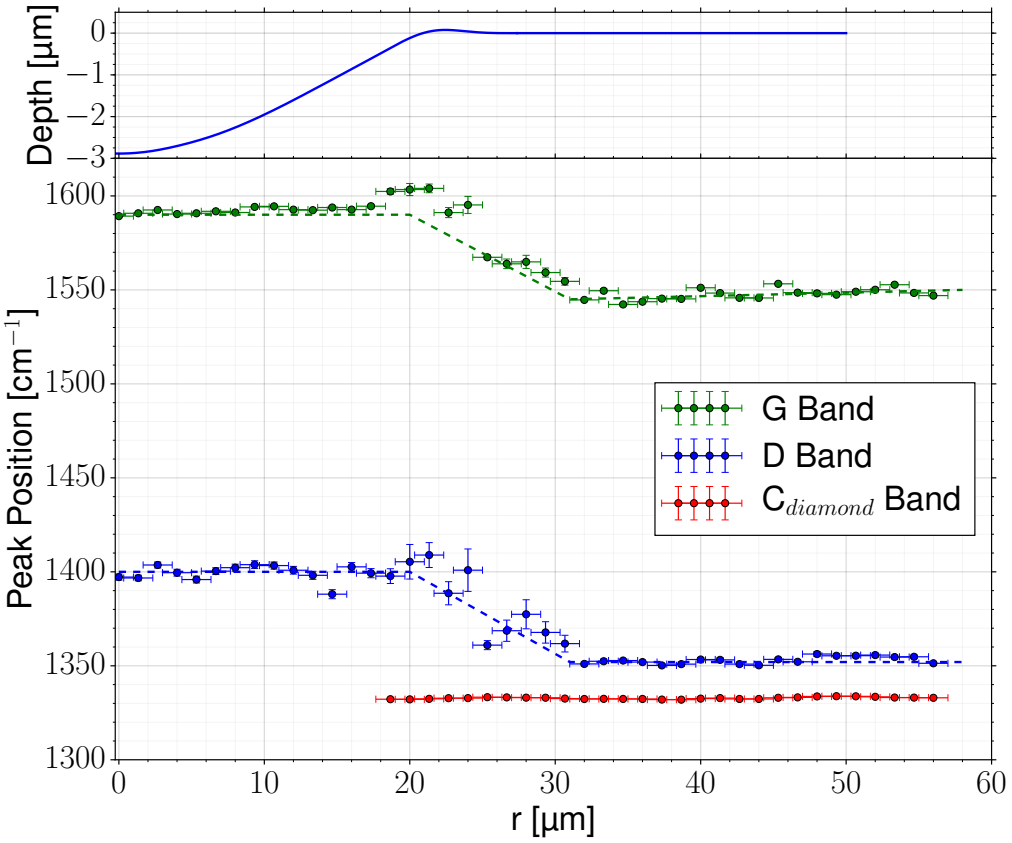

Figure 6.9 : Position of the band D, G and the diamond peak. The dotted lines are guide to the eye.

graphite with a thin layer of amorphous carbon. This is coherent with the melting and solidification of the graphite during nanosecond pulsed laser ablation creating highly disturbed carbon. For radial distance over 30 µm, the Raman spectra shows that the surface material is composed a thin ($<$ 145 nm) layer of amorphous carbon on top of the undamaged diamond [190]. The presence of the G-band far away from the interaction zone strongly suggests that the amorphous carbon is not created by the direct interaction of the laser with the target but has been transported and deposited by the carbon vapour.

As previously noted, the D-band is not appearing for amorphous carbon, thus the D-band characteristic can be used to investigate the micro-structural state of the underlying nano-crystalline graphite. The FWHM of the D-band

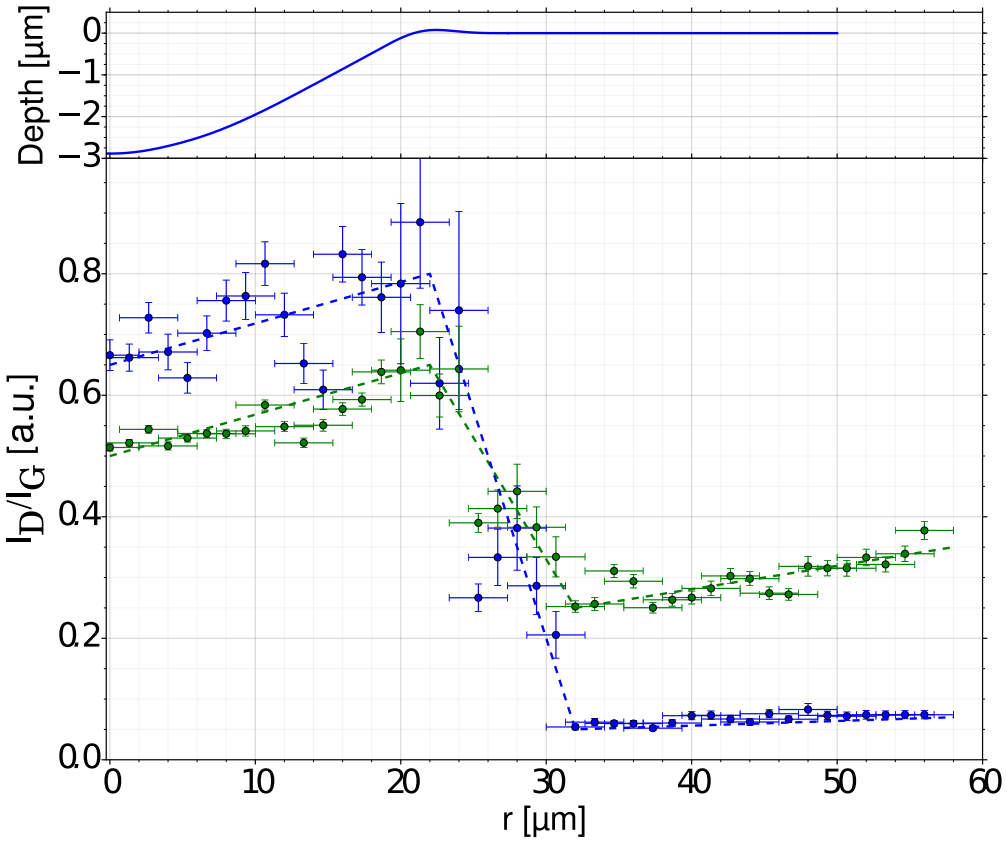

Figure 6.10 : Ratio of the maximum of the peak intensity for the band D and G in green and the Ratio of the integral of the peak intensity for the band D and G in blue. The dotted lines are guide to the eye.

is equal to 200 cm^{-1} at the centre and increases moderately to 250 cm^{-1} with an increase of the radial distance until reaching 24 µm. The moderate increase is suggesting a relative increase of the disorder in the nano-crystalline graphite. Then, the FWHM of the D-band decreases dramatically to around 50 cm^{-1}. The D-band peak also presents a shift from 1400 cm^{-1} to 1350 cm^{-1}. This is in accordance with previously published results that have shown a correlation between the G-band position and the the D-band position [201] further confirming the increase in the disorder for the underlying carbon layer and the amorphous characteristic of the carbon for radial distance over 30 µm. Furthermore, the ratio of the integral of the D-band over the G-band shows that the D-band contribution on the Raman spectra is dramatically

reduced compared to the G-band contribution, which is coherent with a gradual disappearance of the carbon rings that generate the D-band due to the amorphisation of the layer.

6.4.3 TEM analysis

The Raman analysis enables fast analysis of the micro-structure for a wide range of conditions. It has shown that the surface of the crater is composed of nano-crystalline graphite and amorphous carbon. It also suggests that the graphite layer melts for a fluence above 30 J.cm^{-2}. TEM analysis is used to validate the findings of the Raman spectroscopy. Furthermore, TEM enables access to the crystal orientation and understanding of the graphite structure deeper inside the crater [36]. Two lamellae have been prepared to investigate the crystalline structure of the crater for a fluence below and above 30 J.cm^{-2} to investigate the change in crystalline structure. The lamellae are extracted along a radial profile from the centre of the crater. It must be noted that the energy deposited along the profile follows a Gaussian distribution, thus the energy deposited at the centre is higher than at the edge of the crater. The graphite layer has been protected by a Platinum layer during the lamellae preparation, thus the surface layer does not show amorphisation due to the FIB milling.

6.4.3.1 Lamella for a crater exposed to 15 J.cm^{-2}

The area of interest before the lamella extraction at 15 J.cm^{-2} is presented in Figure 6.13.

The lamella for low fluence for a half of the crater is presented in Figure 6.12(a–f). The transition zone between the diamond and the graphite has been highlighted using a blue dashed line and the position of the surface before the ablation (referred to as horizon) is highlighted using a red dotted

line, see Figure 6.12(a). The overview is accompanied by Figure 6.12(b–f) that are HRTEM with the diffraction pattern presented in the inset for each images providing a visual confirmation of the main direction of the c-axis. The transition line between the graphite layer and the diamond is not homogeneous along the crater. This suggests that the mechanism that induces graphitisation at the surface of the diamond is initiated by the nucleation of tiny graphite clusters at the surface assisted by the presence of defects that reduces the graphitisation activation energy [159]. The graphite clusters at the surface defects are used as centres for the propagation of the graphite thus producing a bulging structure along the profile of the crater, see the Figure 6.12(a&b). This effect is especially visible at the edge of the crater for which the energy deposited is low. The propagation of the graphitisation front is also assisted by pre-existing defects in the bulk such as grain boundary that can be observed at the position of the HRTEM in the Figure 6.12(f).

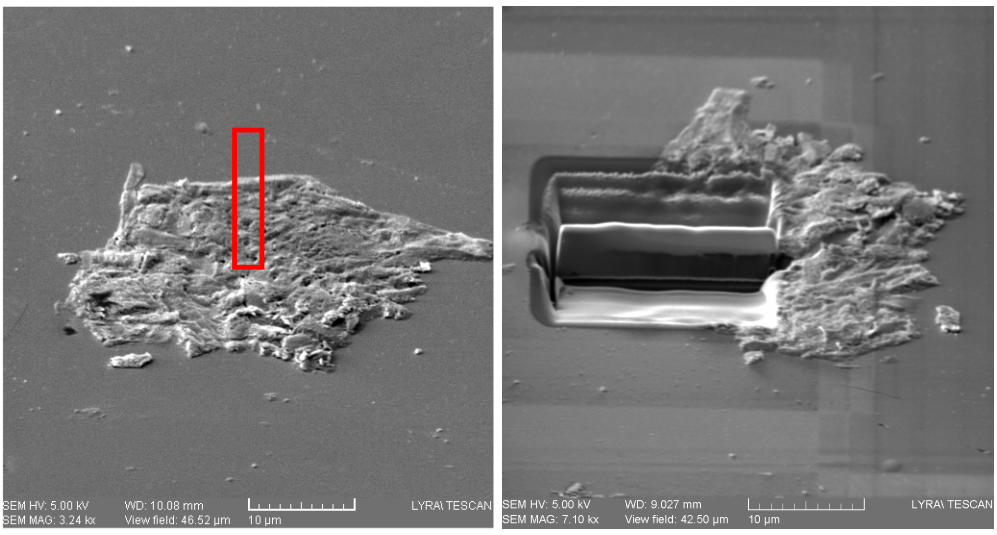

(a) (b)

Figure 6.11 : Overview of the area of interest used to extract the lamella for 15 J.cm^{-2}. The Figure (a) is an overview of the crater before the lamella extraction at an angle of 55°. The red rectangle represents the area of interest for the extraction. The Figure (b) shows the lamella position before lifting.

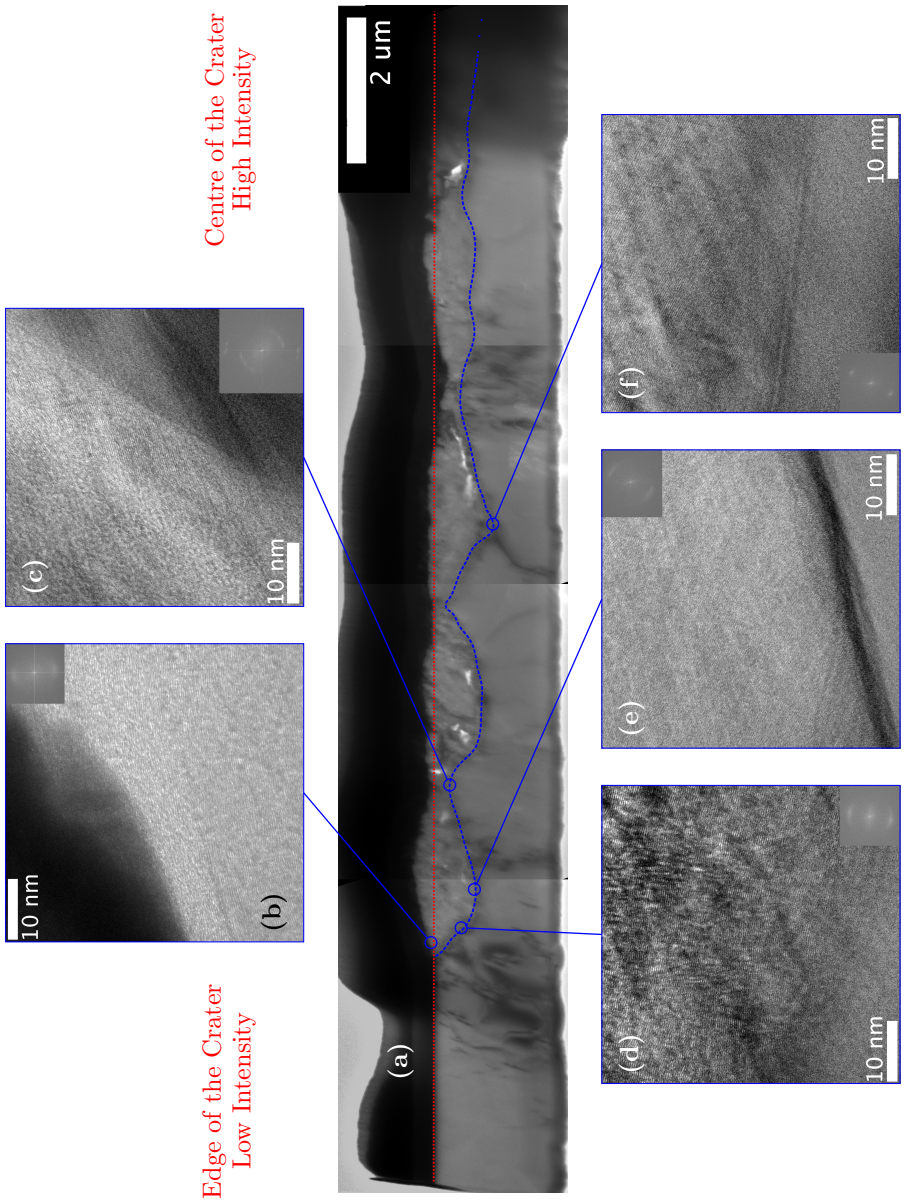

Figure 6.12 : Overview of the TEM lamella for the low power ablation. The red dotted line is the horizon and the blue line represent the transition between diamond and graphite.

At the centre of the crater, the surface is below the horizon, see Figure 6.12(a). The removal of material at the centre of the crater is likely due to the direct sublimation of the graphite without melting. The Raman spectroscopy of craters for fluence below 30 J.cm^{-2} supports this conclusion and shows that the material is composed of nano-crystalline graphite which does not indicate melting. This also suggests that the surface graphite is reaching a temperature above 4000 K and that the pressure above the crater is below 10^7 Pa. At the edge of the crater, the surface is above the horizon, indicating a swelling due to the graphitisation of the diamond, see Figure 6.12(b).

The HRTEM images reveal the formation of orientated graphite layers always in contact with the intact diamond structures. The graphite structures are characterised by a high degree of crystallinity and c-axis alignment toward the surface that is induced by large temperature gradients are generated from the surface towards the interior of the target. In addition, there is no epitaxial (or coaxial) relation between the graphite orientation and the substrate since the graphite c-axis orientation in the same bulge is not directed toward the same direction, see Figure 6.12(b–e). The high degree of c-axis alignment seems also directed toward the centre of each bulge, providing further evidence that the thermal gradient drives the c-axis orientation. The influence of the temperature gradient orientation on the c-axis orientation has been previously observed during pulsed laser machining of trenches [154]. It has previously been discussed that the main driver for the reorientation of the graphite layer is following the same process used to make highly orientated pyrolytic graphite [287]. However, the c-axis orientation in the present experiment is also oriented toward the heat gradient and in the present experiments the graphite is heated above 2000 K for no more than 1 µs that suggests that the graphite directly grows with the observed orientation.

6.4.3.2 Lamella for a crater exposed to 66 J.cm^{-2}

The lamella at high fluence is presented in Figure 6.14, 6.15 and 6.16. The lamella presents three areas, (i) the centre of the crater (at the left side), (ii) the edge of the crater area (in the middle of the lamella) and (iii) buckling/redeposition area outside of the crater.

The first area presents a large recession of the surface due to the laser induced vaporisation of graphite. The thickness of the graphite layer along the profile of the crater is around 450 nm, see Figure 6.14. Interestingly, the graphitisation front between the diamond and the graphite is sharp and presents some variation in the depth of the graphitisation front similar to that present in the TEM from the low fluence lamella showing that the initiation mechanisms for the graphitisation are the same for fluence below and above 30 J.cm^{-2}.

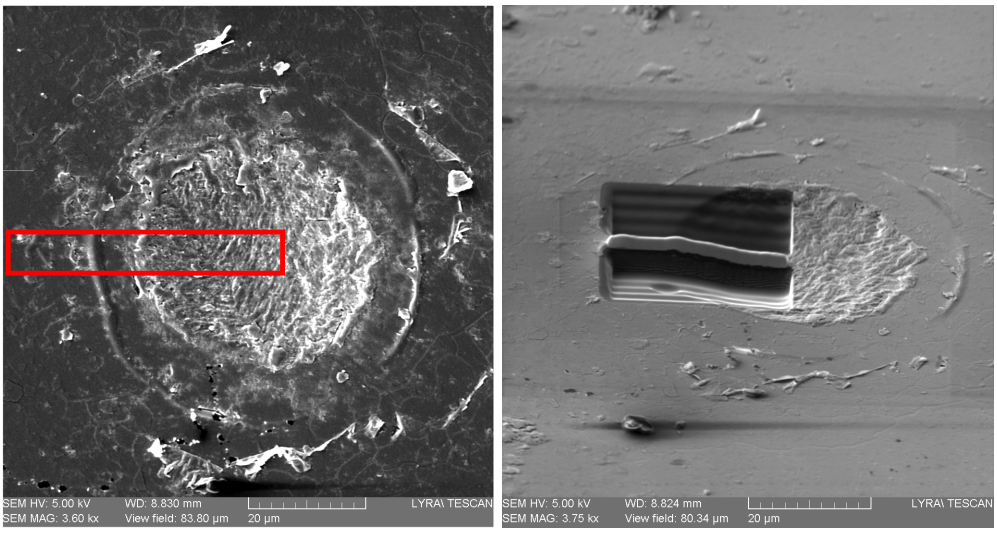

(a) (b)

Figure 6.13 : Overview of the area of interest used to extract the lamella for 66 J.cm^{-1}. The Figure (a) is an overview of the crater before the lamella extraction at an angle of 0°. The red rectangle represents the area of interest for the extraction. The Figure (b) shows the lamella position before lifting.

Figure 6.14 : Overview of the TEM lamella for the high power ablation. The red dotted line is the horizon and the blue line represent the transition between diamond and graphite. The green square is the area for the detailed view of the external part of the crater, see Figure 6.15. The purple square is the area for the detailed view of the buckling, see Figure 6.16.

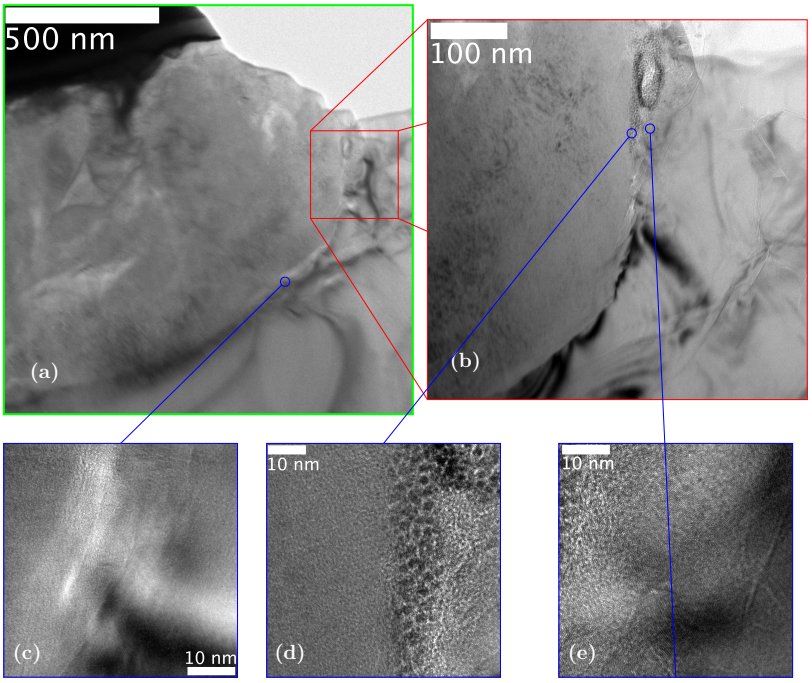

Figure 6.15 : Detailed view of the external part of the crater represented by a green square on Figure 6.14.

The transition area shows a clear swelling with graphite above the horizon ($>$ 200 nm) suggesting that the transition area is largely not affected by material vaporisation, see Figure 6.15. The fluence at the edge of the crater is equivalent to the fluence at the graphitisation threshold, thus one might expect to find similar crystalline structures to the TEM for low fluence. However, the crystalline structure of graphite at the graphitisation interface presents a complex pattern of corrugated graphite for which the c-axis of the graphite layers do not show a preferential direction, see Figure 6.15(c-e). The fringes present in the diamond phase along the interface, see Figure 6.15, indicates a strain of the bulk diamond due to constrained growth of graphite and thermal process. The destruction of crystalline graphite and the formation of nano-crystalline graphite should be a consequence of the strain-induced defects, as reported in HPT results in disordering and amorphisation of materials with covalent bounding [288]. The strain induced defects at the

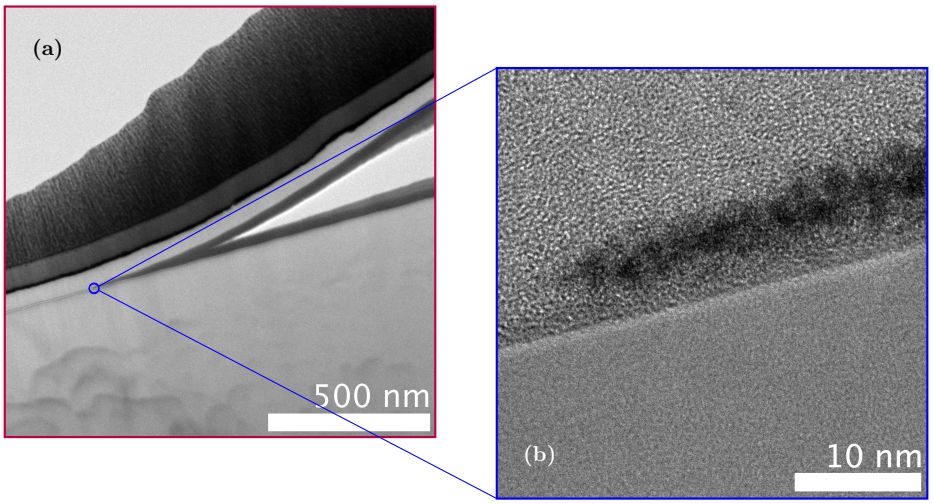

Figure 6.16 : Detailed view of the buckling area represented by a purple square on Figure 6.14.

graphitisation interface suggests that there are two sources of disorder, i.e. the melting at the surface and the strain related to amorphisation inside the bulk of the graphite. Thus, the final crystalline structure alone is not a good indicator of the thermodynamics path that the material undergoes during the laser induced processes and care should be taken when interpreting such results.

Finally, the area outside of the crater presents a thin ($\sim$ 100 nm) and homogeneous layer of redeposited material, see Figure6.16(a). It must be noted that the layer is composed of highly amorphous carbon that correlates well with the Raman spectroscopy measurement, see Figure 6.8 and 6.9. Furthermore, the amorphous carbon thickness is also in agreement with the maximum thickness expected from the absorption length at the Raman excitation wavelength. Interestingly, the amorphous layer presents a buckling around some of the craters in a circular pattern, see Figure 6.16(b). The buckling of amorphous carbon films has already been observed for various deposition techniques [289] and is usually associated with high stress and strain in the film. The circular buckling occurring in these ablation experiments

exhibits the presence of a radial stress originating from the radial variation in the condensation of carbon on the diamond substrate. It must be noted that the crack propagation occurs inside the amorphous carbon and not at the interface between the diamond and amorphous carbon, see Figure 6.16, showing that the fracture surface energy between diamond and amorphous carbon is higher than the energy of crack propagation in carbon.

6.4.3.3 Key findings of the crystalline structure investigations

Finally, the Raman spectroscopy and the TEM analysis show that the level of disorder in the graphite layer dramatically increases for fluence over 30 J.cm^{-2} suggesting graphite melting. The graphite melting is accompanied with evaporation at the surface and re-deposition of carbon during the cooling stage. The redeposited carbon is in amorphous states and its thickness is lower than 145 nm justifying the assumption made in the model for the material condensation. The layer of graphite is composed of a thin layer of amorphous carbon (< 145 nm) with an underlying nano-crystalline layer. The underlying graphite layer increases in disorder when the laser fluence increases. The disorder increase could be due to the growth of the graphite from the bulk diamond that generates high levels of strain leading to defects and refinement of the graphite cluster at the graphitisation front. Furthermore, the crater is surrounded by an highly stressed amorphous layer of carbon due to the redeposition from the carbon vapour.

The developed model (see Section 6.2) was aimed to improve the understanding of the phenomena occurring during pulsed laser ablation of diamond. The model is able to predict certain aspects of the experimental findings such as the thickness of the graphite layer after the interaction, the amount of material ablated, the position of the surface, the pressure of the carbon vapour over the crater. Furthermore, the model for the temperature and the

pressure over the crater are used to estimate if melting will occur during the interaction between the laser and the target in correlation with the graphite melting line in the P-T diagram [141].

6.4.4 Numerical prediction and discussion in relation to the experimental results

Experimental and numerical studies of the graphitisation and plasma shielding effects have been carried out for a range of fluence levels using a single pulse with 30 ns FWHM pulse at 1064 nm. The heat deposited into the material induces graphitisation, evaporation, and plasma breakdown. These effects are studied using the model previously presented. The results from the model are then discussed and compared to the results from the experimental investigations.

The initial interaction between the laser and the target is dominated by a large absorption length of several µm and high thermal diffusivity that characterises the boron doped diamond. Hence, the temperature at the surface of the target is slowly increasing until the heat deposited in the material causes the target to decompose into graphite. The graphitisation of the surface leads to a dramatic increase of the graphite layer thickness due to the change in the absorption coefficient. The growth of the graphite layer is assisted by the positive feedback loop in the energy deposited at the surface, with an increase of the thickness of the graphitisation layer is further increasing the amount of energy absorbed in the thin graphite layer leading to a further increase in the graphitisation layer, see Figure 6.17.

The large increase in the graphite layer speed is counterbalanced by the time necessary for the heat to transmit to the graphitisation front and the speed induced by the swelling leading to a reduction in the graphitisation speed. Similarly, the large increase in the heat deposited at the surface

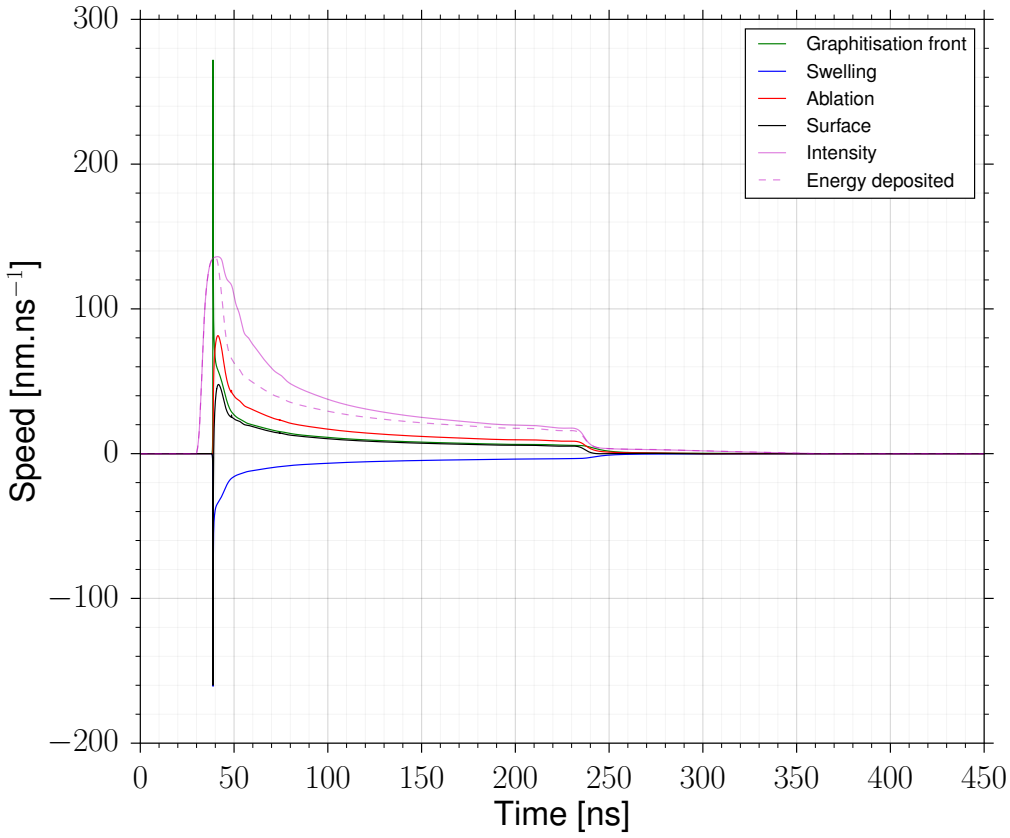

Figure 6.17 : The speed of the graphitisation front, the speed of ablation, the speed of the surface position and the swelling speed due to the density jump at the graphitisation front for a fluence of 63 J.cm^{-2}.

induces the sublimation of the graphite at around 4000 K followed by a melting at 4800 K. The vaporisation of the target leads to a large increase in the pressure of the plume, see Figure 6.19. Then, the position of the interfaces reaches a "steady" state for which the speed of surface position is equal to the speed of the graphitisation front leading to a constant thickness for the graphite layer. It must be noted that the interaction between the target and the plume is crucial in the determination of the amount of material ablated, the amount of energy absorbed by the plasma and the pressure over the plasma. At the initial stage of the plume formation, the plume is characterised by a low temperature for the heavy species ($\sim$ 3000–4000 K) with a high temperature for the electrons. The large difference of temperature is due to

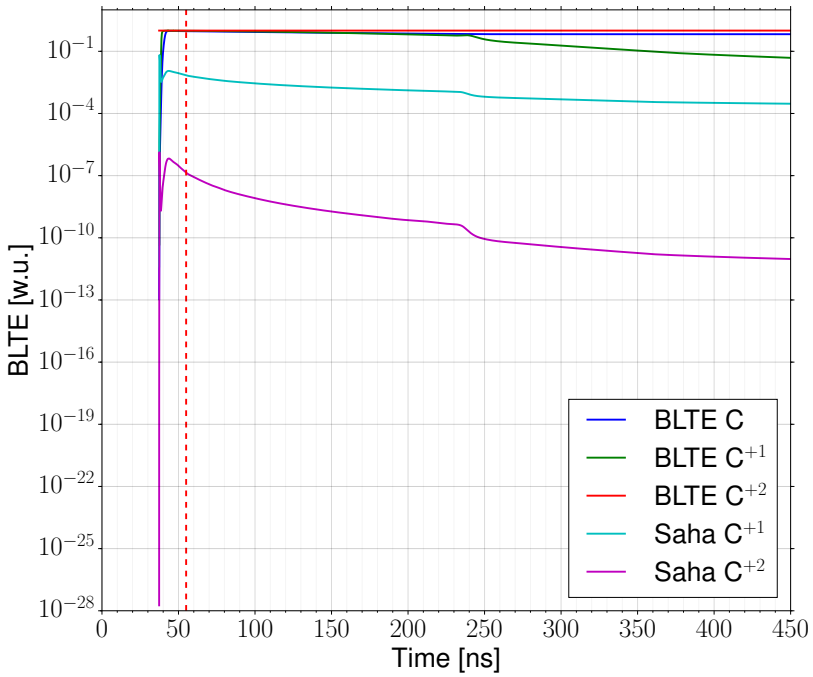

Figure 6.18 : The Boltzmann and Saha equilibrium parameters as a function of the time for a fluence of 66 J.cm^{-2}. The BLTE curves for the heavies species are the minimum ratio of the Boltzmann equilibrium density over the calculated density for all the electronic levels for each degree of ionisation. The Saha curves are calculated using the ratio of the electrons' density and heavies' density with the Saha equilibrium formula [126]. If the Boltzmann-Saha equilibrium is verified the parameters should be equal to 1. If the parameter is greater than 1 then the plasma has a recombination character, while if the parameter is less than 1 the plasma has an ionising character. The red dashed line is represent the breakdown of the plasma for which the plasma reach the Boltzmann equilibrium.

the reduction in temperature predicted by the Knudsen-Knight formulation, see Equation (6.12)–(6.46), with a small population ($\sim 10^{17}$ m^{-3}) of electrons that is heated by the inverse Bremsstrahlung. The temperature of the heavy species is not affected by the increase in the electrons' temperature due to the large difference in the population density (between 5-6 orders of magnitudes). The local thermal equilibrium is not achieved until after the breakdown of the plasma. The increase electron population and temperature is the dominant driver for the breakdown of the plasma that occurs for electron temperature around 10000 K. Interestingly, the electronic levels for the heavies do not

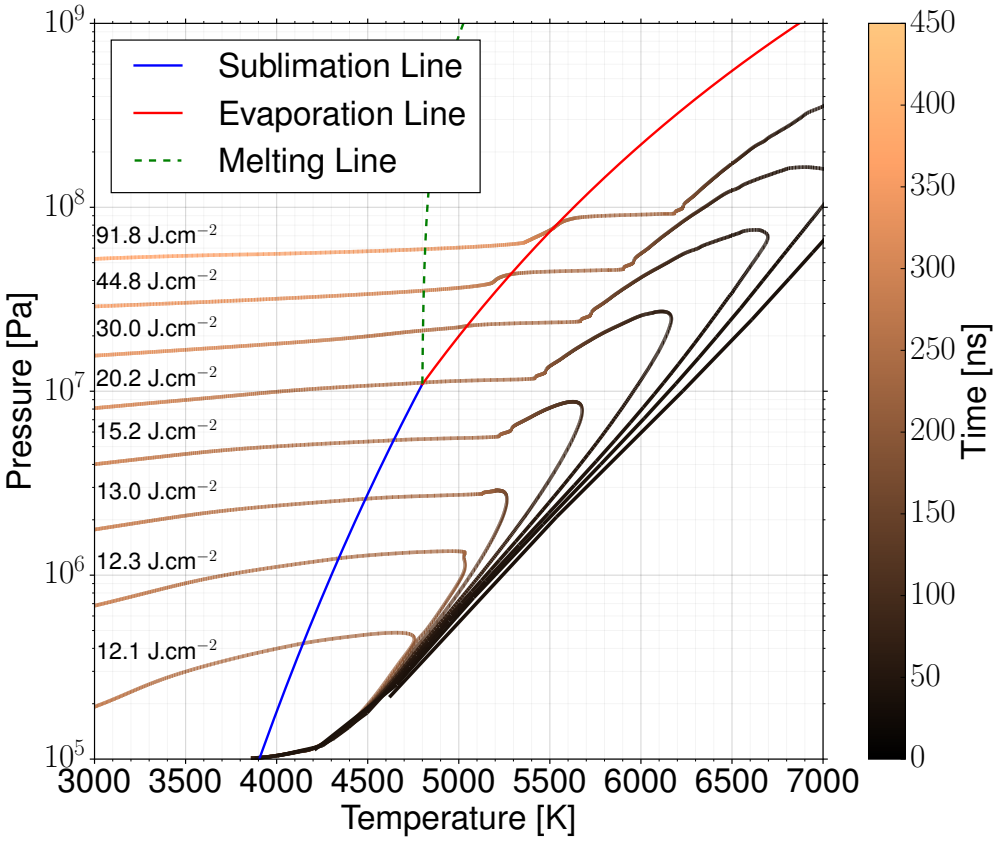

Figure 6.19 : The thermodynamics process path for the surface of the target for several fluences.

present a Boltzmann-Saha equilibrium at the initiation of the plume due to the low amount of collisions with the electrons. The Boltzmann equilibrium for the single ionised carbon is reached after the plasma breakdown marked by the dashed line in the Figure 6.18. It must be noted that the neutral carbon reaches Boltzmann equilibrium after the single ionised carbon, see Figure 6.18. One might expect the neutral carbon to reach Boltzmann equilibrium level first due to the lower energy separation between the electronic levels [126] however the neutral carbon presents low lying levels that are not connected by optically allowed transition to the ground level. This induces a delay in the population levels that rely on the higher density level and the spin/parity forbidden transition to be populated.

The Boltzmann and Saha equilibrium is usually used after the plasma

breakdown [23, 120]. However in the present model, the Saha equilibrium is not established during the duration of the laser pulse, see Figure 6.18. The plasma never reaches the Saha-Boltzmann equilibrium although the Boltzmann and the local temperature equilibrium between the heavy and electrons is reached. The model predicts an electron density higher than the Saha formula [126], see Figure 6.18. For nanosecond plasma during LIP, the density of electrons measured is usually higher than the prediction from the Saha formula [126] suggesting the present model is correctly predicting the plasma evolution occurring during the initial stages of the plasma breakdown and expansion. Usually, models that consider the interaction between a target and nanosecond laser coupled with a collisional radiative model for the plasma consider a relatively small number of fictitious electronic levels [23, 120]. These models have shown that the plasma reaches a Boltzmann-Saha equilibrium after the breakdown that it is in contradiction with experimental results [126] and the present study. This suggests previous studies might not be described correctly the plasma evolution for the electronic levels density if the number of fictitious electronic levels used in the model is too low. Furthermore, electronic levels with different parities and spins for previous model are mixed thus losing the description of the allowed and forbidden transition that might also affect the final distribution of the density in the plasma.

The increase of the temperature and density of the electrons is providing a positive feedback loop for the amount of intensity absorbed by the plasma [269]. The fast and dramatic absorption of energy from the laser generates a large increase in the plasma pressure over the crater, Figure 6.19. The plasma then reaches the maximum pressure and this is followed by an irreversible expansion and decrease of pressure, temperature, density and absorption coefficient. The Raman spectroscopy at the centre of the crater shows

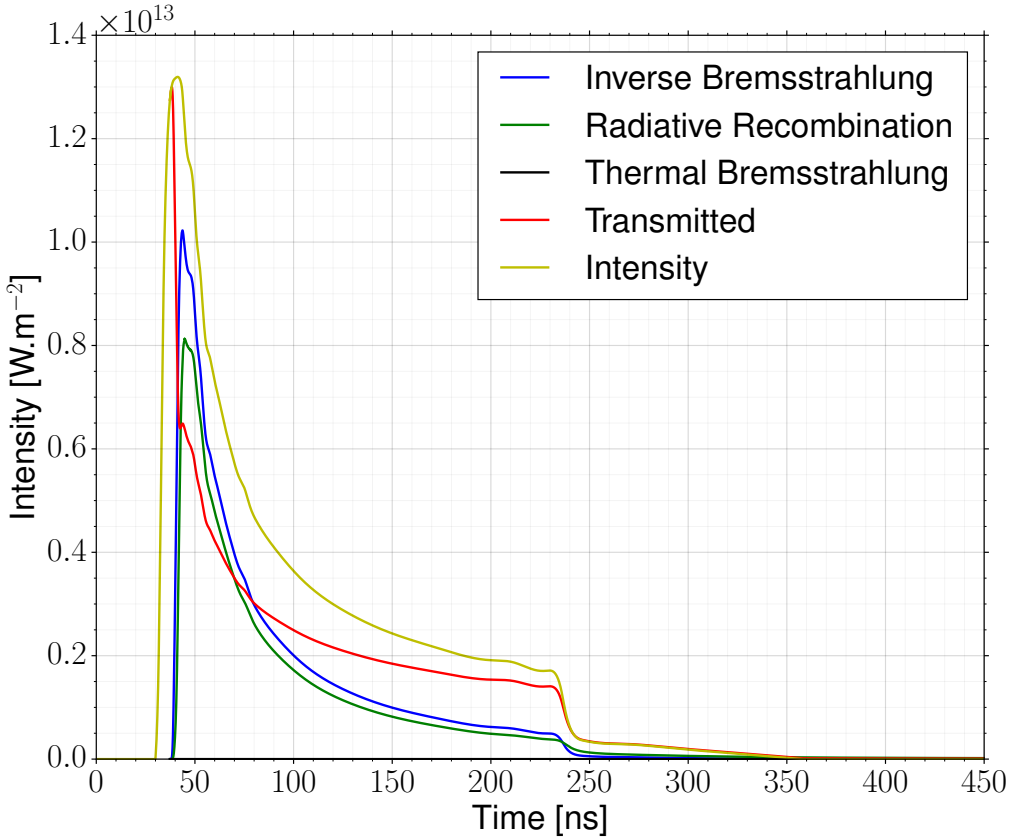

Figure 6.20 : Intensity for the laser intensity, the absorbed intensity, the emitted intensity by the radiative recombination and the thermal Bremsstrahlung and the intensity reaching the target at 66 J.cm^{-2}.

that the crystalline structure of the graphite is altered for fluence over 30 J.cm^{-2}. Interestingly, the plume pressure reaches 10^7 Pa over 30 J.cm^{-2} which corresponds to the experimental melting pressure for graphite [141]. It must be noted that the temperature during the main interaction with the laser pulse (between 50-300 ns) is above 5000 K. Hence, melting should not occur for pressure below several 10^9 Pa [141]. However, the temperature at the end of the pulse reduces dramatically until reaching the triple point temperature ($\sim$ 4800 K). Thus, melting does not occur during the heating phase of the graphite layer but during the cooling phase for which the pressure is above 10^7 Pa, see Figure 6.19. This confirms that the sudden crystalline structure degradation is due to the melting and freezing of graphite during

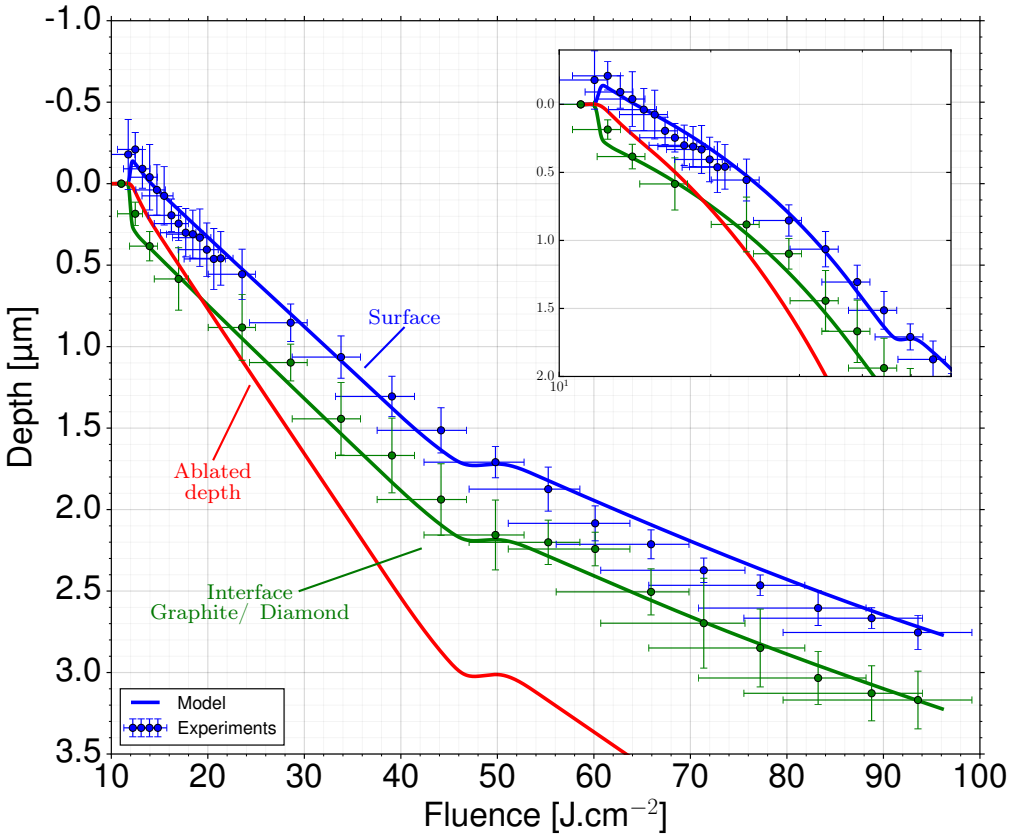

Figure 6.21 : Position of the interfaces for the model and the experiments for the boron doped diamond. The red, blue and green lines are the ablated depth, the interface position of graphite/vacuum and interface position of diamond/graphite respectively. The inset shows a subset of the data in a logarithm scale for the fluence.

the single pulsed ablation of diamond.

The fluences leading to the breakdown of the plasma are also characterised by strong re-emission of UV light due to the radiative recombination of the electrons with the ionised species, see Figure 6.20. The radiative recombination is usually not taken into account for pulsed laser ablation model considering the plasma absorption using a Collisional-Radiative model [23, 120, 125]. In this study, the inclusion of the radiative recombination into the model leads to a reduction of the total amount of energy absorbed by the plasma due to the reduction of the plasma temperature and by the re-emission of energy toward the target. Numerical experiments have shown that the

radiative recombination is essential to the correct prediction of the amount of material removed. The removal of the radiative contribution in the plasma evolution leads to a reduction of the amount of material ablated for higher fluence due to the dramatic increase of energy absorbed after the breakdown. It must be noted that the inclusion of the radiative recombination does not significantly change the amount of energy absorbed from the laser pulse (at the laser wavelength) by the plasma. Thus, this explains the good results provided by previous models when tested only against the intensity measured through the plasma at the laser wavelength [23, 120].

Finally, the positions of the interfaces predicted using the model are in good agreement with the experiment results for the position of the graphitisation front and the surface, see Figure 6.21. It must be noted that the thickness of the graphite layer is almost constant over the range of fluence tested. This is in accordance with the experimental results from the TEM for which the thickness of the graphite layer is constant over the profile of the crater. This confirms that the disorder present deep inside the graphite layer is not due to the melting and recrystallisation, see Figure 6.15.

6.5 Conclusion

Theoretical and experimental results have been used to investigate the ablation of boron doped diamond with nanosecond laser pluses. The simulation shows that the plasma formed by the ablation of diamond is not in Boltzmann and Saha equilibrium during the temporal length of the laser pulse. This suggests that the lumping procedure for the fictitious electronic levels needs to conserve the parity and spin of the electronic levels as well as grouping electronic levels with an energy separation lower than the thermal energy of the plasma during the initial formation. Furthermore, the simulation shows

that the radiative recombination is essential to model the plasma evolution and the amount of energy deposited in the target correctly. For a fluence above 30 J.cm^{-2}, numerical simulations show that the pressure of the plume is above 10^7 Pa. This confirms that melting is the root cause of the change in crystalline structure observed in the graphite layer after 30 J.cm^{-2}. It must be noted that the melting does not occur during the heating phase of the target but during the cooling phase. The analysis of the graphite layer after the laser ablation by Raman spectra and TEM analysis shows a nano-crystalline graphite for low fluence. For fluence over 30 J.cm^{-2}, an thin layer (< 145 nm) of amorphous carbon is redeposited at the surface in association with a large increase in disorder in the nano-crystalline graphite. The simulation and the experimental results suggest that the graphite layer is melting for fluence over 30 J.cm^{-2}. The graphite nuclei are initiated on defect at the surface although the initial position of the nuclei has an influence in the final shape of the graphite layer, the Arrhenius law used in the model correctly predicts the total thickness of the graphite layer suggesting that graphitisation of diamond is thermally driven.

Chapter 7

Conclusion

The main goal of the work done in this thesis was to develop new mathematical frameworks to predict the amount of material ablation and the damage done during nanosecond laser pulse ablation. The main findings of this thesis are that graphitisation is mainly a thermal process, radiative recombination is not negligible during nanosecond pulsed laser ablation once the plasma ignite, graphitisation melting due not occurs during nanosecond pulsed laser ablation of diamond target for low fluence, and the influence of the power and feed speed can be separated to the influence of the material characteristics using a continuous framework. The literature review, see Chapter 2, presents the current state-of-the-art in PLA machining with a particular attention to the specific of diamond target. The development of pulsed laser ablation for diamond workpieces is identified as a promising process for the development of innovative geometry with minute details. However, it has been shown that current approaches lack accurate estimations of the amount of material removed as well as consistency in the understanding of the processes leading to material ablation. Since, PLA cannot be easily observed due to the short time and small space in which the phenomena occur, as well as the large amount of noise produced during the ablation, the development of the models has been focused on the prediction of the thermal damages caused by PLA and the prediction of the resulting topography for large areas machined by PLA. This aim has been pursued in this thesis by developing two new modelling frameworks, validating them, and experimentally investigating

the change in crystalline structure during PLA. First, a physical model in which the mass conservation during the graphitisation of the diamond is taken into account. This work focuses on validating the model approach for two types of carbon allotropes with high sp^3 bounds. Secondly, a simplified model that uses the geometrical properties of the ablation rate to provide accurate and fast predictions on the resulting topography change during PLA machining. Finally, the physical model has been coupled with a collisional radiative model to predict the evolution of the plume over the crater and the shielding provided by the plasma. The change in crystalline structure has been identified as graphitisation due to the thermal transformation and melting during the cooling part of the ablation cycle. It has been proven that both frameworks can predict the amount of ablated material accurately, and the advantages and limitations of each model have previously been discussed in Chapters 4 and 5. Furthermore, the development of the physical model and the understanding of the thermal damage produced by PLA for diamond target is presented in Chapter 6. These developments are therefore a significant contribution to the field, since they address the fundamental understanding of the processes as well as the practical limitation with regards to use of PLA for machining. As a result, the modelling tools presented in this work might enable the development of new practical applications for diamond and related materials. A summary of the major contributions of the thesis are given in the sections below.

7.1 Laser induced surface swelling of high content sp^3 carbon allotrope

In previous work on the simulation of ablation of diamond and related material, the graphitisation of diamond has been treated with a temperature

threshold or by considering only the photo-graphitisation that is negligible for laser in the VIS or IR. Furthermore, the dynamic positions of each interface is not dynamically described, thus the large variation for thermo-optical properties between graphite and diamond cannot be taken into account during the interaction. The new modelling framework discussed in Chapter 4 regards the graphitisation of diamond as a dynamics system for which the graphitisation induces a change in the thermo-optical properties and a swelling of the surface. The new modelling framework allows consistent simulation of the physical processes leading to the swelling of the surface and the vaporisation of the target at the surface. Finally, the model is tested on two carbon materials with high content of sp^3 bounds. The main contributions are summarised below:

- Previous studies rely on constant material properties, and the modelling frameworks used consider the diamond to have similar properties compared to the underlying high content sp^3 bounds carbon allotropes. The study presented in Chapter 4 considers the temperature dependent material properties enabling accurate predictions of the target response to the incoming laser.

- The dynamic position of the interfaces is consistently taken into account, allowing investigations of the target response to the incoming laser. Accurate simulation of the swelling induced by the graphitisation at the surface is essential for correct prediction of the surface position and the graphite layer thickness. Previous modelling approaches usually convert the diamond material to graphite material without changing the position of the interfaces. This means that the system does not conserve the mass of the target during graphitisation. Therefore these approaches overestimate the amount of material ablated at the surface

by using the graphite density for the target evaporation without the corresponding spatial swelling at the surface.

- The model presented in this study has shown good agreement with experimental results from Boron doped diamond, validating the novel approach. Agreement is particularly good for low fluence. This work also shows that the thermal Arrhenius law for graphitisation provides good agreement with experimental results showing that graphitisation during nanosecond pulsed ablation is a thermally induced process.

- Finally, the model is used to predict the positions of the interfaces for tetrahedral amorphous carbon. The model accurately predicts the surface position. Furthermore, the framework is used to estimate the activation energy and rate of graphitisation for ta-C and provides values with an improved accuracy compared to the previously published values.

7.2 Simplified modelling of PLA using continuous trench

In contrast with the physical model, a simplified approach has been developed to enable fast prediction of PLA machining footprints. This is accomplished by focusing on the geometry of the problem and modelling the PLA as an ablation profile which accounts for detailed physical aspects of the system. As discussed in Chapter 2, previous works have focused on modelling the footprint for a single pulse, however they have shown to provide poor agreement with experimental results. A new framework has been developed to accurately predict the topography changes due to laser machining by using trenches to calibrate the model. The model has been developed for generic PLA machining and so does not require material properties, highlighting the

potential of this approach to be extended to a wide range of materials. The model is then calibrated for three targets, a graphite target POCO AF-5, a metal-matrix polycrystalline diamond, and a mechanical CVD diamond. The main developments provided from the study are given below:

- Previous modelling approaches focused on estimating the footprint for a single pulse. These methods are mostly based on the instantaneous removal of material from the target using geometrical methods. The interaction between multiple pulses and trenches is not directly taken into account in the modelling framework, leading to poor agreement with experimental results. The novel methodology presented in this work provides a framework for which the interaction between multiple consecutive pulses is implicatively taken into account during the calibration process. This improvement not only provides more accurate predictions, but also enables the development of novel research lines for PLA machining since the model could be improved to account for a wider number of phenomena occurring during PLA.

- In Chapter 5, the modelling framework is tested against a wide variety of quantifiable tests such as the prediction of the cross-section of trenches for a single trench at constant speed, the depth at the centre of a trench machined using a variable feed speed, and the overlapping of trenches. The model shows good agreement with experimental results and gives on average error lower than 5% for the amount of material removed for a single trench and overlapped trenches at constant speed. The model shows excellent agreement for the depth at the centre of the trench using a variable feed speed with the error between the model and the experimental data lower than the experimental variance of the depth observed.

- The modelling framework also enables understanding of the influence of the surface slope on the amount of ablated material. Previous modelling frameworks have used the surface slope to empirically correct the amount of material ablated at the surface in correlation with the reduction of local fluence on the surface due to the slope. Experimental results have shown that this is not the case. The use of the local fluence to calculate the amount of ablated material is due to a misunderstanding of the ablation process impediment at the surface. The reduction of heat deposited at the surface is partially compensated by an increase in surface area which occurs until the reflectivity at the surface increases due to the incidence angle of the light. The maximum angle for which a constant ablation has been observed for graphite POCO AF-5 is around 70° which is close to Brewster's angle for graphite (θ_B = 75.365 °at 1061 nm). This suggests that the increase of reflectivity with angle of incidence is the main mechanism for the reduction of the ablation with non-flat surface during the machining of trenches.

- One of the main challenges in developing a simplified model which uses empirical results for its calibration is the development of a methodology which provides accurate model parameters. The calibration method associated with the model detailed in Chapter 5 enables accurate calculation of the model parameters from a reduced amount of experimental trials. This is a major advantage with regards to wide acceptance of the model for a variety of experimental conditions which would otherwise hinder usability of the model in a real-world environment.

- The study presented in Chapter 5 shows that the model accurately predicts the topography change for a large area machined using PLA, providing further support for the development of a simplified model

using trenches as a basis for calibration. It must be noted that the tests enable development of a CAD/CAM system which will lead to automation of the tool-path strategy creation for PLA. This will then allow the use of new optimisation methods for PLA machining and the wider use of PLA machining in industries in the same way traditional machining methods (milling, drilling, cutting) are currently used. The validation of a model using trenches-based calibration is therefore a major finding resulting from this work.

7.3 Investigation of crystalline structure due to phase transition

As explained previously in Chapter 6, a new experimental results are presented about the influence of the fluence on the crystalline structure of the target material after the interaction between laser and diamond. This is performed by comparing the PLA specimens for different fluences using Raman spectroscopy and TEM analysis. Experimental results, presented in Chapter 6, illustrate the change in crystalline structure in the graphitised layer with the change of thermodynamic process path leading to a melting of graphite and strain-induced amorphisation at the graphitisation front. Since the experimental results highlight the importance of the pressure applied by the plasma over the crater, the model presented in Chapter 4 is updated to consider the coupled evolution of the target and the carbon plume over the crater. The main contributions of this work are discussed below:

- The aim of this thesis was to develop mathematical frameworks for accurate prediction of PLA surface topography changes and laser induced damages on the target for a wide range of experimental conditions (laser fluence, laser pulse temporal profile, laser wavelength, high sp^3 bounds

carbon allotrope type, etc.). In Chapter 4, a new modelling tool has been presented for the surface graphitisation of diamond during pulsed laser ablation of carbon allotrope with high content sp^3 bounds. The results show that the activation energy for two different types of high content sp^3 bounds carbon target are distinct (3.15 eV for ta-C and 11.0 eV for diamond) suggesting different graphitisation mechanisms. Study of the crystalline structure after the laser-target interaction is a new way to study the fast thermal graphitisation for high content sp^3 bounds, since it enables the description of the thermodynamics process path that the target is going through.

- The use of advanced material characterisation has enable insight into the phenomena occurring during PLA. The use of Raman spectroscopy has resulting in the observation of the graphite melting for an increase of fluence linked to the pressure over the crater. This is the first time that such study has been documented linking directly the thermodynamics process path to the resulting micro-structure in diamond and related material. Moreover, the formation of an amorphous layer from the deposition of the carbon vapour at the surface has also been observed at the centre of the crater as well as outside of the area directly affected by the laser. Furthermore, Raman spectroscopy have shown that there is an increase in the disorder of the graphite lattice for higher fluence. This is likely due to an increase in strain during the growth of the graphite layer from the diamond, which is due to the mechanical constraint of the expanding graphite and the thermal strain induced during ablation.

- TEM analysis has shown that the graphite lattice c-axis for low fluence is oriented toward the surface, suggesting that the temperature gradient is the main driver for crystal orientation. The short time of interaction

between the laser and diamond (< 100 ns) indicates that the graphite directly grows with the c-axis orientated toward the temperature gradient. Investigation of the crystalline structure for high fluence suggest high strain at the interfaces leading to strain-induced amorphisation at the graphitisation front. It also shows that redeposited carbon at the surface is a highly strained amorphous layer leading to buckling of the thin-layer around the crater. It must be noted that the TEM analysis corroborates with the Raman spectroscopy interpretations.

- Modelling results have shown for the first time that the particular melting curve of graphite in the P-T diagrams leads to graphite melting at the cooling stage of the laser ablation. The material therefore reaches a metastable state after crossing the sublimation line, leading to volumetric ablation of the crystal. Numerical experiments have shown that the ablation of diamond, and by extension of graphite cannot be simulated using a traditional description of evaporation without considering influence of the plasma pressure on the thermodynamic process path.

- Previous models that coupled a CR model and heat equations mostly used a relatively small number of fictitious levels. This leads to inconsistent result compared to the literature on Laser Induced Plasma (LIP). Modelling of the carbon plume evolution into a fully ionised plasma requires the consideration of a reasonable number of fictitious electronic levels. Furthermore, the lumping procedure must conserve the azimuthal quantum number and the total angular momentum to enable accurate description of the density of the fictitious electronic levels. Numerical investigations have shown that evolution of the plasma from the initial breakdown cannot be done using the equilibrium relations of

Saha-Boltzmann for PLA. The results presented in Chapter 6 shows that the plasma reaches a Boltzmann equilibrium for a short instant at the peak of pressure and temperature and the Saha equilibrium is never reached during the simulation. The simulation leads to a plasma with an ionising character that is in accordance with experimental results of LIP.

7.4 Future works

The significant contribution of this work to the understanding of PLA opens new opportunities for further research. The limitations and drawbacks of the current approaches will drive further development of improved models that will enhance the current understanding and capability of PLA to manufacture complex 3D parts.

- The development of the 1D finite volume methods can be improved significantly by introducing an EOS for the carbon. Thus, it is enabling future work to provide an improved accuracy for the prediction of the crystalline structure as well as the validation of the state of the carbon during high temperature and high pressure state.

- The validation and integration of stability criteria for liquid metastable phase near the vaporisation curve is already available for coupled plasma-target model for PLA. However, the current work shows the need for a stability criteria in the case of metastable crystal phase near the sublimation curve for PLA of graphite. There is currently, to the knowledge of the author, no stability criteria for metastable crystal near the sublimation curve that have been developed. The ablation of graphite presents an interesting case for which the sublimation of the crystal and the metastability of the crystal phase during the leading

part of the pulse is likely to occurs for nanosecond pulses. Thus, it is providing an experimental validation for an stability criteria of metastable crystal near the sublimation curve.

- The study of the interaction of multiple pulses with diamond target can accelerate understanding of the final thermal damage to the piece during PLA as well as understanding of the formation of highly oriented graphite during the machining of trenches. Study of multiple interactions should be done using a 2D or 3D framework enabling understanding of the amount of material removed during the machining of trenches and the variation of material properties produced by the crystalline structure change.

- The novel simplified model, which can predict the change of topography during PLA machining accurately and at low computational cost, could be extended to other range of materials such as ceramic and metal. Consideration of new materials would be challenging due to the displacement of melted material that might be complex to account for in a simplified manner.

- The final aim for the development of a simplified model is its integration into a CAD/CAM package, thus enabling prediction of the topography change for full 3D workpieces. Furthermore, the simplified model can be used for numerical optimisation of the tool-path, however further works need to be carried out to develop a complete optimisation routine.

- Experimental and numerical results have shown that accurate simulation of the cooling part of the pulse is essential in the description of the crystalline structure. Improvement of the plasma description using the conservation of mass and momentum with a 1D framework will provide further understanding of the plasma evolution and interaction with the

target. Shadowgraphy and measurement of the intensity absorbed by the plasma should provide further constraints on the model, enabling deeper understanding of the material properties and plasma interaction.

Appendix A

Example of the RS274 GCode used for the control of the Aerotech system

A.1 G-code for control of the set-up

Listing A.1: An example of the RS274 G-Code/AeroBasic used for the control of the Aerotech system.

```
1
2 DVAR $hFile
3
4 #include "Definitions.pgm"
5
6 $ComPort=4 // COM used for laser control
7
8 RAMP MODE RATE
9 RAMP RATE 1000000
10 RAMP TYPE SCURVE
11
12 WAIT MODEL AUTO
13
14 #define LASER_ON  GALVO LASEROVERRIDE C ON
15 #define LASER_OFF GALVO LASEROVERRIDE C OFF
16
17 GALVO LASERMODE C 4
```

```
18
19 LASER_OFF
20
21 VELOCITY ON // Continuous control of the speed
22 LOOKAHEAD FAST // Fast lookahead for optimum control
23 ABSOLUTE // Absolute coordinate for continuous control
24
25 $STRGLOB0 = "SH 100" //Set power-amplifier Simmer Current
26 CALL serialwrite
27 $STRGLOB0 = "SW 0" //Set Waveforms number
28 CALL serialwrite
29 $STRGLOB0 = "SR 35000" //Set Pulse Repetition Frequency
30 CALL serialwrite
31 $STRGLOB0 = "SI 950" //Set power-amplifier Active State
32 CALL serialwrite
33
34 G1 X0. Y0. A0. Z11.18 F0.5 // Positioning of the sample
35 G1 C-1. F10 // Positioning of the Axis C
36 DWELL 1. // Pause to stabilise the Axis C
37 SCOPETRIG // Turn on the Scope
38
39 // Start of the continuous move
40 G41 C-1.   F100.
41 G41 C0.000 F100.
42 LASER_ON // Start laser
43 G41 C0.2 F100.
44 G41 C0.4 F200.
45 G41 C0.7 F400.
46 G41 C1. F400.
47 LASER_OFF // End laser
48 G41 C1.5 F300.
49 // End of the continuous move
50 DWELL 0.03
51 SCOPETRIG STOP // Turn off the Scope
```

```
52 G1 C0. // Reset the position of the Axis C
53
54 $STRGLOB0 = "SH 45" // Turn down the Simmer Current
55 CALL serialwrite
56
57 end program // End of the main program
```

Appendix B

Additional information for electron microscopy

B.1 SEM investigation for surface characterisation

The BSE carry a considerable amount of energy. The electric field or gas of the chamber has little influence on the direction of the electrons in the vacuum therefore they will have a straight path from the surface into the detector. To maximise the signal/noise ratio the BSE detector is placed close to the sample and in most designs it is placed just above the sample. The emission of the BSE is strongly influenced by the angle of the beam to the surface. In Figure 3.10(a–b), the angular dependency of the backscattered emission is plotted for two cases. The topography contrast is strong for BSE signal, a relative change of angle dramatically reduces the amount of electrons reaching the detector. Furthermore the BSE move in a straight path toward the detector leading to a strong shadowing, see Figure 3.10(c). The BSE signal is highly dependent on the topography of the surface and topographical information can be extracted. However, the accuracy of the topography contrast is counterbalanced by the penetration depth of the PE. In effect, the PE are tightly focused to a spot size around 2–20 nm [9] but due to multiple scattering the volume of interaction is rather large, see Table B.1 and Figure 3.10. Therefore, the BSE signal is not useful for topographical information. Nevertheless, the

Table B.1: The penetration depth of the primary electron for some chemical elements at two acceleration voltages.

Element (Z)	Acceleration Voltage [kV] 5	Acceleration Voltage [kV] 30
C (6)	0.33	5.27
Al (13)	0.12	1.95
Cu (29)	0.04	0.59
Ag (47)	0.03	0.5

Penetration depth [µm]

Penetration depth [µm]

BSE signal is highly dependent on the atomic number of the element, see Figure B.1, and can be used to differentiate between phases with different elemental compositions. It must be noted that the signal is entangled with the topography contrast, complicating the interpretion of the signal in the case of a rough surface. For polycrystalline material with a specific lattice orientation, a change in contrast can be observed by sample tilting. This is due to the specific arrangement of the atoms in the lattice and different grains can be separated using this phenomenon. In general, BSE signals are useful to image the chemical composition for flat surfaces but are not used to extract topographical information of the surface.

The SE signal is usually used to extract information about the topography. It has many advantages compared to the BSE signal, (i) the proportion of SE is important that facilitate a high signal/noise ratio, see Figure 3.9, (ii) the SE arise from a thin layer of material at the surface of the sample, the signal generation is closely located near the impact of the PE, (iii) the shadowing effect is low because the electrons are attracted by the bias voltage to the detector and do not follow a straight path to the detector, (iv) the yield

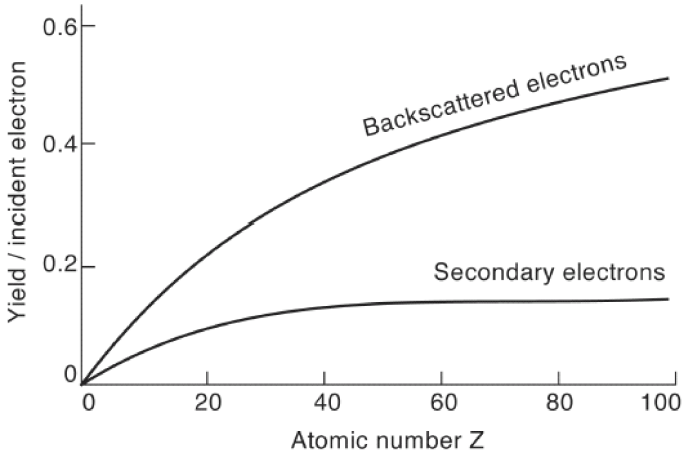

Figure B.1 : The dependency on the atomic number of the yield for BSE and SE.

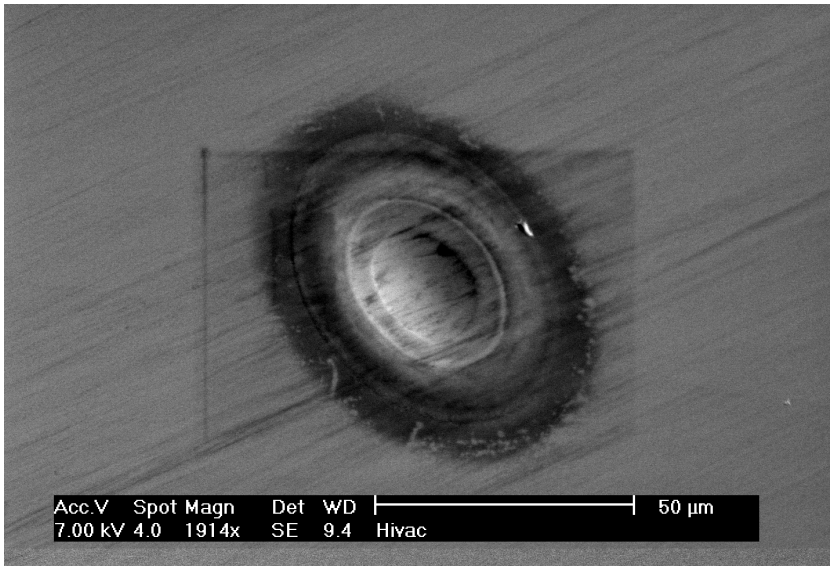

Figure B.2 : The SE image from a Si PLA crater. The edges of the crater are darkened due to oxidation of the silicon occurring during the heating process.

is relatively constant for atomic number over twenty. The topographical information is extracted with the signal dependency of the angle of the surface in relation to the PE beam. The higher the angle, the larger the surface of interaction and the higher the emission of SE. The topography can therefore be deduced from this information. However, the SE signal is not free of

defects. The main SE signal is produced by the interaction of the PE with the sample but it is also likely that the BSE interact with the surface in the same manner as the PE. The BSE are not scattered in the vacuum chamber and thus can travel long distances whilst conserving their energy. The BSE finish their path towards one of the elements in the chamber, creating SE signals from all over the chamber that are attracted to the detector. This creates a background signal that reduces the signal/noise ratio and deteriorates the signal quality. The atomic dependency is negligible for atomic number higher than twenty but the yield is variable for elements with a small atomic number (such as carbon, oxygen or silicon). Furthermore, oxide and impurity lead to strong contrast on the surface (usually appear dark in SE images), see Figure B.2. Moreover, the signal is also dependent on the density of the sample. It is possible to identify the diamond and graphite phase with accuracy due to the change in material properties that changes the yield of SE, see Figure B.5. The edge effect can be problematic for accurate interpretation of the image to extract the topographical information. The beam of PE hits the sample next to the "cliff" because the volume of interaction can be large compared to the radius of curvature of the surface, the SE produced in the volume can escape from the side of the wall and the top. This artificially increases the surface available for the emission of low energy electrons and increases the signal received by the detector. In Figure B.3, the SE signal and its distortion are presented for a typical surface. The simple description of the signal strength presented above need to be commented. The signal is also affected by a shading effect due to the position of the SE detector. If the surface is "hidden" behind another material the signal coming from it will be reduced. Therefore a dip of the signal can be observed after stepped features and this could cause misinterpretation of the surface topography. Furthermore, more SE are excited near edges by the BSE leaving the side wall and BSE can also

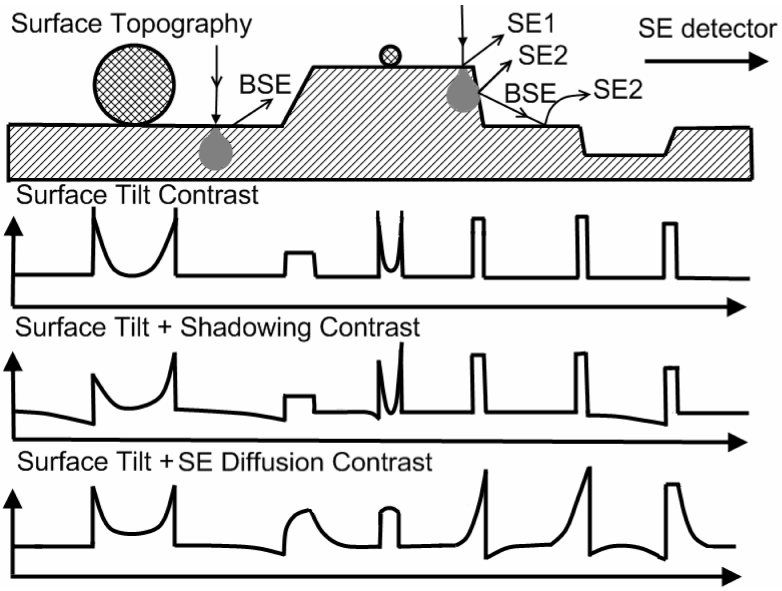

Figure B.3 : The SE signal corrected for the surface tilt contrast, shadowing contrast and the SE diffusion contrast [9].

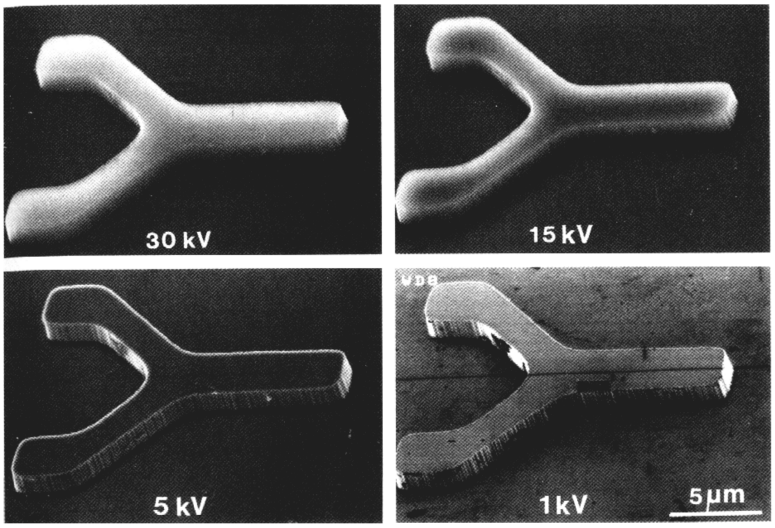

Figure B.4 : The imaging of the SE signal for different acceleration voltages [9].

excite SE when they hit the sample again, see Figure B.3. The SE signal increasing at the edge can be reduced by choosing the right acceleration voltage. In effect, the volume of interaction is greatly dependent on the kinetic energy of the PE, see Table B.1. The reduction of the acceleration voltage can greatly reduce the edge effect and facilitate image interpretation of the topography, see Figure B.4. The image for 1 kV acceleration voltage is clear and the topography contrast can be interpreted accurately. There is little edge effect on the image, only the shadowing contrast can be observed. For 5 kV, the edge are bright and the surface topography is occulted by the brightness of the edge. For higher voltage the edge effect is clearly visible, this is due to the high BSE coefficient of the material imaged. For 30 kV, the topographical information is lost and cannot be interpreted accurately. The acceleration voltage is not neutral on the imaging of the sample topography and must be taken into account for interpretation of the image. Finally, the SE signal is mostly used to extract topographical information about the surface but caution must be taken if the material is not homogeneous or if a high acceleration is used.

The last diagnostic commonly used with SEM is the analysis of the X-Ray signal produced during inelastic collisions. The transition of an electron of

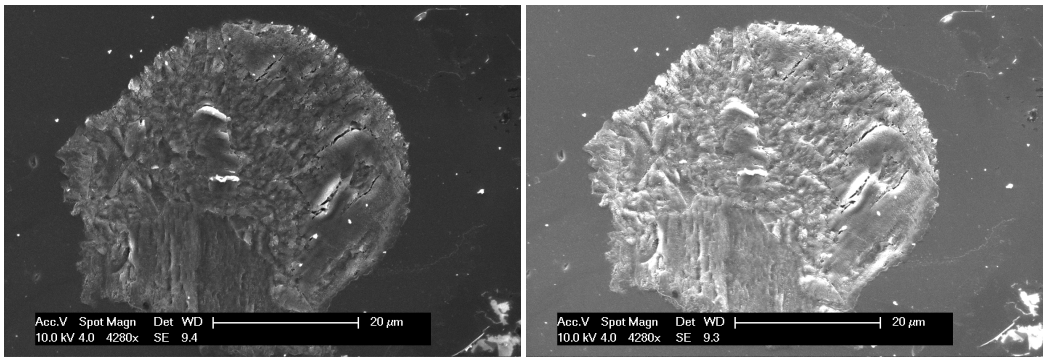

(a) (b)

Figure B.5 : The imaging of the SE signal for a single ablation crater on boron doped diamond for a fluence of 20 J.cm^{-2} at an angle of -10° (a) and 15°(b).

the upper layer to a lower layer of the electron shell produces characteristic energetic X-Ray photons, it is therefore possible to image the qualitative elemental distribution of the sample by measuring the energy distribution in the wavelength space. The volume of interaction is approximately twice the volume for BSE, see Figure 3.9(b). The spatial accuracy of the method is low and is dependent on the acceleration voltage. Furthermore, the cross sections for inelastic collisions are highly dependent on the electron kinetic energy. It is therefore necessary to reach a certain energy before the X-Ray generation is sufficient to be measured by the detector, see Figure B.6. The deconvolution of the peak is done using specialist software. Knowing the peak intensity for pure material, the relative chemical composition can be extracted. The creation of artefacts (doubling energy or re-emission of an X-Ray photon by the detector) generates secondary peaks that worsen the deconvolution of the peak. The technique is reliable but sensitive to impurities on the surface due to the dangling links that attach oxygen or carbon atoms from the atmosphere. Usually, oxygen is neglected in the relative composition of the material. It is also possible to extract information about the subsurface composition of the sample. The volume change with the increase of kinetic energy can be used to extract information about the subsurface chemical composition, however quantitative interpretation of the data is complex and only gives qualitative information about the sample composition.

Finally, the SEM and associate diagnostics offer a fast and reliable way to investigate the surface topography, composition and microstructure, but the signal measurement system and related disadvantages need to be taken into account to correctly interpret the image of the signal. The information presented in this section has shown that signal interpretation can be more complicated and errors can arise from a number of factors that bias the results if not taken into account.

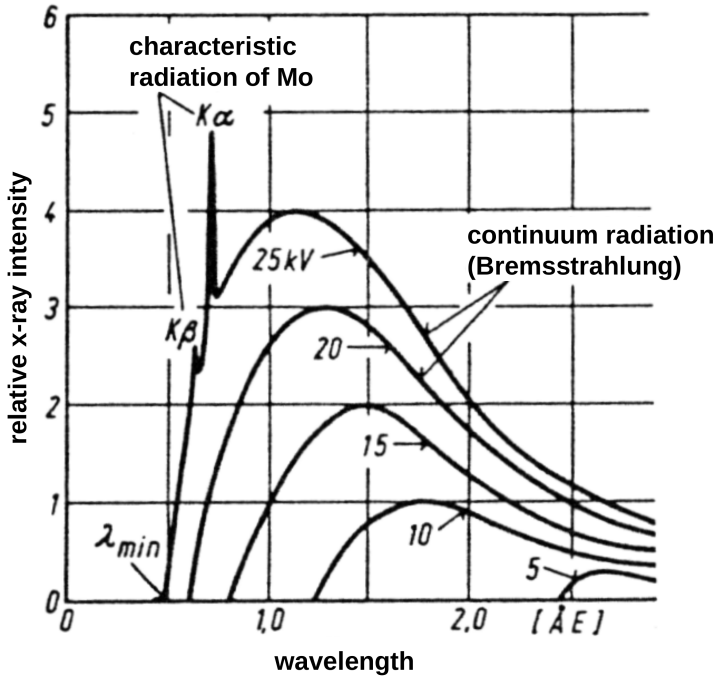

Figure B.6 : The spectral distribution of the X-Ray for Molybdenum for several acceleration voltages. The K_α and K_β are only distinct from the background (due to the Bremsstrahlung radiation) at 25 kV.

Bibliography

[1] G. B. J. Cadot, D. A. Axinte, and J. Billingham. "Continuous trench; pulsed laser ablation for micro-machining applications". In: *International Journal of Machine Tools and Manufacture* 107 (2016), pp. 8–20. ISSN: 08906955. DOI: 10.1016/j.ijmachtools.2016.04.011. URL: (Link).

[2] G. B. J. Cadot, J. Billingham, and D. A. Axinte. "A study of surface swelling caused by graphitisation during pulsed laser ablation of carbon allotrope with high content of sp^3 bounds". In: *Journal of Physics D: Applied Physics* 50 (2017), p. 245301. DOI: 10.1088/1361-6463/aa70fe. URL: (Link).

[3] G. B. J. Cadot, K. Thomas, J. Best, A. Taylor, D. A. Axinte, J. Michler, and J Billingham. "Investigation of the fluence on the microstructure due to phase transition in nanosecond pulsed laser processing of diamond." In: *Carbon – Under Review –* (2017), pp. 1–36. ISSN: 08906955.

[4] A. Bilbao-Guillerna, D. A. Axinte, J Billingham, and G. B. J. Cadot. "Waterjet and laser etching : the nonlinear inverse problem Subject Category : Subject Areas :" in: *Royal Society Open Science* 4 (2017), p. 161031. DOI: 10.1098/rsos.161031. URL: (Link).

[5] A. Bilbao-Guillerna, R. Thiruvallur-Eachambadib, G. B. J. Cadot, D. A. Axinte, J. Billingham, and M. Rommel. "Novel approach based on continuous trench modelling to predict focused ion beam prepared freeform surfaces". In: *Applied Surface Science – Under Review* (2017).

[6] G. B. J. Cadot, A. Bilbao-Guillerna, D. A. Axinte, and J. Billingham. "Modelling pulsed laser ablation using continuous trench for micro-machining applications". In: *AILU Micro-Nano Workshop*. AILU. 14th September 2016, Southampton, 2016.

[7] G. B. J. Cadot, J. Mei, A. Bilbao-Guillerna, D. A. Axinte, and J. Billingham. "Dedicated software platform simulates laser machining". In: *The Laser User* 83 (2017), pp. 34–35.

[8] S. R. P. Silva. *Properties of Amorphous Carbon*. first. EMIS Datareviews Series n°.29. London, UK: INSPEC, 2003, p. 367. ISBN: 9780852969618. URL: (Link).

[9] L. Reimer. *Scanning Electron Microscopy – Physics of Image Formation and Microanalysis*. 2nd ed. Springer-Verlag Berlin Heidelberg, 1998, p. 529. ISBN: 978-3-540-63976-3. DOI: 10.1007/978-3-540-38967-5. URL: (Link).

[10] E. O. Ezugwu, R. B. Da Silva, J. Bonney, and A. R. Machado. "Evaluation of the performance of CBN tools when turning Ti-6Al-4V alloy with high pressure coolant supplies". In: *International Journal of Machine Tools and Manufacture* 45.9 (2005), pp. 1009–1014. ISSN: 08906955. DOI: 10.1016/j.ijmachtools.2004.11.027. URL: (Link).

[11] B. Zhang and T. D. Howes. "Subsurface Evaluation of Ground Ceramics". In: *CIRP Annals - Manufacturing Technology* 44.1 (1995), pp. 263–266. ISSN: 00078506. DOI: 10.1016/S0007-8506(07)62322-1. URL: (Link).

[12] E. O. Ezugwu, J. Bonney, R. B. Da Silva, and O. Çakir. "Surface integrity of finished turned Ti-6Al-4V alloy with PCD tools using conventional and high pressure coolant supplies". In: *International Journal of Machine Tools and Manufacture* 47.6 (2007), pp. 884–891.

ISSN: 08906955. DOI: 10.1016/j.ijmachtools.2006.08.005. URL: (Link).

[13] S. Agarwal and P. V. Rao. "Experimental investigation of surface/-subsurface damage formation and material removal mechanisms in SiC grinding". In: *International Journal of Machine Tools and Manufacture* 48.6 (2008), pp. 698–710. ISSN: 08906955. DOI: 10.1016/j.ijmachtools.2007.10.013. URL: (Link).

[14] STEEP Consortium. *A Synergetic Training Network on Energy Beam Processing: from modelling to industrial applications*. URL: (Link) (visited on 04/17/2015).

[15] N. B. Dahotre and S. P. Harimkar. *Laser fabrication and machining of materials*. First. New York, USA: Springer Science + Business Media, 2008, pp. 1–561. ISBN: 9780387723433. DOI: 10.1007/978-0-387-72344-0. URL: (Link).

[16] FILCO Consortium. *Fibre Delivered Laser Beam Cutting Optimisation*. URL: (Link) (visited on 04/16/2015).

[17] TISA-TD Consortium. *Ultrafast High-Average Power Ti:Sapphire Thin-Disk Oscillators and Amplifiers*. URL: (Link) (visited on 04/17/2015).

[18] HALO Consortium. *High power Adaptable Laser beams for materials prOcessing*. URL: (Link) (visited on 04/16/2015).

[19] ADALAM Consortium. *Sensor based adaptive laser micromachining using ultrashort pulse lasers for zero-failure manufacturing*. URL: (Link) (visited on 04/17/2015).

[20] DIPLAT Consortium. *Enabling advanced functionalities of Diamond and other ultra-hard materials by Integrated Pulsed Laser Ablation Technologies*. URL: (Link) (visited on 04/17/2015).

[21] APPOLO Consortium. *Hub of Application Laboratories for Equipment Assessment in Laser Based Manufacturing*. URL: (Link) (visited on 04/17/2015).

[22] G. Overton, A. Nogee, and C. Holton. *Laser Marketplace 2014: Lasers forge 21st century innovations*. 2014. URL: (Link) (visited on 04/17/2015).

[23] G. Galasso, M. Kaltenbacher, A. Tomaselli, and D. Scarpa. "A unified model to determine the energy partitioning between target and plasma in nanosecond laser ablation of silicon". In: *Journal of Applied Physics* 117.12 (2015), p. 123101. ISSN: 0021-8979. DOI: 10.1063/1.4915118. URL: (Link).

[24] X. Zhao and Y. C. Shin. "Femtosecond laser ablation of aluminum in vacuum and air at high laser intensity". In: *Applied Surface Science* 283 (2013), pp. 94–99. ISSN: 01694332. DOI: 10.1016/j.apsusc.2013.06.037. URL: (Link).

[25] L. Li, M. Hong, M. Schmidt, M. Zhong, A. Malshe, B. Huis in'tVeld, and V. Kovalenko. "Laser nano-manufacturing – State of the art and challenges". In: *CIRP Annals - Manufacturing Technology* 60.2 (2011), pp. 735–755. ISSN: 0007-8506. DOI: 10.1016/j.cirp.2011.05.005. URL: (Link).

[26] C Momma, U Knop, and S Nolte. "Laser cutting of slotted tube coronary stents - state-of-the-art and future developments". In: *Progress in Biomedical Research* 1.February (1999), pp. 39–44. URL: (Link).

[27] P. Butler-Smith, D. Axinte, and M. Daine. "Solid diamond micro-grinding tools: From innovative design and fabrication to preliminary performance evaluation in Ti-6Al-4V". In: *International Journal of Machine Tools and Manufacture* 59 (2012), pp. 55–64. ISSN: 08906955. DOI: 10.1016/j.ijmachtools.2012.03.003. URL: (Link).

[28] V. I. Konov, T. V. Kononenko, and V. V. Kononenko. "Laser Micro- and Nanoprocessing of Diamond Materials". In: *Optical Engineering of Diamond*. Ed. by M. Rich. Weinheim, Germany: John Wiley & Sons, 2013. Chap. 12, pp. 385–443. ISBN: 9783527411023. URL: (Link).

[29] P. W. Butler-smith, D. A. Axinte, M. Pacella, and M. W. Fay. "Micro / nanometric investigations of the effects of laser ablation in the generation of micro-tools from solid CVD diamond structures". In: *Journal of Materials Processing Technology* 213 (2013), pp. 194–200.

[30] D. Autrique, G. Clair, D. L'Hermite, V. Alexiades, A. Bogaerts, and B. Rethfeld. "The role of mass removal mechanisms in the onset of ns-laser induced plasma formation". In: *Journal of Applied Physics* 114.2 (2013), pp. 023301–1–10. ISSN: 00218979. DOI: 10.1063/1.4812577.

[31] M. Stafe. "Theoretical photo-thermo-hydrodynamic approach to the laser ablation of metals". In: *Journal of Applied Physics* 112.12 (2012), p. 123112. ISSN: 00218979. DOI: 10.1063/1.4771692. URL: (Link).

[32] N. M. Bulgakova, A. B. Evtushenko, Y. G. Shukhov, S. I. Kudryashov, and A. V. Bulgakov. "Role of laser-induced plasma in ultradeep drilling of materials by nanosecond laser pulses". In: *Applied Surface Science* 257.24 (2011), pp. 10876–10882. ISSN: 01694332. DOI: 10.1016/j.apsusc.2011.07.126. URL: (Link).

[33] D. Marla, U. V. Bhandarkar, and S. S. Joshi. "Modeling nanosecond pulsed laser ablation: A focus on temperature dependence of material properties". In: *Manufacturing Letters* 2.2 (2014), pp. 13–16. ISSN: 22138463. DOI: 10.1016/j.mfglet.2013.12.001. URL: (Link).

[34] A. Miotello and R. Kelly. "Laser-induced phase explosion: new physical problems when a condensed phase approaches the thermodynamic

critical temperature". In: *Applied Physics A* 73 (1999), pp. 67–73. URL: (Link).

[35] J. Ahn and S.-J. Na. "Three-dimensional thermal simulation of nanosecond laser ablation for semitransparent material". In: *Applied Surface Science* 283 (2013), pp. 115–127. ISSN: 01694332. DOI: 10.1016/j.apsusc.2013.06.048. URL: (Link).

[36] M. Pacella, P. Butler-Smith, D. A. Axinte, and M. Fay. "FIB/TEM/EELS micro/nanometric investigations of the effects of laser ablation on the diamond/binder structure in polycrystalline diamond composites". In: *Journal of Materials Processing Technology* 214.5 (2014), pp. 1153–1161. ISSN: 09240136. DOI: 10.1016/j.jmatprotec.2013.10.007. URL: (Link).

[37] S. Odake, H. Ohfuji, T. Okuchi, H. Kagi, H. Sumiya, and T. Irifune. "Pulsed laser processing of nano-polycrystalline diamond: A comparative study with single crystal diamond". In: *Diamond and Related Materials* 18.5-8 (2009), pp. 877–880. ISSN: 09259635. DOI: 10.1016/j.diamond.2008.10.066. URL: (Link).

[38] T. Kononenko and V. Ralchenko. "Ablation of CVD diamond with nanosecond laser pulses of UV–IR range". In: *Diamond and Related Materials* 7.April (1998), pp. 1623–1627. URL: (Link).

[39] M. C. Kong, C. B. Miron, D. A. Axinte, S. Davies, and J. Kell. "On the relationship between the dynamics of the power density and workpiece surface texture in pulsed laser ablation". In: *CIRP Annals - Manufacturing Technology* 61.1 (2012), pp. 203–206. ISSN: 00078506. DOI: 10.1016/j.cirp.2012.03.038. URL: (Link).

[40] D. Gilbert, M. Stoesslein, D. Axinte, P. Butler-Smith, and J. Kell. "A time based method for predicting the workpiece surface micro-

topography under pulsed laser ablation". In: *Journal of Materials Processing Technology* 214.12 (2014), pp. 3077–3088. ISSN: 09240136. DOI: 10.1016/j.jmatprotec.2014.07.008. URL: (Link).

[41] B. F. Yousef, G. K. Knopf, E. V. Bordatchev, and S. K. Nikumb. "Neural network modeling and analysis of the material removal process during laser machining". In: *The International Journal of Advanced Manufacturing Technology* 22.1-2 (2003), pp. 41–53. ISSN: 0268-3768. DOI: 10.1007/s00170-002-1441-9. URL: (Link).

[42] S. Mishra and V. Yadava. "Modeling and optimization of laser beam percussion drilling of nickel-based superalloy sheet using Nd: YAG laser". In: *Optics and Lasers in Engineering* 51.6 (2013), pp. 681–695. ISSN: 01438166. DOI: 10.1016/j.optlaseng.2013.01.006. URL: (Link).

[43] A. K. Dubey and V. Yadava. "Laser beam machining — A review". In: *International Journal of Machine Tools and Manufacture* 48.6 (2008), pp. 609–628. ISSN: 0890-6955. DOI: 10.1016/j.ijmachtools.2007.10.017. URL: (Link).

[44] J. Hoffman. "The effect of recoil pressure in the ablation of polycrystalline graphite by a nanosecond laser pulse". In: *Journal of Physics D: Applied Physics* 48.23 (2015), p. 235201. ISSN: 0022-3727. DOI: 10.1088/0022-3727/48/23/235201. URL: (Link).

[45] A. I. Lvovsky. "Fresnel Equations". In: *Encyclopedia of Optical Engineering*. August. 2013, pp. 37–41. DOI: 10.1081/E-EOE-120047133. URL: (Link).

[46] N. A. Vasantgadkar, U. V. Bhandarkar, and S. S. Joshi. "A finite element model to predict the ablation depth in pulsed laser ablation".

In: *Thin Solid Films* 519.4 (2010), pp. 1421–1430. ISSN: 0040-6090. DOI: 10.1016/j.tsf.2010.09.016. URL: (Link).

[47] H. D. Vora, S. Santhanakrishnan, S. P. Harimkar, S. K. S. Boetcher, and N. B. Dahotre. "One-dimensional multipulse laser machining of structural alumina: evolution of surface topography". In: *The International Journal of Advanced Manufacturing Technology* 68.1-4 (2013), pp. 69–83. ISSN: 0268-3768. DOI: 10.1007/s00170-012-4709-8. URL: (Link).

[48] L. Balazs, R. Gijbels, and A. Vertes. "Expansion of laser-generated plumes near the plasma ignition threshold". In: *Analytical chemistry* 63.4 (1991), pp. 314–320. URL: (Link).

[49] D. Bergström. "The Absorption of Laser Light by Rough Metal Surfaces". Doctoral Thesis. Luleå University of Technology, 2008, p. 226.

[50] Y. Zhang, S. Li, G. Chen, and J. Mazumder. "Experimental observation and simulation of keyhole dynamics during laser drilling". In: *Optics & Laser Technology* 48 (2013), pp. 405–414. ISSN: 00303992. DOI: 10.1016/j.optlastec.2012.10.039. URL: (Link).

[51] D. Bergstr om, J. Powell, and a. F. H. Kaplan. "A ray-tracing analysis of the absorption of light by smooth and rough metal surfaces". In: *Journal of Applied Physics* 101.11 (2007), p. 113504. ISSN: 00218979. DOI: 10.1063/1.2738417. URL: (Link).

[52] M. Courtois, M. Carin, P. L. Masson, S. Gaied, and M. Balabane. "A new approach to compute multi-reflections of laser beam in a keyhole for heat transfer and fluid flow modelling in laser welding". In: *Journal of Physics D: Applied Physics* 46.50 (2013), p. 505305. ISSN: 0022-3727. DOI: 10.1088/0022-3727/46/50/505305. URL: (Link).

[53] N. M. Bulgakova, V. P. Zhukov, S. V. Sonina, and Y. P. Meshcheryakov. "Modification of transparent materials with ultrashort laser pulses: What is energetically and mechanically meaningful?" In: *Journal of Applied Physics* 118.23 (2015), p. 233108. ISSN: 0021-8979. DOI: 10.1063/1.4937896. URL: (Link).

[54] A. H. A. Lutey. "An improved model for nanosecond pulsed laser ablation of metals". In: *Journal of Applied Physics* 114.8 (2013), p. 083108. ISSN: 00218979. DOI: 10.1063/1.4818513. URL: (Link).

[55] D. Marla, U. V. Bhandarkar, and S. S. Joshi. "Models for predicting temperature dependence of material properties of aluminum". In: *Journal of Physics D: Applied Physics* 47.10 (2014), p. 105306. ISSN: 0022-3727. DOI: 10.1088/0022-3727/47/10/105306. URL: (Link).

[56] T Rangel, D Kecik, P. E. Trevisanutto, G.-M. Rignanese, H. Van Swygenhoven, and V Olevano. "Band structure of gold from many-body perturbation theory". In: *Physical Review B* 86.April 2016 (2012), p. 125125. ISSN: 1098-0121. DOI: 10.1103/PhysRevB.86.125125. arXiv: 1203.4508. URL: (Link).

[57] B. N. Chichkov, C. Momma, S. Nolte, F. von Alvensleben, and A. Tünnermann. "Femtosecond, picosecond and nanosecond laser ablation of solids". In: *Applied Physics A* 63.2 (1996), pp. 109–115.

[58] J. Chelikowsky and M. Cohen. "Nonlocal pseudopotential calculations for the electronic structure of eleven diamond and zinc-blende semiconductors". In: *Physical Review B* 14.2 (1976). URL: (Link).

[59] B. R. Tull. "Femtosecond Laser Ablation of Silicon : Nanoparticles , Doping and Photovoltaics". PhD thesis. Havard University, 2007, p. 174.

[60] R. F. Haglund, J. C. Miller, T Lucatorto, and M De Graef. *Laser Ablation and Desorption*. Experimental Methods in the Physical Sciences. Elsevier Science, 1997, p. 647. ISBN: 9780080860206. URL: (Link).

[61] A. D. Rakic, A. B. Djurisic, J. M. Elazar, and M. L. Majewski. "Optical properties of metallic films for vertical-cavity optoelectronic devices." In: *Applied optics* 37.22 (1998), pp. 5271–5283. ISSN: 0003-6935. DOI: 10.1364/AO.37.005271.

[62] H. R. Phillip and E. A. Taft. "Kramers-Kronig Analysis of Reflectance Data for Diamond". In: *Physical Review* 136.5A (1964), pp. 1445–1448. ISSN: 0031899X. DOI: 10.1103/PhysRev.136.A1445.

[63] P. Dore, A. Nucara, D. Cannavò, G. De Marzi, P. Calvani, A. Marcelli, R. S. Sussmann, A. J. Whitehead, C. N. Dodge, A. J. Krehan, and H. J. Peters. "Infrared Properties of Chemical-Vapor Deposition Polycrystalline Diamond Windows". In: *Applied Optics* 37.24 (1998), p. 5731. ISSN: 0003-6935. DOI: 10.1364/AO.37.005731. URL: (Link).

[64] M. A. Green and M. J. Keevers. "Optical properties of intrinsic silicon at 300 K". In: *Progress in Photovoltaics: Research and Applications* 3.3 (1995), pp. 189–192. ISSN: 1099-159X. DOI: 10.1002/pip.4670030303. URL: (Link).

[65] D. Chandler-Horowitz and P. M. Amirtharaj. "High-accuracy, mid-infrared (450 $\text{cm}^{-1} \leq \omega \leq 4000\ \text{cm}^{-1}$) refractive index values of silicon". In: *Journal of Applied Physics* 97.2005 (2005), p. 123526. ISSN: 00218979. DOI: 10.1063/1.1923612. URL: (Link).

[66] W. Saslow, T. K. Bergstresse, and M. L. Cohen. "Band structure and optical properties of diamond". In: *Physical review letters* 16.9 (1966), pp. 354–356. ISSN: 0031-9007. DOI: 10.1103/PhysRevLett.16.354.

[67] R. P. Mildren. "Intrinsic Optical properties of Diamond". In: *Optical Engineering of Diamond*. Vol. 1. Weinheim, Germany: John Wiley & Sons, 2013. Chap. First, pp. 1–34. ISBN: 9783527411023. DOI: 10.1002/9783527648603.ch1. URL: (Link).

[68] K. Sokolowski-Tinten, J. Bialkowski, and D. Von Der Linde. "Ultrafast laser-induced order-disorder transitions in semiconductors". In: *Physical Review B* 51.20 (1995), pp. 14186–14198. ISSN: 01631829. DOI: 10.1103/PhysRevB.51.14186.

[69] P. Pronko, P. V. Rompay, C. Horvath, X. Liu, T. Juhasz, and G. Mourou. "Avalanche ionization and dielectric breakdown in silicon withlaser pulses". In: *Physical Review B* 58.5 (1998), pp. 2387–2390. ISSN: 0163-1829. DOI: 10.1109/CLEO.1998.676562.

[70] H. B. Nielsen, J Reif, E Matthias, E Westin, and A Rosén. "Multiphoton-Induced Desorption from BaF_2(111)". In: *Desorption Induced by Electronic Transitions DIET III: Proceedings of the Third International Workshop*. Ed. by R. H. Stulen and M. L. Knotek. Berlin, Heidelberg: Springer Berlin Heidelberg, 1988. Chap. Multiphoto, pp. 266–273. ISBN: 978-3-642-73728-2. DOI: 10.1007/978-3-642-73728-2_39. URL: (Link).

[71] H. Dachraoui and W. Husinsky. "Thresholds of plasma formation in silicon identified by optimizing the ablation laser pulse form". In: *Physical Review Letters* 97.10 (2006), pp. 1–4. ISSN: 00319007. DOI: 10.1103/PhysRevLett.97.107601.

[72] S. I. Kudryashov and V. I. Emel'yanov. "Band gap collapse and ultrafast "cold" melting of silicon during femtosecond laser pulse". In: *Journal of Experimental and Theoretical Physics Letters* 73.5 (2001), pp. 228–231. ISSN: 0021-3640. DOI: 10.1134/1.1371059. URL: (Link).

[73] D. Marla, U. V. Bhandarkar, and S. S. Joshi. "Critical assessment of the issues in the modeling of ablation and plasma expansion processes in the pulsed laser deposition of metals". In: *Journal of Applied Physics* 109.2 (2011), p. 021101. ISSN: 00218979. DOI: 10.1063/1.3537838. URL: (Link).

[74] G. Tas and H. J. Maris. "Electron diffusion in metals studied by picosecond ultrasonics". In: *Physical Review B* 49.21 (1994), pp. 15046–15054. ISSN: 01631829. DOI: 10.1103/PhysRevB.49.15046.

[75] E. Gamaly. "The physics of ultra-short laser interaction with solids at non-relativistic intensities". In: *Physics Reports* 508.4-5 (2011), pp. 91–243. ISSN: 03701573. DOI: 10.1016/j.physrep.2011.07.002. URL: (Link).

[76] X. Zhao and Y. C. Shin. "A two-dimensional comprehensive hydrodynamic model for femtosecond laser pulse interaction with metals". In: *Journal of Physics D: Applied Physics* 45.10 (2012), p. 105201. ISSN: 0022-3727. DOI: 10.1088/0022-3727/45/10/105201. URL: (Link).

[77] M. S. Brown and C. B. Arnold. "Laser Precision Microfabrication". In: *Springer Series in Materials Science* 135.0933-033X (2010), pp. 91–120. ISSN: 00914916. DOI: 10.1007/978-3-642-10523-4. arXiv: arXiv:1011.1669v3. URL: (Link).

[78] S. Garnov, V. Konov, and T Kononenko. "Microsecond Laser Material Processing at 1.06 µm". In: *LASER PHYSICS - Rapid Communications* 14.6 (2004), pp. 910–915. URL: (Link).

[79] V. V. Semak and T. F. Miller. "Simulation of laser penetration efficiency". In: *Journal of Physics D: Applied Physics* 46.38 (2013), p. 385501. ISSN: 0022-3727. DOI: 10.1088/0022-3727/46/38/385501. URL: (Link).

[80] J. Eizenkop, I. Avrutsky, D. G. Georgiev, and V. Chaudchary. "Single-pulse excimer laser nanostructuring of silicon: A heat transfer problem and surface morphology". In: *Journal of Applied Physics* 103.9 (2008), pp. 1–6. ISSN: 00218979. DOI: 10.1063/1.2910196.

[81] K. L. Wlodarczyk, N. J. Weston, M. Ardron, and D. P. Hand. "Direct CO_2 laser-based generation of holographic structures on the surface of glass". In: *Optics Express* 24.2 (2016), p. 1447. ISSN: 1094-4087. DOI: 10.1364/OE.24.001447. URL: (Link).

[82] A. Ben-Yakar, A. Harkin, J. Ashmore, R. L. Byer, and H. a. Stone. "Thermal and fluid processes of a thin melt zone during femtosecond laser ablation of glass: the formation of rims by single laser pulses". In: *Journal of Physics D: Applied Physics* 40.5 (2007), pp. 1447–1459. ISSN: 0022-3727. DOI: 10.1088/0022-3727/40/5/021. URL: (Link).

[83] W. B. Pietenpol. "Surface tension of molten glass". In: *Journal of Applied Physics* 7.1 (1936), pp. 26–31. ISSN: 01486349. DOI: 10.1063/1.1745341.

[84] S. C. Chen, D. G. Cahill, and C. P. Grigoropoulos. "Melting and Surface Deformation in Pulsed Laser Surface Micromodification of Ni-P Disks". In: *Journal of Heat Transfer* 122.1 (2000), p. 107. ISSN: 00221481. DOI: 10.1115/1.521441.

[85] K.-H. Leitz, B. Redlingshöfer, Y. Reg, A. Otto, and M. Schmidt. "Metal Ablation with Short and Ultrashort Laser Pulses". In: *Physics Procedia* 12 (2011), pp. 230–238. ISSN: 18753892. DOI: 10.1016/j.phpro.2011.03.128. URL: (Link).

[86] D. A. Willis and X Xu. "Transport Phenomena and Droplet Formation During Pulsed Laser Interaction With Thin Films". In: *J. Heat Transfer* 122.November 2000 (2000), p. 763.

[87] N. Bulgakova, R. Stoian, a. Rosenfeld, I. Hertel, and E. Campbell. "Electronic transport and consequences for material removal in ultrafast pulsed laser ablation of materials". In: *Physical Review B* 69.5 (2004), p. 054102. ISSN: 1098-0121. DOI: 10.1103/PhysRevB.69.054102. URL: (Link).

[88] I. Langmuir. "The Vapor Pressure of Metallic Tungsten". In: *Physical Review* 2.5 (1913), pp. 329–342.

[89] N. Bulgakova and A. Bulgakov. "Pulsed laser ablation of solids : transition from normal vaporization". In: *Applied Physics A: Materials Science & Processing* 208.2 (2001), pp. 199–208.

[90] C. J. Knight. "Theoretical Modeling of Rapid Surface Vaporization with Back Pressure". In: *AIAA Journal* 17.5 (1979), pp. 519–523. ISSN: 0001-1452. DOI: 10.2514/3.61164. URL: (Link).

[91] S. Anisimov. "Vaporization of metal absorbing laser radiation". In: *Soviet Physics JETP* 27.1 (1968), pp. 2–3. URL: (Link).

[92] O. Ellegaard, J. Schou, and H. Urbassek. "Monte Carlo description of gas flow from laser-evaporated silver". In: *Applied Physics A: Materials Science & Processing* 69.7 (1999), S577–S581. ISSN: 0947-8396. DOI: 10.1007/s003390051479. URL: (Link).

[93] A. V. Gusarov and I. Smurov. "Gas-dynamic boundary conditions of evaporation and condensation: Numerical analysis of the Knudsen layer". In: *Physics of Fluids* 14.12 (2002), pp. 4242–4255. ISSN: 1070-6631. DOI: 10.1063/1.1516211. URL: (Link).

[94] N. Bulgakova, A. Bulgakov, and L. Babich. "Energy balance of pulsed laser ablation: thermal model revised". In: *Applied Physics A: Materials Science & Processing* 79.4-6 (2004), pp. 1323–1326. ISSN: 0947-8396. DOI: 10.1007/s00339-004-2763-2. URL: (Link).

[95] A. Morozov. "Thermal model of pulsed laser ablation: back flux contribution". In: *Applied Physics A: Materials Science & Processing* 79.4-6 (2004), pp. 997–999. ISSN: 0947-8396. DOI: 10.1007/s00339-004-2613-2. URL: (Link).

[96] J. H. Yoo, S. H. Jeong, X. L. Mao, R. Greif, and R. E. Russo. "Evidence for phase-explosion and generation of large particles during high power nanosecond laser ablation of silicon". In: *Applied Physics Letters* 76.6 (2000), p. 783. ISSN: 00036951. DOI: 10.1063/1.125894. URL: (Link).

[97] Q. Lu, S. S. Mao, X. Mao, and R. E. Russo. "Theory analysis of wavelength dependence of laser-induced phase explosion of silicon". In: *Journal of Applied Physics* 104.8 (2008), p. 083301. ISSN: 00218979. DOI: 10.1063/1.2978369. URL: (Link).

[98] C. Porneala and D. a. Willis. "Time-resolved dynamics of nanosecond laser-induced phase explosion". In: *Journal of Physics D: Applied Physics* 42.15 (2009), p. 155503. ISSN: 0022-3727. DOI: 10.1088/0022-3727/42/15/155503. URL: (Link).

[99] J. M. Fishburn, M. J. Withford, D. W. Coutts, and J. A. Piper. "Study of the fluence dependent interplay between laser induced material removal mechanisms in metals: Vaporization, melt displacement and melt ejection". In: *Applied Surface Science* 252.14 (2006), pp. 5182–5188. ISSN: 01694332. DOI: 10.1016/j.apsusc.2005.07.053.

[100] V. P. Skripov. *Metastable liquids*. Ed. by D. Slutzkin. Halsted press book. New York: John Wiley & Sons, 1974, p. 272. ISBN: 9780470795460. URL: (Link).

[101] J. D. van der Waals. *Over de continuiteit van den gas- en vloeistoftoestand*. Leiden: A. W. Sijthoff, 1873, p. 135. URL: (Link).

[102] E. A. Guggenheim. "The Principle of Corresponding States". In: *The Journal of Chemical Physics* 13.7 (1945), pp. 253–261. ISSN: 00219606. DOI: 10.1063/1.1724033. URL: (Link).

[103] R. M. More, K. H. Warren, D. A. Young, and G. B. Zimmerman. "A new quotidian equation of state (QEOS) for hot dense matter". In: *Physics of Fluids* 31.10 (1988), pp. 3059–3078. ISSN: 10897666. DOI: 10.1063/1.866963. URL: (Link).

[104] G. I. Kerley and L. Chhabildas. *Multicomponent-Multiphase Equation of State for Carbon*. Tech. rep. September. Albuquerque: Sandia National Laboratories, 2001, pp. 1–43. URL: (Link).

[105] F. Colonna, A. Fasolino, and E. Meijer. "High-pressure high-temperature equation of state of graphite from Monte Carlo simulations". In: *Carbon* 49.2 (2011), pp. 364–368. ISSN: 00086223. DOI: 10.1016/j.carbon.2010.09.029. URL: (Link).

[106] G. Soave. "Equilibrium constants from a modified Redlich-Kwong equation of state". In: *Chemical Engineering Science* 27.6 (1972), pp. 1197–1203. ISSN: 00092509. DOI: 10.1016/0009-2509(72)80096-4.

[107] S. Faik, M. M. Basko, A. Tauschwitz, I. Iosilevskiy, and J. a. Maruhn. "Dynamics of volumetrically heated matter passing through the liquid-vapor metastable states". In: *High Energy Density Physics* 8.4 (2012), pp. 349–359. ISSN: 15741818. DOI: 10.1016/j.hedp.2012.08.003. arXiv: 1205.2579. URL: (Link).

[108] R. W. Munn. "Role of the elastic constants in negative thermal expansion of axial solids". In: *Journal of Physics C: Solid State Physics* 5 (1971), pp. 535–542. ISSN: 0022-3719. DOI: 10.1088/0022-3719/5/5/005.

[109] D. Johnston. "Advances in Thermodynamics of the van der Waals Fluid". In: 83.6 (2014), p. 573. ISSN: 1943-2909. DOI: 10.1088/978-1-627-05532-1. arXiv: 1402.1205. URL: (Link).

[110] S Balibar and F Caupin. "Metastable liquids". In: *Journal of Physics: Condensed Matter* 15.1 (2002), S75–S82. ISSN: 0953-8984. DOI: 10.1088/0953-8984/15/1/308.

[111] R. Apfel. "Water superheated to 279.5 °C at atmospheric pressure". In: *Nature* 238 (1972), pp. 63–64. URL: (Link).

[112] Q. Zheng, D. J. Durben, G. H. Wolf, and C. A. Angell. "Liquids at large negative pressures: water at the homogeneous nucleation limit." In: *Science (New York, N.Y.)* 254.5033 (1991), pp. 829–32. ISSN: 0036-8075. DOI: 10.1126/science.254.5033.829. URL: (Link).

[113] Q. Lu, S. S. Mao, X. Mao, and R. E. Russo. "Delayed phase explosion during high-power nanosecond laser ablation of silicon". In: *Applied Physics Letters* 80.17 (2002), p. 3072. ISSN: 00036951. DOI: 10.1063/1.1473862. URL: (Link).

[114] P. V. Skripov and A. P. Skripov. "The phenomenon of superheat of liquids: In memory of Vladimir P. Skripov". In: *International Journal of Thermophysics* 31.4-5 (2010), pp. 816–830. ISSN: 0195928X. DOI: 10.1007/s10765-010-0738-4.

[115] J. V. Sengers and J. M. H. L. Sengers. "THERMODYNAMIC BEHAVIOR OF FLUIDS NEAR THE CRITICAL POINT". In: *Annual Review of Physical Chemistry* 37 (1986), pp. 189–222. DOI: 10.1146/annurev.pc.37.100186.001201.

[116] K. H. Song and X. Xu. "Explosive phase transformation in excimer laser ablation". In: *Applied Surface Science* 127-129 (1998), pp. 111–

116. ISSN: 01694332. DOI: 10.1016/S0169-4332(97)00619-3. URL: (Link).

[117] F. Vidal, T. Johnston, S. Laville, O. Barthélemy, M. Chaker, B. Le Drogoff, J. Margot, and M. Sabsabi. "Critical-Point Phase Separation in Laser Ablation of Conductors". In: *Physical Review Letters* 86.12 (2001), pp. 2573–2576. ISSN: 0031-9007. DOI: 10.1103/PhysRevLett.86.2573. URL: (Link).

[118] J. J. Chang and B. E. Warner. "Laser-plasma interaction during visible-laser ablation of methods". In: *Applied Physics Letters* 69.4 (1996), p. 473. ISSN: 00036951. DOI: 10.1063/1.118144. URL: (Link).

[119] J König, S Nolte, and a Tünnermann. "Plasma evolution during metal ablation with ultrashort laser pulses." In: *Optics express* 13.26 (2005), pp. 10597–607. ISSN: 1094-4087. URL: (Link).

[120] D. Autrique, I. Gornushkin, V. Alexiades, Z. Chen, A. Bogaerts, and B. Rethfeld. "Revisiting the interplay between ablation, collisional, and radiative processes during ns-laser ablation". In: *Applied Physics Letters* 103.17 (2013), pp. 174102–1–5. ISSN: 00036951. DOI: 10.1063/1.4826505.

[121] D. Autrique, V. Alexiades, and H. Khanal. "HYDRODYNAMIC MODELING OF ns—LASER ABLATION". In: *Ninth Mississippi State Conference on Differential Equations and Computational Simulations*. Ed. by R. P. Agarwal. Starkville: Departement of Mathematics, Texas State University, 2012, pp. 1–14.

[122] D. Autrique and V. Alexiades. "Comment on "laser ablation of Cu and plume expansion into 1 atm ambient gas" [J. Appl. Phys. 97, 063305 (2005)]". In: *Journal of Applied Physics* 115.16 (2014). ISSN: 10897550. DOI: 10.1063/1.4872325. URL: (Link).

[123] S. Amoruso, R. Bruzzese, N. Spinelli, and R Velotta. "Characterization of laser-ablation plasmas". In: *Journal of Physics B: Atomic, Molecular and Optical Physics* 32.14 (1999), R131. ISSN: 0953-4075. DOI: 10.1088/0953-4075/32/14/201. URL: (Link).

[124] R. Rozman, I. Grabec, and E. Govekar. "Influence of absorption mechanisms on laser-induced plasma plume". In: *Applied Surface Science* 254.11 (2008), pp. 3295–3305. ISSN: 01694332. DOI: 10.1016/j.apsusc.2007.11.029. URL: (Link).

[125] V. Morel and A. Bultel. "Theoretical study of the formation mechanism of laser-induced aluminum plasmas using Nd:YAG fundamental, second or third harmonics". In: *Spectrochimica Acta - Part B Atomic Spectroscopy* 94-95 (2014), pp. 63–70. ISSN: 05848547. DOI: 10.1016/j.sab.2014.03.003. URL: (Link).

[126] G. Cristoforetti, A. De Giacomo, M. Dell'Aglio, S. Legnaioli, E. Tognoni, V. Palleschi, and N. Omenetto. "Local Thermodynamic Equilibrium in Laser-Induced Breakdown Spectroscopy: Beyond the McWhirter criterion". In: *Spectrochimica Acta - Part B Atomic Spectroscopy* 65.1 (2010), pp. 86–95. ISSN: 05848547. DOI: 10.1016/j.sab.2009.11.005. URL: (Link).

[127] X. Chen and H. Wang. "A calculation model for the evaporation recoil pressure in laser material processing". In: *Journal of Physics D: Applied Physics* 34 (2001), pp. 2637–2642. URL: (Link).

[128] D. Lee and S. Jeong. "Analysis of recoil force during Nd:YAG laser ablation of silicon". In: *Applied Physics A* 79.4-6 (2004), pp. 1341–1344. ISSN: 0947-8396. DOI: 10.1007/s00339-004-2767-y. URL: (Link).

[129] V. Semak and A. Matsunawa. "The role of recoil pressure in energy balance during laser materials processing". In: *Journal of Physics D: Applied Physics* 30 (1997), pp. 2541–2552. URL: (Link).

[130] K.-H. Leitz, H. Koch, A. Otto, and M. Schmidt. "Numerical simulation of process dynamics during laser beam drilling with short pulses". In: *Applied Physics A* 106.4 (2011), pp. 885–891. ISSN: 0947-8396. DOI: 10.1007/s00339-011-6702-8. URL: (Link).

[131] S. P. Harimkar, A. N. Samant, and N. B. Dahotre. "Temporally evolved recoil pressure driven melt infiltration during laser surface modifications of porous alumina ceramic". In: *Journal of Applied Physics* 101.5 (2007), p. 054911. ISSN: 00218979. DOI: 10.1063/1.2710288. URL: (Link).

[132] M. Hendijanifard and D. a. Willis. "Nanosecond Time-Resolved Measurements of Transient Hole Opening During Laser Micromachining of an Aluminum Film". In: *Journal of Heat Transfer* 135.9 (2013), p. 091202. ISSN: 0022-1481. DOI: 10.1115/1.4024389. URL: (Link).

[133] J. H. Yoo, S. H. Jeong, R. Greif, and R. E. Russo. "Explosive change in crater properties during high power nanosecond laser ablation of silicon". In: *Journal of Applied Physics* 88.3 (2000), p. 1638. ISSN: 00218979. DOI: 10.1063/1.373865. URL: (Link).

[134] C. Porneala and D. a. Willis. "Observation of nanosecond laser-induced phase explosion in aluminum". In: *Applied Physics Letters* 89.21 (2006), p. 211121. ISSN: 00036951. DOI: 10.1063/1.2393158. URL: (Link).

[135] A. V. Pakhomov, M. S. Thompson, and D. A. Gregory. "Laser-induced phase explosions in lead, tin and other elements: microsecond regime and UV-emission". In: *Journal of Physics D: Applied Physics* 36 (2003), pp. 2067–2075. URL: (Link).

[136] S. G. Demos, R. A. Negres, R. N. Raman, Michael D. Feit, K. R. Manes, and A. M. Rubenchik. "Relaxation dynamics of nanosecond laser superheated material in dielectrics". In: *Optica* 2.8 (2015), pp. 765–772. ISSN: 23342536. DOI: 10.1364/OPTICA.2.000765.

[137] S. G. Demos, R. A. Negres, R. N. Raman, A. M. Rubenchik, and M. D. Feit. "Material response during nanosecond laser induced breakdown inside of the exit surface of fused silica". In: *Laser and Photonics Reviews* 7.3 (2013), pp. 444–452. ISSN: 18638880. DOI: 10.1002/lpor.201200100.

[138] T. Kononenko, V. Kononenko, S. Pimenov, E. Zavedeev, V. Konov, V. Romano, and G. Dumitru. "Effects of pulse duration in laser processing of diamond-like carbon films". In: *Diamond and Related Materials* 14.8 (2005), pp. 1368–1376. ISSN: 09259635. DOI: 10.1016/j.diamond.2005.02.009. URL: (Link).

[139] A. Savvatimskiy. "Experimental electrical resistivity of liquid carbon in the temperature range from 4800 to ∼ 20,000 K". In: *Carbon* 47.10 (2009), pp. 2322–2328. ISSN: 00086223. DOI: 10.1016/j.carbon.2009.04.009. URL: (Link).

[140] A. Savvatimskiy. "Measurements of the melting point of graphite and the properties of liquid carbon (a review for 1963–2003)". In: *Carbon* 43.6 (2005), pp. 1115–1142. ISSN: 00086223. DOI: 10.1016/j.carbon.2004.12.027. URL: (Link).

[141] M. Musella, C. Ronchi, M. Brykin, and M. Sheindlin. "The molten state of graphite: An experimental study". In: *Journal of Applied Physics* 84.5 (1998). ISSN: 00218979. DOI: 10.1063/1.368414. URL: (Link).

[142] C Donnet and A Erdemir. *Tribology of Diamond-like Carbon Films: Fundamentals and Applications*. first. New York, USA: Springer Science + Business Media, 2008, pp. 1–590. ISBN: 9780387498911. DOI: 10.1007/978-0-387-49891-1. URL: (Link).

[143] C. Everson and P. Molian. "Fabrication of polycrystalline diamond microtool using a Q-switched Nd:YAG laser". In: *The International Journal of Advanced Manufacturing Technology* 45.5-6 (2009), pp. 521–530. ISSN: 0268-3768. DOI: 10.1007/s00170-009-1999-6. URL: (Link).

[144] T. Kononenko, V. Ralchenko, A. Bolshakov, V. Konov, P. Allegrini, M. Pacilli, G. Conte, and E. Spiriti. "All-carbon detector with buried graphite pillars in CVD diamond". In: *Applied Physics A* 114.2 (2014), pp. 297–300. ISSN: 0947-8396. DOI: 10.1007/s00339-013-8091-7. URL: (Link).

[145] M. Girolami, P. Allegrini, G. Conte, D. M. Trucchi, V. G. Ralchenko, and S. Salvatori. "Diamond Detectors for UV and X-Ray Source Imaging". In: *IEEE Electron Device Letters* 33.2 (2012), pp. 224–226.

[146] R. S. Sussmann. *CVD Diamond for Electronic Devices and Sensors*. First. Wiley Series in Materials for Electronic & Optoelectronic Applications. Chichester, West Sussex, United Kingdom: John Wiley & Sons, 2009, p. 596. ISBN: 9780470740361. DOI: 10.1002/9780470740392. URL: (Link).

[147] J. V. Beck, A. Osman, and G. Lu. "Maximum temperatures in Diamond Heat Spreaders Using the Surface Element Method". In: *ASME Journal of Heat Transfer* 115.1 (1993), pp. 51–57. DOI: 10.1115/1.2910668. URL: (Link).

[148] H. K. Mao and R. J. Hemley. "Optical transitions in diamond at ultrahigh pressures". In: *Letters to Nature* 351 (1991), pp. 721–724. ISSN: 0028-0836. DOI: 10.1038/351721a0.

[149] G. Zhang, B. Zhang, Z. Deng, and J. Chen. "An Experimental Study on Laser Cutting Mechanisms of Polycrystalline Diamond Compacts". In: *CIRP Annals - Manufacturing Technology* 56.1 (2007), pp. 201–204. ISSN: 00078506. DOI: 10.1016/j.cirp.2007.05.049.

[150] M. D. Shirk, P. A. Molian, and A. P. Malshe. "Ultrashort pulsed laser ablation of diamond". In: *Journal of Laser Applications* 10.2 (1998), p. 64. ISSN: 1042346X. DOI: 10.2351/1.521822. URL: (Link).

[151] P. Butler-Smith, M. Warhanek, D. Axinte, M. Fay, J. F. Bucourt, R. Ragueneau, and K. Wegener. "The influences of pulsed-laser-ablation and electro-discharge-grinding processes on the cutting performances of polycrystalline diamond micro-drills". In: *CIRP Annals - Manufacturing Technology* 65.1 (2016), pp. 105–108. ISSN: 17260604. DOI: 10.1016/j.cirp.2016.04.008. URL: (Link).

[152] J. Jandeleit, A. Horn, E.-W. Kreutz, and R. Poprawe. *Micromachining of metals and ceramics by nano- and picosecond laser radiation*. 1997. DOI: 10.1117/12.284498. URL: (Link).

[153] F. Dausinger, H. Hugel, and V. I. Konov. "Micromachining with ultrashort laser pulses: from basic understanding to technical applications". In: *SPIE 5147, ALT'02 International Conference on Advanced Laser Technologies*. Vol. 5147. Adelboden, Switzerland: SPIE, 2003, pp. 106–115. DOI: 10.1117/12.537496. URL: (Link).

[154] H. Ohfuji, T. Okuchi, S. Odake, H. Kagi, H. Sumiya, and T. Irifune. "Micro-/nanostructural investigation of laser-cut surfaces of single- and polycrystalline diamonds". In: *Diamond and Related Materials* 19.7-9

(2010), pp. 1040–1051. ISSN: 09259635. DOI: 10.1016/j.diamond.2010.02.015. URL: (Link).

[155] M Seal. "Graphitization of diamond". In: *Nature* 185 (1960), pp. 522–523. URL: (Link).

[156] F. S. Phinney. "Graphitization of Diamond." In: *Science* 120.3114 (1954), pp. 393–4. ISSN: 0036-8075. DOI: 10.1126/science.120.3114.393. URL: (Link).

[157] G. Davies and T. Evans. "Graphitization of diamond at zero pressure and at a high pressure". In: *Proceedings of the Royal Society of London* 328 (1972), pp. 413–427. ISSN: 1364-5021. DOI: 10.1098/rspa.1974.0120.

[158] Q. Wu, J. Wang, C. Huang, and H. Li. "Temperature evolution and material removal mechanisms in nanosecond-pulsed laser ablation of polycrystalline diamond". In: *Proceedings of the Institution of Mechanical Engineers, Part B: Journal of Engineering Manufacture* 229.8 (2015), pp. 1357–1372. ISSN: 20412975 09544054. DOI: 10.1177/0954405414535773.

[159] V. Strekalov, V. Konov, V. Kononenko, and S. Pimenov. "Early stages of laser graphitization of diamond". In: *Applied Physics A: Materials Science & Processing* 76.4 (2003), pp. 603–607. ISSN: 0947-8396. DOI: 10.1007/s00339-002-2014-3. URL: (Link).

[160] J.-F. Lin, J.-W. Lin, and P.-J. Wei. "Thermal analysis for graphitization and ablation depths of diamond films". In: *Diamond and Related Materials* 15.1 (2006), pp. 1–9. ISSN: 09259635. DOI: 10.1016/j.diamond.2005.03.012. URL: (Link).

[161] V. Tangwarodomnukun, P. Likhitangsuwat, O. Tevinpibanphan, and C. Dumkum. “Laser ablation of titanium alloy under a thin and flowing water layer”. In: *International Journal of Machine Tools and Manufacture* 89 (2015), pp. 14–28. ISSN: 08906955. DOI: 10.1016/j.ijmachtools.2014.10.013. URL: (Link).

[162] D. Dhupal, B. Doloi, and B. Bhattacharyya. “Pulsed Nd:YAG laser turning of micro-groove on aluminum oxide ceramic (Al2O3)”. In: *International Journal of Machine Tools and Manufacture* 48 (2008), pp. 236–248. ISSN: 08906955. DOI: 10.1016/j.ijmachtools.2007.08.016.

[163] A. N. Samant and N. B. Dahotre. “Laser machining of structural ceramicsâĂŤA review”. In: *Journal of the European Ceramic Society* 29.6 (2009), pp. 969–993. ISSN: 09552219. DOI: 10.1016/j.jeurceramsoc.2008.11.010. URL: (Link).

[164] P. Butler-Smith, D. Axinte, and M. Daine. “Ordered diamond micro-arrays for ultra-precision grinding – An evaluation in Ti-6Al-4V”. In: *International Journal of Machine Tools and Manufacture* 51.1 (2011), pp. 54–66. ISSN: 08906955. DOI: 10.1016/j.ijmachtools.2010.09.006. URL: (Link).

[165] C. Dold, M. Henerichs, P. Gilgen, and K. Wegener. “Laser processing of coarse grain polycrystalline diamond (PCD) cutting tool inserts using picosecond laser pulses”. In: *Physics Procedia* 41 (2013), pp. 610–616. ISSN: 18753892. DOI: 10.1016/j.phpro.2013.03.123. URL: (Link).

[166] C. Walter, M. Rabiey, M. Warhanek, N. Jochum, and K. Wegener. “Dressing and truing of hybrid bonded CBN grinding tools using a short-pulsed fibre laser”. In: *CIRP Annals - Manufacturing Technology*

61.1 (2012), pp. 279–282. ISSN: 00078506. DOI: 10.1016/j.cirp.2012.03.001. URL: (Link).

[167] H. J. Booth. "Recent applications of pulsed lasers in advanced materials processing". In: *Thin Solid Films* 453-454 (2004), pp. 450–457. ISSN: 00406090. DOI: 10.1016/j.tsf.2003.11.130.

[168] J Meijer, K Du, and A Gillner. "Laser machining by short and ultrashort pulses, state of the art and new opportunities in the age of the photons". In: *CIRP Annals - Manufacturing Technology* 51.2 (2002), pp. 531–550. URL: (Link).

[169] D. Von Der Linde and K. Sokolowski-Tinten. "The physical mechanisms of short-pulse laser ablation". In: *Applied Surface Science* 154–155 (2000), pp. 1–10.

[170] P. W. Butler-Smith, D. A. Axinte, and M. Daine. "Preferentially oriented diamond micro-arrays: A laser patterning technique and preliminary evaluation of their cutting forces and wear characteristics". In: *International Journal of Machine Tools and Manufacture* 49.15 (2009), pp. 1175–1184. ISSN: 08906955. DOI: 10.1016/j.ijmachtools.2009.08.007. URL: (Link).

[171] P. Parandoush and A. Hossain. "A review on modelling and simulation of laser beam machining". In: *International Journal of Machine Tools and Manufacture* 85 (2014), pp. 135–145. ISSN: 08906955. DOI: 10.1016/j.ijmachtools.2014.05.008. URL: (Link).

[172] G. Pastras, A. Fysikopoulos, P. Stavropoulos, and G. Chryssolouris. "An approach to modelling evaporation pulsed laser drilling and its energy efficiency". In: *The International Journal of Advanced Manufacturing Technology* 72 (2014), pp. 1227–1241. ISSN: 0268-3768. DOI: 10.1007/s00170-014-5668-z. URL: (Link).

[173] A. S. Holmes, A. I. Onischenko, D. S. George, and J. E. Pedder. "Modelling of solid-state and excimer laser processes for 3D micro-machining". In: *SPIE Proceeding*. Vol. 5713. Williamsburg VA, USA, 2005, pp. 1–10. DOI: 10.1117/12.600632.

[174] J. Billingham, C. B. Miron, D. A. Axinte, and M. C. Kong. "Mathematical modelling of abrasive waterjet footprints for arbitrarily moving jets: Part II — Overlapped single and multiple straight paths". In: *International Journal of Machine Tools and Manufacture* 68 (2013), pp. 30–39. ISSN: 08906955. DOI: 10.1016/j.ijmachtools.2013.01.003. URL: (Link).

[175] M. C. Kong, S. Anwar, J. Billingham, and D. A. Axinte. "Mathematical modelling of abrasive waterjet footprints for arbitrarily moving jets: Part I — single straight paths". In: *International Journal of Machine Tools and Manufacture* 53 (2012), pp. 58–68. ISSN: 0890-6955. DOI: 10.1016/j.ijmachtools.2011.09.010. URL: (Link).

[176] P Lozano Torrubia, J Billingham, and D. A. Axinte. "Stochastic simplified modelling of abrasive waterjet footprints". In: *Proceedings of the Royal Society A: Mathematical, Physical and Engineering Sciences* 472.20150836 (2016). DOI: 10.1098/rspa.2015.0836.

[177] P. Torrubia Lozano. "Stochastic modelling of abrasive waterjet controlled-depth machining". PhD thesis. University of Nottingham, 2016, pp. 1–276.

[178] D. A. Axinte, D. S. Srinivasu, J. Billingham, and M. Cooper. "Geometrical modelling of abrasive waterjet footprints: A study for 90 °jet impact angle". In: *CIRP Annals - Manufacturing Technology* 59.1 (2010), pp. 341–346. ISSN: 0007-8506. DOI: 10.1016/j.cirp.2010.03.112. URL: (Link).

[179] A. Grudinin, D. Payne, P. Turner, L. Nilsson, M. Zervas, M. Ibsen, and M. Durkin. *Multi-fibre arrangements for high power fibre lasers and amplifiers*. 2004.

[180] SPI Lasers UK, Ltd. *G3.0 Pulsed Fibre Laser*. Tech. rep. 2007, pp. 1 –105.

[181] D. Rowe. *CRC Handbook of Thermoelectrics*. CRC Press, 1995, p. 701. ISBN: 9781420049718. URL: (Link).

[182] *ISO 11146-1: Lasers and laser-related equipment — Test methods for laser beam widths, divergence angles and beam propagation ratios — Part 1: Stigmatic and simple astigmatic beams*. Tech. rep. International standard organization, 2005, p. 23. URL: (Link).

[183] *ISO 11146-2: Lasers and laser-related equipment — Test methods for laser beam widths, divergence angles and beam propagation ratios — Part 2 : General astigmatic beams*. Tech. rep. International Standard Organization, 2005, p. 22. URL: (Link).

[184] V. Tangwarodomnukun, J. Wang, C. Huang, and H. Zhu. "Heating and material removal process in hybrid laser-waterjet ablation of silicon substrates". In: *International Journal of Machine Tools and Manufacture* 79 (2014), pp. 1–16. ISSN: 08906955. DOI: 10.1016/j.ijmachtools.2013.12.003. URL: (Link).

[185] A. Bilbao-Guillerna, J. Billingham, D. A. Axinte, and G. B. J. Cadot. "Waterjet and Laser Etching : The Non-Linear Inverse Problem". In: *Royal Society Open Science – Under Review* – (2017), pp. 1–22.

[186] E. Abbe. "Über einen neuen Beleuchtungsapparat am Mikroskop". In: *Archiv für mikroskopische Anatomie* 9 (1873), pp. 469–480. DOI: 10.1007/BF02956173. URL: (Link).

[187] P. F. Schmidt, L. J. Balk, and R. Blaschke. *Praxis der Rasterelektronenmikroskopie und Mikrobereichsanalyse*. Renningen: Expert Vlg., 2002. ISBN: 3816910386.

[188] H. J. Butler, L. Ashton, B. Bird, G. Cinque, K. Curtis, K. Esmonde-white, N. J. Fullwood, B. Gardner, P. L. Martin, M. J. Walsh, M. R. Mcainsh, N. Stone, F. L. Martin, H. J. Butler, and P. L. Martin-hirsch. "Using Raman spectroscopy to characterise biological materials". In: *Nature Protocols* 11.4 (2016), pp. 1–47. ISSN: 1754-2189. DOI: 10.1038/nprot.2016.036. URL: (Link).

[189] T. Bocklitz, A. Walter, K. Hartmann, P. R osch, and J. Popp. "How to pre-process Raman spectra for reliable and stable models?" In: *Analytica Chimica Acta* 704.1-2 (2011), pp. 47–56. ISSN: 00032670. DOI: 10.1016/j.aca.2011.06.043.

[190] A. C. Ferrari. "Raman spectroscopy of graphene and graphite: Disorder, electron-phonon coupling, doping and nonadiabatic effects". In: *Solid State Communications* 143.1-2 (2007), pp. 47–57. ISSN: 00381098. DOI: 10.1016/j.ssc.2007.03.052. arXiv: arXiv:0709.1174v1.

[191] P. Szirmai, T. Pichler, O. A. Williams, S. Mandal, C. Bäuerle, and F. Simon. "A detailed analysis of the Raman spectra in superconducting boron doped nanocrystalline diamond". In: *Physica Status Solidi (B) Basic Research* 249.12 (2012), pp. 2656–2659. ISSN: 03701972. DOI: 10.1002/pssb.201200461. arXiv: arXiv:1204.5305v1.

[192] A. C. Ferrari and J. Robertson. "Raman spectroscopy of amorphous, nanostructured, diamond-like carbon, and nanodiamond." In: *Philosophical transactions. Series A, Mathematical, physical, and engineering sciences* 362.1824 (2004), pp. 2477–2512. ISSN: 1364-503X. DOI: 10.1098/rsta.2004.1452.

[193] C. Neumann, S. Reichardt, P. Venezuela, M. Drögeler, L. Banszerus, M. Schmitz, K. Watanabe, T. Taniguchi, F. Mauri, B. Beschoten, S. V. Rotkin, and C. Stampfer. "Raman spectroscopy as probe of nanometre-scale strain variations in graphene". In: *Nature Communications* 6.May (2015), p. 8429. ISSN: 2041-1723. DOI: 10.1038/ncomms9429. arXiv: arXiv:1406.7771v2. URL: (Link).

[194] V. A. Krivchenko, D. V. Lopaev, P. V. Minakov, V. G. Pirogov, a. T. Rakhimov, and N. V. Suetin. "Study of polycrystalline boron-doped diamond films by Raman spectroscopy and optical absorption spectroscopy". In: *Technical Physics* 52.11 (2007), pp. 1471–1474. ISSN: 1063-7842. DOI: 10.1134/S106378420711014X.

[195] S. Stehlik, M. Varga, M. Ledinsky, V. Jirasek, A. Artemenko, H. Kozak, L. Ondic, V. Skakalova, G. Argentero, T. Pennycook, J. C. Meyer, A. Fejfar, A. Kromka, and B. Rezek. "Size and Purity Control of HPHT Nanodiamonds down to 1 nm". In: *Journal of Physical Chemistry C* 119.49 (2015), pp. 27708–27720. ISSN: 19327455. DOI: 10.1021/acs.jpcc.5b05259.

[196] A. Ferrari and J. Robertson. "Interpretation of Raman spectra of disordered and amorphous carbon". In: *Physical Review B* 61.20 (2000), pp. 14095–14107. ISSN: 0163-1829. DOI: 10.1103/PhysRevB.61.14095.

[197] S. Reich and C. Thomsen. "Raman spectroscopy of graphite." In: *Philosophical transactions. Series A, Mathematical, physical, and engineering sciences* 362.1824 (2004), pp. 2271–2288. ISSN: 1364-503X. DOI: 10.1098/rsta.2004.1454. URL: (Link).

[198] C. A. Lieber and A. Mahadevan-Jansen. "Automated Method for Subtraction of Fluorescence from Biological Raman Spectra". In: *Appl. Spectrosc.* 57.11 (2003), pp. 1363–1367. URL: (Link).

[199] S. Li and L. Dai. "An Improved Algorithm to Remove Cosmic Spikes in Raman Spectra for Online Monitoring". In: *Appl. Spectrosc.* 65.11 (2011), pp. 1300–1306. URL: (Link).

[200] A. Ferrari and D. Basko. "Raman spectroscopy as a versatile tool for studying the properties of graphene". In: *Nature nanotechnology* 8.4 (2013), pp. 235–46. ISSN: 1748-3395. DOI: 10.1038/nnano.2013.46. arXiv: arXiv:1306.5856v1. URL: (Link).

[201] J. Schwan, S. Ulrich, V. Batori, H. Ehrhardt, and S. Silva. "Raman spectroscopy on amorphous carbon films". In: *Journal of Applied Physics* 80.1 (1996), p. 440. ISSN: 00218979. DOI: 10.1063/1.362745. URL: (Link).

[202] W. S. Bacsa, J. S. Lannin, D. L. Pappas, and J. J. Cuomo. "Raman scattering of laser-deposited amorphous carbon". In: *Physical Review B* 47.16 (1993), pp. 10931–10934. ISSN: 01631829. DOI: 10.1103/PhysRevB.47.10931.

[203] A. C. Ferrari and J. Robertson. "Resonant Raman spectroscopy of disordered, amorphous, and diamondlike carbon". In: *Physical Review B* 64.7 (2001), p. 075414. ISSN: 0163-1829. DOI: 10.1103/PhysRevB.64.075414. URL: (Link).

[204] M. Birkholz. "Principles of X-ray Diffraction". In: *Thin Film Analysis by X-Ray Scattering*. 1st ed. Weinheim, Germany: Wiley-VCH, 2006. Chap. 1, pp. 1–41. ISBN: 9783527310524. DOI: 10.1002/3527607595.ch1. URL: (Link).

[205] C. D. Gómez-Esparza, F. Baldenebro-López, L. González-Rodelas, J. Baldenebro-López, and R. Martínez-Sánchez. "Series of Nanocrystalline NiCoAlFe(Cr, Cu, Mo, Ti) High-Entropy Alloys produced by Mechanical Alloying". In: *Materials Research* ahead (2016). ISSN: 1980-5373. DOI: 10.1590/1980-5373-MR-2015-0668. URL: (Link).

[206] M. A. O'Keefe, P. R. Buseck, and S. Iijima. *Computed crystal structure images for high resolution electron microscopy*. 1978. DOI: 10.1038/274322a0.

[207] P. Pavliček and O. Hýbl. "Measurement Uncertainty Caused By Surface Roughness". In: *Applied Optics* 47.16 (2008), pp. 2941–2949.

[208] F. Gao, R. K. Leach, J. Petzing, and J. M. Coupland. "Surface measurement errors using commercial scanning white light interferometers". In: *Measurement Science and Technology* 19.1 (2008), p. 015303. ISSN: 0957-0233. DOI: 10.1088/0957-0233/19/1/015303. URL: (Link).

[209] A. Pförtner and J. Schwider. "Dispersion error in white-light Linnik interferometers and its implications for evaluation procedures". In: *Applied Optics* 40.34 (2001), pp. 6223–6228. DOI: 10.1364/AO.40.006223. URL: (Link).

[210] P. Lehmann, P. Kühnhold, and W. Xie. "Reduction of chromatic aberration influences in vertical scanning white-light interferometry". In: *Measurement Science and Technology* 25.6 (2014), p. 065203. ISSN: 0957-0233. DOI: 10.1088/0957-0233/25/6/065203. URL: (Link).

[211] R. Berger, T. Sure, and W. Osten. *Measurement errors of mirrorlike, tilted objects in white light interferometry*. 2007. DOI: 10.1117/12.726142. URL: (Link).

[212] P. Kühnhold, W. Xie, and P. Lehmann. *Comparison of Michelson and Linnik interference microscopes with respect to measurement capabilities and adjustment efforts*. Ed. by P. H. Lehmann, W. Osten, and A. Albertazzi. 13–16 May 2013, Munich, Germany, 2013. DOI: 10.1117/12.2020250. URL: (Link).

[213] S. Anwar. "Modelling of Abrasive Waterjet Milled Footprints". PhD thesis. Nottingham, 2013, pp. 1–229.

[214] Taylor Hobson Precision. *High-resolution 3D Surface Profiling systems*. Tech. rep. Leicester: Taylor Hobson Precision, 2008, pp. 1 –16. URL: (Link).

[215] M. R. H. Knowles, G. Rutterford, D. Karnakis, and A. Ferguson. "Micro-machining of metals, ceramics and polymers using nanosecond lasers". In: *International Journal of Advanced Manufacturing Technology* 33.1-2 (2007), pp. 95–102. ISSN: 02683768. DOI: 10.1007/s00170-007-0967-2. URL: (Link).

[216] C. Z. Wang, K. M. Ho, M. D. Shirk, and P. A. Molian. "Laser-Induced Graphitization on a Diamond (111) Surface". In: *Physical Review Letters* 85.19 (2000), pp. 4092–4095.

[217] R. K. Singh, O. W. Holland, and J. Narayan. "Theoretical model for deposition of superconducting thin films using pulsed laser evaporation technique". In: *Journal of Applied Physics* 68.1 (1990), p. 233. ISSN: 00218979. DOI: 10.1063/1.347123. URL: (Link).

[218] D. Marla, U. V. Bhandarkar, and S. S. Joshi. "Transient Analysis of Laser Ablation Process With Plasma Shielding: One-Dimensional Model Using Finite Volume Method". In: *Journal of Micro and Nano-Manufacturing* 1.1 (2013), p. 011007. ISSN: 2166-0468. DOI: 10.1115/1.4023287. URL: (Link).

[219] A. Bulgakov and N. Bulgakova. "Thermal model of pulsed laser ablation under the conditions of formation and heating of a radiation-absorbing plasma". In: *Quantum Electronics* 433.29 (1999), pp. 433–437. URL: (Link).

[220] G. Lamé and B. P. Clapeyron. "Mémoire sur la solidification par refroidissement d'un globe liquide". In: *Annales de Chimie et de Physique* 47 (1831), pp. 250–256.

[221] L. H. Long, L. Brewer, P. W. Gilles, and F. A. Jenkins. "The Vapor Pressure and Heat of Sublimation of Graphite". In: *The Journal of Chemical Physics* 16.8 (1948), p. 797. ISSN: 00219606. DOI: 10.1063/1.1746999. URL: (Link).

[222] H. Leider, O. Krikorian, and D. Young. "Thermodynamic properties of carbon up to the critical point". In: *Carbon* 11.5 (1973), pp. 555–563. ISSN: 00086223. DOI: 10.1016/0008-6223(73)90316-3. URL: (Link).

[223] V. R. Voller. "An overview of numerical methods for solving phase change problems". In: *Advances in Numerical Heat Transfer*. Ed. by W. J. Minkowycz, E. M. Sparrow, and J. P. Abraham. 1st. Washington, DC: Taylor & Francis, 1996. Chap. Nine, pp. 341–441. ISBN: 978-1-4200-9521-0. DOI: 10.1201/9781420095227.fmatt.

[224] J. W. Demmel, S. C. Eisenstat, J. R. Gilbert, X. S. Li, and J. W. H. Liu. "A supernodal approach to sparse partial pivoting". In: *SIAM J. Matrix Analysis and Applications* 20.3 (1999), pp. 720–755.

[225] Element Six™. *Thermal and Optical Properties of Element Six materials*. ElementSix2016, 2016.

[226] B. Vrolijk. "Optical Grade CVD, Single Crystal Diamond". In: *Element Six ™* (2014), p. 2.

[227] D. Wu, Z. L. Wang, Q Luo, C. Z. Gu, N. L. Wang, C. Y. Li, X. Y. Lu, and Z. S. Jin. "Optical properties of boron-doped diamond". In: *Physical Review B* 73 (2006), pp. 1–5. DOI: 10.1103/PhysRevB.73.012501. arXiv: 0508540v2 [arXiv:cond-mat]. URL: (Link).

[228] F. D. Rossini and R. S. Jessup. "Heat and free energy of formation of carbon dioxide, and of the transition between graphite and diamond". In: *Journal of Research of the National Bureau of Standards* 21.4 (1938), p. 491. ISSN: 0091-0635. DOI: 10.6028/jres.021.028.

[229] T Inushima, A Ogasawara, T Shiraishi, S Ohya, S Karasawa, and H Shiomi. "Optical and electrical investigation of boron-doped homoepitaxial diamond". In: *Diamond and Related Materials* 6.5-7 (1997), pp. 835–838. ISSN: 09259635. DOI: 10.1016/S0925-9635(96)00722-4. URL: (Link).

[230] E. Gheeraert, A. Deneuville, and J. Mambou. "Boron-related infra-red absorption in homoepitaxial diamond films". In: *Diamond and Related Materials* 7.10 (1998), pp. 1509–1512.

[231] M. Ficek, M. Sobaszek, M. Gnyba, J. Ryl, Ł. Gołuński, M. Smietana, J. Jasiński, P. Caban, and R. Bogdanowicz. "Optical and electrical properties of boron doped diamond thin conductive films deposited on fused silica glass substrates". In: *Applied Surface Science* 387 (2016), pp. 846–856. ISSN: 01694332. DOI: 10.1016/j.apsusc.2016.06.165. URL: (Link).

[232] D. Prikhodko, S. Tarelkin, V. Bormashov, A. Golovanov, M. Kuznetsov, D. Teteruk, A. Volkov, and S. Buga. "Thermal conductivity of synthetic boron-doped single-crystal HPHT diamond from 20 to 400 K". In: *MRS Communications* 6.2 (2016), pp. 71–76. ISSN: 2159-6859. DOI: 10.1557/mrc.2016.12. URL: (Link).

[233] S. A. Herr, J. V. Beck, J. J. McGrath, S. Sahli, and M. Aslam. "An optimized experimental method for measuring thermal conductivity of thin, boron-doped diamond films". In: *Review of Scientific Instruments* 66.10 (1995), p. 4967. ISSN: 00346748. DOI: 10.1063/1.1146182. URL: (Link).

[234] C Moelle, M Werner, F Sz ucs, D. Wittorf, M. Sellschopp, J. von Borany, H.-J. Fecht, and C. Johnston. "Specific heat of single-, poly- and nanocrystalline diamond". In: *Diamond and Related Materials* 7 (1998), pp. 499–503. ISSN: 09259635. DOI: 10.1016/S0925-9635(97)00202-1. URL: (Link).

[235] E. A. Ekimov, V. Ralchenko, and A. Popovich. "Synthesis of superconducting boron-doped diamond compacts with high elastic moduli and thermal stability". In: *Diamond and Related Materials* 50 (2014), pp. 15–19. ISSN: 09259635. DOI: 10.1016/j.diamond.2014.09.001. URL: (Link).

[236] E. V. Ivakin, A. V. Sukhodolov, V. G. Ralchenko, A. V. Vlasov, and A. V. Khomich. "Measurement of thermal conductivity of polycrystalline CVD diamond by laser-induced transient grating technique". In: *Quantum Electronics* 32.4 (2007), pp. 367–372. ISSN: 1063-7818. DOI: 10.1070/QE2002v032n04ABEH002200.

[237] B. Wu and Y. C. Shin. "Absorption coefficient of aluminum near the critical point and the consequences on high-power nanosecond laser ablation". In: *Applied Physics Letters* 89.11 (2006), p. 111902. ISSN: 00036951. DOI: 10.1063/1.2352804. URL: (Link).

[238] A. Libassi, A. C. Ferrari, V. Stolojan, B. K. Tanner, J. Robertson, and L. M. Brown. "Density, sp3 content and internal layering of DLC films by X-ray reflectivity and electron energy loss spectroscopy".

In: *Diamond and Related Materials* 9.3 (2000), pp. 771–776. ISSN: 09259635. DOI: 10.1016/S0925-9635(99)00233-2.

[239] H. Schulz, H. J. Scheibe, P. Siemroth, and B. Schultrich. "Pulsed arc deposition of super-hard amorphous carbon films". In: *Applied Physics A: Materials Science & Processing* 78.5 (2004), pp. 675–679. ISSN: 09478396. DOI: 10.1007/s00339-003-2280-8.

[240] J. I. Larruquert, L. V. Rodriguez-de Marcos, J. A. Mendez, P. J. Martin, and A Bendavid. "High reflectance ta-C coatings in the extreme ultraviolet". In: *Optics Express* 21.23 (2013), pp. 435–438. ISSN: 10944087. DOI: 10.1364/OE.21.027537. URL: (Link).

[241] M. Hakovirta, J. E. Vuorinen, X. M. He, M. Nastasi, and R. B. Schwarz. "Heat capacity of hydrogenated diamond-like carbon films". In: *Applied Physics Letters* 77.15 (2000), p. 2340. ISSN: 00036951. DOI: 10.1063/1.1290387. URL: (Link).

[242] M. Shamsa, W. L. Liu, A. A. Balandin, C. Casiraghi, W. I. Milne, and A. C. Ferrari. "Thermal conductivity of diamond-like carbon films". In: *Applied Physics Letters* 89.16 (2006), pp. 1–3. ISSN: 00036951. DOI: 10.1063/1.2362601.

[243] B. Tay, X Shi, L. Cheah, and D. Flynn. "Optical properties of tetrahedral amorphous carbon films determined by spectroscopic ellipsometry". In: *Thin Solid Films* 308-309 (1997), pp. 268–272. ISSN: 00406090. DOI: 10.1016/S0040-6090(97)00425-2.

[244] D. S. Grierson, A. V. Sumant, A. R. Konicek, T. A. Friedmann, J. P. Sullivan, R. W. Carpick, D. S. Grierson, A. V. Sumant, A. R. Konicek, T. A. Friedmann, and J. P. Sullivan. "Thermal stability and rehybridization of carbon bonding in tetrahedral amorphous carbon Thermal stability and rehybridization of carbon bonding in

tetrahedral". In: *Journal of Applied Physics* 107 (2010), p. 033523. DOI: 10.1063/1.3284087.

[245] A. C. Ferrari, S. E. Rodil, J. Robertson, and W. I. Milne. "Is stress necessary to stabilise sp3 bonding in diamond-like carbon?" In: *Diamond and Related Materials* 11.3-6 (2002), pp. 994–999. ISSN: 09259635. DOI: 10.1016/S0925-9635(01)00705-1.

[246] A. I. Savvatimskiy. "Liquid carbon density and resistivity." In: *Journal of physics. Condensed matter : an Institute of Physics journal* 20.11 (2008), p. 114112. ISSN: 0953-8984. DOI: 10.1088/0953-8984/20/11/114112. URL: (Link).

[247] A. B. Djurišić and E. H. Li. "Optical properties of graphite". In: *Journal of Applied Physics* 85.10 (1999), p. 7404. ISSN: 00218979. DOI: 10.1063/1.369370. URL: (Link).

[248] A. M. Malvezzi and N. Bloembergen. "Time-Resolved Picosecond Optical Measurements of Laser-Excited Graphite". In: *Physical Review Letters* 57.1 (1986), pp. 146–149.

[249] M. Akoshima, B. Hay, J. Zhang, L. Chapman, and T. Baba. "International Comparison on Thermal-Diffusivity Measurements for Iron and Isotropic Graphite Using the Laser Flash Method in CCT-WG9". In: *International Journal of Thermophysics* 34.5 (2012), pp. 763–777. ISSN: 0195-928X. DOI: 10.1007/s10765-012-1209-x. URL: (Link).

[250] G. Pottlacher, R. Hixson, S. Melnitzky, E. Kaschnitz, M. Winkler, and H. Jäger. "Thermophysical properties of POCO AXF-5Q graphite up to melting". In: *Thermochimica Acta* 218 (1993), pp. 183–193. ISSN: 00406031. DOI: 10.1016/0040-6031(93)80421-6. URL: (Link).

[251] V. N. Korobenko, A. I. Savvatimski, and R. Cheret. "Graphite Melting and Properties of Liquid Carbon". In: *International Journal of Thermophysics* 20.4 (1999), pp. 1247–1256. ISSN: 0195928X. URL: (Link).

[252] A. M. K. Fujii. "Effect of Nanoporosity on the Thermal Conductivity of Amorphous Carbon". PhD thesis. University of California, 2014, pp. 1–64. URL: (Link).

[253] M. Komlenok, S. Pimenov, V. V. Kononenko, V. I. Konov, and H.-J. Scheibe. "Laser Microstructuring of the surface of ta-C films". In: *Journal of Nano and Microsystem technique* 3 (2008), pp. 48–53.

[254] N Dubrovinskaia, R Wirth, J Wosnitza, T Papageorgiou, H. F. Braun, N Miyajima, and L Dubrovinsky. "An insight into what superconducts in polycrystalline boron-doped diamonds based on investigations of microstructure." In: *Proceedings of the National Academy of Sciences of the United States of America* 105.33 (2008), pp. 11619–11622. ISSN: 0027-8424. DOI: 10.1073/pnas.0801520105.

[255] D. W. Hogg, J. Bovy, and D. Lang. "Data analysis recipes: Fitting a model to data". In: *eprint arXiv* 1008 (2010), p. 4686. DOI: arxiv.org/abs/1008.4686. arXiv: 1008.4686. URL: (Link).

[256] V. Morel, A. Bultel, and B. G. Chéron. "Modeling of thermal and chemical non-equilibrium in a laser-induced aluminum plasma by means of a Collisional-Radiative model". In: *Spectrochimica Acta - Part B Atomic Spectroscopy* 65.9-10 (2010), pp. 830–841. ISSN: 05848547. DOI: 10.1016/j.sab.2010.08.002. URL: (Link).

[257] D. Foreman-Mackey. "corner.py: Scatterplot matrices in Python". In: *The Journal of Open Source Software* 1.2 (2016), pp. 1–2. DOI: 10.21105/joss.00024. URL: (Link).

[258] N. H. Abel. "Auflösung einer mechanischen Aufgabe". In: *Journal fur die reine und angewandte Mathematik* 1 (1826), pp. 153–157.

[259] D. J. Schrock, D. Kang, T. R. Bieler, and P. Kwon. "Phase Dependent Tool Wear in Turning Ti-6Al-4V Using Polycrystalline Diamond and Carbide Inserts". In: *Journal of Manufacturing Science and Engineering* 136.4 (2014), p. 041018. ISSN: 1087-1357. DOI: 10.1115/1.4027674. URL: (Link).

[260] I. Beniaminy and M. Deutsch. "ABEL: Stable, high accuracy program for the inversion of Abel's integral equation". In: *Computer Physics Communications* 27.4 (1982), pp. 415–422. ISSN: 0010-4655. DOI: 10.1016/0010-4655(82)90102-3. URL: (Link).

[261] J. Weima, A. Zaitsev, R. Job, G. Kosaca, F. Blum, G. Grabosch, W. Fahrner, and J. Knopp. "Investigation of non-diamond carbon phases and optical centers in thermochemically polished polycrystalline CVD diamond films". In: *Journal of Solid State Electrochemistry* 4 (2000), pp. 425–434.

[262] A. Bilbao Guillerna, D. Axinte, and J. Billingham. "The linear inverse problem in energy beam processing with an application to abrasive waterjet machining". In: *International Journal of Machine Tools and Manufacture* 99 (2015), pp. 34–42. ISSN: 08906955. DOI: 10.1016/j.ijmachtools.2015.09.006. URL: (Link).

[263] G. Clair and D. L'Hermite. "1D modelling of nanosecond laser ablation of copper samples in argon at P = 1 atm with a wavelength of 532 nm". In: *Journal of Applied Physics* 110.8 (2011). ISSN: 00218979. DOI: 10.1063/1.3651497.

[264] A. V. Gusarov and I. Smurov. "Thermal model of nanosecond pulsed laser ablation: Analysis of energy and mass transfer". In: *Journal*

of Applied Physics 97.1 (2005). ISSN: 00218979. DOI: 10.1063/1.1827321.

[265] R. J. Conant, K. L. Telschow, and J. B. Walter. "Mathematical modeling of laser ablation in liquids with application to laser ultrasonics." In: *Ultrasonics* 40.10 (2002), pp. 1065–1077. ISSN: 0041-624X. DOI: 10.1016/S0041-624X(02)00257-3. URL: (Link).

[266] V. Morel. "Dynamique de la création d'un plasma d'aluminium induit par laser : Élaboration et validation d'un modèle collisionnel-radiatif". PhD thesis. Université de Rouen, 2011, p. 296.

[267] V. Mazhukin, V. Nossov, and I Smurov. "Analysis of laser-induced evaporation of Al target under conditions of vapour plasma formation". In: *Thin Solid Films* 453-454 (2004), pp. 353–361. ISSN: 00406090. DOI: 10.1016/j.tsf.2003.11.104. URL: (Link).

[268] NIST-ASD-Team. "NIST Atomic Spectra Database (ver. 6.0)". In: *http://physics.nist.gov/asd* (2016). URL: (Link).

[269] G. M. Weyl and D. Rosen. "Laser-induced breakdown in argon at 0.35 μ m: Theory and experiments". In: *Physical Review A* 31.4 (1985), pp. 2300–2313. ISSN: 0556-2791. DOI: 10.1103/PhysRevA.31.2300. URL: (Link).

[270] I. B. Zeldovich, I. P. Raizer, W. D. Hayes, and R. F. Probstein. *Physics of shock waves and high-temperature hydrodynamic phenomena*. Ed. by W. D. Hayes. 1st. London: Academic Press Inc., 1967, p. 916. ISBN: 9780123956729. DOI: 10.1016/B978-0-12-395672-9.50001-1. URL: (Link).

[271] H. W. Drawin. *Collision and transport cross-sections*. DPh-PFC/SR. Fontenay-aux-Roses: European Atomic Energy Community, Commis-

sariat a l'Energie Atomique, Centre d'Etudes Nucleaires, 1967, p. 383. URL: (Link).

[272] V. Morel, A. Bultel, and B. G. Chéron. "The Critical Temperature of Aluminum". In: *International Journal of Thermophysics* 30.6 (2009), pp. 1853–1863. ISSN: 0195-928X. DOI: 10.1007/s10765-009-0671-6. URL: (Link).

[273] A. Müsing, U. Riedel, J. Warnatz, W. Herden, and H. Ridderbusch. "Laser-induced breakdown in air and behind droplets: A detailed Monte-Carlo simulation". In: *Proceedings of the Combustion Institute* 31.2 (2007), pp. 3007–3014. ISSN: 15407489. DOI: 10.1016/j.proci.2006.07.185.

[274] T. Holstein. "Imprisonment of Resonance Radiation in Gases". In: *Physical Review* 72.12 (1947), pp. 1212–1233. ISSN: 0031-899X. DOI: 10.1103/PhysRev.72.1212. URL: (Link).

[275] L. D. Pietanza, G. Colonna, A. De Giacomo, and M. Capitelli. "Kinetic processes for laser induced plasma diagnostic: A collisional-radiative model approach". In: *Spectrochimica Acta - Part B Atomic Spectroscopy* 65.8 (2010), pp. 616–626. ISSN: 05848547. DOI: 10.1016/j.sab.2010.03.012. URL: (Link).

[276] Y. S. Kim and R. H. Pratt. "Direct radiative recombination of electrons with atomic ions: Cross sections and rate coefficients". In: *Physical Review A* 27.6 (1983), pp. 2913–2924. ISSN: 0556-2791. DOI: 10.1103/PhysRevA.27.2913. URL: (Link).

[277] S. Ali. "Electron - ion recombination data for plasma applications". PhD thesis. Stockholm University, 2012, p. 64. ISBN: 9789174474978.

[278] J. D. Huba. *NRL PLASMA FORMULARY Supported by The Office of Naval Research*. Tech. rep. Washington, DC: The Office for Naval Research, 2013, pp. 1–71. DOI: 10.1109/MEI.2003.1178121. URL: (Link).

[279] J. W. Cooper and J. B. Martin. "Electron Photodetachment from Ions and Elastic Collision Cross Sections for 0, C, Cl, and F". In: *Physical Review* 126.4 (1962), pp. 1482–1488.

[280] H. Yuan-zhong and W. Hui. "Elastic cross sections for electron-carbon scattering". In: *Chinese Physics* 16.01 (2007), pp. 0072–05. ISSN: 0028-0836. DOI: 10.1038/196844a0. arXiv: arXiv:0902.0270.

[281] J. V. Macpherson. "A practical guide to using boron doped diamond in electrochemical research". In: *Physical chemistry chemical physics* 17.5 (2015), pp. 2935–2949. ISSN: 1463-9076. DOI: 10.1039/C4CP04022H. URL: (Link).

[282] H. Pang, X. Wang, G. Zhang, H. Chen, G. Lv, and S. Yang. "Characterization of diamond-like carbon films by SEM, XRD and Raman spectroscopy". In: *Applied Surface Science* 256.21 (2010), pp. 6403–6407. ISSN: 01694332. DOI: 10.1016/j.apsusc.2010.04.025.

[283] W. Ji, R. I. Todd, W. Wang, H. Wang, J. Zhang, and Z. Fu. "Transient liquid phase spark plasma sintering of B4C-based ceramics using Ti-Al intermetallics as sintering aid". In: *Journal of the European Ceramic Society* 36.10 (2016), pp. 2419–2426. ISSN: 1873619X. DOI: 10.1016/j.jeurceramsoc.2016.03.028. URL: (Link).

[284] P. W. May, W. J. Ludlow, M. Hannaway, P. J. Heard, J. A. Smith, and K. N. Rosser. "Raman and conductivity studies of boron-doped microcrystalline diamond, facetted nanocrystalline diamond and cauliflower

diamond films". In: *Diamond and Related Materials* 17.2 (2008), pp. 105–117. ISSN: 09259635. DOI: 10.1016/j.diamond.2007.11.005.

[285] M. Pimenta, G. Dresselhaus, M. Dresselhaus, L. Cançado, A. Jorio, and R. Saito. "Studying disorder in graphite-based systems by Raman spectroscopy". In: *Physical Chemistry Chemical Physics* 9.11 (2007), pp. 1276–1291. ISSN: 1463-9076. DOI: 10.1039/b613962k. URL: (Link).

[286] F. Tuinstra and L. Koenig. "Raman Spectrum of Graphite". In: *The Journal of Chemical Physics* 53.1970 (1970), pp. 1126–1130. ISSN: 00219606. DOI: 10.1063/1.1674108. arXiv: arXiv:1011.1669v3. URL: (Link).

[287] K Watanabe, T Hoshi, and S Yoshimura. "HIGH-QUALITY AND HIGHLY ORIENTED GRAPHITE BLOCK FROM POLYCONDENSATION POLYMER FILMS". In: *Carbon* 30.2 (1992), pp. 255–262.

[288] K. Edalati, T. Daio, Y. Ikoma, M. Arita, and Z. Horita. "Graphite to diamond-like carbon phase transformation by high-pressure torsion". In: *Applied Physics Letters* 103.3 (2013). ISSN: 00036951. DOI: 10.1063/1.4816082.

[289] X. D. Zhu, K Narumi, and H Naramoto. "Buckling instability in amorphous carbon films". In: *J. Phys.: Condens. Matter* 19.23 (2007), p. 236227. ISSN: 0953-8984. DOI: 10.1088/0953-8984/19/23/236227. URL: (Link).